Finite Element Analysis to Examine the Mechanical Stimuli Distributions in the Hip with Cam Femoroacetabular Impingement

by

K.C. Geoffrey Ng

A thesis submitted to the Faculty of Graduate and Postdoctoral Studies
in partial fulfillment of the requirements for the degree of

MASTER OF APPLIED SCIENCE
in Biomedical Engineering

Ottawa-Carleton Institute for Biomedical Engineering
University of Ottawa
Ottawa, Ontario, Canada

January 2011

to Mom and Poys…

my two greatest heroines, inspirations, teachers, coaches, supporters, and fans.

Acknowledgements

It is my utmost pleasure to thank those who have made this research possible. I was privileged to have been supervised by two prominent researchers and professors: Dr. Gholamreza Rouhi of the Department of Mechanical Engineering and Dr. Mario Lamontagne of the School of Human Kinetics. Both Reza and Mario were able to maximize my potential as a researcher in a multi-disciplinary field. Sincere thanks to Reza for his natural ambitious drive and knowledge in bone remodelling, which provided many insights on the area of mechanical stimuli. Sincere thanks to Mario for his influential guidance and experimental expertise, which provided many resources and much of the underlying basis of the research.

I would like to express my sincerest gratitude to Dr. Paul E. Beaulé of the Ottawa Hospital. Paul's leadership in clinical research and feedback provided much of the foundation of our research scope. His active participation represented the collaboration of our multi-disciplinary study and the significant assimilation between emerging engineering principles and orthopaedic applications.

I would like to give special thanks to Dr. Michel Labrosse, Director of the Ottawa-Carleton Institute for Biomedical Engineering, who was always willing and able to help. Michel's guidance in the areas of segmentation and simulations, using 3-D Doctor and ANSYS, was very much appreciated. His superior knowledge in computational finite element modelling and analysis permitted this research to represent the hip joint as an engineering continuum.

Sincere thanks to Mr. Matthew J. Kennedy of the Human Movement Biomechanics Laboratory and to Mr. Andrew D. Speirs of the Ottawa Centre for Joint Restoration. Matthew's previous master's research on the effect of cam femoroacetabular impingement on hip motion provided the patient-specific biomechanics data needed to establish the comparison groups for our finite element simulations. Andrew's input towards the finite element modelling of the hip joint, from an engineering perspective, was very significant towards the realization of our research methodology.

I would also like to thank Mr. Xian Jie Li and Mr. Noam S. Lightstone of the Department of Mechanical Engineering. Their participation and support with computational modelling provided many solutions towards formulating finite element modelling procedures.

Table of Contents

List of Figures

List of Tables

Nomenclature

2-D	two dimensional
3-D	three dimensional
$\propto$	alpha (angle)
$\propto_x$	angular acceleration (rad/s^2)
ε	normal strain
ν	Poisson's ratio
σ	normal stress
σ_i	principal stress
τ	shear stress
a	linear acceleration (m/s^2)
A	area (m^2 unless otherwise specified)
A-P	anterior-posterior (view)
BW	body weight
CAD	computer-aided design
CAM	computer-aided manufacturing
CE	centre-edge (angle)
CT	computed tomography
DICOM	digital imaging and communications in medicine
E	modulus of elasticity; Young's modulus (GPa, MPa, or unless otherwise specified)
F	force (N unless otherwise specified)
FAI	femoroacetabular impingement
FE	finite element
FEA	finite element analysis
FEM	finite element model
g	gravitational constant (m/s^2)
G	shear modulus (GPa)
GPa	gigapascals (10^9 N/m^2)
HRA	hip resurfacing arthroplasty
I_x	moment of inertia (kg·m^2) where subscript *x* denotes the body segment of focus
IGES	initial graphics exchange specification

kPa	kilopascals (10^3 N/m^2)
LCP	Legg-Calvé-Perthes (disease)
m	mass (kg)
M_x	moment (N·m) where subscript x denotes the rigid body segment of focus
MSS	maximum-shear stress
MPa	megapascals (10^6 N/m^2)
MRI	magnetic resonance imaging
NURBS	non-uniform rational B-splines
OA	osteoarthritis
Pa	Pascals (N/m^2)
R	Pearson correlation coefficient
R^2	Coefficient of determination
$r_{CM,d}$	distance from centre of mass (*CM*) to distal (*d*) end body
$r_{CM,p}$	distance from centre of mass (*CM*) to proximal (*p*) end of body
ROI	region of interest
ROM	range of motion
RST	result (ANSYS post-processing) file
SCFE	slipped capital femoral epiphysis
SE	strain energy
SED	strain energy density
S-I	superior-inferior (view)
STL	stereolithography
T_x	torque moment (N·m) where subscript x denotes the body segment of focus
THA/THR	total hip arthroplasty/replacement
VM	von Mises (stress analysis and failure criterion)
X_T	parasolid CAD file

Abstract

Femoroacetabular impingement (FAI) is recognized as a pathomechanical process that leads to hip osteoarthritis (OA). It is hypothesized that mechanical stimuli are prominent at higher range of motions in hips with cam FAI (aspherical femoral head-neck deformity). Adverse loading conditions can impose elevated mechanical stimuli levels at the articulating surfaces and underlying subchondral bone, which plays a predominant mechanical role in early OA. The aim of this research was to determine the levels of mechanical stimuli within the hip, examining the effects of severe cam impingement on the onset of OA, using patient-specific biomechanics data, CT data, and finite element analysis (FEA).

Patient-specific hip joint reaction forces were applied to two symptomatic patient models and two control-matched models, segmented from patient-specific CT data. The finite element models were simulated to compare the locations and magnitudes of mechanical stimuli during two quasi-static positions from standing to squatting. Maximum-shear stress (MSS) was analyzed to determine the adverse loading conditions within the joint and strain energy density (SED) was determined to examine its effect on the initiation of bone remodelling.

The results revealed that peak mechanical stimuli concentrations were found on the antero-superior acetabulum during the squatting position, underlying to the cartilage. The MSS magnitudes were substantially higher and concentrated for the FAI patients (15.145 $\pm$ 1.715 MPa) in comparison with the MSS magnitudes for the control subjects (4.445 $\pm$ 0.085 MPa). The FAI group demonstrated a slight increase in peak SED values on the acetabulum from standing (1.005 $\pm$ 0.076 kPa) to squatting (1.018 $\pm$ 0.082 kPa). Marginal changes in SED values were noticed for the control subjects. Squatting orients the femoral head into the antero-superior acetabulum, increasing the contact area with the cartilage and labral regions, thus resulting in higher peaks behind the cartilage on the acetabulum.

The resultant location of the peak MSS and SED concentrations correspond well with the region of initial cartilage degradation and early OA observed during open surgical dislocation. Due to the relatively low elastic modulus of the articular cartilage, loads are transferred and amplified to the subchondral bone. This further suggests that elevated stimuli levels can provoke stiffening of the underlying subchondral plate, through bone remodelling, and consequently accelerating the onset of cartilage degradation. Since mechanical stimuli results are unique to their patient-specific loading parameters and conditions, it would be difficult to determine a patient-specific threshold to provoke bone remodeling at this stage.

1.0 Introduction

1.1 Motivation

The hip joint is one of the most stable and largest joints in the body. It provides stability to support the upper body and a wide range of motion to control the lower limbs. Altered stress distributions in the joint cartilage and bone, caused by repetitive impact forces to the hip, contribute to degenerative osteoarthritis (OA) (Beck, Kalhor, Leunig, & Ganz, 2005; Herzog & Federico, 2006; Macirowski, Tepic, & Mann, 1994) causing an undesirable progressive state to eventual painful bone-on-bone contact at the joint. OA is associated with a gradual wearing away of the articular cartilage of the joint surfaces caused by several primary factors of biomechanical injury, joint instability, and hip pathologies (Kellgren, 1961); by inappropriate responses to mechanical stimuli (Aigner & McKenna, 2002); or by neuromuscular dysfunctions (Sims, 1999), altering the natural orientation of the hip joint, thus accelerating the process of OA. A well-documented cause of OA is directly associated with structural deformities or geometric incongruences of the hip joint (Brandt, Dieppe, & Radin, 2008; Harris, 1986; Murray, 1965; Solomon, 1972; Tepper & Hochberg, 1993). Femoroacetabular impingement (FAI) has been identified as one such recurring geometric deformity in the hip joint (Ito, Minka, Leunig, Werlen, & Ganz, 2001; Myers, Eijer, & Ganz, 1999), presenting many questions and obstacles for clinicians to overcome.

Mechanical failures at the hip constitute a large proportion of problems confronting clinicians and researchers in the orthopaedic realm. It was not until recent years that a closer assimilation was established by Reinhold Ganz's group between FAI and the etiopathogenesis of early OA in young adults (Ganz, Leunig, Leunig-Ganz, & Harris, 2008; Ganz et al., 2003). FAI, also known simply as hip impingement, is now becoming a common abnormality in the femoral head, acetabulum, or sometimes in both sites. It can be described as a mechanical disorder of the hip causing stiffness and pain. The structural abnormality can be found at the femoral head-neck junction (cam impingement), at the acetabular rim (pincer impingement), or at both sites (mixed impingement). The impingement is experienced at the maximum of the ROM in flexion caused by a lack of space between the femoral head and the rim of the acetabulum socket. This interference fit causes the femoral head-neck junction and the acetabulum to jam together as the hip is flexed, generating pain and eventually leading to early degenerative cartilage of the hip (Ganz, et al., 2003). Symptoms of impingement include restriction of hip movement and pinching pain in the groin and hip during high flexion activities.

Many of the current literatures pertaining to FAI focus on presenting radiographic indications, surgical methods, follow-up data, and subsequent comprehensive literature reviews, however, very little research has been carried out to discuss the subject as an engineering continuum. In addition, very few studies have been aimed at exhibiting the stresses and strains within a hip joint with cam FAI using computational modelling methods (Chegini, Beck, & Ferguson, 2009). The intention of this study, as a whole, is to further explain the morphological deformity in cam FAI from a biomechanical engineering perspective.

1.2 Thesis Statement

Based on theories that the subchondral plate plays a predominant mechanical role in early stages of cartilage degeneration (Day et al., 2004; Radin, Paul, & Tolkoff, 1970; von Eisenhart-Rothe et al., 1997; Wang, Wei, Yu, & Cheng, 2007; Wei, Sun, Jao, Yeh, & Cheng, 2005), elevated stress levels can impose adverse loading conditions to the underlying surfaces at the subchondral bone. It is thought that the highest stresses may not be found at the cartilage layer, but rather at the underlying bone of the articulating surfaces. Initially postulated by Radin and associates (1970), the elevated levels of mechanical stimuli could subsequently increase the rate of bone remodelling in the subchondral bone, thus stiffening the bone plate – inhibiting the cartilage to distribute stresses effectively and ultimately accelerate the onset of early OA. As a consequence in the presence of cam FAI, cartilage damage may be secondary to the adverse loading conditions endured by the adjacent bone. The proposed research hypothesizes that the level of mechanical stimuli would be much more prominent in an impinged joint. Furthermore, since symptomatic FAI is experienced at the maximal ROM of the hip, it is hypothesized that mechanical stimuli would be much higher during an activity requiring a large ROM (e.g. squatting), in comparison with a normal standing position and with healthy asymptomatic hips.

1.3 Objectives and Conceptual Framework

Despite the attempts in the past to characterize the mechanism by which cam FAI leads to OA, no in vitro study has integrated clinical patient-specific data to determine stresses and strains within the impinged hip. Using cam FAI as the basis of this research, the aim is to **examine the effects of the cam deformity on joint mechanical stimuli by incorporating finite element analysis (FEA) with patient-specific CT, kinetic, and kinematic data.**

A co-requisite objective is to develop 3-D computational geometries, as patient-specific as possible in terms of structural conformance with original patient CT data, using finite element (FE) modelling principles and methods to develop a relevant finite element model (FEM). This would be an improvement to existing idealized ball-and socket models on cam FAI (Chegini, et al., 2009).

In addition, the intention of this multidisciplinary research is to further apply previous patient-specific biomechanics results, pertaining to the effect of cam FAI on pelvic motion (Lamontagne, Kennedy, & Beaule, 2009) towards computational visual representations. The kinematics and kinetics data were recorded earlier for a cam FAI study in the Human Movement Biomechanics Laboratory at the University of Ottawa. To reiterate patient-specific aspects of implementation, the biomechanics data will combine with the patient-specific geometric models to yield FEA results.

Figure 1.1 summarizes the process flow of the patient-specific inputs towards reaching the research objectives. After assembling and simulating the cam FAI 3-D FEMs, the magnitudes and locations of the mechanical stimuli (i.e. stress and strain energy density (SED)) within cam FAI joints would be determined and compared with healthy control models. Considering the hip model as an assembly, the magnitudes and regions of mechanical stimuli would need to be determined to ascertain where maximum bone remodelling could likely occur first. This study aims at answering the following questions:

- What are the magnitudes and locations of the mechanical stimuli in a hip with cam FAI, in comparison with healthy participants?
- Which anatomical parts and regions of the hip experience the highest mechanical stimuli?
- How different are the experimental results, using a patient-specific geometric model, in comparison with results from literature, that used a parametric idealized model?
- Which of the stress and SED indicators is a better candidate for initiating and controlling the bone remodelling process?

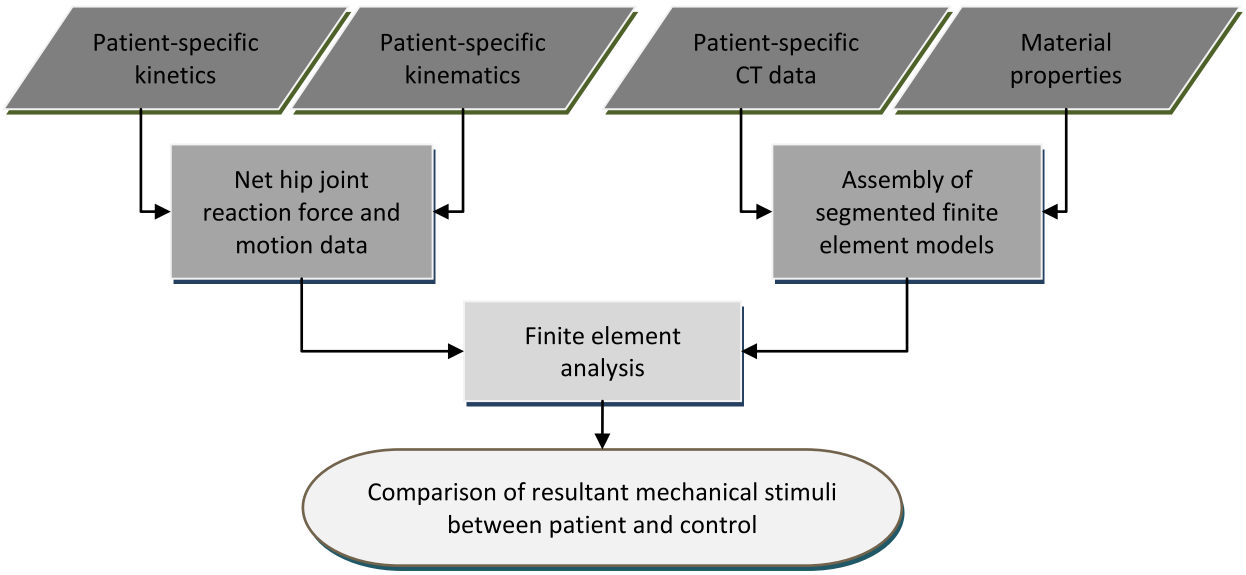

Figure 1.1: Process flow of patient-specific inputs to reach research objective – to determine the magnitudes and locations of the mechanical stimuli in cam hips and comparing them with control hips – ascertaining the location of OA onset.

1.4 Relevance and Theoretical Framework

Findings from this study would be most relevant towards clinicians and researchers in orthopaedic practices. Realizing the relative mechanical stimuli magnitudes in a cam hip, in comparison with a healthy control hip, could provide the surgeon indications of where initial cartilage delamination would likely occur. The hypothesis that peak mechanical stimuli would be located on the subchondral plate in a hip with cam FAI would further iterate the postulated theory, by Radin and associates (1970), that the stiffening of the subchondral bone plays a mechanical role towards the process of OA. The outcome of this study could influence a different approach towards theorizing the onset of OA due to cam type FAI, suggesting that cartilage degradation might not be only due to direct contact shear stresses, but rather can be due to the indirect effects of a stiffer underlying bone plate.

Also, by determining the locations of the mechanical stimuli concentrations, it would allow radiologists to diagnose for progressive OA earlier based on more preliminary indications prior to any articular cartilage damage (e.g. radiographic findings indicating changes to the stiffness of the subchondral plates or density of adjacent trabecular matrices prior to any joint-space narrowing). From a patient's perspective, an early and accurate diagnosis could inhibit the cartilage degradation and the progression of OA, ultimately avoiding or delaying the need for early surgical treatments (e.g. osteotomy and arthroplasty). Therefore, not only would the objective of operative assessments be to resolve a "best-fit" of the hip joint, but also to result with a hip that would provide better long term inherent stability.

2.0 Background

2.1 Anatomy

During activities of daily living, whether it is a simple gait or a more strenuous load-bearing activity, load intensities fluctuate instantaneously, thus creating various cyclic loading and impact forces on the hip region. Due to these loads, mechanical hip failures constitute a large proportion of problems confronting clinicians. Classified as a synovial joint, the hip is made up of the innominate bone, muscles, soft tissues, and membranes overlying it. A stable and large joint, the hip joint provides intrinsic rigidity and a wide ROM. Prior to describing the cam deformity of the femoral head, it would be beneficial to understand the key components that make up the hip joint.

2.1.1 Bones

The hip is often termed as the ball-and-socket joint; the ball being the head of the femur and the socket being the acetabulum of the innominate bone. Lattice-oriented spongy bone is positioned within the shell of the compact bone. The acetabulum (Figure 2.1), the joint cavity of the union site, is located on the lateral region of the innominate bone. The fossa forms the central non-articular floor of the acetabulum. The lunate surface forms an articulating horseshoe dome above the fossa, where the body weight (BW) is transmitted to the femoral head at the union site. The pubis and ischium sweep from the antero-lateral to postero-lateral direction of the inferior pelvis, forming the hollow space of the obturator foramen. The flat regions of the superior pelvis are comprised of the ilium and iliac crest, giving the pelvis the flared structure and surface area for muscle attachments.

The femoral head (Figure 2.2) is directed supero-medially to fit within the acetabulum. The femoral head is conformed to a conchoidal shape rather than a perfect sphere (Menschik, 1997). The concave notch centred at the femoral head's site of union is the fovea, where the attachment of the ligamentum teres, an intracapsular ligament, unites the femoral head with the acetabulum. The femoral neck connects the head to the shaft. The narrow extension of the neck permits a wider ROM of the lower limb. The protrusion supero-lateral to the femoral neck is the greater trochanter and the smaller protrusion postero-medial to the neck-shaft is the lesser trochanter; both of which mark the intertrochanteric line for the fibrous capsular attachment. Important features to be included in modelling can be seen on Figure 2.1 and Figure 2.2.

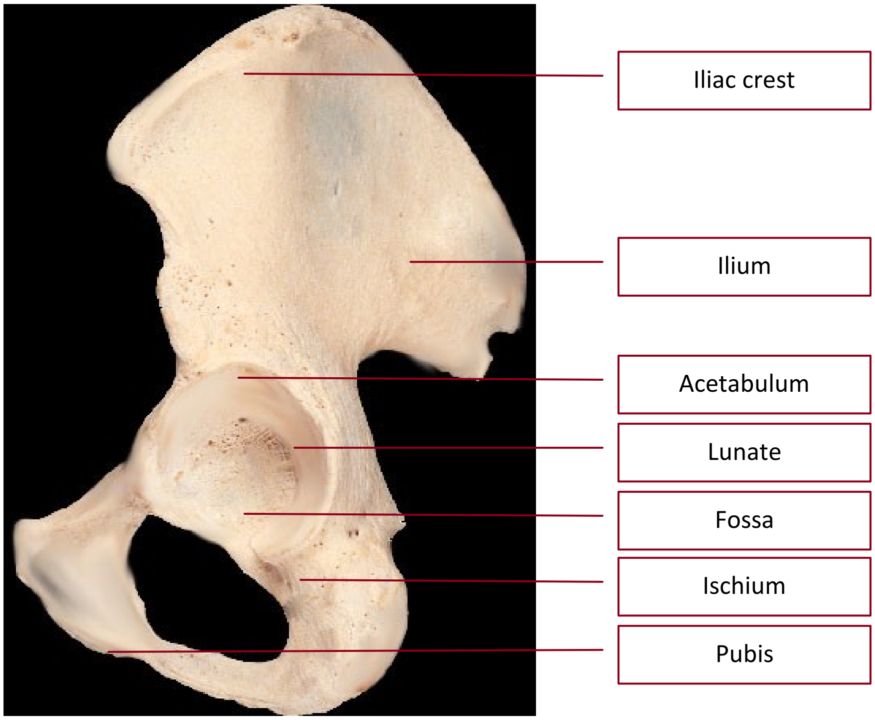

Figure 2.1: View from lateral side of left innominate bone and the acetabulum. Reproduced with permission of Elsevier from Standring, 2008.

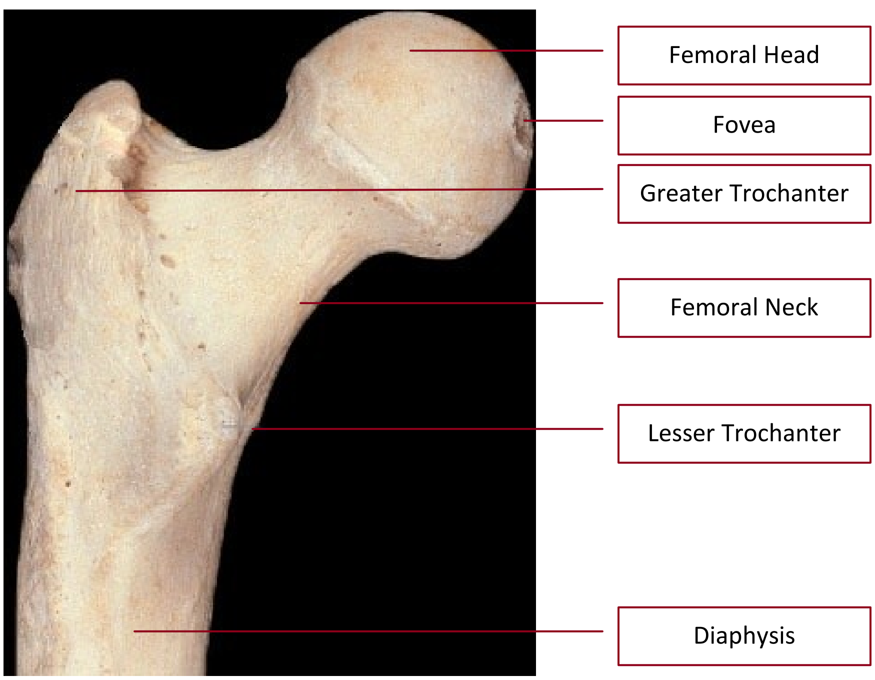

Figure 2.2: View from posterior of the left proximal femur showing the characteristic components. Reproduced with permission of Elsevier from Standring, 2008.

2.1.2 Capsule

The mating surfaces are covered by the articular hyaline cartilage, a thick and lubricated protective layer. The labrum, a fibrocartilaginous rim located at the depth of the acetabulum, grips the head of the femur and secures it in the joint – orientating it inferiorly, laterally, and anteriorly (creating the angle of acetabular anteversion). Hyaline cartilage covers the surface of the femoral head except for the fovea pit, where the femoral head is attached to the acetabulum via the ligamentum teres. The femoral head articulates with the surfaces of the concaved cotyloid acetabulum. A combination of longitudinal and circular fibres make up the capsule: circular fibres form a stability-induced collar around the femoral neck called the zona orbicularis (Figure 2.3); whereas longitudinal retinacular fibres travel along the neck and contain the travelling blood vessels.

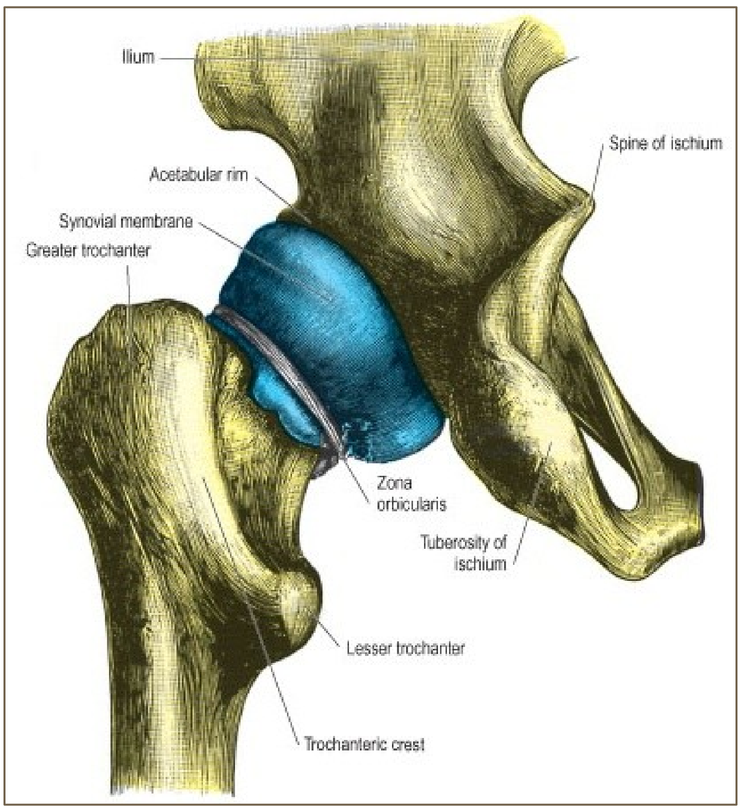

Figure 2.3: Hip joint capsule relative to the femoral head and the acetabulum. The fibrous retinacular fibres are removed from view showing the synovial capsule and the zona orbicularis. Reproduced with permission of Elsevier from Standring, 2008.

The articulating acetabular cartilage forms a horseshoe shape mapped onto the lunate surface, broadest superiorly above where the pressure of body weight falls in the erect posture, and narrowest in its medial pubic regions (Athanasiou, Agarwal, & Dzida, 1994; Macirowski, et al., 1994; Russell, Shivanna, Grosland, & Pedersen, 2006; Standring, 2008). The labrum, a cartilaginous ring attached to the acetabular rim, deepens the cup and bridges the acetabular notch as the transverse acetabular ligament. The width and depth of the acetabulum is constrained by the labrum, which acts as a static stabilizer for the joint (Ferguson, Bryant, Ganz, & Ito, 2000b; Standring, 2008).

2.1.3 Ligaments

The hip joint is reinforced by three primary ligaments:

- Iliofemoral – is located at the front of the joint (Figure 2.4). Often considered as strongest ligament in the body, the Y-shaped ligament extends from the pelvis to femur. This ligament seeks to resist excessive extension of the hip joint.
- Pubofemoral – attaches across the front of the joint from the pubis bone of the pelvis to the femur (Figure 2.4). This ligament reinforces the inferior part of the hip joint capsule and is orientated inferiorly in comparison with the iliofemoral ligament.
- Ischiofemoral – extends from the ischial part of the acetabular rim to the femur and reinforces the capsule (Figure 2.4).

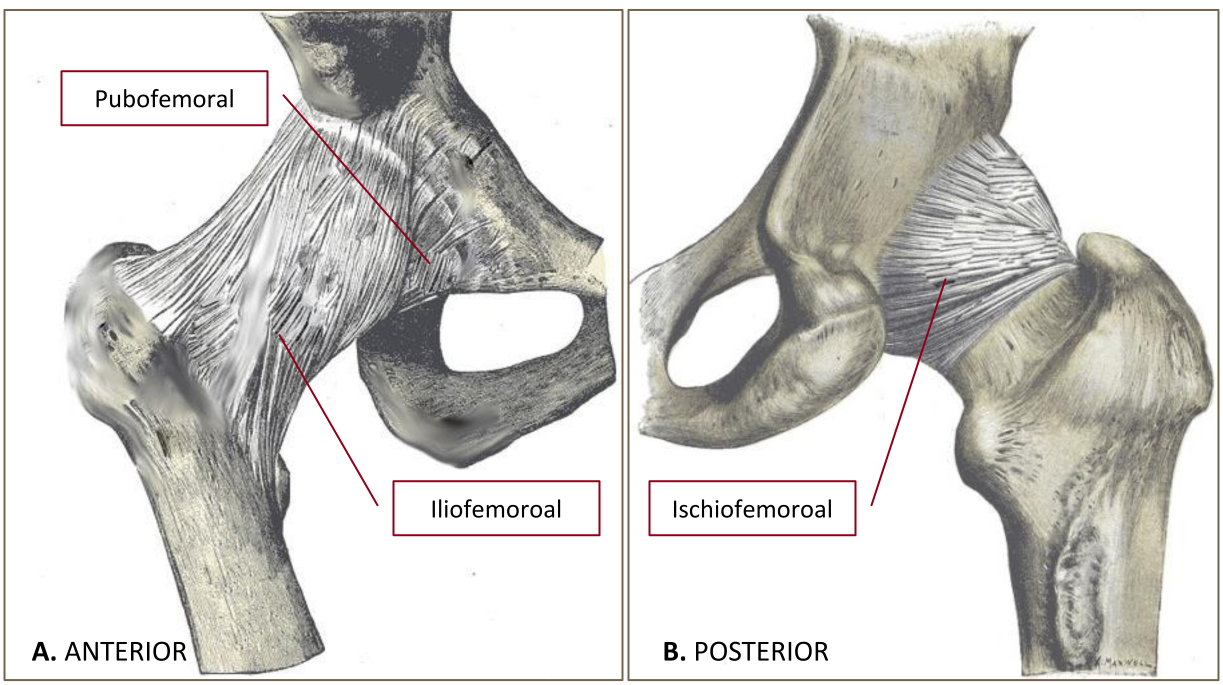

Figure 2.4: Fibrous ligament attachments about the hip joint capsule; anterior view of right hip (A) showing the inferior pubofemoral and the long iliofemoral ligament attachments; posterior view (B) showing the ischiofemoral ligament. Reproduced with permission of Elsevier from Standring, 2008.

A small auxiliary ligament, the ligamentum teres, is a triangular-shaped band on both sides of the peripheral acetabular notch, at the inferior end of the acetabulum (Figure 2.5). Though not as important in terms of structural stability, in comparison with the primary ligaments, the varying thickness of the ligamentum teres acts as reinforcement between the acetabulum and the fovea of the femoral head – providing itself as a conduit for small vessels and innervations to the head of the femur.

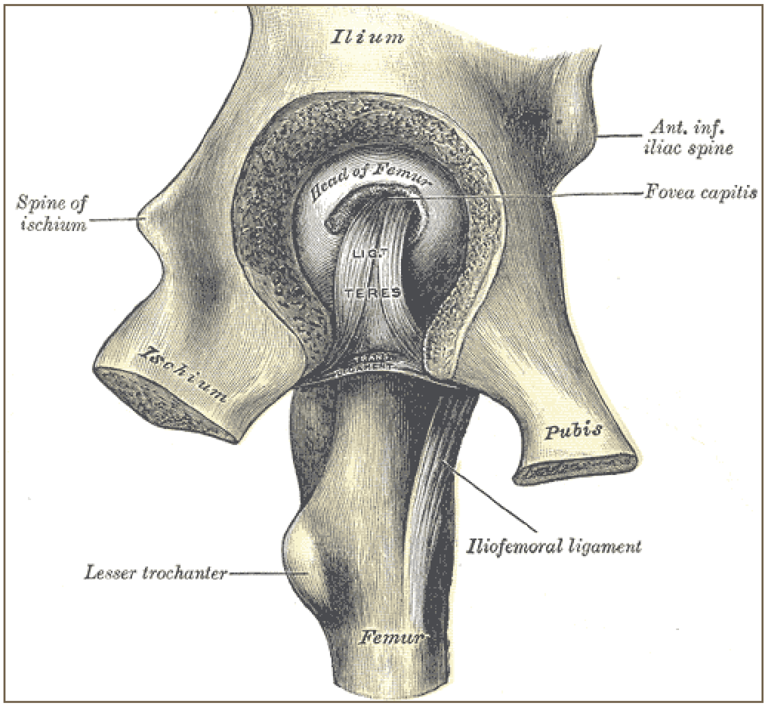

Figure 2.5: Cross-sectional view in the lateral direction of ligamentum teres attachment. The fossa has been removed to show how the ligamentum teres is attached to the fovea from the branched acetabular notch. Reproduced with permission of Elsevier from Standring, 2008.

2.1.4 Motion

Motion in the hip takes place in all three planes: sagittal (flexion-extension), frontal (abduction-adduction), and transverse (internal-external rotation). ROMs in these three planes during daily routines fluctuate and vary depending on the activity and level of difficultly. ROM is greatest in the sagittal plane when the hip is flexed. In the gait analysis of the hip's ROM in the sagittal plane, maximum flexion in the joint occurs during the late swing phase of gait – as the limb moves forward to lay the heel down. Maximum extension occurs when the heel is removed from the ground. Abduction reaches maximum just after the toe comes off the ground; whereas, continual adduction occurs when the heel hits the ground. Throughout the swing phase, the joint remains externally rotated, until just before the heel hits the ground, when it rotates internally.

There are several other activities that would require greater degrees of hip flexion, abduction, and rotations. In a study of 33 male subjects (Johnston & Smidt, 1970; Nordin, 2001), ROMs were analysed in the three planes of motion for common daily activities, as seen in Table 2.1.

Table 2.1: Mean values for maximum hip ROM for common activities
(Johnston & Smidt, 1970; Nordin, 2001)

Activity	Plane of Motion	ROM (Degrees)
Shoe tying with foot (shoe to be tied) flat on floor and other foot posterior to subject	Sagittal	124
	Frontal	19
	Transverse	15
Sitting down on a chair and rising from chair	Sagittal	110
	Frontal	23
	Transverse	33
Squatting	Sagittal	122
	Frontal	28
	Transverse	26
Stair ascent	Sagittal	67
	Frontal	16
	Transverse	18
Stair descent	Sagittal	36
	Frontal	16
	Transverse	18

It was noticed that ROM was greatest in the sagittal plane in all tasks, with the shoe tying task requiring the highest degree of sagittal flexion and the squatting task having the absolute highest ROM. Since these study presented mean values as results, it does not reflect the exact maximum ROM that each individual can reach. Flexibility, daily physiological loading, and functional demand all vary among individuals. However, the values provide an indication, among the different activities, of how the maximum ROM can compare with other daily routines. Seeing that the shoe tying and squatting tasks require a higher and wider ROM, it would be beneficial to further study squat depths and understand the loading conditions that these tasks exert on the hip joint.

To accomplish the ROMs, many of the hip muscles are responsible for more than one type of movement in the hip. According to their orientation around the hip joint, the muscles that provide movement in the hip can be divided into five groups, as follows:

- Flexors – iliopsoas, rectus femoris, tensor fascia lata, and sartorius
- Extensors – gluteus maximus and hamstrings
- Abductors – gluteus medius and minimus
- Adductors – pectineus, adductor brevis, longus and magnus
- Rotators – obturator internus and externus, gemellus superior and inferior, quadratus femoris and piriformis

The group of muscles for recruitment during flexion, adduction, and rotation from the anterior perspective can be seen on Figure 2.6. Moreover, the muscles for recruitment during extension, abduction-adduction, and rotation can be seen on Figure 2.7.

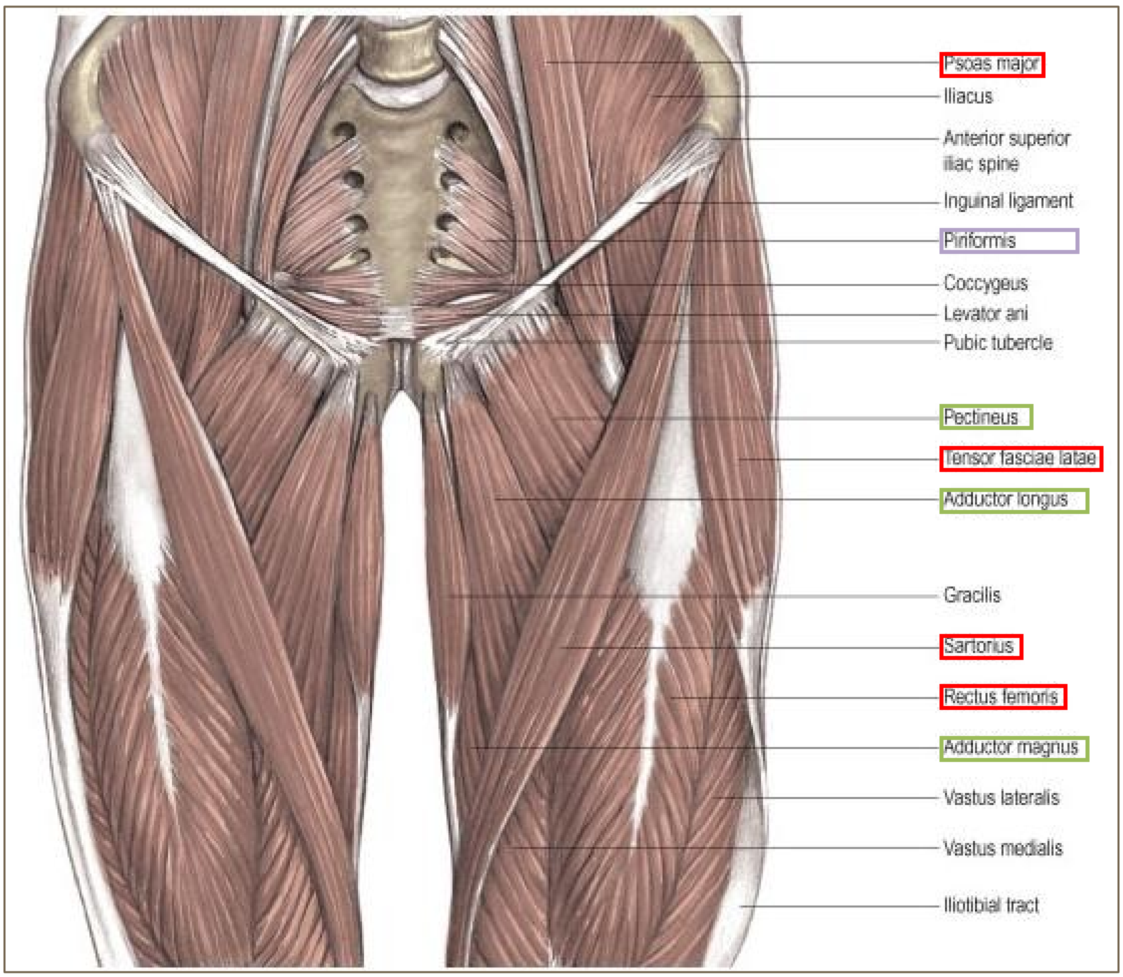

Figure 2.6: A-P view of muscles at iliac and thigh region. Muscles for recruitment: flexors (red), adductors (green), rotators (purple). Reproduced with permission of Elsevier from Standring, 2008.

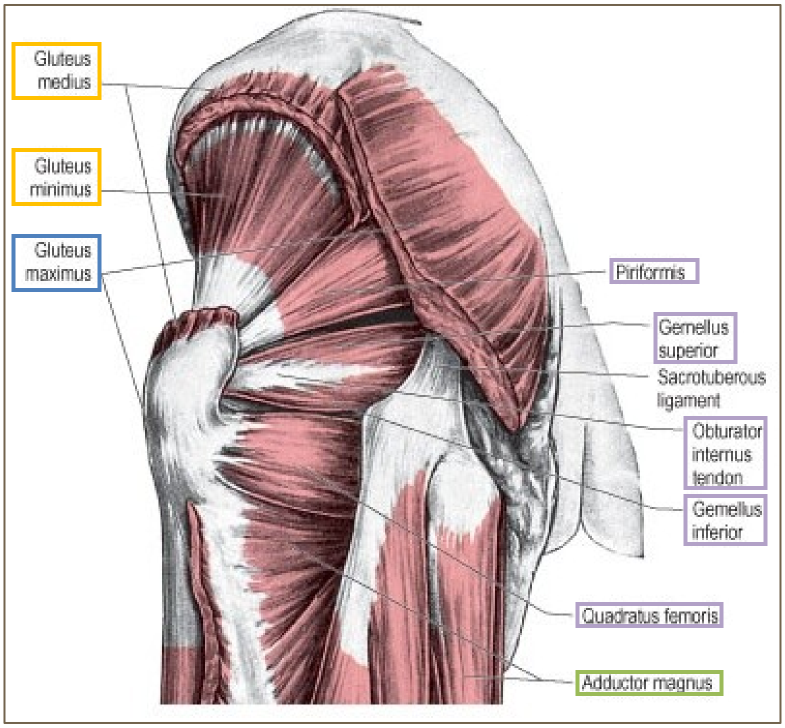

Figure 2.7: Posterior view of muscles at iliac region. Muscles for recruitment: extensors (blue), abductors (orange), adductors (green), rotators (purple). Reproduced with permission of Elsevier from Standring, 2008.

Although in many cases, many diagnostic tools are used to determine if a hip is healthy or not, one of the primary assessments to diagnose hip deformities is to compare radiographs (e.g. X-ray, CT, MRI) with healthy anatomical data. This data would help distinguish physical differences, and visually identify the deformity. For assurance, performing dynamic ROM tests can help further determine the presence of any joint impingements or deformities.

2.2 History of FAI

The concept of FAI is still considered to be recent. Since having been introduced as a successor of various mechanical hip disorders and multi-factorial failure processes, FAI as a subject of research has received a great extent of clinical interest over the last decade with a substantially increasing rate of scientific publications over the years (Leunig, Beaule, & Ganz, 2009). It was not until this period that associated geometric hip deformities, demonstrating similar disorders and pathologies, were beginning to be acknowledged as FAI (Eijer, Myers, & Ganz, 2001; Ganz, et al., 2003; Myers, et al., 1999). Prior to then, like many pathologies and aetiologies, the concept of FAI was ill-defined and misunderstood.

In 1965, a relationship was initially established between abnormal deformities of the proximal femur with the onset of hip OA (Murray, 1965). A correlation was observed between the two and it was noted that the deformities occurred following a slipped capital femoral epiphysis (SCFE). Due to the intricacy of the new proposed correlation, many researchers supported the theory that the minor developmental deformities would cause OA (Harris, 1986; Solomon, 1972); however, none yet were able to support the theory with clinical evidence.

An emphasis was placed on distinguishing the relative causes of OA, trying to determine the severity of the hip deformity that would initiate cartilage degeneration (Ganz, et al., 2008; Loder et al., 2008; Murray, 1965). To avoid confusion and to isolate the pathomechanical process of the proposed theory, a set of exclusions were established to neglect other morphological abnormalities and hip deformities (e.g. Legg-Calvé-Perthes (LCP), avascular necrosis due to abnormal bone growth or loss at the femoral head; SCFE, slippage fracture of the overlying epiphysis; mild dysplasia, undercoverage of the acetabulum). The exclusions were necessary to better characterize the definition of OA without extraneous aetiologies due to inflammation, trauma, and metabolic causes (Ganz, et al., 2008). Moreover, some patients with severe SCFE, LCP disease, or a gross deformity may develop late OA (Siebenrock et al., 2004; Skaggs & Tolo, 1996).

The term, "pistol grip" deformity (Figure 2.8), was first introduced to describe the contour of the femoral head-neck (for hips with cam impingement), in comparison with the shape of a pistol from anterior-posterior (A-P) radiographs (Stulberg, Cordell, Harris, Ramsey, & MacEwen, 1975). At this point, it was mentioned that abnormal geometric configurations did reveal signs of early cartilage degeneration; however, did not discuss any direct correlation between the deformity with OA and also the location of OA onset. The observations were based on visual interpretations of radiographic evidence and no work was done yet to determine the ROMs within the "pistol grip" hip joint (Harris, 1986; Stulberg, et al., 1975).

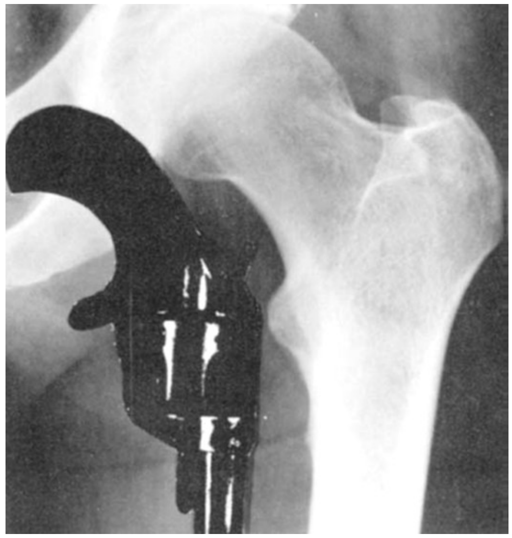

Figure 2.8: "Pistol grip" deformity – comparison of the enlarged aspherical femoral head with the contour of pistol's handling grip on an anterior-posterior radiograph. The extension on the aspherical abnormality was an early physical representation that characterised the deformity. Reproduced with permission of Elsevier from Stulberg, et al., 1975.

In attempts to explain an interference fit experienced when the symptomatic hip joint was at high flexion, general terms were then used to describe FAI based on a combination of visual radiographic and preliminary motion analyses – previously referring to FAI as acetabular rim syndrome (Klaue, Durnin, & Ganz, 1991; Tannast, Siebenrock, & Anderson, 2007) and cervico-acetabular impingement (Ganz, Bamert, Hausner, Isler, & Vrevc, 1991; Tannast, Siebenrock, et al., 2007). FAI was also given the terms "head tilt" and "post-slip" to describe the epiphyseal deformity and the displacement of the SCFE (Goodman et al., 1997; Leunig & Ganz, 2005; Murray, 1965). From these works, it was then noted that impingement would be experienced at high ROMs, where the interference and abutment would be most prominent in the joint's motion. It was suggested that the abutment could offset an abnormal configuration within the joint structure; however, no strong correlation between the deformity and OA has yet been established.

Myers and associates (1999) introduced the concept of anterior FAI as a consequence to peri-acetabular osteotomy. The authors proposed a root cause to the deformity, suggesting that the impingement was noticed to be secondary as a result from surgical treatment to reposition dysplastic acetabulums. As a result of the osteotomy, it could have been possible that the newly re-aligned bone structure over-compensated for the adjusted adverse conditions during the reparative phase of bone remodelling (Henriksen, 2009; Martin & Seeman, 2008), subsequently causing an abnormal rate of bone turnover and forming a bony protrusion. Variable degrees of groin pain and limited hip motion were observed in the patients, explaining the ossification of the anterior rim. Dynamic hip flexion and internal rotation were tested and noticed to be restricted.

An additional follow-up study was conducted to investigate the presence of protrusions after femoral neck fractures (Eijer, et al., 2001). Similar consequences of secondary anterior FAI were observed. In this study, the focus was on the femoral head where an oversized bony protrusion was formed at the site of the anterior fracture, bridging between the femoral head and neck. The bridge of the bump again could be explained by the reparative phase of bone remodelling during fracture healing. The intention of these combined studies conducted by Myers, Eijer, and Ganz was to explain the mechanisms that initiate FAI. These follow-up studies were again proposing that an abutment or deformity can be remodelled and formed at the femoral neck or at the acetabular rim due to severe trauma or surgical treatment. Though no conclusion was made to explain the mechanism of FAI as a complex structural deformity, the term FAI was further defined to be an abnormality occurring at high ROMs.

The continuing research led to Reinhold Ganz and his group to recognize FAI as, or as part of, a pathomechanical disease process unto itself and a contributor to early adult hip pain and OA (Ganz, et al., 2003). The intention of their research was to assimilate the link between FAI, as a hip deformity, with the pathogenesis of idiopathic OA. Having gathered a multitude of clinical experience, a total of more than 600 surgical hip dislocation, and follow-up studies, FAI was now proposed as a mechanism for the development of early OA for most non-dysplastic hips (Ganz, et al., 2003), by in situ methods of inspecting damage patterns of surgical dislocations. As a result, labral and chondral lesions were apparent in the cases of severe joint deformities. In this case, it was suggested that FAI was no longer just a resolute deformity of the hip joint, but rather a failure process initiated by a multitude of possible biological and mechanical mechanisms that would eventually provoke the onset of OA.

Ganz and associates' work in 2003 remains to be one of the most referred studies of its kind and has established itself as an exploratory breakthrough on the subject of idiopathic hip deformities. This notion of FAI causing OA in Ganz et al.s' 2003 work focuses more on dynamic motion as opposed to directional axial loading of the hip. The theory of axial hip overload to provoke OA was disputed, further elaborating that the development of OA in young adults, with normal hip configurations, cannot be correctly justified with solely concentric and eccentric overload (Bombelli, 1976, 1993; Nordin, 2001). Ganz et al.'s 2003 research was not able to discuss the mechanisms that initiate FAI and justify the origins of the deformity; however, the work provided important clinical and radiographic assessments to distinguish the types of FAI and was among the first studies to discuss the abnormal contact experienced during the impinged state at an excessive ROM.

Today, FAI has been appropriately deemed a pathomechanical process by which a human hip can fail (Clohisy, St John, & Schutz, 2010; Leunig, et al., 2009) rather than a disease. It has been disputed that the relationship between FAI and hip OA has not been well-defined (Goodman, et al., 1997; Standaert, Manner, & Herring, 2008). The aetiology and the pathogenesis of FAI remain elusive. The term FAI was then associated with a possible cause of hip pain and labral tears in young adults, further iterating that FAI was being recognized as a leading cause of hip OA (Beaule, 2009; Clohisy, et al., 2010).

With the methodology of reverse-engineering to comprehend the pathology of FAI, the mechanisms of OA due to the idiopathic hip deformity have now been acknowledged. As mentioned, evidence has emerged to propose that FAI provokes hip OA (Beck, et al., 2005; Ganz, et al., 2003; Laude, Boyer, & Nogier, 2007; Leunig, et al., 2009; Leunig & Ganz, 2005) and active adults with groin pain may now be successfully treated by addressing FAI early (Clohisy & McClure, 2005; Ilizaliturri, Orozco-Rodriguez, Acosta-Rodriguez, & Camacho-Galindo, 2008; Larson & Giveans, 2008; Leunig, et al., 2009; Leunig et al., 2005). From the result of the systematic review of literature on the subject of FAI, a great extent of past research has been focused on treatments and devising surgical solutions for FAI rather than assimilating the link between FAI with the progression of OA. Since this research topic in orthopaedics is considered to be still new, not much research has been established to find the mechanisms that initiate the failure process of FAI. Only a few studies have attempted to incorporate computer models to simulate biomechanical loading scenarios to partially address the subject of FAI (Anderson, Ellis, Maas, & Weiss, 2010; Chegini, et al., 2009). Moreover, most recent published contributions have been literature reviews compiling existing information from radiographic evidence, surgical techniques and approaches, and follow-ups studies. Therefore, it would still be too soon to determine the rate of cartilage degeneration within a symptomatic hip without any theoretical indication of the possible resultant magnitudes and locations of OA.

2.3 Types

FAI can be classified as either cam or pincer impingement (Ganz, et al., 2003). For cam, the structural abnormality can be found at the femoral head-neck junction, where an oversized contour at the junction leads to an insufficient femoral head-neck offset. The cam deformity is characterized by an enlarged aspherical femoral head, limiting clearance at the junction between the head-neck and the labral regions of the acetabulum. For pincer, the deformity is located at the acetabular rim where an ossified labrum provides over-coverage of the femoral head. It is characterized by an ossified labrum, stiffening the joint and limiting movement. A combination of both impingement types are often found in patients, with 86% of patients suffering from mixed impingement (Beck, et al., 2005); while 14% have a unique FAI type. In general, the impingement occurs at a high ROM for either type (Leunig, Beck, Dora, & Ganz, 2005), resulting in an interference fit between the femoral head-neck junction and the labrum (Figure 2.9).

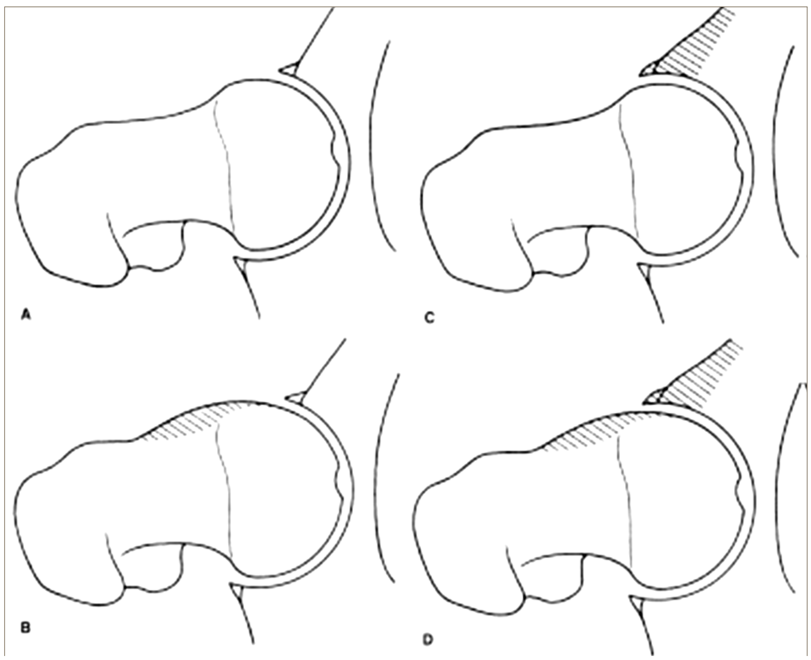

Figure 2.9: Comparison of normal hip with hips with FAI on the axial plane. (A) Normal clearance of the hip; (B) Cam FAI with reduced femoral head-neck offset; (C) Pincer FAI with ossified labrum and excessive over-coverage; (D) Mixed FAI with combination of cam and pincer types. Reproduced with permission of Lippincot Williams & Wilkins from Lavigne, et al., 2004.

2.3.1 Cam Impingement

Cam impingement is due to a decreased head-neck offset with an aspherical contour of the femoral head-neck junction (Ganz, et al., 2003; Kassarjian, Brisson, & Palmer, 2007; Tannast, Siebenrock, et al., 2007) and described as a “bump” antero-laterally with a relative retroversion of the femoral head (Ito, et al., 2001; Siebenrock, et al., 2004). The radius of curvature is larger than average around the head-neck junction resulting in a bony triangular shaped extension and articular cartilage onto the femoral neck (Clohisy & McClure, 2005), thus characterizing the appearance of a “bump”. The impingement is caused by a jamming of the abnormally aspherical femoral head with increasing ROMs – most noticeably, the osteochondral lesion impacts the acetabular rim with flexion, internal rotation (Clohisy & McClure, 2005; Siebenrock, et al., 2004), and with squatting motions (Chegini, et al., 2009; Lamontagne, et al., 2009).

A method to quantify the severity of cam FAI is the use of the alpha angle (Figure 2.10) – mathematically measuring the angle of curvature of the dysmorphic bump (Notzli et al., 2002) to quantify the head-to-neck relationship on CT and MRI radiographs. The alpha angle is the angle formed by the line parallel to the femoral neck axis and the femoral head-neck offset, as seen in Figure 2.10.

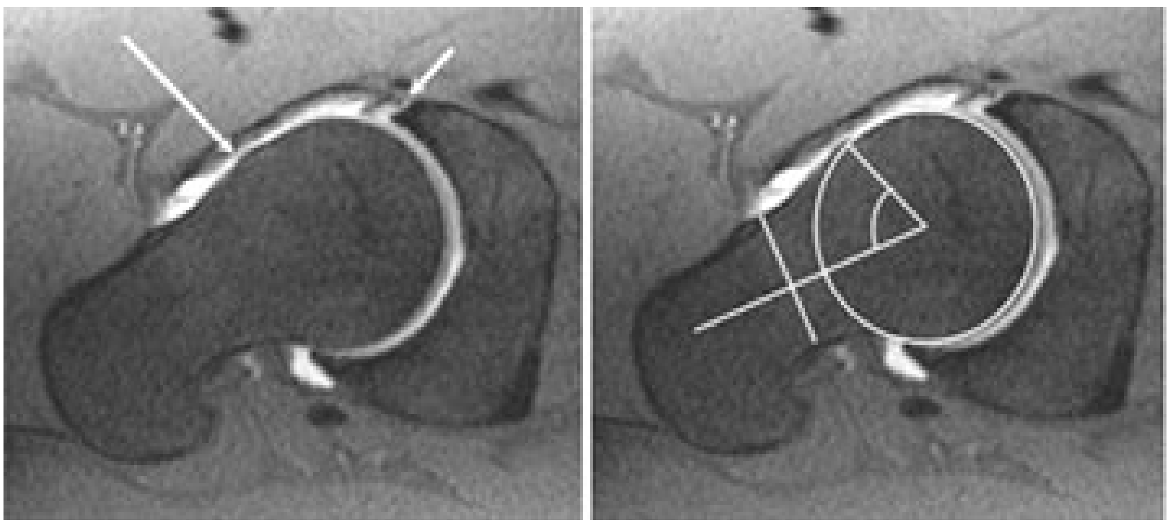

Figure 2.10: (Left image) oblique image shows femoral head-neck offset (long arrow) and labral lesion (short arrow). (Right image) measurement of the alpha angle – circle centred over the femoral head. The axis is drawn parallel to the neck in line with the head. Reproduced with permission of Elsevier from Kassarjian, et al., 2007.

A hip with an alpha greater than 55^{o} indicates an abnormality with cam FAI in either the axial-oblique plane or the radial plane; while an angle less than 55^{o} indicates a normal hip (Kassarjian, et al., 2007; Notzli, et al., 2002; Nouh, Schweitzer, Rybak, & Cohen, 2008). It has been questioned that taking the alpha angle measurement may not be necessary to directly quantify the severity of cam FAI (Meyer, Beck, Ellis, Ganz, & Leunig, 2006). Moreover, in a study to estimate and compare alpha angle measurements (Nouh, et al., 2008), it was acknowledged that many radiologists, in practice, visually estimate the angles without high levels of accuracy and precision – potentially leading the radiologist to misinterpret the alpha angle. The reason not to use the alpha angle to assess cam FAI has never been properly justified, only that the measurements did not bring much value to the accuracy of the final assessment.

On the contrary, in a study involving 3-D CT data of the hip to assess FAI, it was determined that the alpha angle was indeed a practical tool to quantify the severity of cam FAI (Beaule, Zaragoza, Motamedi, Copelan, & Dorey, 2005). In the study, the 3-D CT results correlated closely with Notzli and associates' findings (Notzli et al., 2002) justifying the importance of the alpha angle as a preliminary assessment tool to quantify the degree of the cam deformity. Though some minor differences in methods were noticed between the two works, both works demonstrated the importance of accuracy and precision in the assessment and diagnosis for the severity of cam FAI. The use of 3-D CT provided the additional surface rendering that a two-dimensional image could not, giving clinicians the extra perspective and confirmation of any offset deformity.

In the study of Beaulé and associates (2005) on 3-D CT, an alpha angle of 50^{o} was considered to be a suitable threshold in this case to determine a potentially abnormal hip, slightly different from Notzli et al.'s 55^{o} threshold. Similarly, Tannast et al.'s radiographic observations also accepted 50^{o} as a suitable threshold to assess the cam severity (Tannast, Siebenrock, et al., 2007). The symptomatic group from Beaulé et al.'s study was represented at 74^{o} and the control group was represented at 42^{o} (Beaule, et al., 2005). Individuals with a higher alpha angle, thus more severe cam deformity, had prevalent labral and cartilage lesions at the antero-superior regions; which was confirmed with other open dislocation approaches and radiographic evidence (Beck, et al., 2005; Bittersohl, Steppacher, et al., 2009; Tannast, Siebenrock, et al., 2007). The aforementioned studies confirmed that damage was mainly situated at the antero-superior regions of the acetabular cartilage; indicating cartilage degradation, tears, lesions, and delamination – all precursors to OA. In any case, the higher the alpha angle, the more severe the cam deformity is. In all of these studies on the alpha angle, there was no mention that the measurement should be gender-specific, suggesting that a different threshold to assess the cam severity should be considered for male and female subjects.

Though the mechanisms that initiate FAI remain to be elusive (Kassarjian, et al., 2007; Laude, et al., 2007; Leunig, Beck, Dora, et al., 2005), the pathomechanical process of cam FAI is associated with various hip deformities (Figure 2.11) such as: an onset of the physeal development (Goodman, et al., 1997; Siebenrock, et al., 2004); SCFE (Leunig et al., 2000; Rab, 1999; Siebenrock, et al., 2004); LCP disease (Clohisy & McClure, 2005; Jaberi & Parvizi, 2007); and mal-union due to post-trauma and femoral neck fracture (Eijer, et al., 2001).

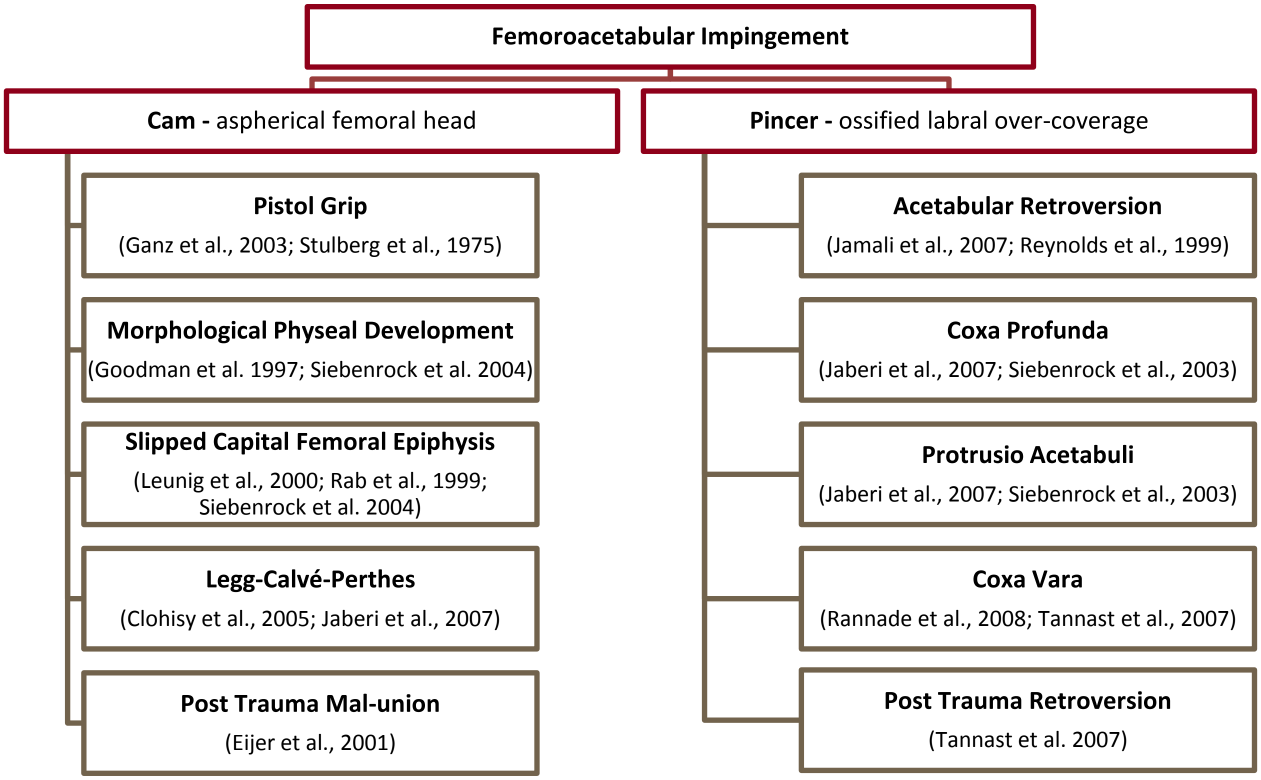

Figure 2.11: Summary of FAI types and breakdown of associated hip disorders.

2.4 Associated Casualties

Many researchers suggested that the causes of FAI is likely due to a combination of an individual's genetics and environment – beginning at birth as a congenital deformity or developing during growth as an acquired secondary disorder (Ganz, et al., 2008; Ganz, et al., 2003; Leunig, et al., 2009). It is believed that substantial athletic activity before skeletal maturity increases the risk of FAI, going further to elaborate that minor trauma (Ganz, et al., 2003) and contact sports may even exacerbate impingement (Laude, et al., 2007; Myers, et al., 1999). Though the mechanisms that initiate FAI are elusive and considered to be multi-factorial, it is evident that each FAI type has its own respective root causes, precursors, and associated hip disorders; moreover, each one has its own respective group of associated common sufferers.

Cam impingement is statistically more common with young athletic males (C. Kang, Hwang, & Cha, 2009; Kassarjian, et al., 2007; Lavigne et al., 2004; Tannast, Siebenrock, et al., 2007). Since the impingement occurs at high ROM limits, the risk of cam FAI is greatest in young adults who engage in sports requiring wide hip movements (Laude, et al., 2007). On the contrary, pincer impingement is more commonly found in middle-aged and older females with morphological abnormality of the acetabulum (C. Kang, et al., 2009; Kassarjian, et al., 2007; Lavigne, et al., 2004; Leunig, Beck, Kalhor, et al., 2005; Tannast, Siebenrock, et al., 2007).

Though the distribution of cam FAI among the genders is dominantly favouring males, no study has provided an explanation on why and how the relation exists between cam type and its associated group of patients. Similarly, the assimilation between pincer FAI and the older, less-active female group has not been explained. No study has been able to properly, fully explain the origins of the idiopathic process. Siebenrock et al. studied the influence of abnormal epiphyseal extensions of the femoral head on 15 male FAI patients (Siebenrock, et al., 2004). Their findings suggested that the extended femoral head epiphysis was a possible cause of cam impingement, where an increased epiphyseal extension onto the neck was associated with a decreased head-neck offset of the aspherical femoral head.

To properly address the issue of cam FAI, it is imperative to recognize the early symptoms and diagnose the disorder as early as possible. After realizing the association of the age and gender groups with each FAI type, it would be important to focus on the common sufferers of cam FAI to realize the adverse effects on the most targeted individuals.

2.4.1 Indications

FAI is rarely painful in its early stages, thus can go unrecognized for several years during its preliminary asymptomatic settling-in phase (Jaberi & Parvizi, 2007; Standaert, et al., 2008). Early diagnosis and treatment of FAI is important to alleviate severe hip pain, irreparable cartilage damage, and OA. The difficulty sometimes with pre-emptive diagnosis is that cam and pincer FAI appear to look normal during its early stages of development (Laude, et al., 2007). What many articles related to FAI fail to mention is the possibility of implementing additional diagnostic tools in combination with the single tool used to assess the severity of the deformity and impingement.

It has been noted that detection of FAI and onset of cartilage degeneration is often later than hoped for (Ganz, et al., 2008). It has always been a standard practice to use radiographs (e.g. X-ray, CT, MRI data) to confirm the presence of any hip deformity – looking specifically at the sphericity of the femoral head or over-coverage of the acetabulum (Larson & Giveans, 2008; Laude, et al., 2007; Leunig, Beck, Dora, et al., 2005; Nouh, et al., 2008; Tannast, Siebenrock, et al., 2007).

Since impingement occurs at high ROMs, it may be very difficult to determine if an individual is suffering from FAI if dynamic hip motions are not performed. In clinical assessments, a primary symptom of hip impingement is stiffness in the groin, thigh, and the inability to flex the hip beyond a right angle (Laude, et al., 2007). Internal-external rotations along with flexion-extension tests are performed to determine presence of pain and difficulty to attain dynamic ROMs (Figure 2.12). During preliminary phases of the cam disorder, pain may be exacerbated by excessive cyclic loads applied on the hip, such as extensive walking and strenuous activities. Frequently, pain would present itself in the groin region during or after the hip has been in a flexed position; such as running, jumping or prolonged sitting.

When any doubt arises with the preliminary imaging tools and ROM analysis, another approach should be considered. To enhance the ROM study of an FAI patient, it would be beneficial to observe how a FAI patient could perform under a motion-capture environment, where the kinematics and kinetics of the patient's movements and force data could be recorded, thus could be compared to a control group. It was understood that an individual with FAI may perform hip abductions and rotations (Ganz, et al., 2003), walking (Kennedy, Lamontagne, & Beaule, 2009), and squat motions (Lamontagne, et al., 2009) slightly differently in comparison with a normal control group. The importance from the motion studies revealed that cam FAI has an adverse effect on the pelvic motion during squat, where cam FAI tends to limit squat depth. Kinematics during walking and squatting motion for symptomatic cam FAI patients were very similar with respective control groups; however, slightly lower peaks in abduction were noticed. This constrained abduction could be justified by the restricting soft tissues in the hip joint with cam FAI. It was implied that the squat motion could be incorporated as a possible additional diagnostic tool (Lamontagne, et al., 2009), where the biomechanics data could benefit pre-operative measures and understandings of the patient's hip joint – detecting the disorder at an earlier stage and help ascertain the severity of the impingement's motion.

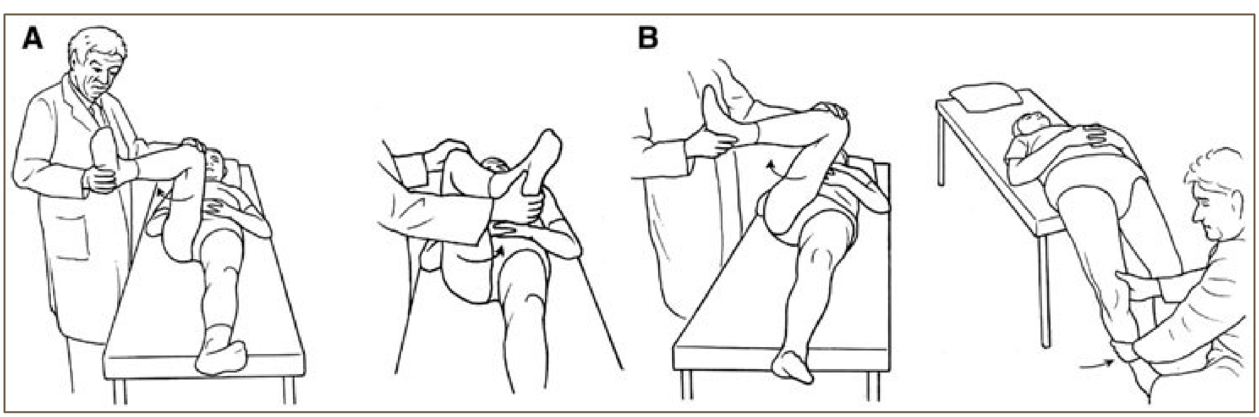

Figure 2.12: (A) Internal and external rotation in flexion; (B-left) Adducted flexion with internal rotation to test for anterior FAI; (B-right) extended external rotation to test for posterior FAI. Reproduced with permission of Elsevier from Leunig, Beckh, Dora, et al., 2005.

Generally, if the affected hip does not show too much cartilage damage, surgical reshaping of the abnormally shaped femoral head or the irregular acetabular edge can be performed. The main goal of these procedures is to eliminate the impingement, thus relieving pain and inhibiting OA. The long-term result of surgery, to eliminate FAI, depends on the amount of cartilage damage present at the time of surgery. Perfect outcomes are possible with joint conservation treatments prior to cartilage damage.

2.5 Computational Modelling

2.5.1 Joint Loading

As one of the early benchmarks for in vitro experimentation, many studies have investigated hip mechanics by testing cadaveric specimens using an instrumented loading apparatus (Hadley, Brown, & Weinstein, 1990; Macirowski, et al., 1994; von Eisenhart-Rothe, et al., 1997). The method of loading was common, where the loading apparatus would exert the unidirectional force from the distal end of the femur to transfer through to the acetabulum. Pressure films were mounted onto the acetabulums to detect contact stress locations and magnitudes. Through cyclic loading, it was noticed that the cartilage began to "weep" (Macirowski, et al., 1994), where synovial fluid was squeezed in and out of the articular cartilage within the joint cavity, supporting McCuthen's early theory of joint lubrication (McCutchen, 1983). Though the benefit was that the fluid could be observed first-hand from the cartilage's viscoelastic nature, this in vitro method eliminated the aspect of physiological loading and functional demand.

The dynamics approach was subsequently implemented, incorporating subject-specific physiological loads, as it could better quantify the hip joint reaction forces through the computational methods of inverse dynamics. Many studies have been published on the hip joint through gait analysis (Alkjaer, Simonsen, & Dyhre-Poulsen, 2001; Nordin, 2001; Pedersen, Brand, & Davy, 1997) all with similar findings.

One of the first ROM studies on FAI used 3-D CT methods for kinematic hip analyses (Kubiak-Langer, Tannast, Murphy, Siebenrock, & Langlotz, 2007). Taking 28 hips with anterior FAI and 33 healthy hips, the study showed decreased flexion, abduction, and internal rotation for hips with FAI. The intention of the study was to provide clinicians with a non-invasive 3-D assessment of the hip prior to surgery (Kubiak-Langer, et al., 2007; Tannast et al., 2007), using the CT data as the reference and the ROM of cam hips as a gauge to determine how much of the joint should be resected during surgery (Figure 2.13).

The most considerable improvement in ROM post-surgery was the internal rotation of the corrected joint. However, the analysis was done through 3-D navigation of segmented CT; no real-time kinetic data was recorded to coordinate with the motion data.

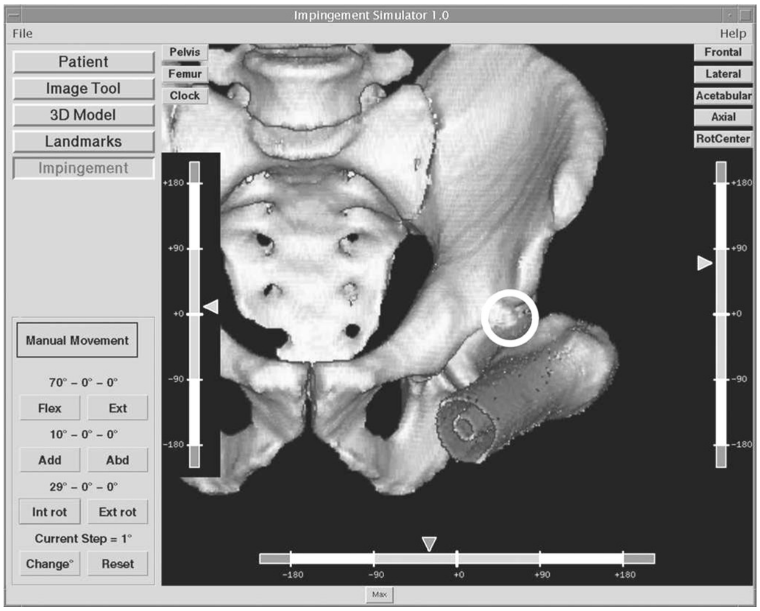

Figure 2.13: Pre-operative ROM test using 3-D reconstructions of CT data to determine amount to be resected. Reproduced with permission of Lippincott Williams & Wilkins from Kubiak-Langer, et al., 2007.

As a comparative study, a similar CT-based navigation system was used to gauge the severity of cam FAI (Brunner, Horisberger, & Herzog, 2009). The intention was again to use the navigation system to determine the amount to be resected. In this case, it was found that a significant amount of patients (24%) showed an insufficient correction of the cam deformity and improper decrease of the alpha angle post-operation.

Very few studies have been published on the biomechanics of cam FAI. In a recent study, it was found that walking biomechanics of cam FAI demonstrated that there was no kinetic difference when compared with a control group (Kennedy, et al., 2009), but did show some constrained ROM in abduction and frontal plane motion for the cam patients. As mentioned earlier in section 2.5.1, since the impingement occurs at a high ROM, most motion analysis studies prior to Kennedy et al.'s would not have been able to distinguish subjects who were or were not suffering from FAI. Furthermore, significant differences in pelvic motion was found between cam FAI and control subjects for a squat motion (Lamontagne, et al., 2009), where participants performed a maximum dynamic squat. Though there were no differences in hip motion during the squat for both groups, it was noticed that the cam group could not squat as low as the control group, further reiterating that the maximal squat depth may be used as a diagnostic test (Lamontagne, et al., 2009).

Though the ROMs and hip joint reaction forces can be quantified using biomechanics testing, the representation of the stresses and strains within the hip joint is lacking. The use of computer modelling and simulation, more specifically FE modelling and analysis, provides an attractive approach to scientific experimentation, since it eliminates the use of more invasive in vivo experimentations. As it offers many real-time input and options, FEA permits the accessibility of varying parameters, providing a reasonable result of the tasks at hand. Like any other theoretical analysis, in order to yield a more accurate approximated result, the inclusion of accurate input variables would be required.

2.5.2 Finite Element Modelling of the Hip Joint

Most researchers have feared the notion of patient-specific reconstruction mostly due to the time consuming efforts or to the complexity of introducing geometric variables. Many studies of hip joint biomechanics have been simplified to a 2-D plane analysis (Rudman, Aspden, & Meakin, 2006; Ueo, Tsutsumi, Yamamuro, & Okumura, 1987; Wei, et al., 2005) or idealized to a ball-and-socket model, which was deemed by some researchers as appropriate for preliminary approximations (Genda et al., 2001). Knowing that the femoral head conforms to a conchoid shape rather than a perfect sphere (Menschik, 1997; Shepherd & Seedhom, 1999), it would be important to incorporate patient-specific contour data and a patient-specific femoral head to accurately estimate the cartilage stresses and contact areas.

Similar to the approach of 3-D CT-based navigation for pre-operative planning, FEMs are now usually reconstructed using CT or MRI data (Arbabi, Boulic, & Thalmann, 2007; Gilles, Moccozet, & Magnenat-Thalmann, 2006) to establish a patient-specific approach. Since the CT segmentation stage is deemed to be time consuming and tedious, many studies have tried to implement semi-automated segmentation methods to extract the objects of interests from CT and MRI data. The clarity and the sensitivity of the images tend to vary from scan to scan, therefore, it is sometimes best to manually segment the objects. Safont and Marroquin devised an algorithm to search for bone contours on the CT plane (Safont & Marroquin, 1999). First, an active contour searched for the proximal femur using a predicted region of interest (Figure 2.14.A). Once the prediction was established on the first slice, search lines from the control points branch out to seek for the contours on the subsequent slices (Figure 2.14.B). However, the final lofted assembly demonstrated the flaws of automated segmentation (Figure 2.15), where the control points from each slice did not conform to the points on adjacent slices, which resulted in jagged and misinterpreted femoral contour.

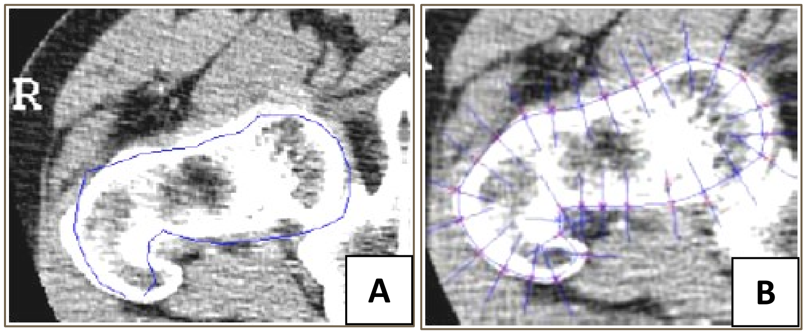

Figure 2.14: (A) Active contour to detect cortical contour of the single slice. (B) After the contour has been established, search lines from each control point branch either converge to or diverge from the centre to predict the contour on the subsequent slices. Reproduced with permission of IEEE from Safont & Marroquin, 1999.

Figure 2.15: Final 3-D representation segmented from CT data using computer algorithm. Due to the jagged contours and the apparent geometric artefacts, the 3-D model cannot be implemented as a FEM. Reproduced with permission of IEEE from Safont & Marroquin, 1999.

Though the algorithm reduced the time to segment the femur and objects of interest, the final segmented representation did not produce an accurate enough model. The approximation of the contour provided a good estimation of the femur's height and dimensions; however, since there were large amounts of geometric artefacts, the model would not have been rendered useful as a FEM. It may have been just as beneficial to have segmented the femur manually. Many improvements have since been implemented to incorporate semi-automated segmentation and radiographic contour detection (Prescott et al., 2009). CTs are usually more readily available for segmentation and are able to provide an indication of any structural bone deformity, though MRIs have the advantage of better identifying soft tissues (Prescott, et al., 2009) such as cartilage and ligaments, especially when incorporating a contrast agent injection or delayed gadolinium-enhanced magnetic resonance imaging (dGEMRIC) (Bittersohl, Hosalkar, et al., 2009).

In order to validate FE predictions, Anderson and associates recently took on the challenge of incorporating patient-specific data to yield a more accurate model and results (Anderson, Ellis, Maas, Peters, & Weiss, 2008). The objectives were to validate the FE method, by comparison with an experimental pressure sensitive film, to assess discrepancies in boundary conditions, cartilage geometry, and material properties. A single cadaveric subject was used in their study. CT images of the cadaveric hip were segmented to assemble a FEM (Figure 2.16). The pressure sensitive film was mounted on the cadaveric acetabular cartilage surface and the femoral head.

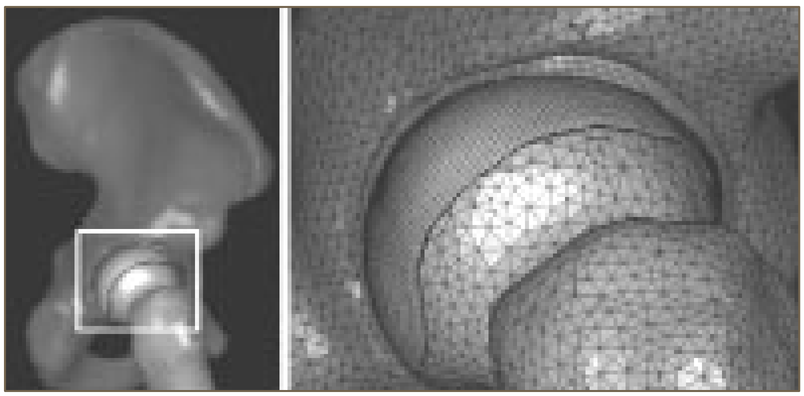

Figure 2.16: Union site of the Anderson et al.'s initial FEM. Bone was modelled as a tetrahedral mesh, whereas the articulating surfaces were modelled as hexahedral swept elements. Reproduced with permission of PubMed from Anderson, et al., 2008.

Load data was applied to the FEM and the cadaveric hip to simulate walking, stairs ascent, and descent. The peak and average surface stresses from the FEM correlated well with the cadaveric model – validating the FE method and experiment. As the focus of the study was to determine the cartilage's contact stresses and areas, muscle attachments and loads were not considered. Moreover, stresses on the acetabulum and regions of the innominate bone were not determined in their FEA or cadaveric in vitro study. In Anderson et al.'s FE assembly, bone was modelled using tetrahedral elements as a hyperelastic isotropic material where as the cartilage layer was modelled using brick elements as a neo-Hookean model. As a follow-up study, the same group had used the same biomechanics approach to examine differences in FE modelling parameters and how altering the femur's and cartilage's material models would impact stress results (Anderson, et al., 2010). Taking the previous hip FEM (Anderson, et al., 2008), then using varying degrees of simplified hip geometries and gradual degrees of patient-specific geometries, each FE assembly was simulated to predict outcomes and differences in stress distributions, as seen in Figure 2.17. The bone-cartilage interface was modelled as subject-specific, spherical, or conchoidal. The cartilage was modelled as either subject-specific derived, cartilage of constant thickness, or varying to a best-fit parameter.

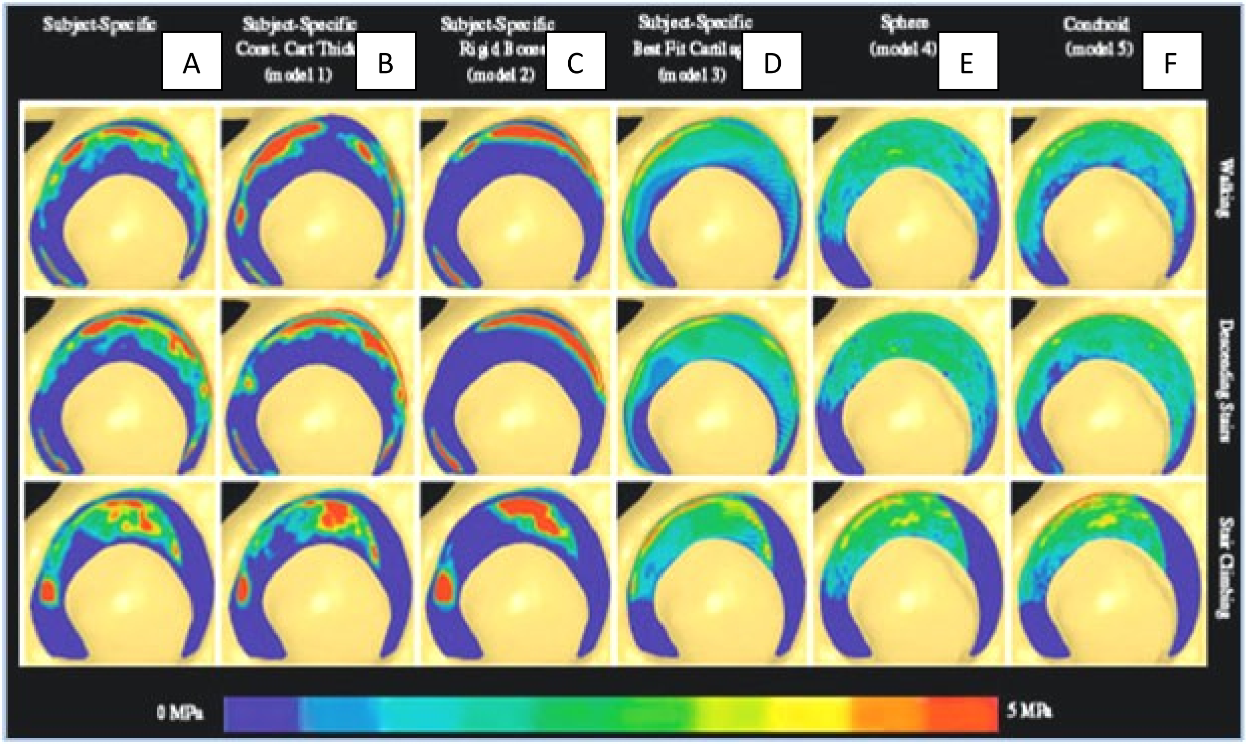

Figure 2.17: Comparison of stresses in Anderson et al's 2010 acetabular cartilage FEM. The study tested for walking, stair ascent, and stair descent for: (A) subject-specific; (B) subject-specific with constant cartilage thickness; (C) subject-specific with rigid bone model; (D) subject-specific using a smooth cartilage model; (E) spherical femoral head; (F) conchoidal femoral head. Stress concentrations are much more apparent when a constant thickness for cartilage was used (B and C). Stress distributed more evenly when a best fit cartilage was used (D, E, and F). Reproduced with permission of Elsevier from Anderson, et al., 2010.

The three activities were walking, stair ascent, and descent. All the boundary conditions were the same in all FEMs tested. The spherical and conchoids models, together with the smooth cartilage, distributed the stresses more evenly, and thus underestimating the peak values. The comparison of the models with respect to the subject-specific model is summarized in Table 2.2.

Table 2.2: Summary of acetabular cartilage results with respect to the subject-specific model (SSM) (Anderson, et al., 2010)

Model / Aspects	SSM with Constant Cartilage Thickness	SSM using Rigid Bone Model	SSM using Best Fit Cartilage	Spherical Femoral Head	Conchoidal Femoral Head
Stress Magnitude	Same magnitudes and region with SSM		Lower than SSM	Substantially lower than SSM	
Stress Distribution	More localized concentrations		Distributed	Evenly dissipated over	
Peak Pressure	Over-estimated	Two times higher	Decreased by half		
Contact Area	Slight decrease		Increase by 25%		

The authors also removed the trabecular bone from the models and argued that a cortical shell was sufficient to demonstrate joint reactions. The study was meant as a comparative study to justify the possible outcomes from various methods. It was noted that the cadaver used in the study was the baseline standard model for all of the FEMs. There was no study to see if the cadaveric hip model had any hip deformities or underlying conditions that could have onset cartilage degeneration or OA. It was explicitly mentioned that a constant cartilage thickness approach that was tested would be less suitable for pathologic hip deformities. The authors did not conclude on which of the FE methods were correct, only suggesting the possible behaviours to expect when utilizing the aforementioned parameters.

2.5.3 Finite Element Modelling of the Cam Deformity

Despite the research that has been done with experimental FE modelling of the hip joint, very little to no research has been contributed towards modelling the cam deformity. No research has been able to represent the cartilage stresses within the hip due to either FAI types until Chegini et al.'s parametric study on the effects of impingement and dysplasia during sitting and walking (Chegini, et al., 2009). The model comprised of an idealized spherical ball-and-cup model, parameterized to vary the alpha and CE angles according to the severity of cam FAI and pincer FAI, respectively (Figure 2.18). Dysplastic hips were accounted for in the simulation with CE angles less than 20^{o}. The alpha angle started at 40^{o} (normal femur; Figure 2.18.A) and increased by increments of 10^{o} up to 80^{o} (severe cam FAI; Figure 2.18.D). The CE angle started at 0^{o} (severe dysplasia; Figure 2.18.C) and increased by increments of 10^{o} up to 40^{o} (pincer FAI; Figure 2.18.B), where measurements of 20^{o} to 30^{o} for the CE angle was deemed as a normal acetabulum (Figure 2.18.A).

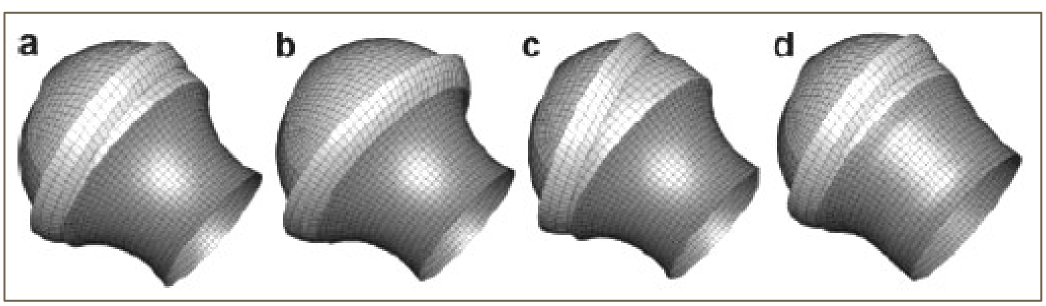

Figure 2.18: Chegini et al.'s assembled hip joint models of varying parameters to simulate the severity of femoral and acetabular deformities: (A) Normal configuration joint; (B) pincer FAI exhibiting a larger coverage of the acetabulum; (C) dysplastic hip exhibiting acetabular under-coverage; (D) cam FAI characterized by an enlarged femoral head at the head-neck junction. Reproduced with permission of Wiley from Chegini, et al., 2009.

The study took a single patient and applied the load through the femoral head, where two loading scenarios were considered: walking and standing to sitting. In each activity, the applied load was multiplied by the body weight (maximum force during walking was 2.30 times the BW and standing to sitting was 1.56 times the BW). The model was meshed using linear elastic isotropic brick elements with a uniform cortical shell of 1.5 mm. Cortical and trabecular bone were given elastic moduli of 20 GPa and 100 MPa, respectively. No Poisson's ratio was disclosed. Cartilage was given an elastic modulus of 12 MPa and a Poisson's ratio of 0.45. A labrum was included as well with an elastic modulus of 20 MPa and a Poisson's ratio of 0.4. No specifications were given on patient details and dimensions of the final model. It was not certain if the acetabulum, or how much of the innominate bone, was actually included with the joint assembly. Peak contact stresses, determined from von Mises (VM) stress analysis, were found on the cartilage layer for both activities: walking (Table 2.3) and standing to sitting (Table 2.4).

Table 2.3: Peak contact stress (MPa) in the acetabular cartilage during the walking activity (Chegini, et al., 2009)

CE Angle (^{o}) / ∝ Angle (^{o})	0	10	20	30	40
40	9.92	6.08	3.55	2.35	1.81
50	9.92	6.08	3.55	2.35	1.81
60	9.92	6.08	3.55	2.35	1.81
70	9.92	6.08	3.55	2.35	1.81
80	9.92	6.08	3.55	2.35	1.81

For the walking activity (Table 2.3), the CE angle had an effect on the peak stresses, but the alpha angle did not. Therefore, no changes in stress were noticed as the alpha angle was increased for the walking activity. Since impingement is experienced at high ROMs, this would justify that peak stresses would vary during activities that would demand for higher dynamic motions (i.e. squatting motions as opposed to walking). As the coverage of the acetabulum progressively increased, a decrease in stresses was noticed (from 9.92 MPa for the dysplastic hip to 1.81 MPa for the pincer FAI hip). There was a large force exerted over a small contact area for the dysplastic hip, thus a higher peak stress.

Table 2.4: Peak contact stress (MPa) in the acetabular cartilage during the standing to sitting activity (Chegini, et al., 2009)

CE Angle (^{o}) / ∝ Angle (^{o})	0	10	20	30	40
40	3.48	3.6	3.66	3.34	3.71
50	3.48	3.6	3.69	3.36	3.64
60	3.48	3.6	3.67	3.68	10.52
70	3.48	3.61	3.78	7.51	16.51
80	3.48	4.7	8.84	12.84	16.51

For the stand-to-sit activity (Table 2.4), it was noticed that as the alpha and CE angles were progressively increased, the peak stresses were increased as well. The cam FAI joints were represented by the parameters of alpha angles from 60^{o} to 80^{o} and CE angles from 20^{o} to 30^{o}. As the alpha angles were increased, the stresses were increased from 3.67 MPa (alpha of 60^{o} and CE of 20^{o}) to 12.84 MPa (alpha of 80^{o} and CE of 30^{o}).

The study only took the axial oblique plane into account when varying the alpha angle and did not measure the alpha angles in the radial plane. The alpha angle did not exceed 80^{o}, thus a more severe cam deformity was not observed. Moreover, CE angles were not increased past 40^{o}, thus a more severe pincer impingement was also not observed.

The more severe mixed impingement cases demonstrated the same peak stresses of 16.51 MPa (alpha of 70^{o} to 80^{o} and CE of 40^{o}). This would represent a substantially rare case. The combination of the two FAI types would limit degrees of ROM and inhibit higher stresses. Since the severity of the cam impingement in Chegini et al.'s study was only limited to an alpha angle of 80^{0}, any alpha angle slightly higher can be compared to the reported mixed impingement magnitudes. For all hip joint models, exhibiting higher severities, the location of the peak stresses were located at the antero-superior regions of the acetabular cartilage (Figure 2.19). However, there was no clear indication in their paper (Chegini, et al., 2009) of what the planar ROMs were for the stand-to-sit activity. As the depth of squat can be a good indicator for the presence of cam FAI (Lamontagne, et al., 2009), it would be important to know what ROM was used in terms of sagittal flexion depth, internal rotation, and abduction in Chegini et al.'s work. Moreover, the model used was not patient-specific to any criteria outlined to previous studies, such as to those of Anderson and associates' (Anderson, et al., 2008; Anderson, et al., 2010), and contrarily conformed to more of an idealized ball-and-socket model. There was no indication of the acetabulum used in the assembly nor were there any indications of the size of the pelvis model. Only cartilage stresses were reported, and no results pertaining to the acetabulum, pelvis, and the femoral head were concluded.

Since there is very little to no papers on the subject of FE modelling and analysis of cam FAI, emerging studies in this specific field would be deemed as exploratory research in its early phases. Chegini and associates' parametric models serve as a preliminary benchmark, even though the model is simple and idealized.

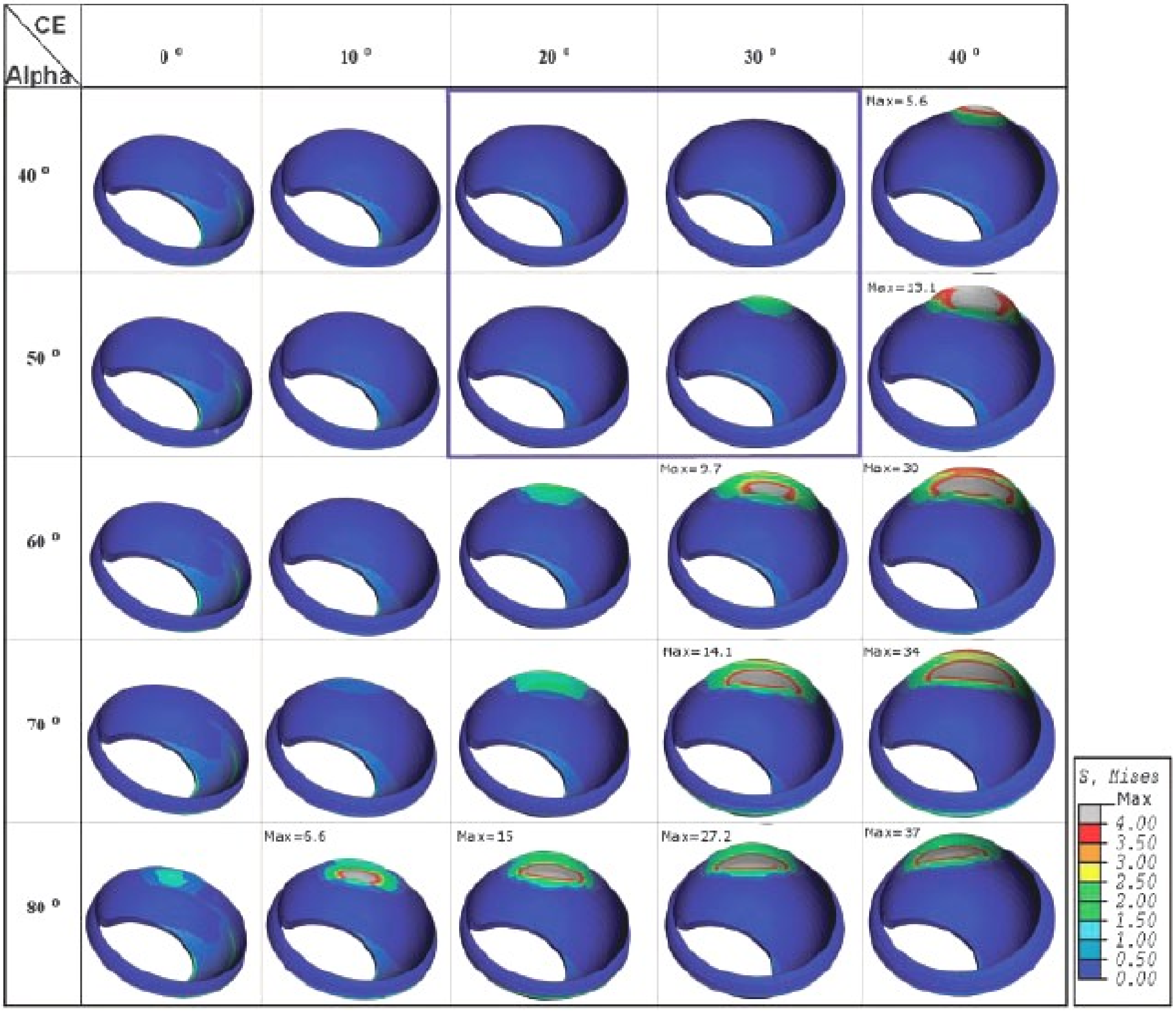

Figure 2.19: von Mises stress distributions (MPa) within the acetabular cartilage during the standing to sitting activity. Reproduced with permission of Wiley from Chegini, et al., 2009.

In our current research, the development of FEMs representing the cam deformity would require taking into account Chegini et al.'s study on the idealized FAI model (Chegini, et al., 2009) and Anderson et al.'s works on the patient-specific hip joint (Anderson, et al., 2008; Anderson, et al., 2010), incorporating the two approaches to yield a more promising result. Both research studies will be examined closely in the subsequent chapter in attempts to produce an improved FEM to represent cam type FAI.

3.0 Theory

3.1 Modelling

3.1.1 CT Sensitivity

As mentioned in section 2.5.2, segmentation and geometric reconstruction of anatomical components are most often done from DICOM (digital imaging and communications in medicine) data. The media used in DICOM data varies from resources to application, often translating CT radiographs or MRIs. The advantage of CT, over conventional 2-D X-rays, is the ability to produce the volumetric data from multi-layered contours. In terms of cost and turnover time, CTs generally cost less than MRIs and the processing time is much shorter (Semelka, 2005). However, MRIs have the ability to display soft tissues since it uses non-ionizing radio frequency signals to detect lower atomic, non-calcified tissues as well. This gives MRIs the advantage over CTs to detect inflammatory soft tissues and necrosis of the hip joint (Mitchell et al., 1986). Though CTs can provide a good diagnosis of bone fractures, it has been argued that MRI can provide a more accurate assessment of the fracture's severity (Cabarrus, Ambekar, Lu, & Link, 2008; Gaeta et al., 2005). For the purpose of replicating bony structures and hard tissues, CT radiographs would be more than adequate to provide the necessary geometric data (Bohndorf & Kilcoyne, 2002; Walde et al., 2005).

During the segmentation process, limiting the amount of artefacts or unwanted incongruent geometries remain to be a challenge in CT imaging, where artefacts are most often due to aliasing, low signal to noise ratio, partial volume detection, and patient movement during the physical acquisition of the CT (Herman, 2009; Mahfouz, Hoff, Komistek, & Dennis, 2005). If any artefacts were to be translated in 3-D along with the CT data, the final output would render extraneous geometric protrusions or inconsistent contours. Artefacts can be generated post-segmentation as well, due to the resolution of the voxels per segmented slice. More will be explained in subsequent section 3.1.2 on the theories of limiting voxel artefacts to render a useable FEM.

The thickness of the slice should be taken into consideration when performing segmentation. The number of slices would greatly increase the number of voxels within a 3-D segmented object, but a necessary amount of slices would be needed to yield an accurate model with minimal artefacts. A thick slice would lose significant data in between the adjacent slices, thus providing poor edge detection. The number of slices recorded for CT data vary according to the anatomical region and the intensity of radiation could vary depending on the level of Hounsfield units (HU), a measure for radiographic density. During the time of segmentation, the contrast of the CT should be considered the correct HU to clearly define the compact bone densities.

Though a 3-mm thickness is suitable for many regions of the body (Cabarrus, et al., 2008; Murphy, 1999), the thickness would be too coarse to render the finer details of the cam deformity at the femoral head. It was determined that decreasing the slice thickness by half (i.e. 3mm to 1.5 mm) can greatly improve the precision of the output by a factor of two (Murphy, 1999).

Figure 3.1 provides a good indication of the detail that is retained when the slice thickness is decreased by a half. Though the thicker slices illustrates the presence of cam FAI, detail is not well retained when looking at adjacent slices in the axial plane in comparison with the CT images with thinner slices. In the example, it is noticed that changes in geometry are more abrupt, more specifically with the change in appearance of the greater trochanter and the femoral head-neck junction.

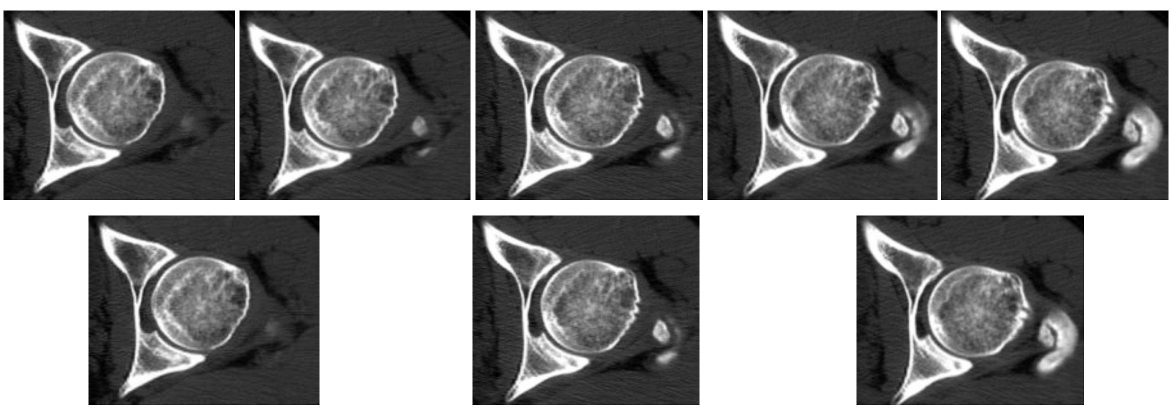

Figure 3.1: Comparison of slice thicknesses and retention of detail in the axial plane of a left hip with cam FAI. (Top row) CT slices calibrated at 1.25 mm the alpha angle of the severe cam deformity in every slice from superior (left) to inferior (right); (bottom row) CT slices calibrated at 2.50 mm showing more abrupt changes of the deformity from slice to slice.

3.1.2 Image Reconstruction

Very few articles have been published to outline the methods involved on how to produce and assemble 3-D FEMs from CT data. As mentioned in section 2.5.2, the segmentation process is likely one of the most time consuming and challenging processes in efforts to produce a FEM. Some studies have used idealized ball-and-socket models to avoid the complexities involved with segmentation and modelling, while some have applied an older idealized CAD model from previous articles.

Many works have achieved good results using an automated edge-detection or region-growing method (Y. Kang, Engelke, & Kalender, 2003; Zoroofi et al., 2003), with some studies establishing specific criterion for diagnosing dysplasia and osteoporosis (de Luis-Garcia & Alberola-Lopez, 2006; Prescott, et al., 2009; Yokota et al., 2009). However, the purpose was to reproduce the 3-D model for diagnostic purposes, thus any presence of small geometric artefacts were negligible. Little to no work has been done to segment hips with cam FAI for FEA. Although many studies have opted to pursue semi-automated segmentation methods, there is always the hesitancy to use an automated method to segment a model for FEA due to the uncertainness of the outcome. Although Safont et al.'s work, as mentioned in section 2.5.2 (Safont & Marroquin, 1999), is considered to be an early trial to loft CT slices using an edge-detection method, it demonstrates a failed process to render a relevant model for diagnostic or FE simulation purposes.

Most often, segmentation software would loft the CT slices and assemble the structure using a tetrahedral or brick element. However, these elements from the segmentation software do not contain mechanical properties (i.e. have not yet been defined by pre-processing FE parameters). Each voxel would be occupied by several of the aforementioned elements, where the quantity would depend on the resolution and complexity of the geometry. The composition would result in an assembly of jagged contours, as seen in Figure 3.2.A. Though representative of a volume, providing a good indication the objects' relative shape and dimensions, the structures would not behave as a proper mechanical structure nor be deemed applicable for FEA. Moreover, due to the large number of elements within a voxel, a much finer element would be required for FE meshing, thus resulting in longer mesh processing and convergence time. This is a common issue in computer modelling, where processing time and lack of memory impedes the output of the results (Aritan, Dabnichki, & Bartlett, 1997; Shaffer & Garland, 2005), especially when dealing with software constraints and limitations on the number of FEs permitted.

A common practice of CAD and CAM in computational engineering design is the implementation of non-uniform rational basis spline (NURBS) modelling. It is a widely used mathematical modelling method for various design, manufacturing, and engineering disciplines (Roger, 2001). Though some anthropomorphic and human modelling studies have used NURBS modelling as an integral component in the design of anatomical structures (Kerr, Ratiu, & Sellberg, 1996; Lee, Lodwick, & Bolch, 2007), NURBS modelling has yet to be a standard practice in orthopaedics and solid modelling of the musculoskeletal system.

The principle of NURBS surfaces is defined by the Bézier curve, where the curve is weighted over a sum of multiple control points (Roger, 2001). Thus, a single arc takes into account many misaligned control points generated by the artefacts and creates a single continual surface, representative of a larger area (Figure 3.2.B). Since NURBS modelling is a CAD process on its own, the best approach to integrate its use with FE modelling is to implement a consistent and efficient, semi-automated resurfacing method that would eliminate a large proportion, if not all, of the geometric artefacts post-segmentation.

Not only will the NURBS surfaces eliminate the jagged artefacts and generate a smooth geometry, the resurfacing procedure would reduce the number of FEs required for the mesh. Since the span of the remodelled surfaces would increase, the number of FEs within a voxel could therefore decrease while the size of the FEs could increase (Figure 3.2.C). The NURBS resurfaces the model, as a whole, replacing the surfaces formed by the jagged voxels and decreasing the number of surfaces. As a result of a lower number of FEs for the mesh, the theoretical computational processing time would likely decrease and converge at a much faster rate.

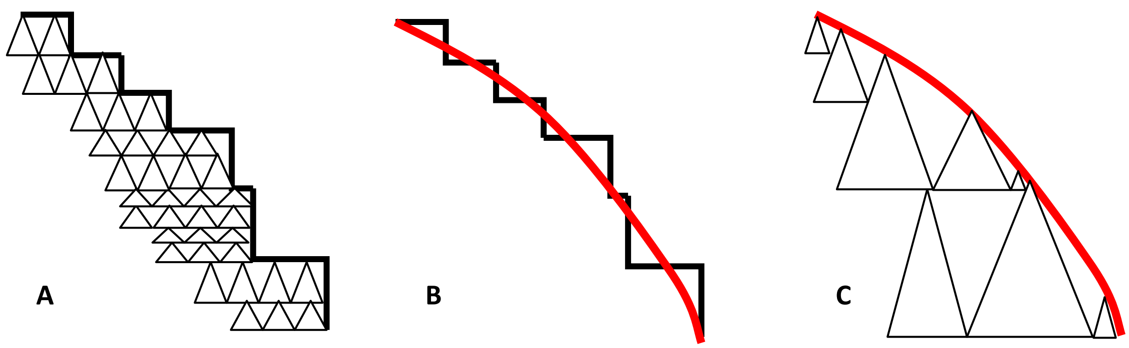

Figure 3.2: Process of NURBS resurfacing for an isolated region of artefacts. (A) Jagged artefacts are prominent on the contour of geometries post-segmentation (outlined in black), thus increasing the number of volumetric FEs, memory, and processing time. (B) NURBS (red curve) resurfaces the geometry using a weighted method to integrate the control points. (C) With the smooth surfaces and larger surface areas, the number of volumetric FEs is decreased along with processing time. By eliminating the artefacts, the appearance of the geometry is also refined.

During the resurfacing process, the concern would be if the accuracy of the contours would remain the same. Since the purpose of smooth surfaces is to eliminate the geometric artefacts and render a compliant FEM, the anatomical structures would need to preserve the distinguishable characteristics and represent correct anatomical features as indicated from CT. Similar with other studies, the femur and the pelvis would be segmented from CT; however, would likely need to be defined as two separate objects within a region of interest (ROI) due to the consideration of two components interacting at a joint assembly (Anderson, et al., 2008; Anderson, et al., 2010; Russell, et al., 2006). The geometry of the anatomical structures would need to be within a level of variance and with marginal degrees of uncertainty. Table 3.1 summarizes the features that would provide structural characteristics and visual appearance of the femur and pelvis.

The two most important components to accurately model would be the femoral head and the acetabulum. To ascertain the precision of the FEM, the alpha angle of the resurfaced femoral component should be measured and compared with the CT radiographs in the axial oblique view. The variance of this measurement, in degrees, between the resurfaced model and the CT data must be minimal to ensure that the asphericity and the severity of the deformity can correctly demonstrate patient-specific accuracy. Moreover, the CE angle of the resurfaced model of the acetabulum should be measured and compared with CT radiographs, in the A-P view, to ascertain the correct coverage onto the femoral head. Secondary anatomical features that define the visual appearance of the femur include: the fovea pit, neck, and greater and lesser trochanters; and for the pelvis: the lunate and fossa within the cup, ischium, ilium, and pubis.

Table 3.1: Anatomical features of the femur and pelvis for comparison between the pre-segmented CT data with the post-segmented resurfaced models

Femur	Pelvis
• Primary • Femoral head • *Alpha angle quantifying severity of cam deformity* • Secondary • Fovea • Femoral neck • Greater trochanter • Lesser trochanter • Height (measured from diaphysis to superior femoral head) to match CT slices	• Primary • Acetabulum • *CE angle measuring acetabular coverage* • Secondary • Lunate • Fossa • Ischium • Pubis • Height (measured from inferior end of pubis to superior end of ilium) to match CT slices

3.1.3 Cartilage Thickness

Modelling the cartilage will be another important challenge as that layer is the articulating surfaces between the deformity of the femoral head and the contact regions of the acetabulum. The cartilage itself is a load-bearing connective tissue comprised of mostly collagen, water, and large proteoglycan complexes, governed by chondroblasts and chondrocytes. The thickness and organization of the cartilage layer can be divided into four zones (Ethier & Simmons, 2007):

- Superficial tangential zone (10-20% cartilage thickness)
- Middle zone (40-60% cartilage thickness)
- Deep zone (30% cartilage thickness)
- Calcified cartilage

The superficial zone is the exterior articulating surface of the cartilage (Figure 3.3). The collagen fibrils are oriented in a parallel fashion to the articulating joint surface, indicating the resistive nature of the orientation to withstand shear stresses (Ethier & Simmons, 2007; Hlavacek, 2001; Macirowski, et al., 1994).

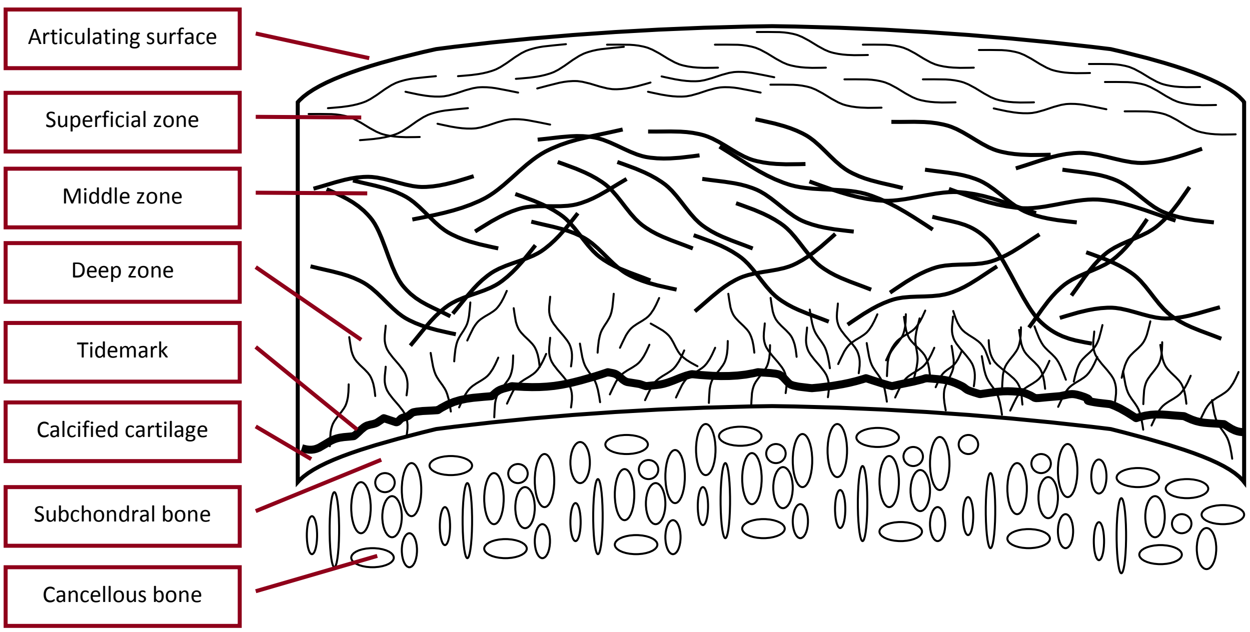

Figure 3.3: Cross-section of articular cartilage indicating the four zones: (1) superficial, (2) middle, (3) deep, (4) calcified cartilage. The tidemark separates the calcified cartilage and the deep zone of within the layer. The subchondral plate is the underlying bone beneath the cartilage.

Knowing that cartilage is very susceptible to shear stresses, it may be valid to conduct a shear stress analysis during the post-processing stages of FEA to examine the adverse loading conditions. Though the constituents and the synthesis of the proteoglycan matrix is a very vital process in the growth and development of articular cartilage, the constituents of cartilage will not be discussed in detail, since the focus is to theoretically understand the methods to model the articulating cartilage in the hip joint.

Previous studies have looked at modelling the four zones of the cartilage separately, in terms of defining unique non-homogeneous material properties, to examine the depth and penetration effects into each zone (Federico, Grillo, La Rosa, Giaquinta, & Herzog, 2005; Korhonen, Julkunen, Wilson, & Herzog, 2008;

Krishnan, Park, Eckstein, & Ateshian, 2003; Owen & Wayne, 2006). It is acknowledged that the accuracy of implementing a non-homogeneous cartilage layer into a FEM would yield a result focused on investigating the mechanical stimuli within the cartilage layers, but would not determine the adverse effects on the entire joint assembly as a whole (Gu, Chen, Dai, Zhang, & Yuan, 2008). Moreover, none of those studies that considered non-homogeneous material properties incorporated a function of physiological loading of an entire joint assembly.

To obtain a more patient-specific cartilage thickness would require other radiological protocols to detect tissues with lower densities than bone (e.g. dGEMRIC, ferumoxytol, contrasting agent, adjustment of greyscale prior to imaging). By theory, with the cartilage images recorded at a supine Dunn view position, where BW and the joint reaction forces of the patient have no loading effect onto the hip joint contact regions and the cartilage, it may be inadequate to proceed with the intricacies of acquiring a patient-specific cartilage layer from radiographs.

In previous studies where an entire hip joint assembly was implemented for FEA, some studies have preferred to apply a constant thickness (Chegini, et al., 2009; Fessler, 1957; Russell, et al., 2006) to only realize that the stress concentrations are more localized and the magnitudes represent an over-estimation due to an inconsistent variation in the contact surface. It was mentioned that a cartilage with constant thickness would be less suitable for pathologic hip deformities, thus would not be adequate for modelling a joint with cam FAI. However, in Chegini et al.'s work, the only published work on the simulation of an idealized joint with cam FAI, a cartilage thickness of 2mm was selected for the acetabulum (Chegini, et al., 2009). Knowing that a constant thickness may not be adequate, a combination of the best-fit cartilage and the mapping of the lunate surfaces of the acetabulum may be the best method to achieve a cartilage layer that would vary in thickness (Anderson, et al., 2010; Russell, et al., 2006), but also can conform with the joint space between the acetabulum and the femoral head.

Although Chegini, et al.'s (2009) idealized geometries included separate femoral cartilage and labral components, it has been disputed that the femoral cartilage (Schmitt, Meiforth, & Lengsfeld, 2001) and the labrum were not necessary (Anderson, et al., 2010). A conventional horseshoe-shape of the acetabular cartilage was more than adequate to determine the stresses within the hip joint (Anderson, et al., 2010; Konrath, Hamel, Olson, Bay, & Sharkey, 1998).

3.1.4 Material Properties

The selection of the material properties would often depend on the physiological application and mechanical assembly of the FEMs. For the implementation of the hip joint's material properties, some previous studies have opted to apply a modulus of elasticity based on an empirical formula derived from the apparent density of bone (Behrens, Nolte, Wefstaedt, Stukenborg-Colsman, & Bouguecha, 2009; Long & Bartel, 2006; Radcliffe & Taylor, 2007; Taddei, Martelli, Reggiani, Cristofolini, & Viceconti, 2006). However, for a quasi-static condition with a low frequency of loading, a linear elastic model would be deemed appropriate to model the structures of the bones. Thus, many previous studies have modelled the femur as two separate, linear elastic, isotropic entities to represent the cortical shell and the internal trabecular structure (Chegini, et al., 2009; Eckstein, Merz, Schmid, & Putz, 1994; Phillips, 2009; Rudman, et al., 2006; Russell, et al., 2006; Speirs, Heller, Duda, & Taylor, 2007; Wei, et al., 2005; Wirtz et al., 2000), as seen in Table 3.2**:**. It was further suggested that the trabecular bone played no role in their FEA simulations (Anderson, et al., 2008; Anderson, et al., 2010), since the trabecular bone contributed very little stiffness to their bone assembly. Anderson et al.'s work justified that the trabecular structure occupied copious amounts of computational memory and did not provide much function within their simulation, thus only a cortical shell was modelled for their study.

Table 3.2: Selected summary of elastic moduli and Poisson's ratios values for assembling FEMs of the cortical and trabecular bone structure of the hip joint

Reference	Cortical Bone		Trabecular Bone	
	Elastic Modulus	Poisson's Ratio	Elastic Modulus	Poisson's Ratio
Anderson, et al., 2010	17 GPa	0.29	Not used	
Chegini, et al., 2009	20 GPa	Not disclosed	100 MPa	Not disclosed
Speirs, et al., 2007	17 GPa	0.3	1 GPa	0.3
Rudman, et al., 2006	17 GPa	0.3	100 to 400 MPa	0.3
Russell, et al., 2006	Not disclosed		120 MPa	0.3
Wei, et al., 2005	17 GPa	0.28 to 0.3	0.6 to 1 GPa	0.3
Wirtz, et al., 2000	18 GPa	0.3	1 GPa	0.2

However, knowing that bone is an anisotropic material, it may be advantageous to implement material properties for which bone could react differently towards various planes and directions in a given coordinate system. Since, bone is macroscopically composed of compact and trabecular bone, both with dissimilar material properties that have different elastic and shear moduli, a homogeneous orthotropic definition for the materials may be beneficial to account for the entire assembly. Previous FEA studies have considered the use of orthotropic material properties to define the structures of the hip joint as a solid model (Asgari et al., 2004; Couteau, Hobatho, Darmana, Brignola, & Arlaud, 1998; Couteau et al., 1998; Estivalezes, Couteau, & Darmana, 2001; Taylor et al., 2002; Wirtz et al., 2003). The use of orthotropic properties for the solid FEM could account for both the cortical and trabecular structures, thus eliminating the need to segment an additional trabecular component and alleviate overuse of FEs and computational memory. Table 3.3 summarizes the material properties for an orthotropic bone representation determined by Couteau and associates.

Table 3.3: Mechanical properties of linear elastic orthotropic bone used for femur and pelvis (Couteau, Hobatho, et al., 1998)

Elastic Modulus (GPa)	$E_x = 11.6$	$E_y = 12.2$	$E_z = 19.9$
Shear Modulus (GPa)	$G_{xy} = 4.0$	$G_{yz} = 5.0$	$G_{xz} = 5.4$
Poisson Ratio	$v_{xy} = 0.42$	$v_{yz} = 0.23$	$v_{xz} = 0.23$

Since two quasi-static positions will be simulated in our study (i.e. stance and squat), orthotropic properties applied to the hip assembly would permit the bones to respond distinctively to the XYZ load direction. An orthotropic material would have a total of nine elastic constants in the constitutive equation, as represented by:

$$\begin{bmatrix} \varepsilon_{xx} \\ \varepsilon_{yy} \\ \varepsilon_{zz} \\ \varepsilon_{yz} \\ \varepsilon_{zx} \\ \varepsilon_{xy} \end{bmatrix} = \begin{bmatrix} \frac{1}{E_x} & -\frac{v_{yx}}{E_y} & -\frac{v_{zx}}{E_z} & 0 & 0 & 0 \\ -\frac{v_{xy}}{E_x} & \frac{1}{E_y} & -\frac{v_{zy}}{E_z} & 0 & 0 & 0 \\ -\frac{v_{xz}}{E_x} & -\frac{v_{yz}}{E_y} & \frac{1}{E_z} & 0 & 0 & 0 \\ 0 & 0 & 0 & \frac{1}{2G_{yz}} & 0 & 0 \\ 0 & 0 & 0 & 0 & \frac{1}{2G_{zx}} & 0 \\ 0 & 0 & 0 & 0 & 0 & \frac{1}{2G_{xy}} \end{bmatrix} \begin{bmatrix} \sigma_{xx} \\ \sigma_{yy} \\ \sigma_{zz} \\ \sigma_{yz} \\ \sigma_{zx} \\ \sigma_{xy} \end{bmatrix} \qquad \textbf{(3.1)}$$

where *E* represents the elastic modulus, *G* represents the shear modulus, and v represents the Poisson's ratio. The subscripts indicate the applied normal plane and coordinate direction, respectively. This property is different from the isotropic model, where the elastic modulus, shear modulus, and Poisson's ratio are independent of direction, as seen by:

$$
\begin{bmatrix} \varepsilon_{xx} \\ \varepsilon_{yy} \\ \varepsilon_{zz} \\ \varepsilon_{yz} \\ \varepsilon_{zx} \\ \varepsilon_{xy} \end{bmatrix} = \frac{1}{E} \begin{bmatrix} 1 & -v & -v & 0 & 0 & 0 \\ -v & 1 & -v & 0 & 0 & 0 \\ -v & -v & 1 & 0 & 0 & 0 \\ 0 & 0 & 0 & 1+v & 0 & 0 \\ 0 & 0 & 0 & 0 & 1+v & 0 \\ 0 & 0 & 0 & 0 & 0 & 1+v \end{bmatrix} \begin{bmatrix} \sigma_{xx} \\ \sigma_{yy} \\ \sigma_{zz} \\ \sigma_{yz} \\ \sigma_{zx} \\ \sigma_{xy} \end{bmatrix} \tag{3.2}
$$

where only two constants are needed to model a FEM. A transversely isotropic material demonstrates isotropic property in the X and Y planes and directions, thus would consist of five constants, as represented by:

$$
\begin{bmatrix} \varepsilon_{xx} \\ \varepsilon_{yy} \\ \varepsilon_{zz} \\ \varepsilon_{yz} \\ \varepsilon_{zx} \\ \varepsilon_{xy} \end{bmatrix} = \begin{bmatrix} \frac{1}{E_p} & -\frac{v_p}{E_p} & -\frac{v_{zp}}{E_z} & 0 & 0 & 0 \\ -\frac{v_p}{E_p} & \frac{1}{E_p} & -\frac{v_{zp}}{E_z} & 0 & 0 & 0 \\ -\frac{v_{pz}}{E_p} & -\frac{v_{pz}}{E_p} & \frac{1}{E_z} & 0 & 0 & 0 \\ 0 & 0 & 0 & \frac{1}{2G_{pz}} & 0 & 0 \\ 0 & 0 & 0 & 0 & \frac{1}{2G_{zp}} & 0 \\ 0 & 0 & 0 & 0 & 0 & \frac{1+v_p}{E_p} \end{bmatrix} \begin{bmatrix} \sigma_{xx} \\ \sigma_{yy} \\ \sigma_{zz} \\ \sigma_{yz} \\ \sigma_{zx} \\ \sigma_{xy} \end{bmatrix} \tag{3.3}
$$

where the subscript *p* represents the normal plane and coordinate direction for both X and Y.

Various models for the articular cartilage have also been implemented in the past. Some researchers have exploited the biphasic property of cartilage (Garcia & Cortes, 2006; Hosoda, Sakai, Sawae, & Murakami, 2009) considering cartilage as a poroelastic material (Carter & Wong, 2003; Ferguson, et al., 2000b). However, in studies looking at the articular cartilage as a whole-body layer, as opposed to focusing on the fluid exudation and intermittent hydrostatic pressures, a simplified isotropic property has often been implemented for the articular cartilage (Anderson, et al., 2008; Anderson, et al., 2010; Asgari, et al., 2004; Chegini, et al., 2009; Rudman, et al., 2006; Wei, et al., 2005). Since the quasi-static loading parameters involve non-cyclic loads, time-dependent and viscoelastic behaviours can also be ignored for the cartilage layer as well (Ateshian, Ellis, & Weiss, 2007; Chegini, et al., 2009; Macirowski, et al., 1994).

3.1.5 Mechanical Stimuli Analysis

Most FEA softwares provide an assortment of nodal and element solution tools for post-processing analysis. Many researchers have opted to use the von Mises (VM) stress analysis to calculate the FE nodal solutions to examine the loading conditions in the hip joint (Chegini, et al., 2009; Eckstein, et al., 1994; El-Asfoury & El-Hadek, 2009). The VM stress analysis calculates the equivalent stress state of the body. The corresponding VM failure criterion considers the squared differences of the principal stresses, then compares the equivalent stress with the material's yield stress, as stated by:

$$\frac{1}{2}[(\sigma_1-\sigma_2)^2+(\sigma_2-\sigma_3)^2+(\sigma_3-\sigma_1)^2] \leq {\sigma_y}^2 \tag{3.4}$$

where σ_1, σ_2, σ_3 represent the principal stresses and σ_y represent the yield stress. By taking the equilibrium state of a material's distortion energy into account, VM's failure theory acts as a conservative failure criterion and is often used for assessing most ductile engineering materials (Huebner, Dewhirst, Smith, & Byrom, 2001; Zienkiewicz, Taylor, & Zhu, 2005). The choice to use VM's failure criterion to assess the innominate structure may be questionable, since the hip comprises of quasi-brittle hard biological tissues. Even if VM's failure criterion is implemented to assess soft biological tissues in the hip joint, it may be too conservative of a stress analysis to examine the principal stresses that exceed its yield stress boundaries. Despite the nature of VM's analysis being a more conservative failure criterion for ductile materials, some researchers have implemented the VM stress analysis to examine the loads exerted on the bone models in FEA of the hip (Durr et al., 2004; Jonkers et al., 2008; Ruan, El-Jawahri, Barbat, Rouhana, & Prasad, 2008; Ryan & van Rietbergen, 2005; Schmitt, et al., 2001), while others have examined individual principal stresses, but were unable to conclude on the importance of each individual principal stress (Rudman, et al., 2006; Russell, et al., 2006).

As an alternative to VM's failure criterion and to account for the principal stresses, a maximum-shear stress (MSS) analysis can provide a less conservative and more accurate indication of the stresses within the hip joint. By theory, the MSS analysis (or also known as Tresca's failure criterion) takes into account the differences between the maximum and minimum principal stresses. The failure criterion would require for one half of the difference between the principal stresses to be less than the yield shear stress, as stated by:

$$\tau_{max} = \sqrt{\left(\frac{\sigma_x - \sigma_y}{2}\right)^2 + \tau_{xy}{}^2} = \frac{\sigma_1 - \sigma_3}{2} \leq \tau_y \quad \textbf{(3.5)}$$

where τ_{max} represents the MSS, τ_{xy} represents the in-plane shear stress, σ_1 represents the maximum principal stress, σ_3 represents the minimum principal stress, and τ_y represents the yield shear stress value. Knowing that cartilage is mostly under shear stresses (Ethier & Simmons, 2007; Hlavacek, 2001; Macirowski, et al., 1994), it may be appropriate to examine the adverse loading conditions of the cartilage and the acetabulum by taking into account the principal stresses to determine the resultant shear stresses. Though the MSS analysis is another conventional failure criterion for ductile materials, it is less conservative in comparison with the VM method (Hibbeler, 2010; Wempner & Talaslidis, 2003), as seen in Figure 3.4, and the resultant shear stress magnitudes may draw comparisons between the cartilage layer and surface of the acetabulum. By using the same stress analysis for both components of the cartilage and bone, it may indicate how much of the stresses are transferred to the adjacent component when going from a standing position to a squatting position.

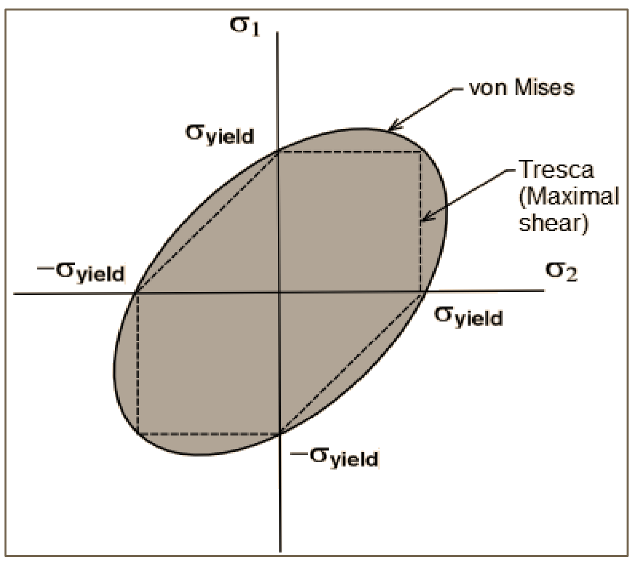

Figure 3.4: Comparison of von Mises failure criterion (solid ellipse) using equivalent stresses with Tresca's failure criterion (dotted hexagonal outline) using maximum-shear stresses determined from principal stresses. Any stresses exceeding the boundaries of the ellipse and hexagon (yield stress limit) would be considered as a failure according to von Mises and Tresca's failure criteria, respectively. Reproduced with permission of Pearson from Hibbeler, 2010.

To examine the initiation and rate of bone remodelling, many researchers have implemented strain energy density (SED) as a mean to examine its effects of mechanical stimulus on the bone apparent density and strength (Cowin, 1995; Huiskes et al., 1987; Jang, Kim, & Kwak, 2009; Ruimerman, Van Rietbergen, Hilbers, & Huiskes, 2005; Vahdati & Rouhi, 2009). The coupled bone resorption and formation process (Figure 3.5) functions in response to physiological demands and to functional mechanical loading.

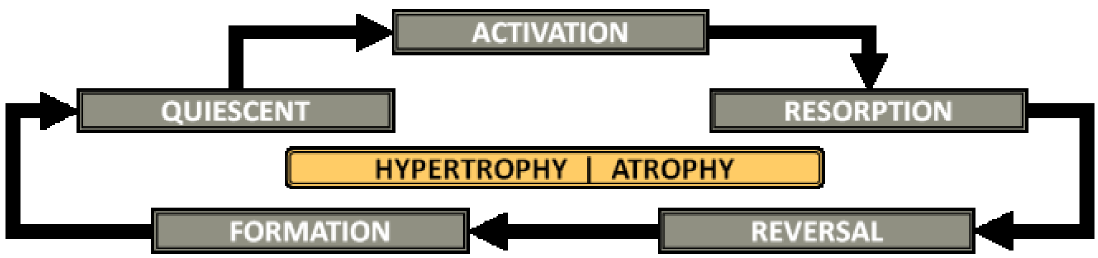

Figure 3.5: The bone remodelling process comprised of a five-step coupled process. (1) Quiescence: the resting state of the bone surfaces; (2) activation: osteoclast recruitment and coupling of osteoblast; (3) resorption: removal of bone by osteoclasts; (4) reversal: coupling of bone formation to bone resorption; (5) formation: osteoblasts resurfaces new layer of bone.

From Huiskes et al.'s early theories on the assimilation between SED and bone remodelling, a linear relationship was established to explain bone formation as a function of SED (Huiskes, Ruimerman, van Lenthe, & Janssen, 2000). An increasing level of SED, beyond the "dead zone", forms bone; whereas a decreasing level of SED, under the "dead zone", resorbs bone (Carter, Van Der Meulen, & Beaupre, 1996), as seen in Figure 3.6. The "dead zone" (or the lazy zone) corresponds with the region where SED levels are not above or below the threshold, thus net bone remodelling is equal to zero.

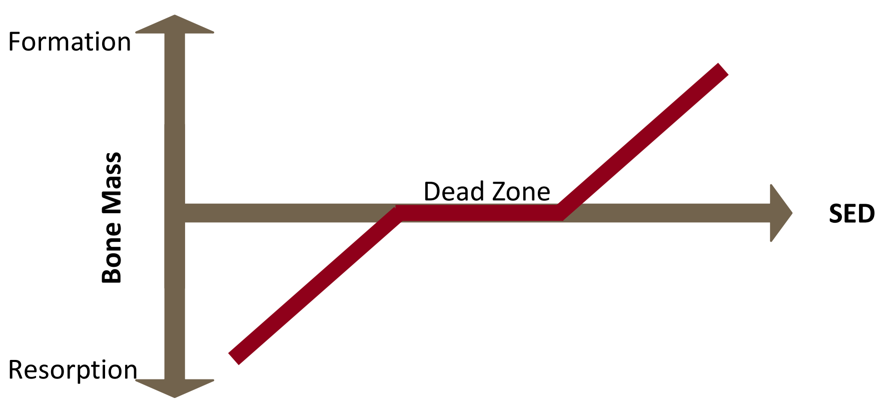

Figure 3.6: Bone adaptation law where mechanical stimulus levels (SED) beyond the dead zone forms bone, whereas levels below the dead zone resorbs bone.

Given that SED is linearly proportional to the rate of bone formation (Huiskes, et al., 2000; Vahdati & Rouhi, 2009), it may be beneficial to determine the regions of high SED levels in a loaded hip joint. Thus, high levels and isolated SED concentrations on the surface of a bone may provide an expected indication of any mechanical stimulus and where bone stiffening would likely occur.

3.2 Maximum Squat Depth

3.2.1 Rationale

To correctly determine discrepancies in mechanical stimuli between a hip with cam FAI and a control hip, force and motion inputs would be required for FEA to simulate mechanical stimuli experienced during a specific activity. Many FEA studies implement gait cycle analyses, incorporating kinetic and kinematic motion, to simulate lower limb, joint, and implant loading. However, as mentioned in sections 2.1.4 and 2.5.1, since squatting tasks require a higher ROM, it would be beneficial to further study squat depths and understand the loading conditions that this task exerts on the hip joint (Lamontagne, et al., 2009).

From Chegini et al.'s work on the parametric FEA of hip impingement and dysplasia as discussed in section 2.5.3, there was no change in stress when the alpha angle was increased for the walking cycle (Chegini, et al., 2009). Peak stresses decreased as the CE angle increased progressing from a dysplastic hip (9.92 MPa at 0^{o} CE) to a severe pincer FAI (1.81 MPa at 40^{o} CE). As the CE angle increased, the surface area of the acetabulum increased and provided a larger contact area between the articulating surfaces to distribute the contact forces. Regardless of the degree of alpha angle, with the exposed contact area defined by the coverage of the acetabulum, it could be justified that the peak stresses remained the same at such low ROMs. Due to the low ROMs, the walking cycle did not demonstrate how the alpha angle (i.e. cam FAI) can affect peak stresses in the hip.

It was in Chegini et al.'s simulation involving the standing to sitting activity that displayed changes in peak cartilage stresses, reiterating again that the maximal squat depth may be a good diagnostic indicator for cam FAI (Lamontagne, et al., 2009). As the severity of the impingement increased for the stand-to-sit activity, the cartilage peak stresses increased varying from 3.68 MPa (alpha of 60^{o} and CE of 30^{o}) to 12.84 MPa for (alpha of 80^{o} and CE of 30^{o}). A more severe mixed impingement case reported a peak stress of 16.51 MPa (alpha from 70 to 80^{o} and CE of 40^{o}). With the constrained ROM during the stand-to-sit activity, caused by the severe deformities, a discrepancy in peak stresses between a FAI group and a healthy group was observed. The data of the motion analysis used in Chegini et al.'s study was not provided, therefore the hips' ROMs to obtain the peak stress results during the walking and stand-to-sit activities were never disclosed. Though Chegini et al.'s simulation used an idealized parametric model, it provided an indication of what was to be expected if one was to implement a patient-specific model during a squat exercise.

3.2.2 Methods

Lamontagne et al.'s study on the effect of cam FAI on pelvic motion and forces (Lamontagne, et al., 2009) was incorporated as the force and motion inputs for FEA in our research. From the biomechanics study, a sample size of 15 patients diagnosed with unilateral cam FAI and 11 control participants were used. The control subjects were matched with patients by age, gender, body mass index, and relative physical activity level. Indications of the cam patients were confirmed by alpha angle measurements from A-P and Dunn View radiographs, where participants were in the supine position. Participants completed a WOMAC (Western Ontario and McMaster Universities) Osteoarthritis Index questionnaire and a Research Consent Form prior to participation. Exclusions of the participants included evidence of OA or joint space narrowing, lower limb surgeries, or serious lower limb injuries. The Research Consent Form explains the purpose, procedures, and possible risks of the study in greater detail to the participants prior to conducting the study. A sample copy of the Research Consent Form, from the initial FAI study, can be found in Appendix A of section 9.1.

The 3-D kinematics of the squat motion was recorded using seven Vicon MX-13 motion capture cameras (Vicon, Los Angeles, CA, USA) adjusted at 200 Hz. Retro-reflective markers were placed on the participants' anatomical landmarks according to a modified Helen-Hayes method (Kadaba, Ramakrishnan, & Wootten, 1990). Additional markers were placed at the greater trochanter, medial knee and ankle to identify the static joint angles and improve the estimation of the hip joint centre, as seen in Figure 3.7.

The 3-D kinetics was recorded using an AMTI OR6-6-2000 force plate (AMTI, Watertown, MA, USA) fixed to the ground and set at 1000 Hz. Participants were asked to perform a dynamic squat, squatting down to a maximal depth and return to a standing position, maintaining heel contact with the force plate throughout the cycle (Figure 3.7). Both arms of each participant were extended anteriorly for balance. A bench was placed behind the participant, adjusted at one-third of the participant's tibial height. The purpose of the bench was to gauge the maximal squat depth and to also serve as a safety device if in case the participant was to lose his or her balance and fall backwards. Participants were asked not to exceed respective maximal squat depths, thus BW was not transferred onto the bench.

Figure 3.7: Maximal squat depth analysis. Participants performed dynamic squats with both feet on AMTI force plates with retro-reflective marking anatomical positions and VICON motion capture cameras recording kinematics. Reproduced with permission of Springer from Lamontagne, et al., 2009.

Five squat trials were performed by each participant and the hip motion and force data was averaged. Lower limb motions were processed using Vicon Workstation software. Net reaction forces of the participants' hip joints were calculated from kinematic and kinetic data using an inverse dynamics approach (Davis, 1997; Kadaba, et al., 1990; Mow & Huiskes, 2005), an approach that considers interconnected limbs as link-segment models.

3.2.3 Principles of Inverse Dynamics

Unlike forward dynamics, inverse dynamics computes the interaction forces in between the link-segments and internal moments derived from the external ground reaction force (measured from the force plate) and the kinematic motion of the rigid bodies (measured from the retro-reflective markers), as seen in Figure 3.8. The forces interacting at the segmented joints are determined from a series of Newton-Euler mechanical principal equations as represented by:

$$\sum F = \sum ma \tag{3.6}$$

$$\sum M = \sum I\alpha \tag{3.7}$$

where *F* is force, *m* is mass, *a* is linear acceleration, and *M* is moment, *I* is moment of inertia, and α is angular acceleration. Each equation corresponds with each link-segment as a rigid body (Equation 3.6 and 3.7) in orthogonal vector planes.

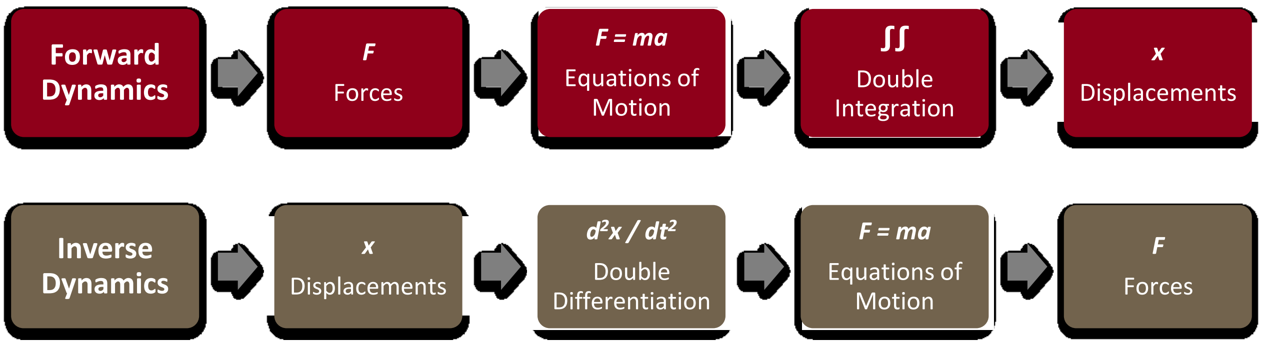

Figure 3.8: Comparison of forward dynamics (top) and inverse dynamics (bottom). Inverse dynamics takes the external loads acting on the leg, the inertial forces and moments, and the location of the landmarks (displacements) to compute a rigid-body equilibrium equation.

In the case of determining the forces at the hip joint, the process first involves measuring the inertial properties of the segments (Andriachhi, 2005; Mow & Huiskes, 2005). The calculation starts from the distal end of the leg assembly at the foot, where the ground reaction force is taken, and then proceeds proximally towards the shank then thigh, as seen in Figure 3.9. Newton's second law of motion is written as an equilibrium equation centred at the foot. Equation 3.8 represents the equilibrium equation, of the segmented foot as the starting point, under external loads. Equation 3.9 represents the moment equilibrium equation. The two fundamental equations are considered as 3-D vector quantities. The unknown forces and moments are then determined at the proximal end of the foot, where the ankle links the shank and foot. The opposing reaction forces are applied to the next segment, the shank, and can then determine the unknown inter-segmental forces and moments, working towards the proximal direction.

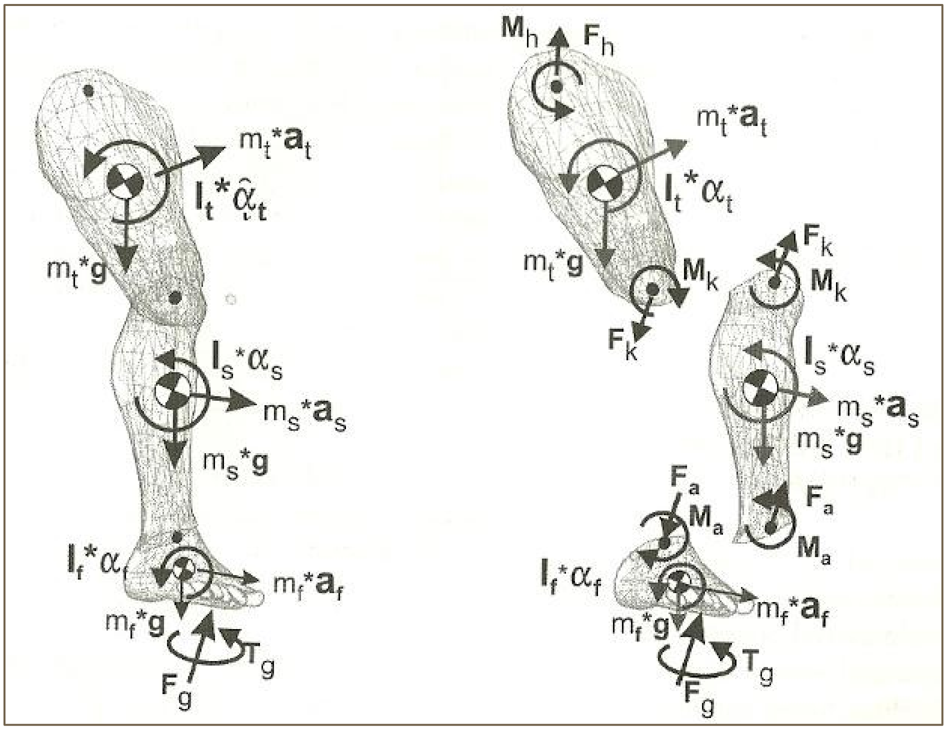

Figure 3.9: The external loads acting on the leg (left) and the intersegmental forces and moments acting on the lower limb (right). Reproduced with permission of Lippincot Williams & Wilkins from Mow & Huiskes, 2005.

To determine the unknown forces of the ankle, force and moment equilibrium equations are set to solve for the unknowns, as described by:

$$F_a = m_f a_f - F_g - m_f g \tag{3.8}$$

$$M_a = -T_g - \left(r_{CM,p} \times F_a\right) - \left(r_{CM,d} \times F_g\right) + I_f \alpha_f \tag{3.9}$$

where g represents the gravitational constant, T is torque, and r is the distance measured from the centre of mass (CM) to either of the proximal (p) or distal (d) end. Subscript a represents the ankle, subscript f is the foot, and subscript g is the ground reaction point.

Taking the known inter-segmental force and moment at the ankle, the next rigid body segment of the shank is calculated to determine the proximal inter-segmental force and moment at the knee. The force and moment equilibrium equations are described as:

$$F_k = m_s a_s - F_a - m_s g \tag{3.10}$$

$$M_k = -M_a - \left(r_{CM,p} \times F_k\right) - \left(r_{CM,d} \times F_a\right) + I_s \alpha_s \tag{3.11}$$

where subscript *k* represents the knee and subscript *s* is shank. Knowing the inter-segmental force and moment at the knee, the equilibrium equation of the thigh segment can then determine the unknown proximal force and moment at the hip, as described by:

$$F_h = m_t a_t - F_k - m_t g \tag{3.12}$$

$$M_h = -M_k - (r_{CM,p} \times F_h) - (r_{CM,d} \times F_k) + I_t \alpha_t \tag{3.13}$$

where subscript *h* represents the hip and subscript *t* is the thigh segment.

The resultant force indicates the joint reaction force acting at the inter-segmental hip. The use of inverse dynamics to calculate joint reaction forces provides an estimation of hip loading during quasi-static situations. A more complete representation of the forces acting at the hip would require a combination of internal force calculations and muscle optimization methods (Andriachhi, 2005). Calculations of internal and muscle reaction forces were not determined or estimated at this time. Some FEA studies have incorporated muscle vectors, approximated to a proportion of the overall inter-segmental reaction force (Behrens, et al., 2009; Phillips, 2009; Rudman, et al., 2006), while others incorporated a reduction method that integrated muscles into similar functional groups (Mow & Huiskes, 2005; Park, Park, & Won, 2007). However, poorly assumed or a redundancy of muscles cannot equilibrate the external forces and moments of the joint properly (Andriachhi, 2005; Brand et al., 1994; Mow & Huiskes, 2005; Pedersen, et al., 1997).

At the time of FE pre-processing, the load input for the FEM will not be implemented as a contact force at a single contact point on the model, as the 3-D biomechanics result represents the net joint reaction forces acting at the hip position as a whole. Moreover, since no muscle loads were determined over the course of the biomechanics study, no additional muscle vectors will be included in the FEA. Instead, the net reaction forces would be emphasized as a force distribution acting through the femoral head, thus creating a joint reaction. Without an accurate measurement of the muscle loads, internal muscle reactions and soft tissues were not quantified in the biomechanics study, therefore will be excluded from the FEA.

4.0 Implementation

The implementation of FEA can be broken down into three main processes:

- Analysis of the hip joint reaction forces for loading parameters
- CT segmentation and development of 3-D models
- Development of FEM and post-processing computational analysis

Figure 4.1 outlines the flowchart of the iterative design process involved to determine the locations and magnitudes of the peak mechanical stimuli. The process applies to each subject model and oriented position. The subsequent sections will elaborate in detail the methods of the FEA.

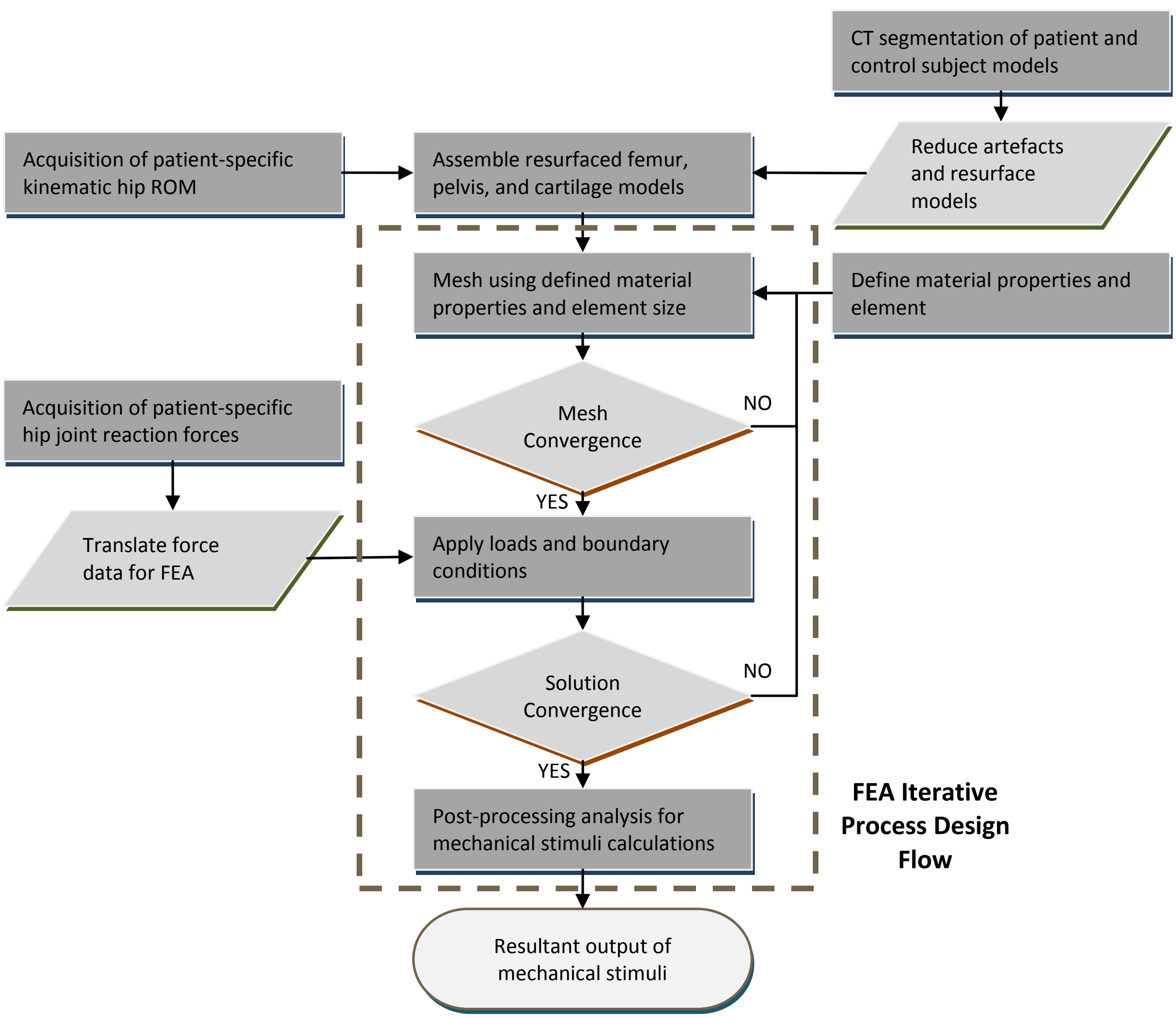

Figure 4.1: Flow chart of the iterative design process. If convergence is not attained during the solving process, the mesh and boundary conditions are re-evaluated to ensure the assembly is constrained and properly represented.

4.1 Biomechanics

As mentioned in the previous chapter, the hip joint loading parameters were taken from participants performing squat depth motions to compare between cam FAI patients and healthy control subjects. The biomechanics data were calculated from kinematics and kinetics data, using an inverse dynamics method of analysis. Data acquisition and processing were performed earlier at the Human Movement Biomechanics Laboratory at the University of Ottawa to compare the effects of cam FAI on pelvic hip motions (Lamontagne, et al., 2009), as part of a multitude of studies on the research of cam FAI, for the Ottawa Centre for Joint Restoration.

4.1.1 Subjects

Of the initial 15 patients and 11 control participants that were tested from the original study, two cam FAI patients were selected for this FEA study. The two selected patients were clinically assessed to have extremely severe cases of cam FAI, as defined by the alpha angle (Beaule, et al., 2005; Notzli, et al., 2002) with alpha angles well above 50^{o}. Moreover, the selected patients were both male, as this gender represented the common sufferers of cam FAI (C. Kang, et al., 2009; Kassarjian, et al., 2007; Lavigne, et al., 2004; Tannast, Kubiak-Langer, et al., 2007). The two FAI patients were control-matched for gender, body mass index (BMI), and physical activity level. An additional FAI patient was included, as a pilot subject to test FE modelling methods and FEA parameters. Table 4.1 summarizes the list of FAI patients and control subjects and their respective clinical assessments. The criterion for age-matching was secondary to physical activity level, as age was not a factor in many of the participants' abilities to reach maximal depth of the squat. The affected hip for both patients was coincidentally on the left side. As a result, only the left hip model of each control subject was segmented and matched with the respective patient model.

The clinical assessments were determined with respect to the alpha angle measurements, ranging from control ($\leq 50^{o}$), mild ($> 50^{o}$), moderate ($> 60^{o}$), and extreme ($> 70^{o}$) in the axial plane. The alpha angles provided with the clinical assessment, for both patients and both control subjects, were preliminary evaluations to estimate the severity of the cam deformity. Prior to CT segmentation, a more precise measurement of the alpha angles will be needed to ascertain the clinical assessments. Moreover, alpha angles will need to be re-confirmed from the FEMs to validate the accuracy and precision of the modelling methods.

Table 4.1: Subject list and clinical assessment for cam FAI patients and control subjects

Subject	Affected Leg	Gender	Age (yrs)	Weight (kg)	Height (cm)	BMI (kg/m^2)	α (°)	Clinical Assessment	Label
14_NG_FAI	Left	Male	44	72.7	177.7	23.0	> 80 axial	Extreme Cam	FAI 1
18_LD_FAI	Left	Male	29	74.9	182	22.6	> 70 axial > 80 radial	Extreme Cam	FAI 2
27_GM_Cont	Left	Male	54	67.4	169	23.6	< 50 axial	Control	Control 1
29_JD_Cont	Left	Male	36	67.9	163.5	25.4	< 50 axial	Control	Control 2
2_MH_FAI	Left	Female	47	55.8	163.5	20.9	> 40 axial > 70 radial	Mild Cam	Pilot

For subject identification purposes, the subjects will be labelled according to a simpler form and method for identification and control-matching purposes. The emphasis of the methods and results will be focused on the patients and the matching control subjects. Subjects will be referred as:

- 14_NG_FAI → FAI Patient 1
- 18_LD_FAI → FAI Patient 2
- 27_GM_Cont → Control Subject 1
- 29_JD_Cont → Control Subject 2
- 2_MH_FAI → pilot subject

4.1.2 Loading Parameters

Full dynamic motions and forces were recorded for all the subjects performing a maximum squat depth cycle. The hip forces were processed, providing kinematic ROM data of the femur with respect to the pelvis in the global frontal, sagittal, and transverse planes; and translated intersegmental hip vectors in the Cartesian XYZ coordinate system. At the time of force data processing for the left hips, the positive X direction points posteriorly; positive Y axis points medially for the left hip; and the positive Z axis was taken as the direction along the longitudinal axis of the femur during stance, superior being the positive direction, pointing away from the knee joint centre.

It was hypothesized that the highest loading scenario could occur when the subjects attain the maximum or near maximum depth of the squat motion. The hip joint loading can confirm when the highest magnitude of intersegmental force that occurs during the squat motion – near the maximal depth. Since muscles forces were not considered, the intersegmental forces would be considered to be an underestimation of the overall joint loading. Thus, with the recorded squat motions to test maximal depths, two quasi-static loading conditions were considered to simulate the patient and control subject models:

- Stance
- Maximum force endured during the squat

The maximum force endured during the squat was selected as the loading parameter for comparison, as opposed to the peak sagittal hip flexion, due to the higher magnitudes in force vectors produced during this quasi-static state in the cycle. Though very close to the actual maximum depth of squat, the peak inter-segmental force during the squat motion was never necessarily at the point of peak hip flexion or at the maximal depth of squat. In most cases, the peak inter-segmental force vectors were highest just prior to the maximal depth of squat, perhaps suggesting the state of highest hip impingement. From these two loading conditions for all four subject models, comparisons in mechanical stimuli in the hip will be made between the cam FAI patient and control subject models during the squatting position. Moreover, mechanical stimuli in the hip during the standing position will be compared with the hip during the squatting position.

4.1.3 Load Data

The ROM and force data for the FAI patients are summarized in Table 4.2; and for the control subjects in Table 4.3. For the kinematic ROM, measured in degrees, a positive value for motion in the sagittal plane indicates hip flexion, where negative suggests hip extension. A positive value for motion in the frontal plane indicates hip adduction and a positive value for motion in the transverse plane indicates hip internal hip rotation. The force data is reported as a normalized magnitude, independent of the subject's BW. The complete ROM and force raw data can be found in Appendix B of section 9.2.

Table 4.2: ROM and force magnitude of left hip for FAI Patient 1 (14_NG_FAI) and FAI Patient 2 (18_LD_FAI) at stance and squat

Subject	Position	Kinematic ROM (^{o})			Hip Force Magnitude (N/kg)		
		1 (sagittal)	2 (frontal)	3 (transverse)	X (anterior)	Y (medial)	Z (superior)
FAI 1	Stance	1.1183	1.1539	-4.7178	-0.1933	0.1556	3.7048
	Squat	98.7362	-12.0209	11.8998	3.7238	-1.5040	0.7958
FAI 2	Stance	-1.1698	-0.2043	-4.8579	-0.2140	0.1218	3.1260
	Squat	102.3411	-15.5228	19.4653	4.0587	-2.1981	-1.7210

Table 4.3: ROM and force magnitude of left hip for Control Subject 1 (26_JD_Control) and Control Subject 2 (27_GM_Control) at stance and squat

Subject	Position	Kinematic ROM (^{o})			Hip Force Magnitude (N/kg)		
		1 (sagittal)	2 (frontal)	3 (transverse)	X (anterior)	Y (medial)	Z (superior)
Cont 1	Stance	1.2354	-2.6860	-5.3838	-0.4357	-0.1708	3.2301
	Squat	119.6773	-13.5990	36.7715	3.4829	-1.9531	-0.9881
Cont 2	Stance	0.2076	-3.8963	-5.2909	-0.04380	-0.1903	3.3768
	Squat	92.8723	-3.5040	11.7820	4.4851	-0.8420	1.3608

Since the hip forces are reported as normalized magnitudes independent of BW, the force magnitudes will need to be translated into normal forces during the pre-processing stages of FEA. The component of the force magnitudes, in the XYZ coordinate system, will take into account the subject's BW and be reported in Newtons. During pre-processing, the femur will be oriented according to the ROMs of the standing position with respect to the femur; also according to the ROMs for the squat position.

4.2 Modelling

4.2.1 Configuration

CT radiographs were acquired for all subjects. Images were recorded in the Dunn view, where the subjects laid in the supine position. Theoretically, the subjects' hips and lower limbs were not bearing any BW at the time of imaging. It was assumed that a normal reaction force was distributed, from the posterior side of the subject, along the surfaces that was in contact between the subject and the examination table. The hip joint was relaxed at this point, thus it was assumed that the cartilage was not loaded during the acquisition of the CT data. Hounsfield units (HU) were calibrated at the time of CT acquisition, thus were not adjusted during the CT segmentation process. Both the femur and pelvis, being hard tissues with relatively similar densities, were the objects of focus. A-P radiographs were examined first to observe for any pelvic tilt prior to axial plane segmentation.

4.2.2 Segmentation

As mentioned in previous chapters, segmentation from CT images is an important phase in the modelling process to yield accurate and precise 3-D geometries that are representative of the cam FAI deformity. Due to the lengthy and elaborate process, this section will only highlight and summarize the processes that were taken to acquire and segment the 3-D models from CT data. A complete and detailed description of the segmentation procedure using computational software can be found in Appendix C of section 9.3.

CT segmentation was performed using 3D-Doctor 4.0 (Able Software Corp., MA, USA). DICOM series of each patient and control subject was opened in 3D-Doctor. The DICOM sets contained compiled CT stacks in the A-P and axial oblique S-I view. The stacks in the S-I view were segmented to create the 3-D model and to measure the alpha angles of the femoral head. The stacks in the A-P view were used to measure the CE angle. The slices in the axial S-I view were calibrated with a slice thickness of 1.25mm (Figure 4.2), thin enough to account for the innominate bones (Murphy, 1999). The voxel had a dimension of 0.683594mm x 0.683594mm x 1.25mm, thus a 3-D volumetric voxel of 0.584126mm^3.

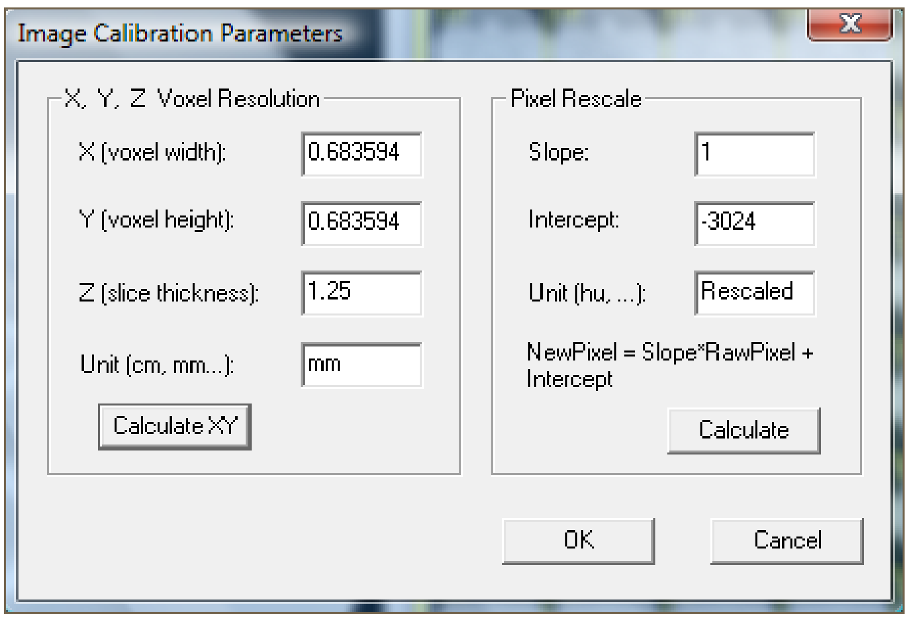

Figure 4.2: The "Image Calibration Parameters" window displaying information pertaining to the dimensions of the voxels (measured in mm) in the Cartesian XY and Z thickness planes.

Each of the data series in the axial plane was imported into 3D-Doctor individually. All the slices within the series were reviewed to ensure continuity of the slices and that all the slices were in the correct numerical order. The contrast of the images were adjusted to prevent contour artefacts and to limit extraneous segmentation of nearby objects. A square-root scale was used to define the upper threshold of the greyscale range (Figure 4.3). By lowering the upper limit and decreasing the overall range (contrast width), much of the other soft tissues become less visible, bringing the femur and the pelvis structures into focus for segmentation.

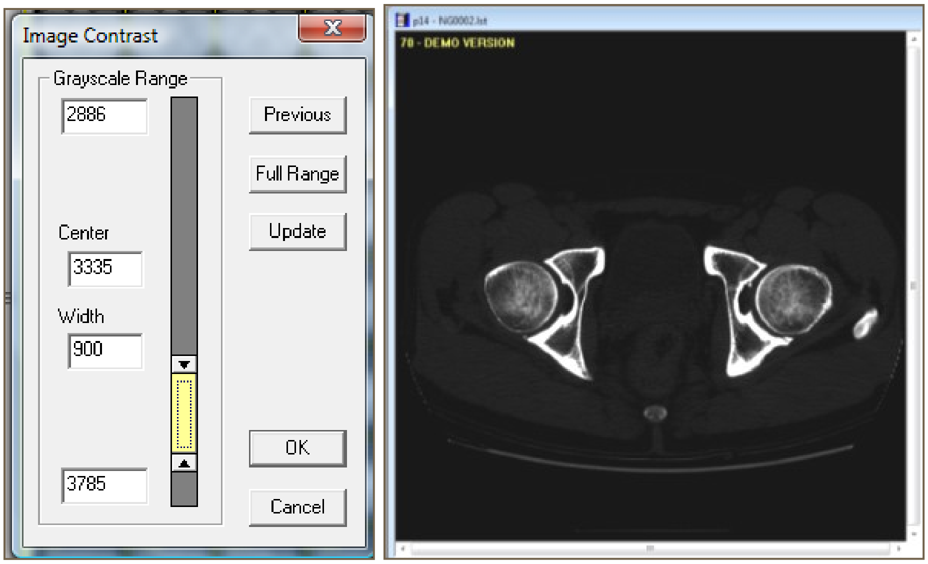

Figure 4.3: Adjusted contrast scale with a range to isolate the hard tissues of the innominate bones and femoral components.

A region of interest (ROI) was then defined around the left hip (femur and pelvis) for a single slice. This ROI was applied to every slice within the series, however, the ROI varied from subject to subject. During the segmentation process, no objects outside this ROI was identified and segmented.

Using an automated edge-detection method, all the planes bounded by the ROI within the series were automatically segmented using an "Interactive Segment All" method. Similar to pre-existing edge-detection methods for CT segmentation, 3D-Doctor attempted to detect the contour of the dense cortical bone structure to characterize the geometry of the volume. The established object contours, as defined by this automated edge-detection method, was primarily used to segment a simple 3-D model and provide a quick visual representation – much like the existing CT navigation tools as mentioned in section 2.5.1. The issue with the "Interactive Segment All" method was that all the detectable objects within the ROI were initially defined as a single object. Thus, if the selected object to segment was the femur, the software recognized anything with similar resolution and visual contrast as a femur (i.e. pelvis and femur were defined as the femur). As the femoral head approached the acetabulum in some image slices, the software assumed that the structure was connected, thus identified the femur and the pelvis as one linked object in several of the image slices (Figure 4.4). Therefore, in many of the slices where both the femur and pelvis components were considered as a single object, the image was segmented once again using a manual segmentation technique to apply two separate contours, one contour each around an object. Respective nodes and boundaries were applied around each of the objects (i.e. femur and the pelvis) and re-identified as respective femur and pelvis objects (Figure 4.5).

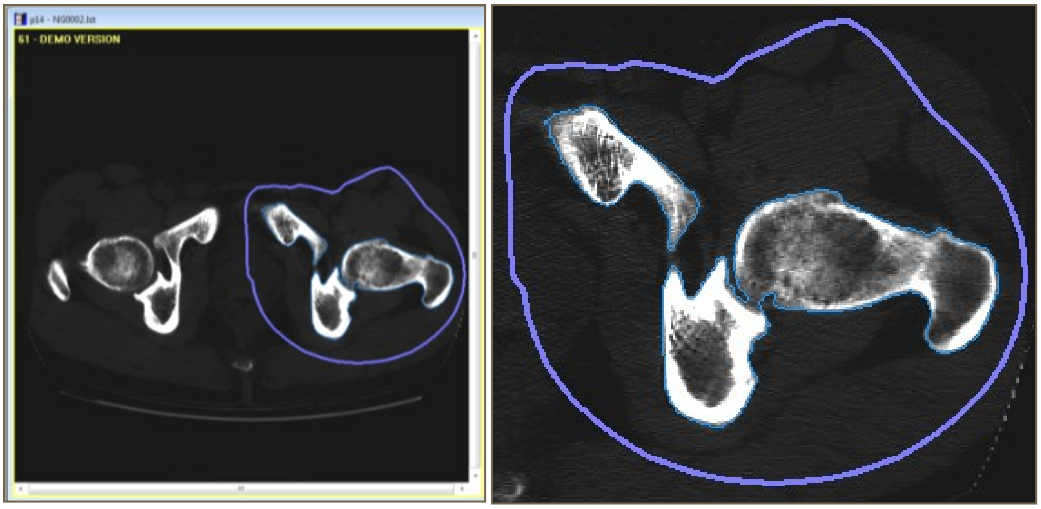

Figure 4.4: The automated "Segment All" feature defines a single object and segments every slice within the ROI (defined by the surrounding blue outline). In many of the slices, where the femoral head is in close proximity with the acetabular structure, the software links both components and defines them as a single object.

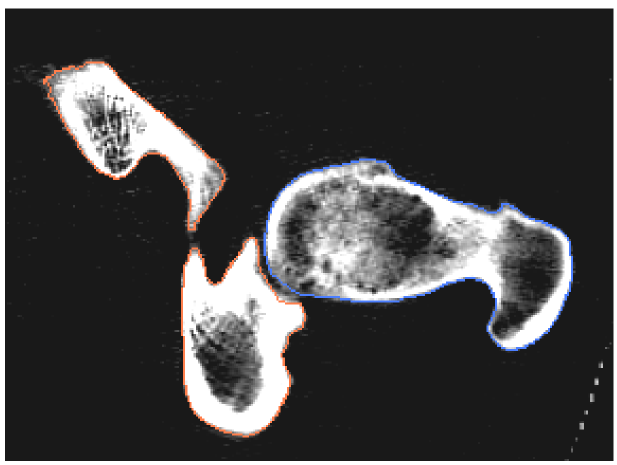

Figure 4.5: The "Boundary Editor" tools allow for manually adjusting the contours that were initially set by the automated edge-detection method. The "Split Boundary" command first breaks the linked objects into two separate objects. The "Set Object" command allows the two objects to be redefined to respective identities of femur and pelvis.

After the boundaries have been defined for both the femur and pelvis for all slices within the series, the 3-D model was generated using a "Complex Surface Rendering" method in 3D-Doctor. All patient and control subject models were generated with a high density setting, creating more triangular surface polygons within a voxel. The purpose for the high density of the surface polygons was to yield a more accurate model and to limit contour artefacts. The final rendered output depicted the two separate segmented objects (Figure 4.6).

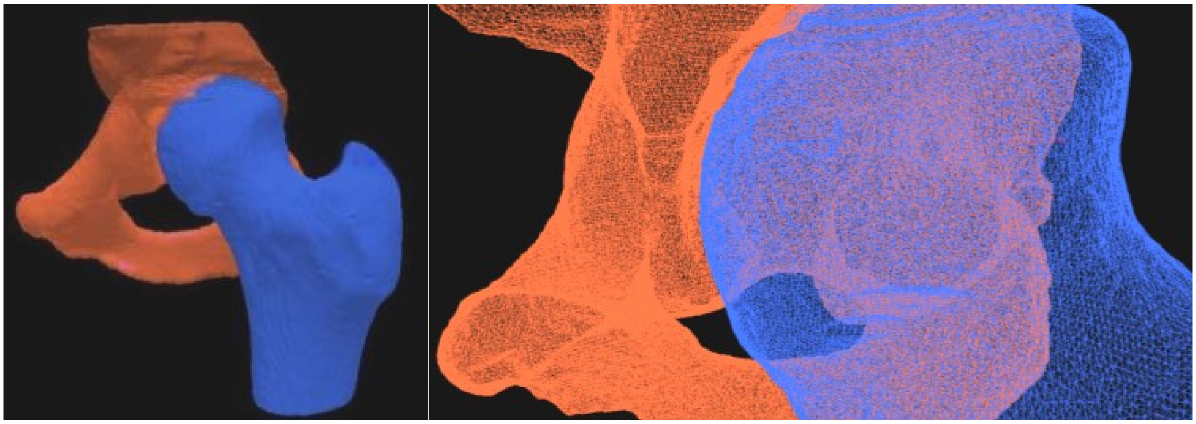

Figure 4.6: The final rendered output of a 3-D model assembly (left) depicting the femur model (blue) and the separate pelvis model (orange). The denseness of the meshes limited the contour artefacts (right).

The number of triangular surface polygons and number of nodes for the femur and pelvis were subsequently reported for all of the segmented assemblies, as indicated in Table 4.4. The number of slices that were used to segment the objects was also reported. It was noticed that the number of triangular polygons and nodes for both of the FAI patients' femur models exceeded the number of polygons and nodes for both of the control subjects' models. This could be likely due to the aspherical femoral head of the cam deformity, providing the protruding "bump" at the femoral head-neck junction, thus required a higher number of polygons and nodes to segment. The number of polygons and nodes for the pelvis models were relatively similar for all four 3-D models.

Table 4.4: Surface information from 3-D surface models segmented from 3D-Doctor

Subject	Number of Slices	Left Femur		Left Pelvis	
		Number of Triangles	Number of Nodes	Number of Triangles	Number of Nodes
FAI 1	110	93556	46780	152752	76376
FAI 2	105	94460	47234	147552	73776
Control 1	106	81224	40614	151884	75942
Control 2	104	85600	42802	145492	72746
Pilot	103	78248	39126	132492	71242

The slices were then overlaid onto the models to provide a final verification of the alignment of the 3-D models prior to exporting the models. The two objects (femur and pelvis model) were each exported individually from 3D-Doctor as separate stereolithography (STL) files.

4.2.3 Resurfacing

Each of the STL files was then imported into Solidworks (Dassault Systèmes, MA, USA) to smooth and resurface the edges. The need to resurface the model, as discussed in Chapter 3.1.2, was to eliminate geometric artefacts and reduce the number of surface polygons to render an adequate FEM. By doing this, larger resurfaced edges would be integrated onto the smoothed contour, thus requiring a lesser amount of FEs per surface and shorter computation time.

To perform the resurfacing in Solidworks, the “ScanTo3D” tool was added into the basic start-up of the program. The “ScanTo3D” tool was designed as an additional component within Solidworks to model point cloud and mesh data. The tool was toggled by accessing the “Add-Ins” command in the “Tools” menu. Each of the STL files was imported and resurfaced individually. One-by-one, the STL file was opened in Solidworks as a “mesh file” and not as a standard “STL file”. This was a crucial step for the software to recognize the object as a mesh cloud and not as a standard graphics file. None of the planar axes and global coordinate systems were altered. The femur was the first to be resurfaced. Using the “Mesh Prep Wizard” from the “ScanTo3D” tool, the model was selected as the mesh file to be cleaned up (Figure 4.7). Extraneous data, such as anatomical features (i.e. greater and lesser trochanter, fovea pit), was not altered or removed.

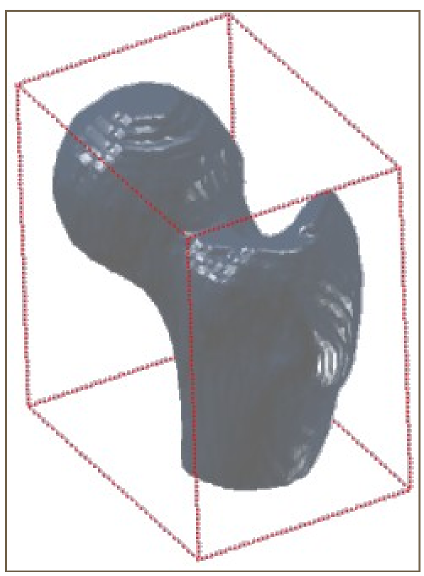

Figure 4.7: Isometric view of the selected STL mesh file in Solidworks from the “Mesh Prep Wizard”. As seen, the femoral component contains many jagged edges and surface artefacts prior to resurfacing.

The next step allowed for any simplification of the model as a whole or within a selected area, by reducing the amount of meshes within the mesh cloud (Figure 4.8.A). No mesh reductions were made at this point to prevent any holes in the geometry; however, the overall smoothness of the model was set at the highest level possible. The “Global Smoothness” command recognized the locations of the point clouds and integrated surface splines over the nodes. This step eliminated much of the jagged edges and lofted plateaus of the initially STL model (Figure 4.8.B). The “Surface Wizard” was then launched to apply surfaces to create a solid from the mesh. The surfaces had NURBS-like qualities as it contained many principal Bézier curves to hold the form of the surfaces (Figure 4.8.C). The detail of the surfaces varied on a sliding scale, depending on the complexity of the geometry and the mesh files.

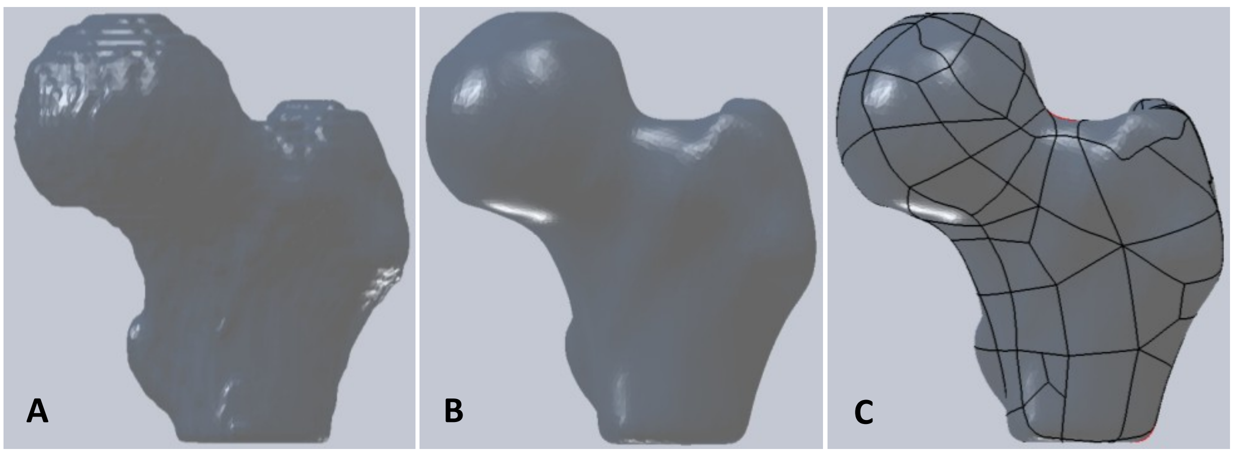

Figure 4.8: The “Mesh Prep Wizard” (A to B) and the “Surface Prep Wizard” (B to C). The model started with jagged edges, lofted from the CT slices (A). After the “Global Smoothness” command, many of the geometric artefacts were minimized (B). The model was then resurfaced to produce a volume (C).

After having generated the resurfaced femur model, there were often spline deformities, obstructions, or self-intersecting surfaces, reported by “Surface Wizard” as red planar curves (Figure 4.9.A). If unrepaired, the discrepancies resulted in holes or missing surfaces. If the number of self-intersecting surfaces were caused by a highly complex mesh file, as in most cases with the pelvis model, the model was resurfaced with a higher level of detail. However, in most cases with fairly few discrepant surfaces, the feature lines were adjusted to fit the planar curve within the missing surface (Figure 4.9.B). The final product resulted in a volume representing the left femur (Figure 4.9.C). Though it was possible to create volumes with the aforementioned self-intersecting surfaces, it was decided that the best method to yield a volumetric model of the femur and pelvis was to utilize the advantage of the feature lines to fit a planar curve within the discrepant regions. The pelvis models were created using the same “Mesh Prep Wizard” and “Surface Wizard” methods (Figure 4.10). All the femur and pelvis models were then exported as parasolid files (X_T files).

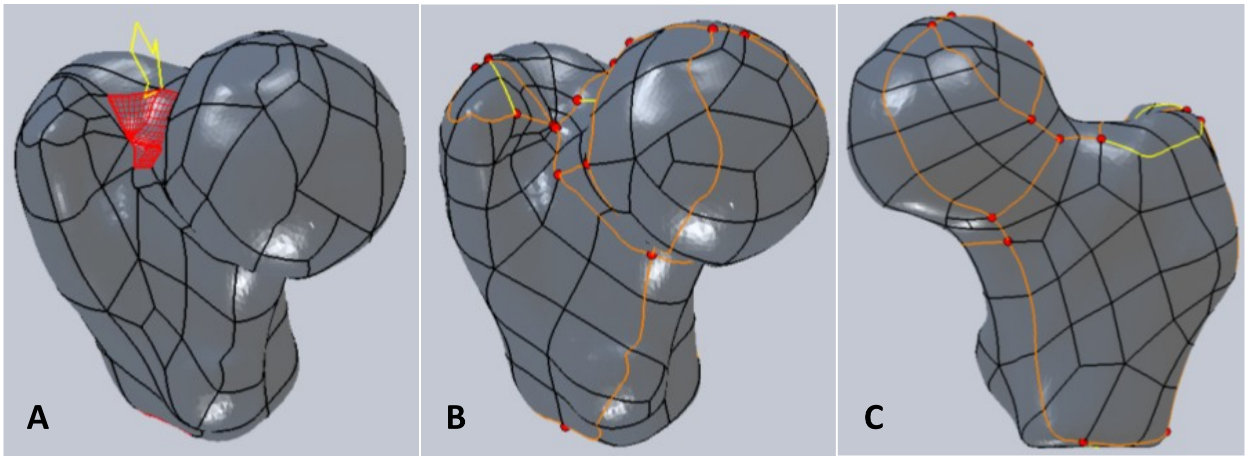

Figure 4.9: The “Surface Wizard” resurfacing process for the femur models. The red areas (A) indicate a region of self-intersecting surfaces, likely in more complex regions requiring a higher number of surfaces. (B) Feature lines, as indicated by the orange lines, were then adjusted to fit a planar curve within the region, as indicated by the yellow lines. The final product resulted in a closed volume (C).

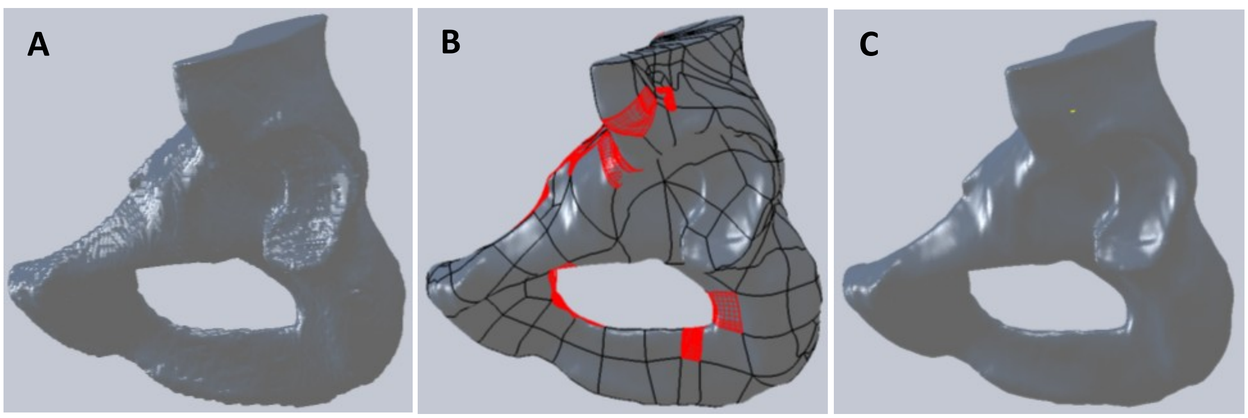

Figure 4.10: The same methods were used to produce the pelvis models. Prior to smoothing and resurfacing, the complex pelvis model had many more artefacts than the femur (A). After reducing the geometric artefacts and lofted, jagged edges, the model was resurfaced (B), with the red regions indicating the discrepant areas. The final product resulted in a closed volume of the pelvis model (C).

After the models were resurfaced, both the femur and pelvis were inspected for structural characteristics and visual appearance. All resurfaced models were confirmed to have retained the anatomical characteristics that define the appearance of a femur and pelvis, as mentioned in Table 3.1 of section 3.1.2.

As mentioned, it was advantageous to resurface the models. Not only did the models provide a more accurate visual representation of the anatomical components, the translation of the triangular surface meshes (from 3D-Doctor) to NURBS-like planar curves (from Solidworks) reduced the amount of surfaces. Table 4.5 summarizes the impact of the resurfacing procedure by indicating the number of surfaces prior to and subsequently after the process. The resurfaced structure will be a benefit to create a mesh based on an optimal number of FEs and will decrease the computation time significantly.

Table 4.5: Number of surfaces on the femur and pelvis models prior to and after resurfacing

Subject	Left Femur		Left Pelvis	
	Triangular Surfaces Pre-resurfacing	Surfaces Post-resurfacing	Triangular Surfaces Pre-resurfacing	Surfaces Post-resurfacing
FAI 1	93556	277	152752	369
FAI 2	94460	324	147552	443
Control 1	81224	322	151884	391
Control 2	85600	311	145492	435
Pilot	78248	207	132492	322

4.2.4 Cartilage Layer

In continuation with the use of Solidworks, the articular cartilage was modelled and resurfaced as a single layer. Both the femur and the matching pelvis model were opened on an assembly layout using the "Instant3D" tool (Figure 4.11.A). The models were placed according to the global coordinate system, as defined during the CT acquisition and segmentation processes. An offset method was used to extrude the entities within the acetabulum of the pelvis (Figure 4.11.B) to the surfaces of the femoral head (Figure 4.11.C).

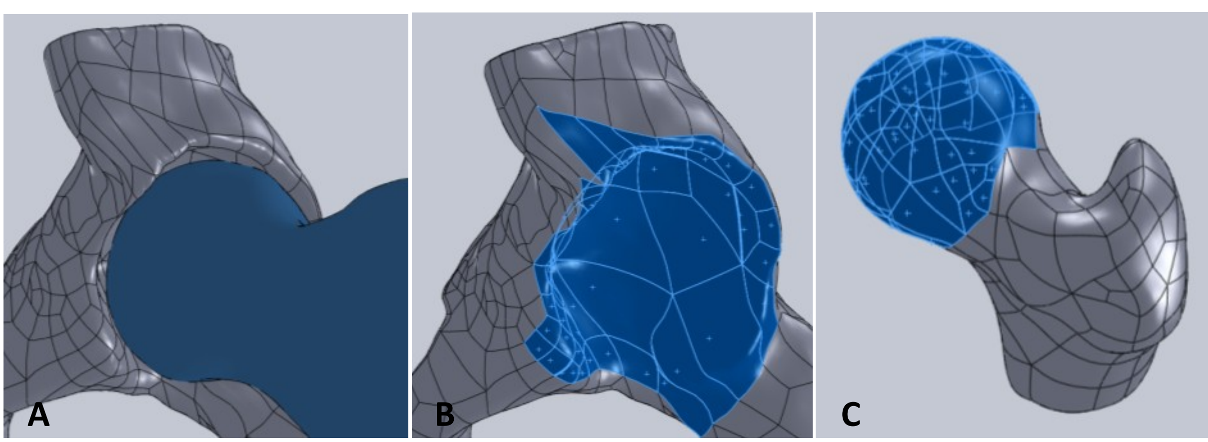

Figure 4.11: The acetabular cartilage was created by an offset method from the acetabulum. Both the femur and pelvis models were opened in an assembly file (A), where the acetabular surfaces were selected as the entities to offset (B) and extrude onto the target surfaces of the femoral head (C).

Since the concavity of the acetabulum did not perfectly match the curvatures of the convex femoral head surfaces, the resultant cartilage layer was variable in thickness. The thickness was relative to the amount of space between the ossified structures of the femoral head and the acetabulum, as detected by CT images. The cartilage was extruded past the periphery of the acetabular rim, thus representative of tissue at the lateral labral region. A separate layer was not created for the labrum, as the inclusion of the labrum in the FEA of the hip joint remains elusive (Anderson, et al., 2010; Konrath, et al., 1998). The region of the cartilage layer at the acetabular fossa was removed, thus the acetabular cartilage was only represented by the surfaces of the lunate and the acetabular dome – the horseshoe shape (Figure 4.12). The acetabular cartilage layer was created for all patients' and control subjects' assembly models. No patient or control subject showed any indications of OA or cartilage delamination, thus the cartilage layer was modelled as an idealized smooth layer with no abrupt surface discrepancies. The cartilage model underwent the same resurfacing methods, as the femur and pelvis models, and was exported as a X_T file. The cartilage was modelled as a uniform, simplified layer. The various zones and the biphasic properties of cartilage were not considered in this study.

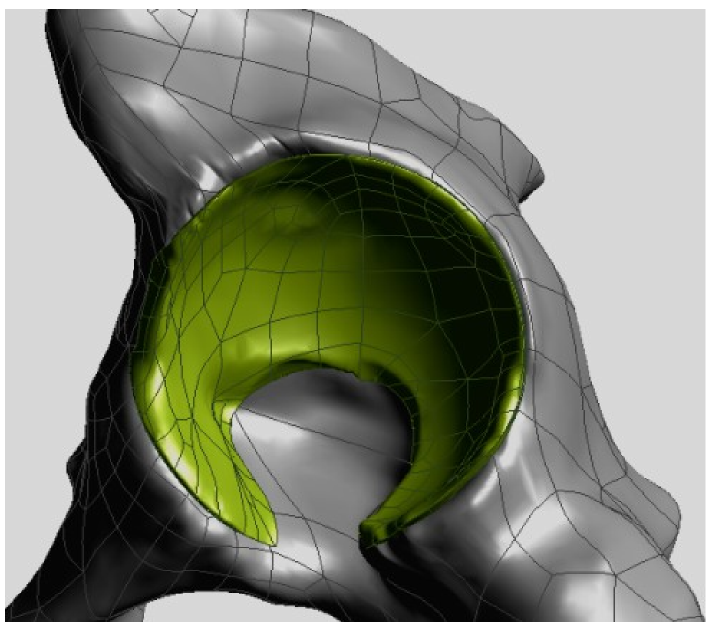

Figure 4.12: The final rendered product of the acetabular cartilage. The layer at the acetabular fossa region was removed, giving the cartilage the conventional horseshoe shape.

The need to include the articular cartilage at the femoral head was questioned. Using the pilot model, the articular cartilage was built from the femoral head using the same aforementioned methods as the acetabular cartilage (Figure 4.13), with the thickest point proximal to the fovea and the thinnest at the periphery of the femoral head distal from the fovea (Chegini, et al., 2009; Russell, et al., 2006). The femoral cartilage layer was not extracted at the region of the fovea.

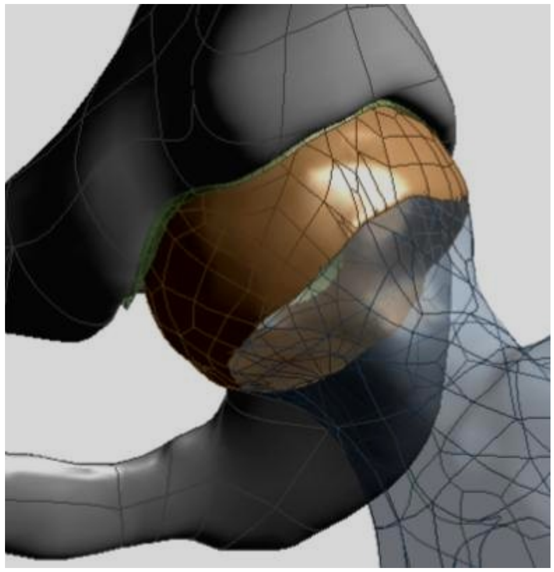

Figure 4.13: The complex articular cartilage model of the femoral head (orange layer) using the same methods as the acetabular cartilage layer. The inclusion of the femoral cartilage did not demonstrate differences, thus was not included with the patient and control models.

From the initial pilot study, it was noticed that the inclusion of the femoral cartilage increased the computational processing time substantially. Moreover, the refined elements that were used to mesh the more complex and smaller femoral cartilage layer risked mal-convergence of the FEA process. Most importantly, when the processing did converge for the pilot study, the quasi-static solution did not demonstrate differences to that of an assembly without a femoral cartilage. It has been disputed in the past that the inclusion of the femoral cartilage has been ineffective for stress analysis of the hip joint using FEA (Schmitt, et al., 2001). In this quasi-static analysis, where the focus was on the acetabular cartilage, it may not be necessary to model the cartilage at the femoral head to examine the mechanical stimuli at the acetabulum. The focus of the femoral head was to model the severity of the structural cam FAI deformity as accurately as possible. The contact interfaces between the femur and the acetabulum would still be modelled as frictionless. Therefore, the articular cartilage at the femoral head was not included for all patient and control subject models.

4.2.5 Measuring the Alpha Angles and CE Angles

To verify the accuracy of the modelling and resurfacing methods, alpha angles of the femoral head were measured in the axial plane; and CE angles of the acetabulum were measured in the A-P view. Measurements were first taken from CT images, in 3D-Doctor using the measurement tool, prior to segmentation of FE modelling (Figure 4.14.A). The alpha angle was determined on the slice where the femoral head was the largest in diameter, thus near the centre-plane of the femoral head. The alpha angle was determined as the angle between the axis on the femoral neck and the emergent sphericity of the femoral head. A single slice was provided in the A-P view, thus the CE angle was determined from the visible bony structure of the centre-edge to the tangent of the acetabular rim (Figure 4.14.B). After resurfacing the segmented model, the alpha and CE angles of the FEMs were measured from the femoral head and acetabulum, respectively (Figure 4.15). Statistical paired t-tests were calculated in Microsoft Excel to verify the FE modelling procedure and to analyze the differences between the alpha and CE angles from each method.

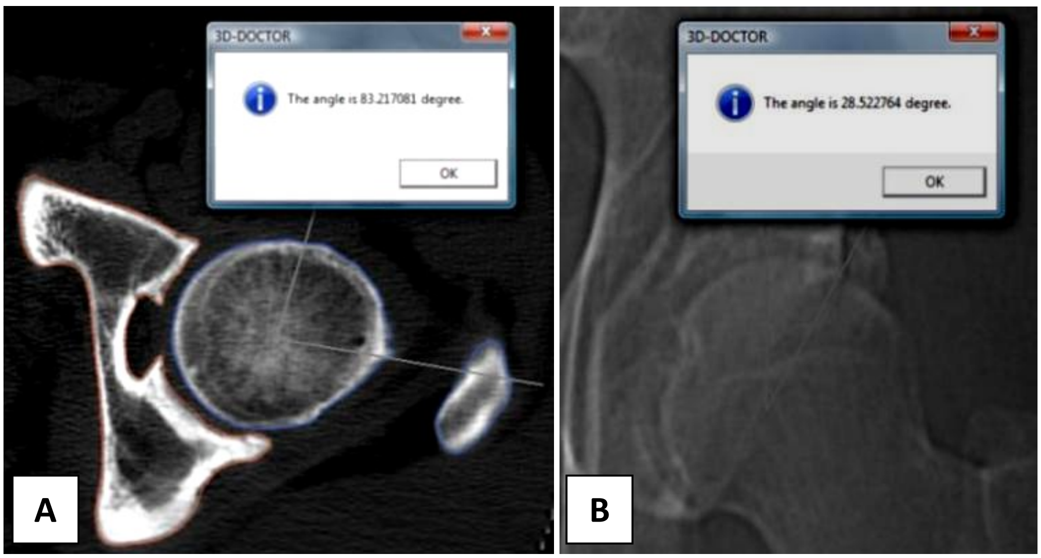

Figure 4.14: The alpha angle measurement in the axial plane of FAI Patient 1 (A) and CE angle measurement in the A-P view (B).

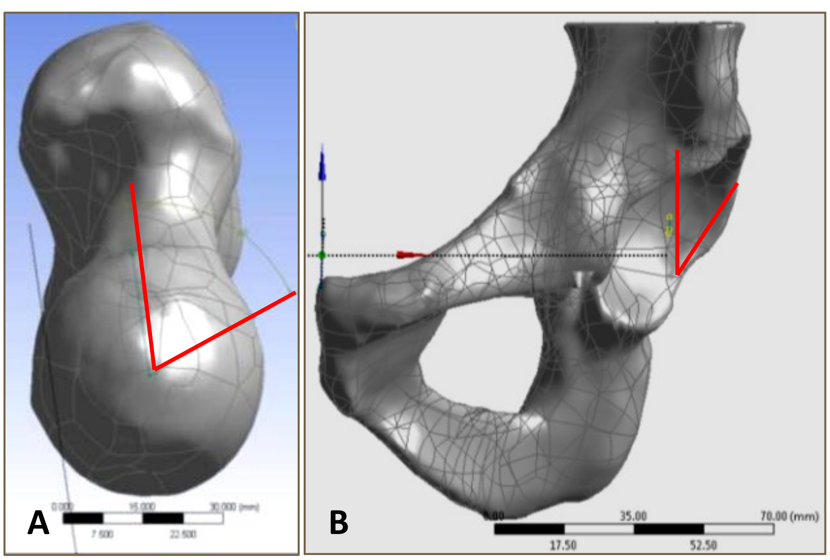

Figure 4.15: The alpha angles (A) and CE angles (B) were measured again from the FEMs to verify the accuracy of the modelling and resurfacing methods.

4.3 Pre-processing

4.3.1 Orientation

The pre-processing, compiling, and solving methods of FEA were performed using ANSYS Workbench (ANSYS, PA, USA). The femur, pelvis, and cartilage models for each patient and control subject series was imported into ANSYS DesignModeler as X_T files, a total of three separate bodies. All solid, surface, and line bodies for each component were processed. Geometries and model topology were not further simplified. Each imported body was positioned according to its original global coordinate system, as defined at the time of segmentation. The pelvis and the cartilage remained fixed onto the global coordinate system. The femur abided by the global coordinate system as well; however, an additional local coordinate system was implemented on the femur, as this was the component that was simulated in various positions (Figure 4.16). The local coordinate system allowed for the femur to retain any anisotropic material properties that were local to its individual planar loads, as opposed to behaving to the planar directions of the global coordinate system.

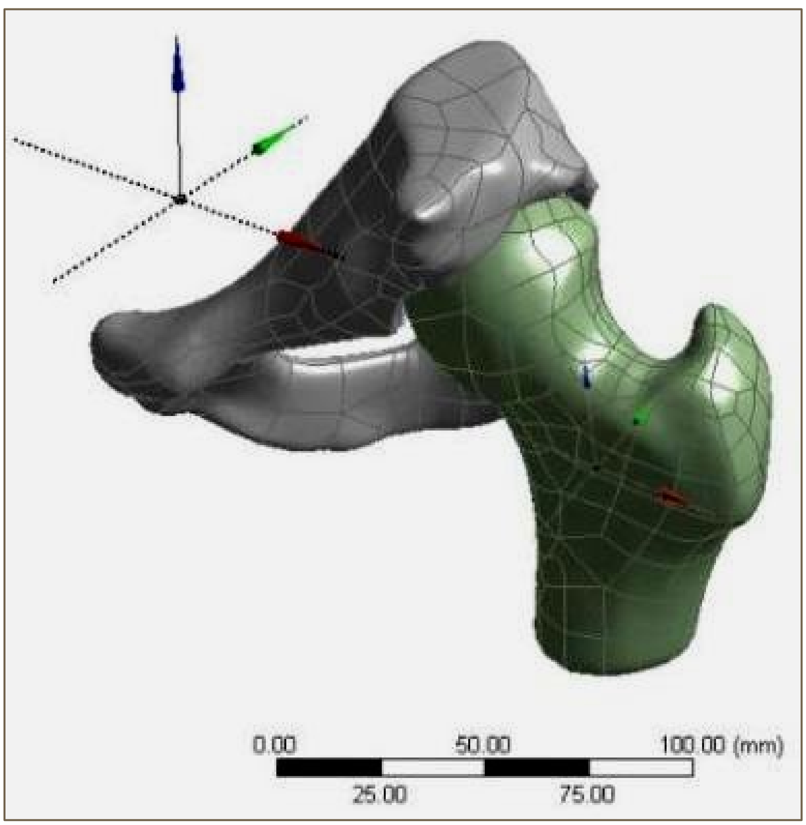

Figure 4.16: The hip joint assembly (comprised of the pelvis, cartilage, femur) imported into DesignModeler. An additional local coordinate system is applied to the femur.

The femur was oriented with respect to the pelvis according to the two positions: (1) at stance and (2) at maximum force endured during the squat position. The centre of joint rotation was approximated about a spherical centre. A sphere was traced around the femoral head to provide a pivotal reference for the femur to rotate about the spherical centre. The patient-specific kinematics data was used to orient the femur with respect to the pelvis (Figure 4.17). The sagittal, frontal, and transverse ROMs, in degrees, were applied to fix the femur for the two quasi-static positions. After the transformations in motions were completed, the traced sphere was removed.

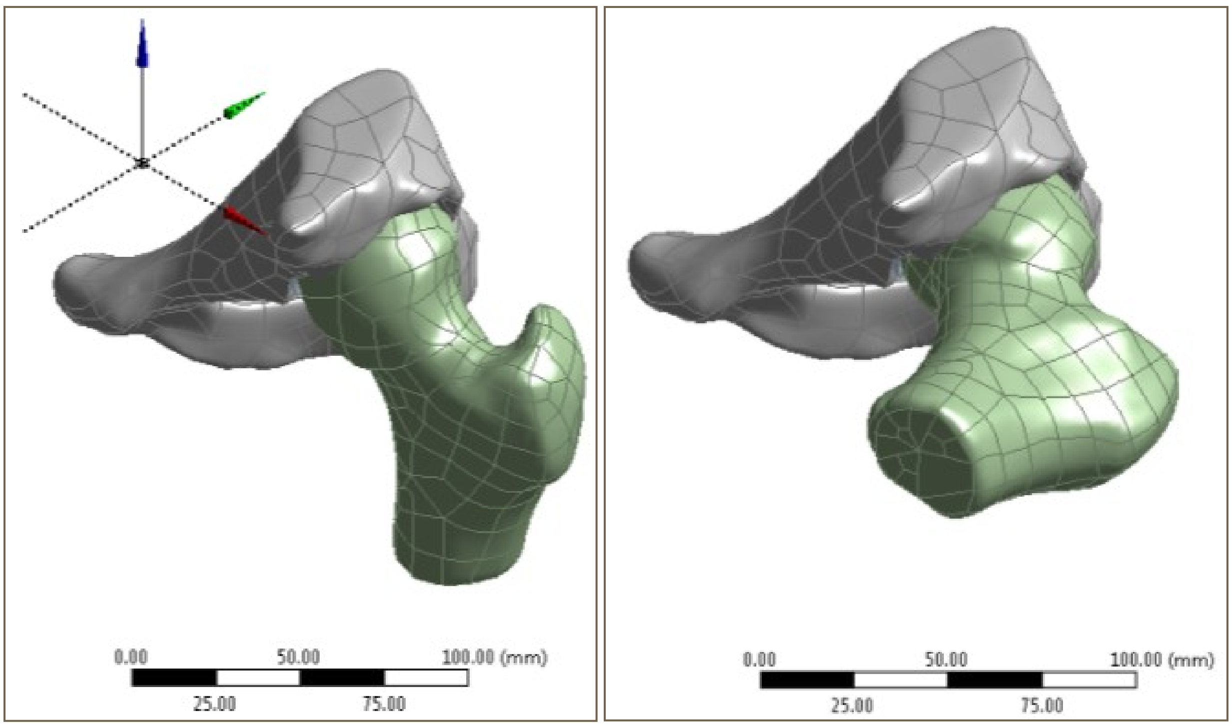

Figure 4.17: The patient-specific kinematics data oriented the femur with respect to the pelvis for the stance (left) and squat (right) positions.

4.3.2 Material properties

The models were then brought into ANSYS Simulation as a full joint assembly. The femur and pelvis structures were modelled as linear elastic orthotropic materials (Couteau, Hobatho, et al., 1998; Couteau, Labey, et al., 1998; Taylor, et al., 2002), as seen in Table 4.6. The acetabular cartilage was modelled as a linear elastic isotropic material (Chegini, et al., 2009), as seen in Table 4.7. Since loading parameters were quasi-static simulations involving non-cyclic loads, time-dependent and viscoelastic behaviours were ignored for the bone and cartilage structures (Ateshian, et al., 2007; Chegini, et al., 2009; Macirowski, et al., 1994).

Table 4.6: Mechanical properties of linear elastic orthotropic bone used for femur and pelvis (Couteau, Labey, et al., 1998)

Elastic Modulus (GPa)	$E_x = 11.6$	$E_y = 12.2$	$E_z = 19.9$
Shear Modulus (GPa)	$G_{12} = 4.0$	$G_{13} = 5.0$	$G_{23} = 5.4$
Poisson Ratio	$v_{12} = 0.42$	$v_{13} = 0.23$	$v_{23} = 0.23$

Table 4.7: Mechanical properties of linear elastic isotropic cartilage used for acetabular cartilage (Chegini, et al., 2009)

Elastic Modulus (MPa)	12
Poisson Ratio	0.45

4.3.3 Contact Pairing

Two contact pairing surfaces were established in each joint assembly: cartilage-to-acetabulum and femur-to-cartilage. Normally, a material that is stiff, concave, with coarse-meshed surfaces should, in principle, be modelled as the target body; whereas a soft material with convex, fine-meshed surfaces should normally be modelled as the contact body (Hutton, 2004). The cartilage layer was bonded to the acetabulum of the pelvis, where the cartilage medial side exposed to the acetabulum represented the contact bodies and the lunate surfaces of the acetabulum was the target bodies (Figure 4.18**:**.A). The femoral head was paired with the cartilage layer, where the femoral head represented the target bodies and the cartilage, exposed laterally, was the contact bodies (Figure 4.18.B). The interface between the femoral head and the cartilage was modelled as frictionless contacts (Unsworth, Dowson, & Wright, 1975).

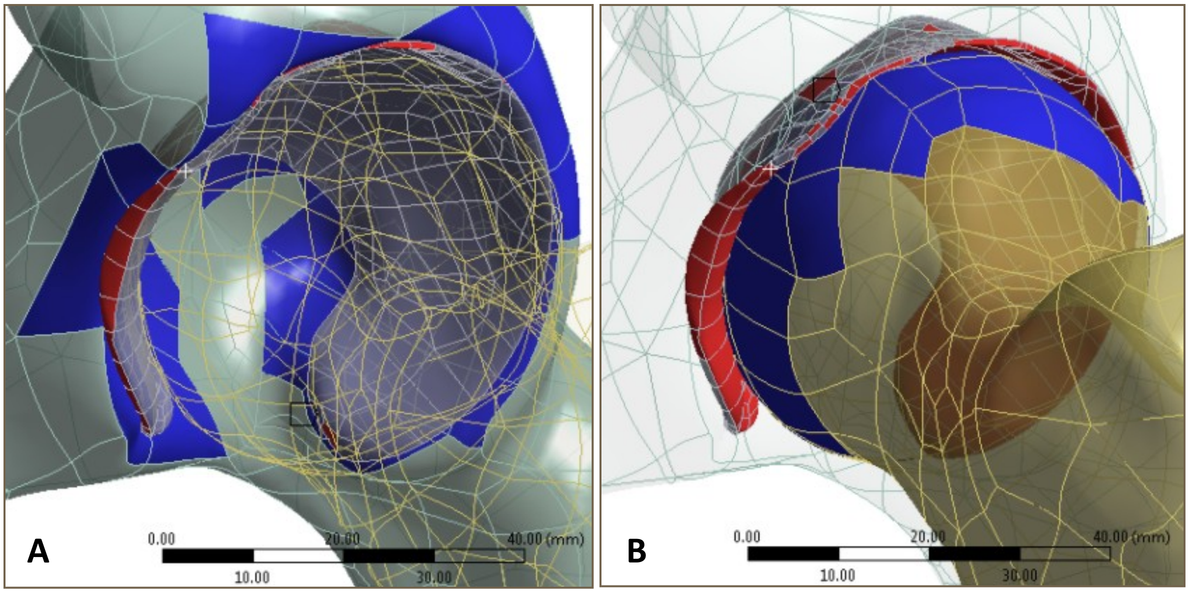

Figure 4.18: Contact pairing of cartilage-to-acetabulum surfaces (A), where the acetabulum was the target body (blue) and the cartilage was the contact body (red). Contact pairing of femur-to-cartilage surfaces (B), where the femoral head was the target body (blue) and the cartilage was the contact body (red).

4.3.4 Finite Elements

The three-component assembly was meshed using SOLID187 element (Figure 4.19), a higher-order, 3-D, tetrahedral, ten-node element (Luo, 2008). The element type is well suited for modelling complex CAD objects and irregular meshes. Generally, tetrahedral elements take a longer convergence time, in comparison with a hex-sweep method. However, the tetrahedral elements are necessary to mesh the intricate curves of the cartilage layers, where a brick node element would require a constant thickness or less complex curves to facilitate the nature of the hex-sweep methods.

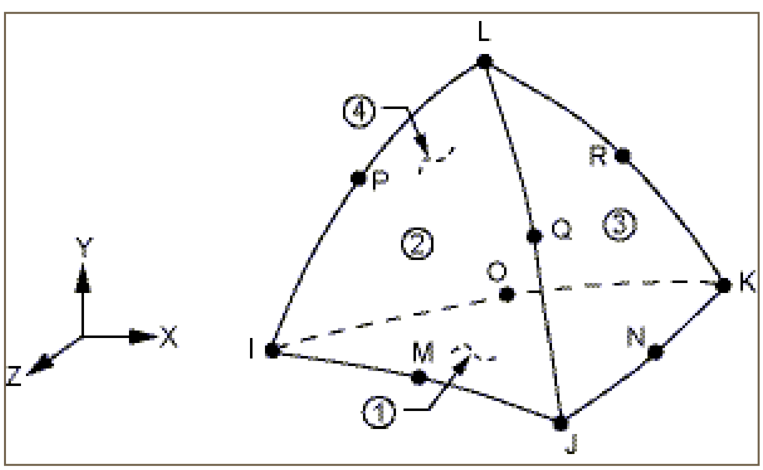

Figure 4.19: The SOLID187 element – 3-D, tetrahedral, ten-node element.

A patch independent scoping method was used along with a global minimum element size to capture the curvatures of the models (Figure 4.20). This eliminated the need to include a convergence study for meshing densities. The global minimum mesh size of 1mm was set for all three components, to limit the level of curvature and proximity refinement. A prescribed element size was set at 4mm, where the mesh was calibrated to subdivide automatically at a tighter radius of curvature. No tolerance limit was set to defeature any of the objects. The target and contact surfaces were meshed as TARGE170 and CONTA174 elements, respectively.

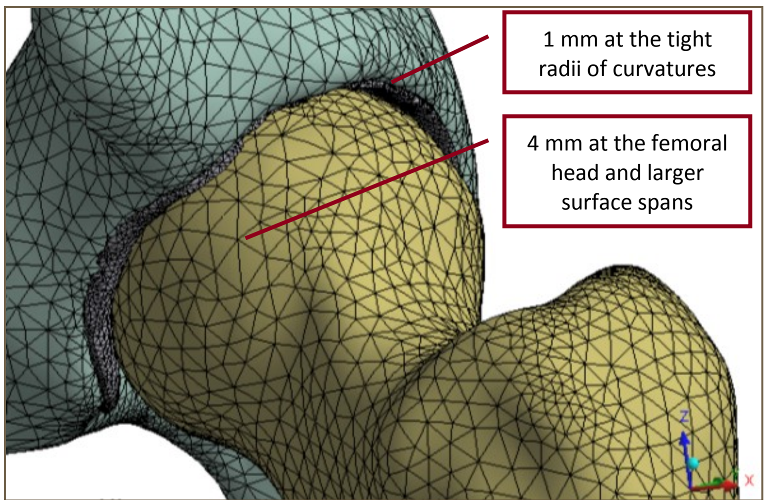

Figure 4.20: View of the different size of the elements. The prescribed size was set at 4mm (situated at large spanned surfaces, as indicated by the femoral head) with an automatic subdivision to a minimum size of 1mm at tighter radii of curvatures (situated at more complex regions of the cartilage and abrupt changes in curvatures).

As a parallel study to consider Anderson et al.'s cortical bone-only model, the implementation of a shell model was considered as an alternative simulation method to account for just the cortical bone structures of the femur and pelvis models (Anderson, et al., 2008; Anderson, et al., 2010). This trial of the shell methods used the same linear elastic, orthotropic material properties for the bone structures with SHELL97 elements (a thin, eight-node structural shell). A constant shell thickness of 1.5 mm was representative of the cortical bone (Chegini, et al., 2009), thus the trabecular bone would be omitted. Using the same boundary conditions as the other subject models and the loading parameters of the pilot subject, it was noticed that the shell model of the femur deflected under small loads. The femoral head collapsed under point loads and the convergence of the solutions was less stable. This contradicts the theories and methods of Anderson et al.'s work, where it was explicitly re-iterated that the trabecular bone can be removed since it has little impact on the outcome of the results (Anderson, et al., 2008; Anderson, et al., 2010). Since the shell structure did not yield promising results for our FAI study, the solid orthotropic method was implemented instead.

4.3.5 Loads and Boundary Conditions

The global coordinate system in ANSYS differed from the coordinate system during the acquisition of the biomechanics data. The hip force magnitude, as discussed in section 4.1.3, established the positive directions for the Cartesian XYZ coordinate system as the posterior, medial, and superior positive directions for the left leg, respectively. However, ANSYS has arranged for the XYZ coordinate system as the positive lateral, posterior, and superior directions, respectively. To correct this discrepancy, the X and Y directions between the two systems have been switched. The hip force vectors in the positive medial direction have been reversed to be considered as a negative vector in the lateral direction. Moreover, the hip force magnitudes were calculated by a function of the individual patient and control subject's BW to determine the hip force in Newtons. Table 4.8 and Table 4.9 summarize the hip force components that were implemented towards the respective patient and control subject FEMs.

Table 4.8: ROM and adjusted force components for ANSYS of left hip for FAI Patient 1 (14_NG_FAI) and FAI Patient 2 (18_LD_FAI) at stance and squat

Subject	Position	Kinematic ROM (^{o})			Hip Force (N)		
		1 (sagittal)	2 (frontal)	3 (transverse)	X (lateral)	Y (posterior)	Z (superior)
FAI 1	Stance	1.1183	1.1539	-4.7178	-11.3166	14.0541	269.3423
	Squat	98.7362	-12.0209	11.8998	109.3420	-270.7266	57.8599
FAI 2	Stance	-1.1698	-0.2043	-4.8579	-9.1298	16.0310	234.1414
	Squat	102.3411	-15.5228	19.4653	164.6379	-304.0037	-128.9102

Table 4.9: ROM and adjusted force components for ANSYS of left hip for Control Subject 1 (26_JD_Control) and Control Subject 2 (27_GM_Control) at stance and squat

Subject	Position	Kinematic ROM (^{o})			Hip Force (N)		
		1 (sagittal)	2 (frontal)	3 (transverse)	X (lateral)	Y (posterior)	Z (superior)
Cont 1	Stance	1.2354	-2.6860	-5.3838	13.2395	33.7711	250.3330
	Squat	119.6773	-13.5990	36.7715	151.3669	-269.9288	-76.5819
Cont 2	Stance	0.2076	-3.8963	-5.2909	12.8292	2.9526	227.6014
	Squat	92.8723	-3.5040	11.7820	56.7526	-302.2967	91.7241

The intersegmental force components were applied through the femoral head of each of the patient's and control subject's hip joint assembly for both stance and squat positions (Figure 4.21). No other muscle vectors or soft tissue approximations were accounted for in the hip joint assembly, thus the joint reactions could be justified as an applied force through the actual hip joint (Anderson, et al., 2008). The boundary conditions were applied to the extremities of the segmented assembly (Figure 4.22). Fixed zero-displacement conditions were fixed at the proximal sectioned plane of the ilium and at the distal sectioned plane of the femur (Anderson, et al., 2010; Bergmann et al., 2001). Both ends were sectioned due to the slicing range of the segmentation process. An additional fixed support was applied to the pubis (Anderson, et al., 2008). The FEMs were then completed and ready to be solved.

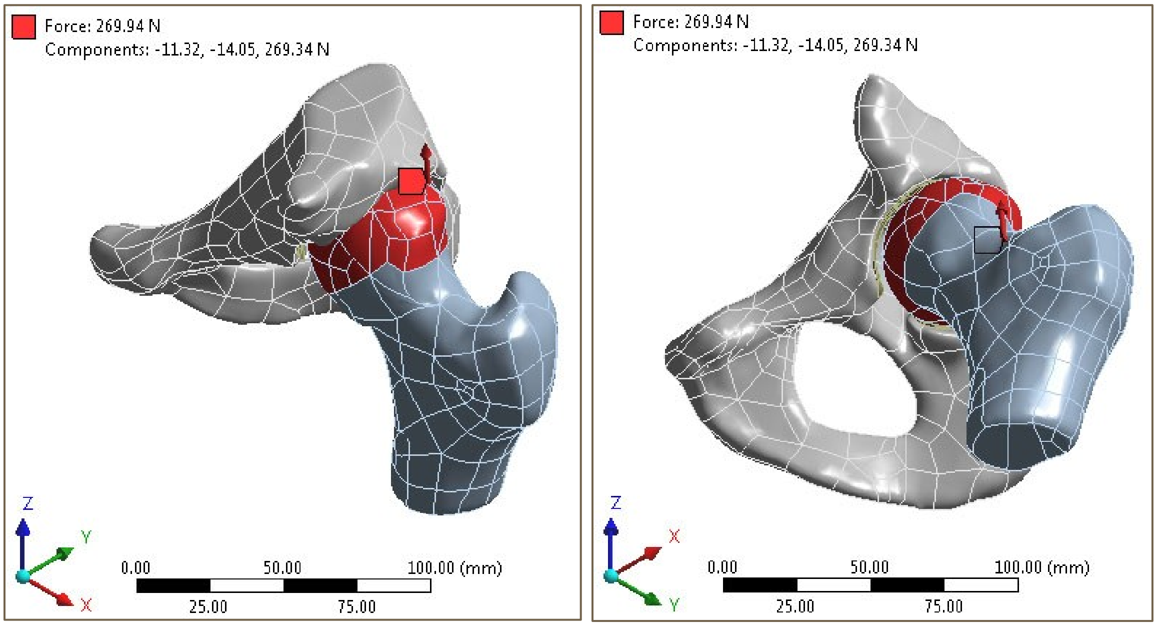

Figure 4.21: Two isometric views of the intersegmental hip forces (red arrow) of FAI Patient 1, where the forces were applied through the femoral head (highlighted by the red surfaces).

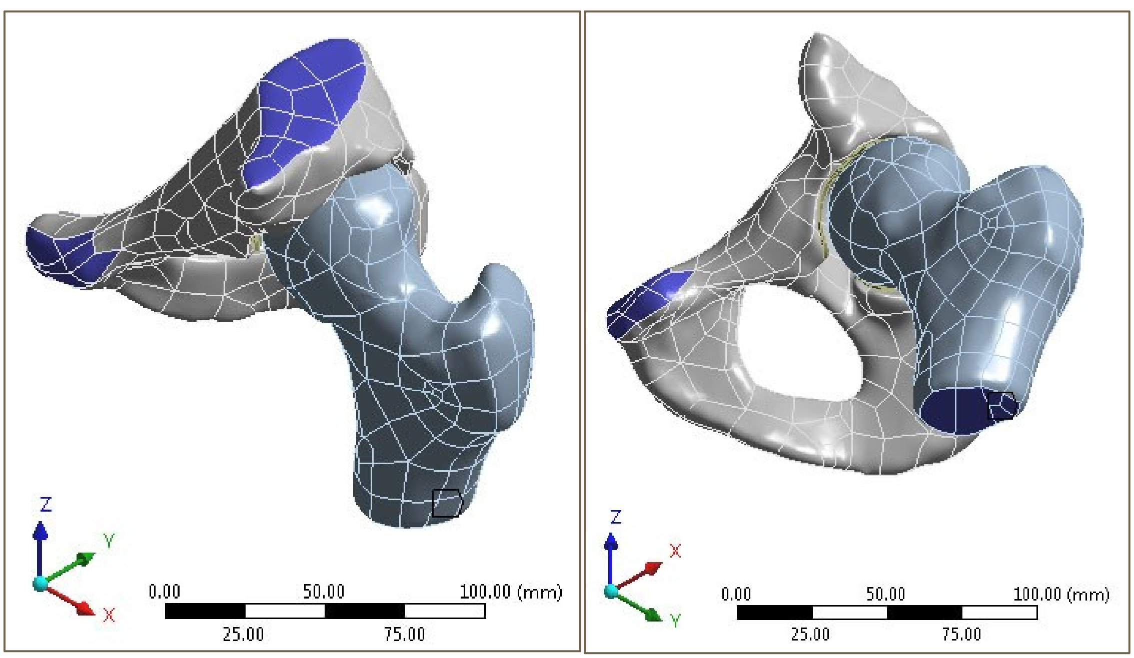

Figure 4.22: Two isometric views of the displacement constraints for FAI Patient 1, where the constraints were fixed at the proximal sectioned plane of the ilium, the distal sectioned plane of the femur, and at the pubis (highlighted in blue).

4.4 Post-Processing

4.4.1 Stress Analysis

ANSYS Simulation contains several post-processing tools for stress and strain analysis. MSS analyses were conducted for all separate components of the assembly: pelvis, cartilage, and femur. It was opted not to use the VM failure criterion as an indication of stress conditions. As discussed in the section 3.1.5, VM stresses accounts for a conservative engineering method, using principal stresses, to determine the state of equilibrium in a ductile material. The focus of the analysis was to determine the adverse stress conditions on the acetabular cartilage and the acetabulum of the pelvis. When the peak MSS was indeterminate or was deemed beyond the regions of focus, an additional MSS analysis was calculated with just the region of focus selected as the boundary for analysis. In other words, if peak stresses were found at distal femur or proximal ilium, the analysis was modified to select only the acetabulum and the femoral head as the regions of focus. Visual outputs of the nodal analysis were recorded for the MSS states of the cartilage and acetabulum.

4.4.2 Strain Energy Density

ANSYS does not contain an automatic solver to directly output solutions for SED; however, it can yield a solution for strain energy (SE) in joules. To calculate SED, a manual method was used to obtain solutions. Unlike the nodal analysis of the stress analysis, peak SE was determined by the elemental analysis. The results, taken from ANSYS Simulation, were then opened in ANSYS Environment for post-processing as a RST file. As the acetabulum was the region of focus, each model was loaded and the elements exposed on the surfaces of the acetabulum were isolated. The cartilage layer and the femur were not considered, since the aim was to determine the changes in SED on the underlying surfaces of the acetabulum. From the “General Post-Processing” command, an element table was defined to provide a list of the SE, volume of the respective element, and location of each element on the X, Y, and Z axes. The data list was exported in Microsoft Excel, where a simple calculation was performed to divide the value of SE by its respective volume of the element, as seen in Equation 4.1.

$$SED = \frac{SE}{Volume_{element}} = \frac{(J)}{(m^3)} = Pa \qquad \textbf{(4.1)}$$

Thus, the units of SE (measure in joules) were divided by the volume of the elements (measured in m^3), resulting in a SED solution in units of Pascal. Having determined the exact location of the elements with the highest SED during the squatting position, the identical elements were taken into consideration for the stance position, as a comparison. Thus, a comparison between the two positions (stance and squat) was established to determine any changes in SED and, consequently, its effects on the rate of subchondral bone remodelling.

5.0 Results

5.1 Alpha and CE Angles

The alpha angles of the femoral head and the CE angles of the acetabulum were measured from CT radiographs in the axial plane and A-P views, respectively. This measurement of the angles, prior to segmentation, provided an indication of the patients' severity and a clinical assessment of the control subjects. After segmentation and resurfacing of the geometries, the alpha and CE angles were recorded again from the geometries to verify the validity of the resurfacing procedure and the accuracy of the FEMs. As seen in Figure 5.1, the alpha and CE angles from the two methods correlate well, where the coefficient of determination (R^2) for the alpha angle was calculated to be 0.99945 and for the CE angle to be 0.99565, validating the resurfacing process. The measured angles and the percent difference of the two methods are summarized in Table 5.1.

For the complete measurement of the alpha and CE angles from 3D-Doctor, refer to Figure 9.23 to Figure 9.26 in Appendix D of section 9.4. For the complete paired two-sample t-test statistical analysis, refer to Table 9.2 and Table 9.3 in Appendix D of section 9.4.

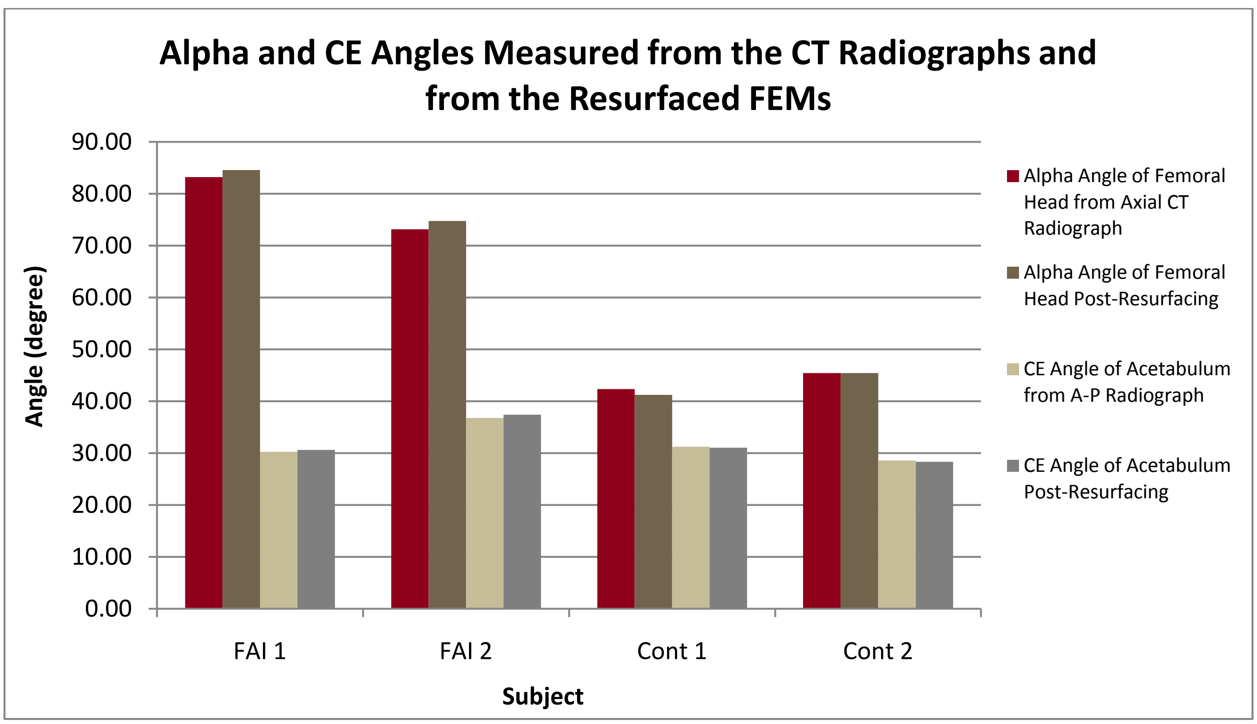

Figure 5.1: Representation of the alpha and CE angles measured from the CT radiographs and from the resurfaced FEMs

Table 5.1: Percent difference between alpha and CE angle measurements taken from CT radiographs and post-resurfacing methods of all FAI patient and control subjects

Subject	Alpha Angle			CE Angle		
	Axial CT Radiograph (°)	Post-Resurfacing (°)	Percent Difference (%)	A-P Radiograph (°)	Post-Resurfacing (°)	Percent Difference (%)
FAI 1	83.22	84.55	*1.59*	30.26	30.58	*1.05*
FAI 2	73.16	74.75	*2.15*	36.79	37.38	*1.59*
Cont 1	42.33	41.24	*2.61*	31.24	31.03	*0.67*
Cont 2	45.41	45.40	*0.02*	28.57	28.34	*0.81*

As seen in Table 5.1, the angles measured post-resurfacing were very similar with the angles measured from CT radiographs prior to segmentation. All percent differences were calculated to be less than 3%. Much of the discrepancy of the alpha angle measurements came from the location of the femoral head-neck offset, accounting for much of the percent differences. The acetabular rim forming the CE angle from the vertical axis was much more apparent from the A-P view, thus the percent differences for the CE angles are relatively lower.

5.2 Maximum-shear Stress

With a minimum nominal size of 1mm for the FEs, all the subject models were able to mesh with no additional refinement steps required. For a complete breakdown of the number of nodes and elements allocated for each component of every subject model, refer to Table 9.4 in Appendix E of section 9.5. The most efficient way to examine the locations of the MSS concentrations is to qualitatively visualize and compare the isolated stress concentration's location and magnitude. The subsequent sub-sections exhibit the MSS distributions on the surfaces of the cartilage and acetabulum from the sagittal view. The stress distributions on the femoral head are not reported, as the focus of the study and the interaction between the articulating surfaces is on the cartilage layer and the underlying acetabulum.

The figures display the distributions of MSS, relative to the peak MSS, where a logarithmic scale is used to assess the magnitudes. An extended list of the high concentrations of MSS magnitudes and locations are included in section 9.5 of Appendix E. The coordinate systems in the sub-sequent figures implement the ANSYS global coordinate system, where X represents the positive lateral direction, Y represents the positive posterior direction, and Z represents the positive superior direction, relative to the left hip.

5.2.1 FAI Patient 1 – Stance

Figure 5.2 shows the orientation of the hip assembly in the standing position, where the femur is oriented in a near-upright position with the Z axis. The cam deformity is very apparent in both the isometric and sagittal plane views. Figure 5.3 indicates the MSS distributions on the surfaces of the cartilage layer and the acetabulum. The peak magnitude on the cartilage layer was 3.70 MPa, at the superior region of the rim, where the femoral head was in most contact with the cartilage during the standing position. Very few isolated concentrations were found on the cartilage. During the standing position, the MSS concentrations were well distributed on the cartilage and acetabulum surfaces. The peak magnitude on the acetabulum was marginally lower at 3.35 MPa, aligned with the direction of loading at the postero-superior region, during the standing position.

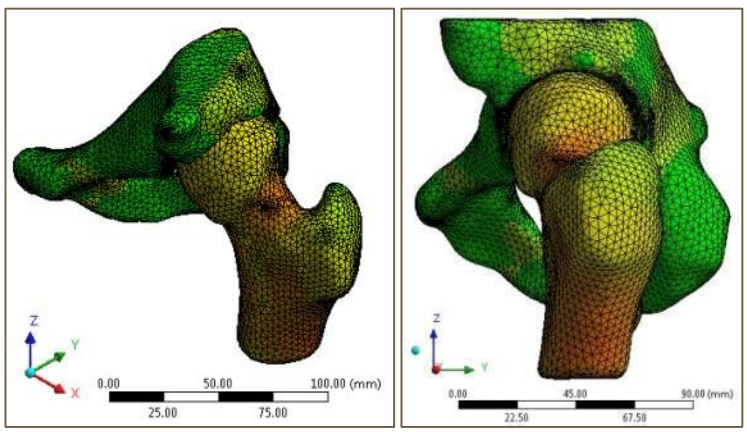

Figure 5.2: Isometric view (left) and sagittal view (right) of FAI Patient 1's hip joint assembly during the standing position.

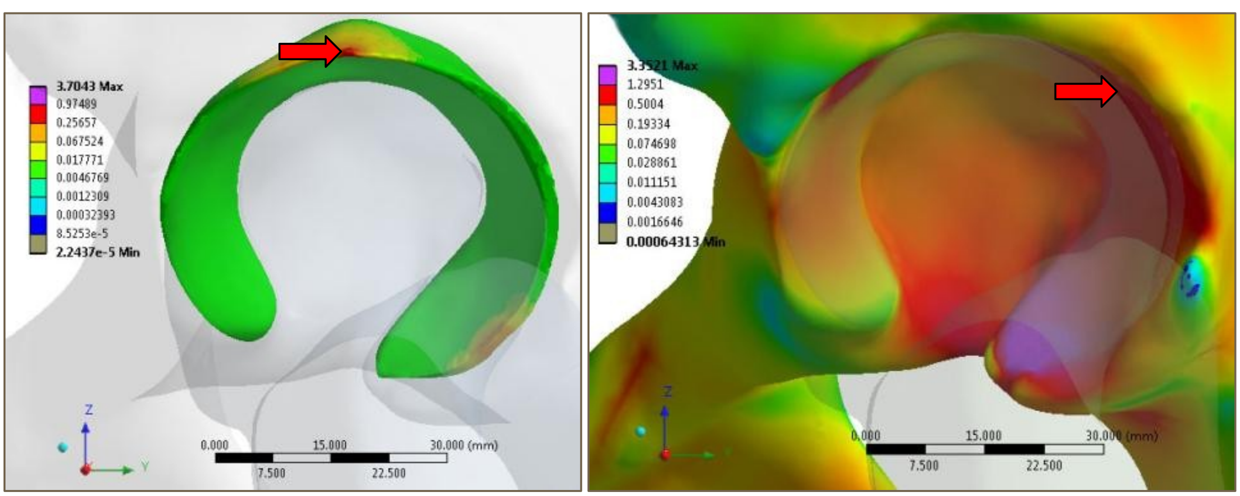

Figure 5.3: MSS distributions on the cartilage layer (left) and the acetabulum (right). Very little difference separates the peak magnitudes situated at the superior cartilage (3.70 MPa) and postero-superior acetabulum (3.35 MPa), where the location of the peak magnitudes are indicated by the red arrow.

5.2.2 FAI Patient 1 – Squat

Figure 5.4 shows the orientation of the hip assembly in the squatting position. The “bump” of the cam deformity prevents extensive physical contact between the femoral head and the acetabular rim. The peak magnitude on the cartilage layer was found to be 3.83 MPa (Figure 5.5), at the antero-superior region, which was marginally higher than the peak magnitude experienced during the standing position. The peak magnitude on the underlying acetabulum was found to be substantially higher at 13.43 MPa, at the antero-superior regions. Several more isolated stress concentrations were evident during the squat position, in comparison with standing position. The location of the stress concentration on the acetabulum was slightly more superior. A secondary concentration of 9.58 MPa was found at the postero-inferior regions of the lunate, which suggested a contre-coup of the intersegmental hip forces.

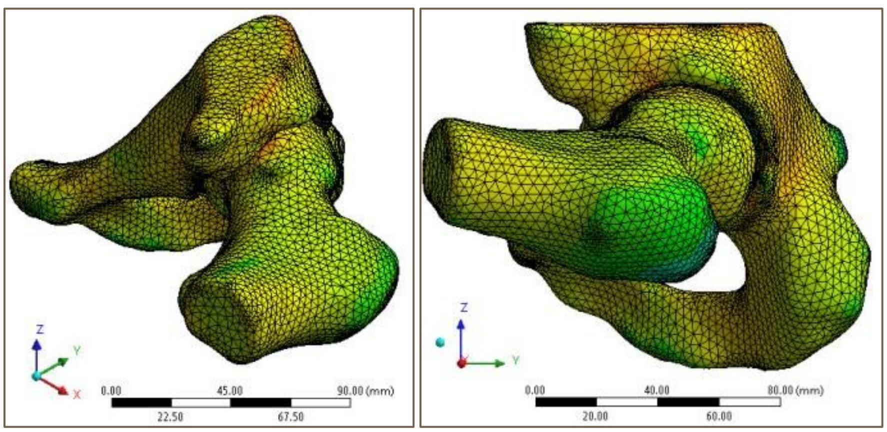

Figure 5.4: Isometric view (left) and sagittal view (right) of FAI Patient 1’s hip joint assembly during the squatting position.

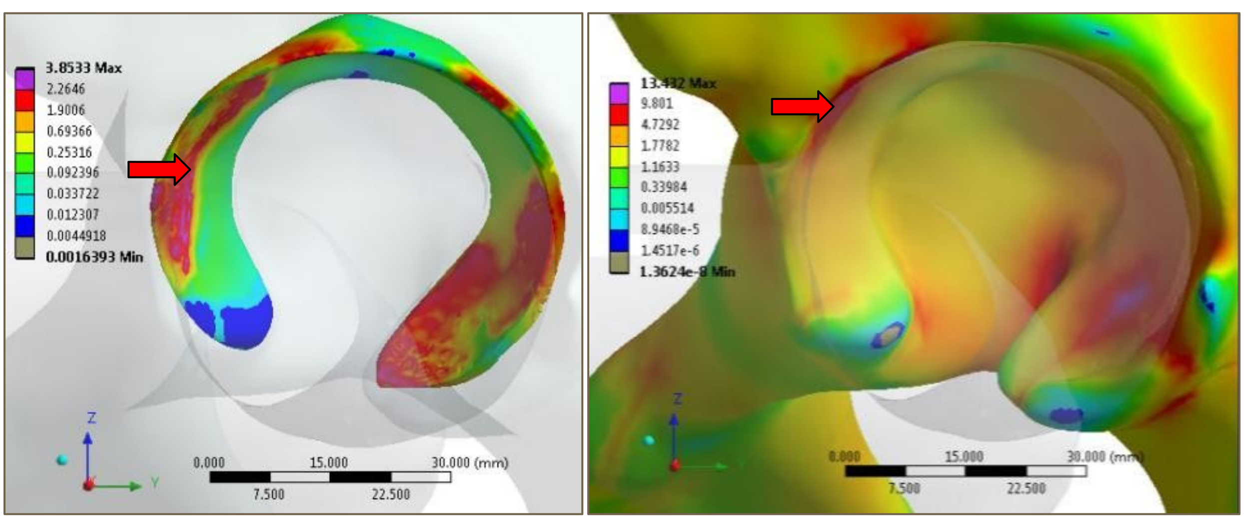

Figure 5.5: MSS distributions of the cartilage (left) and the acetabulum (right). The peak magnitude, situated at the antero-superior cartilage (3.85 MPa), was much less than the peak found at the antero-superior acetabulum (13.43 MPa). The peak magnitudes are indicated by the red arrows

5.2.3 FAI Patient 2 – Stance

Figure 5.6 shows the orientation of the hip assembly in the standing position for FAI Patient 2. This patient had an alpha angle slightly less than the FAI Patient 1, but had an oversized alpha angle in the radial plane. The peak magnitude on the cartilage layer was found to be 4.05 MPa (Figure 5.7) at the superior region. The peak magnitude on the underlying acetabulum was slightly lower at 3.56 MPa, at the superior region as well. Both stress locations were slightly posterior of the superior region, which again suggested an alignment of the applied intersegmental hip loads.

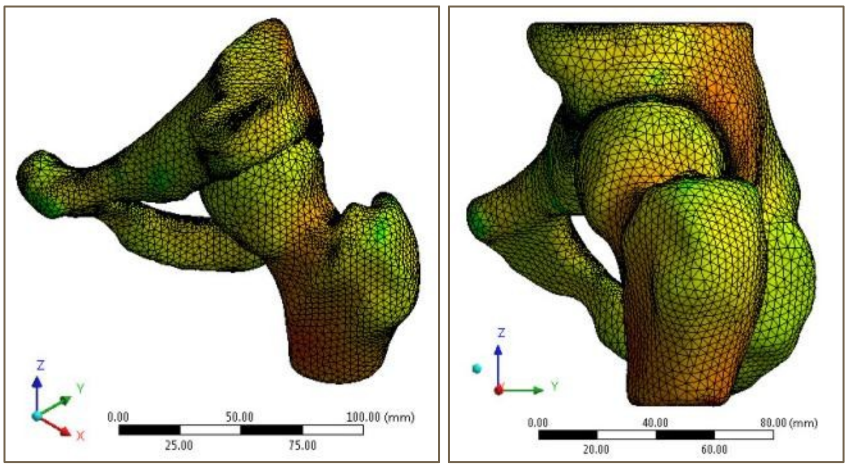

Figure 5.6: Isometric view (left) and sagittal view (right) of FAI Patient 2's hip joint assembly during the standing position.

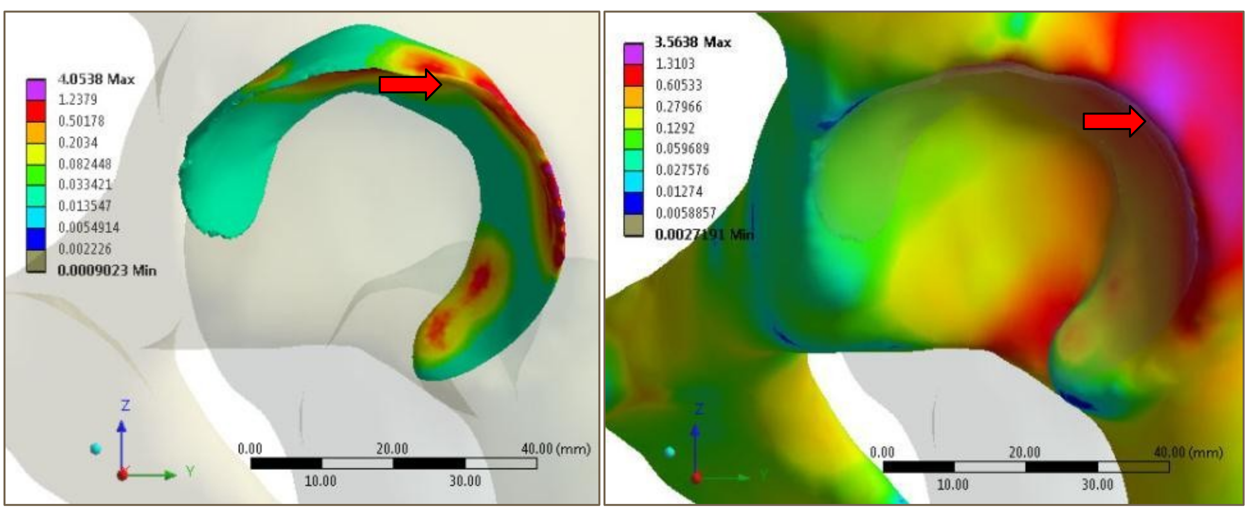

Figure 5.7: MSS distributions of the cartilage layer (left) and the acetabulum (right). The peak magnitudes situated at the superior cartilage (4.05 MPa) was slightly higher than that found at the superior acetabulum (3.56 MPa). The peak magnitudes are indicated by the red arrows.

5.2.4 FAI Patient 2 – Squat

Figure 5.8 shows the orientation of the hip assembly in the squatting position. Though FAI Patient 2 had a smaller alpha angle than Patient 1 in the axial plane, FAI Patient 2 had an apparent deformity in the radial plane. The peak magnitude on the cartilage layer was found to be 3.34 MPa (Figure 5.9), at the antero-superior region, which was slightly less than the peak magnitude experienced during the standing position. The peak magnitude on the acetabulum was found to be 16.86 MPa, at the antero-superior region of the lunate. The MSS was considerably higher at the acetabulum, suggesting that the cartilage transfers much of the load to the stiffer, underlying bone. This peak magnitude was found to be slightly higher than the value for FAI Patient 1 at the squat position, suggesting that the severity of the cam deformity may play a role with the stress conditions of the hip.

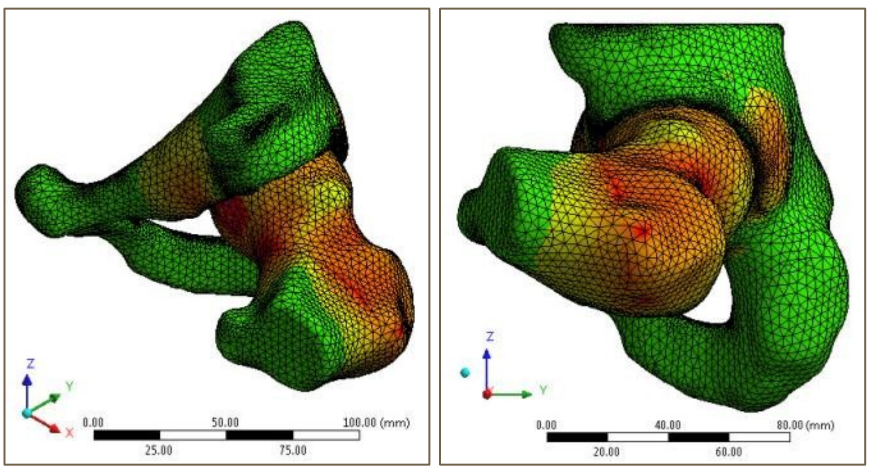

Figure 5.8: Isometric view (left) and sagittal view (right) of FAI Patient 2's hip joint assembly during the squatting position.

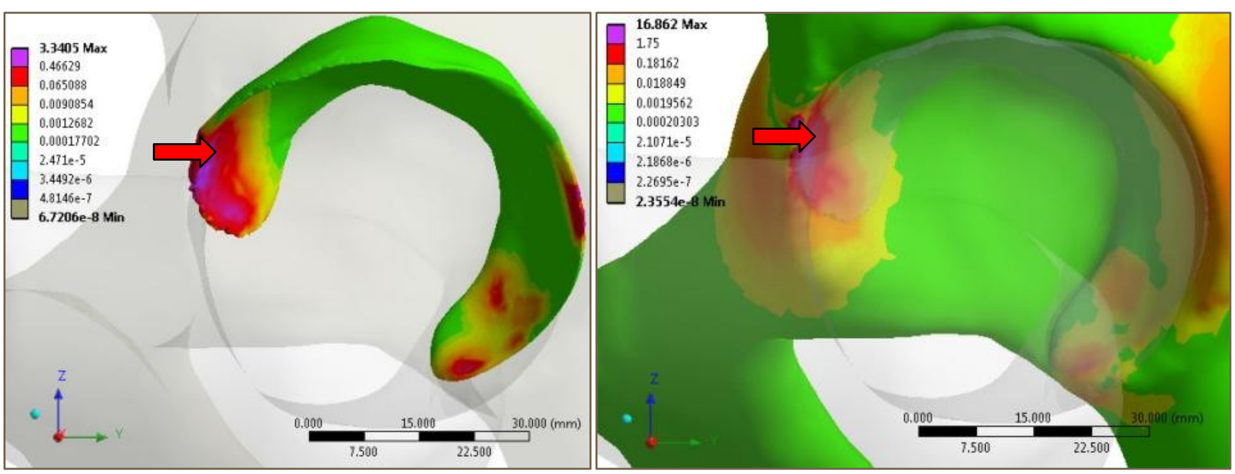

Figure 5.9: MSS distributions of the cartilage layer (left) and the acetabulum (right). The peak magnitude situated at the superior cartilage (3.34 MPa) was much lower than that found at the underlying antero-superior acetabulum (16.86 MPa). The peak magnitudes are indicated by the red arrows.

5.2.5 Control Subject 1 – Stance

Figure 5.10 shows the orientation of the hip assembly in the standing position, where the femur is oriented in a near-upright position with the Z axis. Since hip model has been assessed as a control subject model, no femoral head deformity is evident. Figure 5.11 indicates the MSS distributions on the surfaces of the cartilage layer and the acetabulum. The peak magnitude, at the superior region of the cartilage, was found to be 3.45 MPa. Very few isolated concentrations were found on the cartilage as well; however, all under 1 MPa. The MSS concentrations were well-distributed on the acetabulum. The peak magnitude on the acetabulum was found to be similar at 3.49 MPa, aligned with the direction of loading at the superior region.

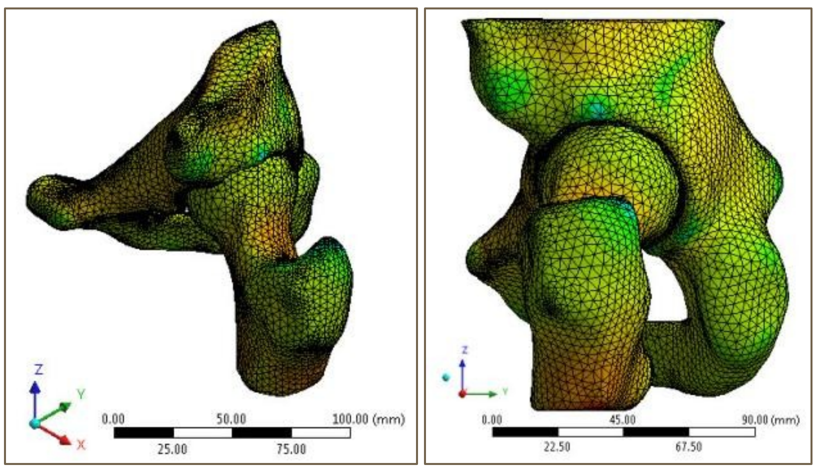

Figure 5.10: Isometric view (left) and sagittal view (right) of Control Subject 1's hip joint assembly during the standing position.

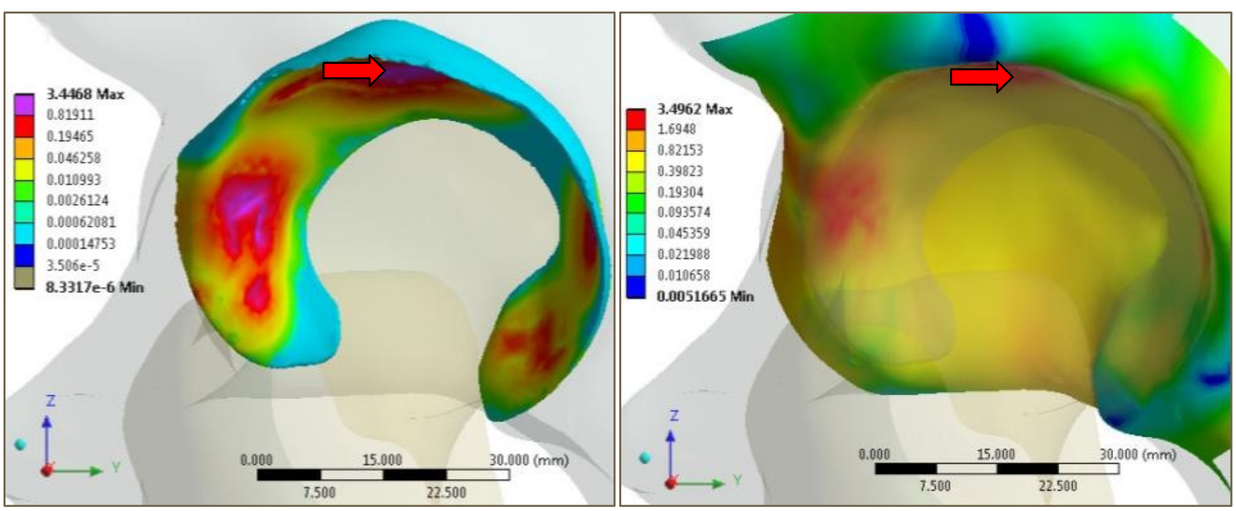

Figure 5.11: MSS distributions of the cartilage layer (left) and the acetabulum (right). The peak magnitude situated at the superior cartilage (3.45 MPa) was similar to that at the underlying antero-superior acetabulum (3.49 MPa). The peak magnitudes are indicated by the red arrows.

5.2.6 Control Subject 1 – Squat

Figure 5.12 shows the orientation of the hip assembly in the squatting position. The angle of sagittal flexion was considered high for a squat depth (119^{o}). The peak magnitude on the cartilage layer was 4.03 MPa (Figure 5.13), at the antero-superior region, which was slightly higher than that experienced during the standing position. The peak magnitude on the underlying acetabulum was marginally similar at 4.54 MPa, at the antero-superior region. There were no other apparent isolated stress concentrations. The MSS concentrations were well distributed on the cartilage layer and on the lunate surface. Thus, for both the stance and squat positions, very little changes in MSS were noticed between peak magnitudes found on the cartilage layer and the acetabulum.

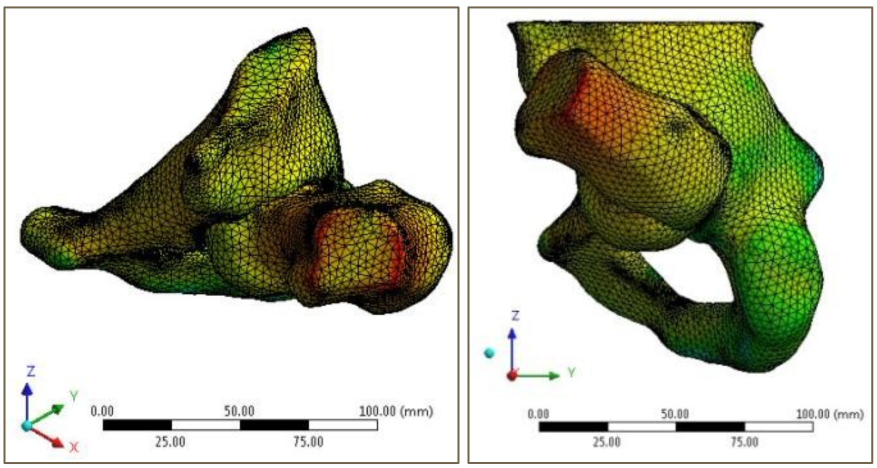

Figure 5.12: Isometric view (left) and sagittal view (right) of Control Subject 1's hip joint assembly during the squatting position.

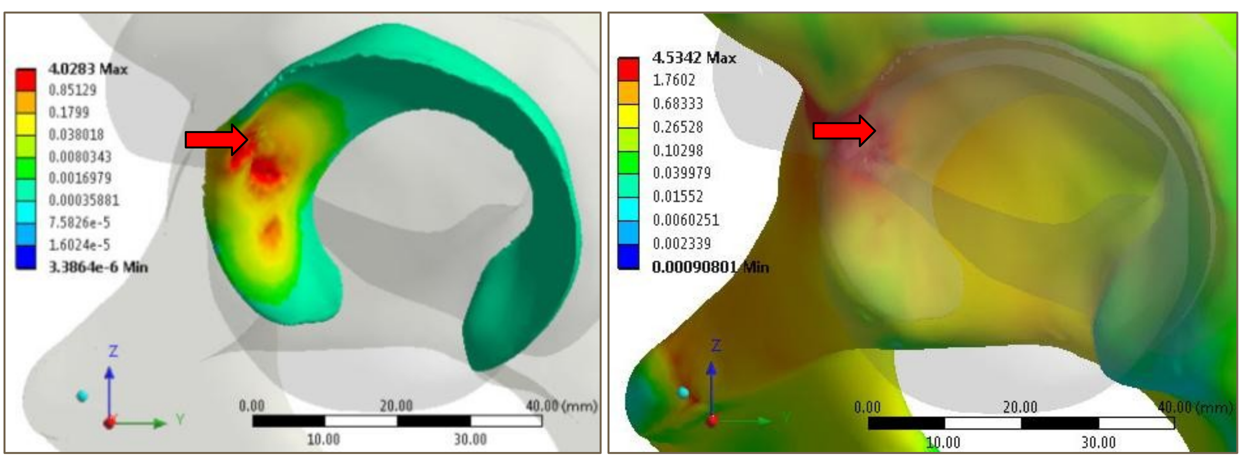

Figure 5.13: MSS distributions of the cartilage layer (left) and the acetabulum (right). The peak magnitude situated at the superior cartilage (4.03 MPa) was similar to that at the underlying antero-superior acetabulum (4.54 MPa). The peak magnitudes are indicated by the red arrows.

5.2.7 Control Subject 2 – Stance

Figure 5.14 shows the orientation of the hip assembly in the standing position for Control Subject 2. The peak magnitude on the cartilage layer was 2.02 MPa (Figure 5.15) at the superior region. There were other apparent concentrations of MSS dissipated around the cartilage, however, were all under 0.6 MPa. The peak magnitude on the underlying acetabulum was slightly higher at 3.19 MPa, at the superior region as well. The MSS concentrations were well distributed on the acetabulum's surface. Both stress locations were slightly posterior of the superior region, suggesting an alignment with the intersegmental hip loads.

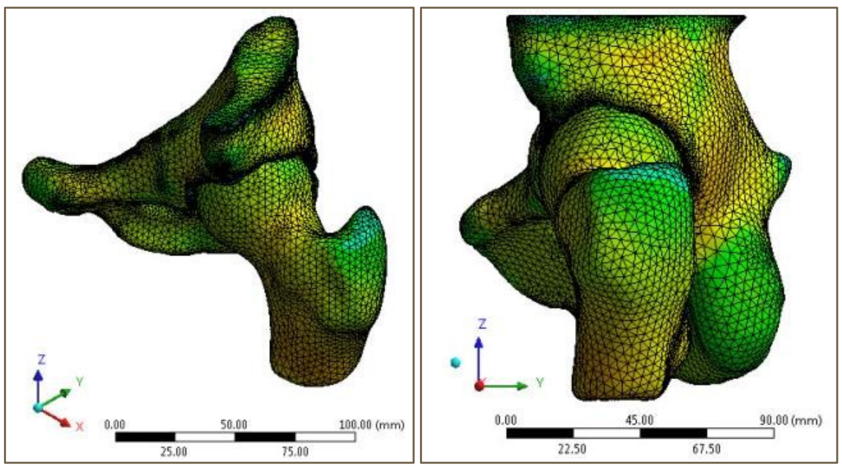

Figure 5.14: Isometric view (left) and sagittal view (right) of Control Subject 2's hip joint assembly during the standing position.

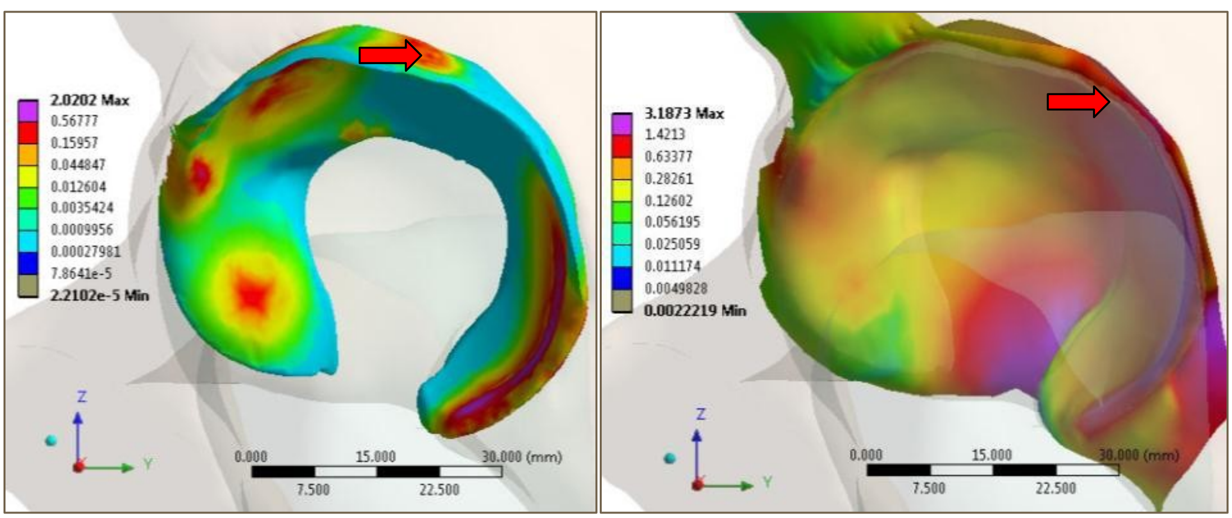

Figure 5.15: MSS distributions of the cartilage layer (left) and the acetabulum (right). The peak magnitudes situated at the superior cartilage (2.02 MPa) was slightly lower than that found at the superior acetabulum (3.19 MPa). The peak magnitudes are indicated by the red arrows.

5.2.8 Control Subject 2 – Squat

Figure 5.16 shows the orientation of the hip assembly in the squat position. The peak magnitude on the cartilage layer was found to be 3.12 MPa (Figure 5.17), at the antero-superior region, which was slightly less than the peak magnitude experienced on the acetabulum, which was found to be 4.37 MPa, situated at the antero-superior region of the rim. The MSS concentrations were well distributed on the cartilage and underlying acetabular surface. A MSS concentration of 3.78 MPa was found exterior to the acetabulum, on the posterior rim. This peak magnitude on the acetabulum's surface was similar with that of Control Subject 1's (4.54 MPa). The MSS on the acetabulum for Control Subject 2 was much lower than that for FAI Patient 2 (16.86 MPa).

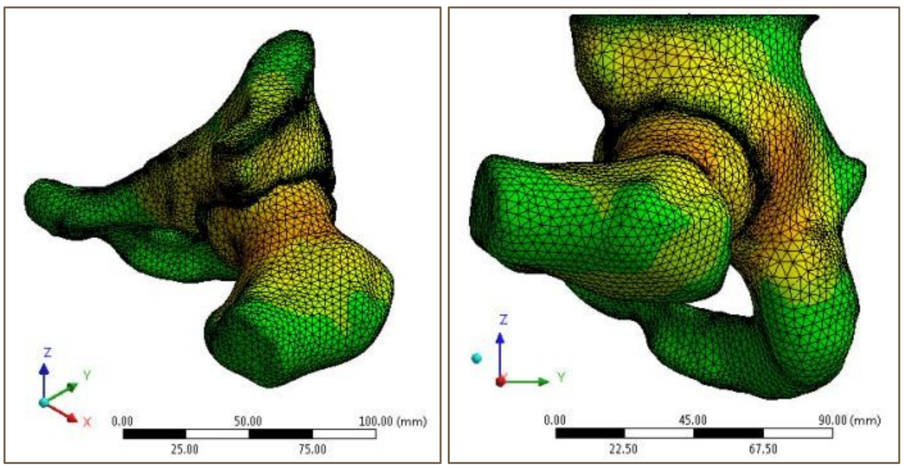

Figure 5.16: Isometric view (left) and sagittal view (right) of Control Subject 2's hip joint assembly during the squatting position.

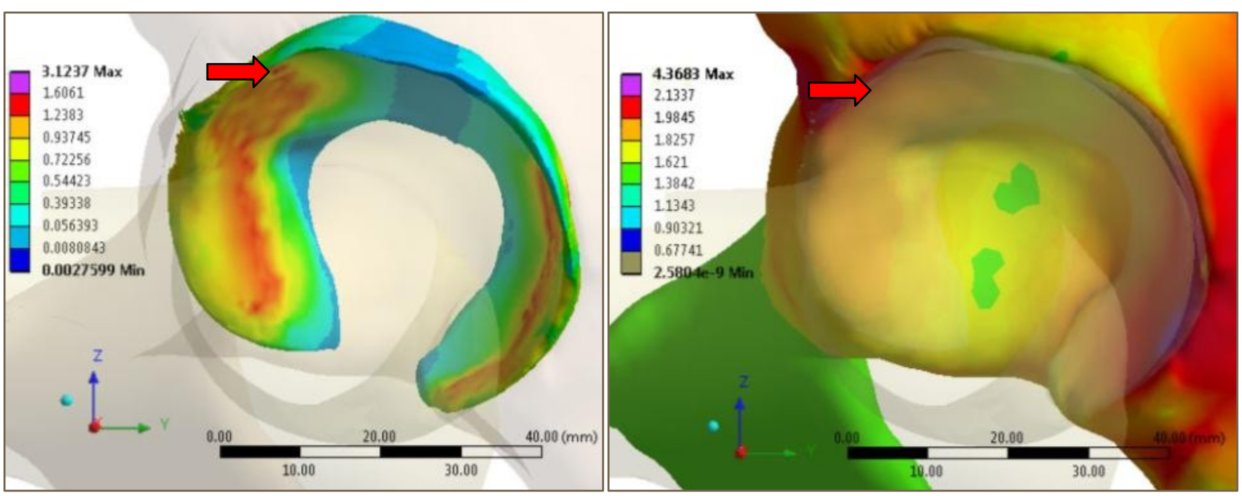

Figure 5.17: MSS distributions of the cartilage layer (left) and the acetabulum (right). The peak magnitude situated at the antero-superior cartilage (3.12 MPa) was lower than that found at the underlying antero-superior acetabulum (4.54 MPa). The peak magnitudes are indicated by the red arrows.

Table 5.2 summarizes the highest MSS values found on the surfaces of the cartilage and acetabulum for each hip assembly model. The locations of the highest MSS during the standing and squatting positions were at the superior region of the cartilage and acetabulum and at the antero-superior region of the cartilage and acetabulum, respectively. At stance, the MSS values were similar between the cartilage and acetabulum for both comparison groups. As the FAI patients and control subjects perform the squat motion, very little changes are noticed on the cartilage layer, except for the location of the peak stimulus values displacing from the superior to the antero-superior regions. However, peak the values increased substantially for the FAI patients on the acetabulum, where the cam deformity was in most contact with the labral regions. The peak MSS values on the acetabulum increased slightly for the control subjects.

Table 5.2: Summary of peak MSS values on the cartilage and acetabulum

Subject	Alpha and CE Angles (^{o})	Stance Position		Squat Position	
		MSS Cartilage (MPa)	MSS Acetabulum (MPa)	MSS Cartilage (MPa)	MSS Acetabulum (MPa)
FAI 1	84.55; 30.58	3.70	3.35	3.85	13.43
FAI 2	74.75, 83.34 (radial); 37.38	4.05	3.56	3.34	16.86
Con 1	41.24; 31.03	3.45	3.49	4.03	4.54
Con 2	45.40; 28.34	2.02	3.19	3.12	4.37

5.3 Strain Energy Density

The following sections will report the distribution of the SE on the acetabulum for each subject's model, indicating the peak SE value and comparing the distributions between the stance and squat positions. Taking the location of the peak SED value into consideration during the squatting position, the identical elements will be taken into consideration for the standing position to compare the changes in SED between the stance and squat positions.

5.3.1 FAI Patients

During the squat position for FAI Patient 1, the highest SED of 1.10 kPa was found on the surface of the acetabulum at the antero-superior region of the acetabulum (Figure 5.18). Taking the same region and element for the hip assembly during the standing position, the SED of the element was determined to be slightly lower at 1.08 kPa. For FAI Patient 2 at squat, the highest SED was 0.936 kPa at the antero-superior acetabulum (Figure 5.19). In comparison, the same element computed at stance, the SED was determined to be 0.929 kPa.

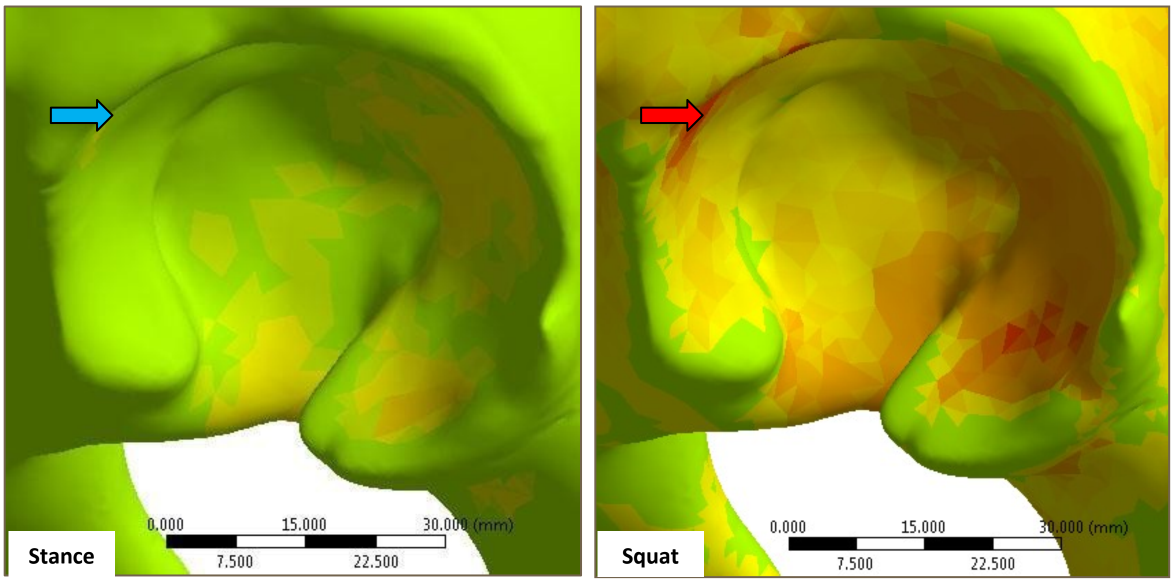

Figure 5.18: SE distribution on FAI Patient 1's acetabulum during the standing (left) and squatting (right) position.

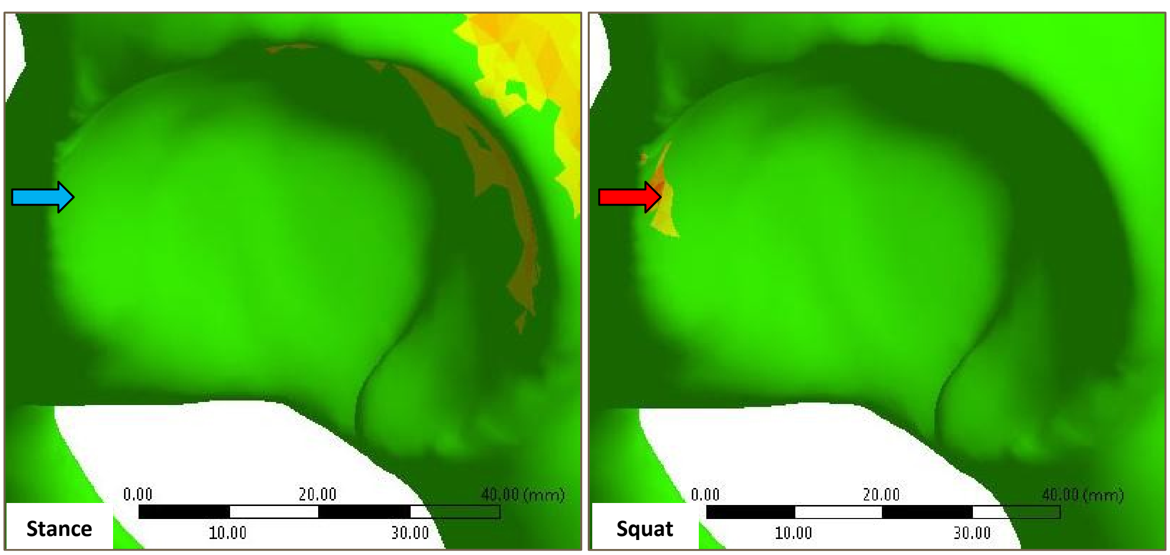

Figure 5.19: SE distribution on FAI Patient 2's acetabulum during the standing (left) and squatting (right) position.

5.3.2 Control Subjects

The highest SED for Control Subject 1 at squat was determined to be 1.20 kPa at the antero-superior acetabulum (Figure 5.20). For same region during the standing position for Control Subject 1, the SED was slightly higher at 1.36 kPa. For Control Subject 2 at squat, the peak SED was determined to be 1.01 kPa, also at the antero-superior acetabulum (Figure 5.21). The SED at the same region for Control Subject 2 during the standing position was determined to be 1.00 kPa.

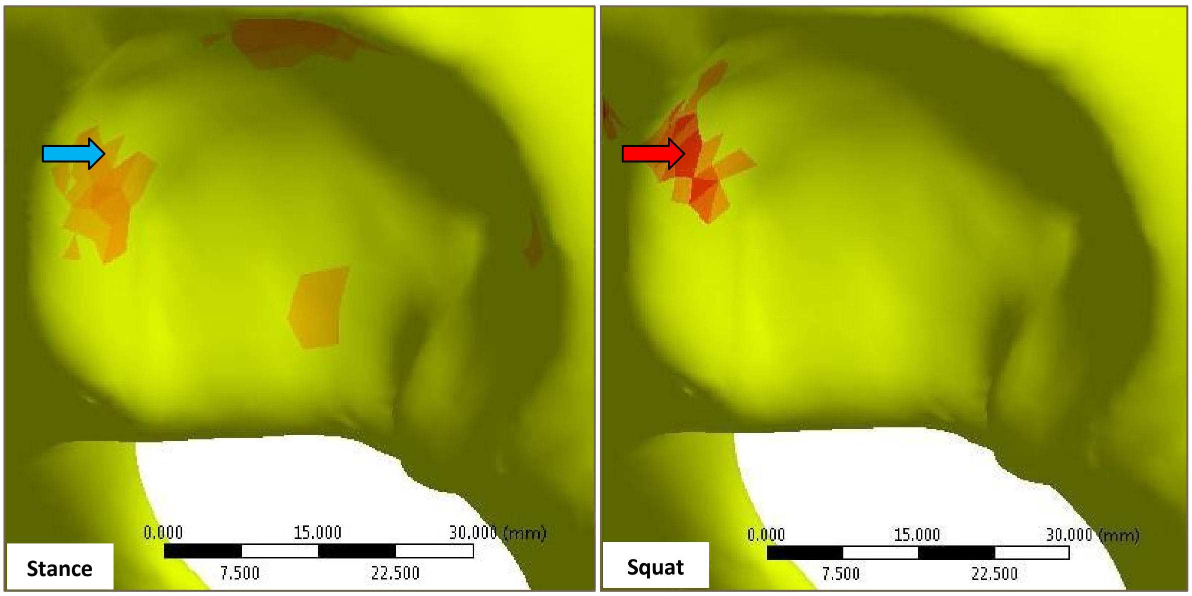

Figure 5.20: SE distribution on Control Subject 1's acetabulum during the standing (left) and squatting (right) position.

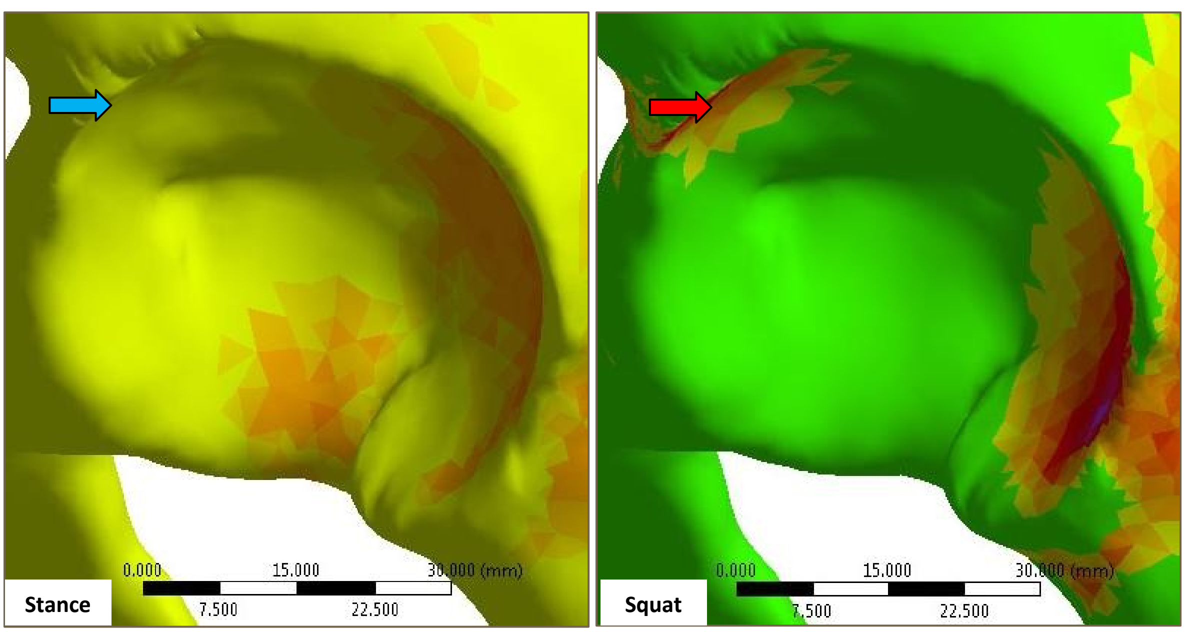

Figure 5.21: SE distribution on Control Subject 2's acetabulum during the standing (left) and squatting (right) position.

Table 5.3 summarizes the highest SED values on the surface of the acetabulum for all patient and control subject models during the standing and squatting positions. During the standing position for both FAI patients, SED was evenly distributed along the superior acetabulum; whereas, during the squatting position for the FAI patients, the SED values were increased and were displaced anteriorly. For the control subjects, the SED concentrations were evenly distributed along the superior acetabulum during the standing position and then were displaced anteriorly during the squatting position. However, unlike the FAI patient models, there were little to no increases in SED for the control subjects when proceeding from stance to squat. For the complete calculations of the peak SED values from the SE values and volumes, refer to Appendix F of section 9.6.

Table 5.3: Summary of peak SED values on the acetabulum

Subject	Alpha and CE Angles (^{o})	Stance Position	Squat Position
		Max SED Acetabulum (kPa)	Max SED Acetabulum (kPa)
FAI 1	84.55; 30.58	1.08	1.10
FAI 2	74.75, 83.34 (radial); 37.38	0.929	0.936
Con 1	41.24; 31.03	1.36	1.20
Con 2	45.40; 28.34	1.00	1.01

6.0 Discussion

6.1 Peak Mechanical Stimuli

During the standing position, both patient models and both control subject models demonstrated similar MSS magnitudes. Marginal differences in MSS values were noticed between the acetabulum and the cartilage layer. This was justified by the evenly distributed surface area of the superior femoral head with the articulating concavity of the cartilage and underlying acetabulum. During the standing position, the cam FAI patients were not at an extreme ROM, thus the deformity of the femoral head was not in contact with the acetabulum to create the interference fit within the hip joint. At stance, the two FAI patients demonstrated similar peak MSS values on the cartilage (3.875 $\pm$ 0.175 MPa) and on the acetabulum (3.455 $\pm$ 0.105 MPa); where the two control subjects demonstrated similar peak MSS values as well on the cartilage (2.735 $\pm$ 0.715 MPa) and on the acetabulum (3.340 $\pm$ 0.15 MPa). With an average deviation of less than 1 MPa, each comparison groups had subjects with similar peak MSS values. Comparing FAI Patient 1 with Control Subject 1 at stance, the MSS values were still quite similar on the cartilage (3.58 $\pm$ 0.125 MPa) and on the acetabulum (3.42 $\pm$ 0.07 MPa); where FAI Patient 2 and Control Subject 2 demonstrated slightly similar peaks on the cartilage (3.035 $\pm$ 1.015 MPa) and very similar peaks on the acetabulum (3.375 $\pm$ 0.185 MPa). It was noticed that Control Subject 2 had slightly lower peaks in comparison with the other subjects. There could have been a misaligned load or an under constrained fixture. The differences between each subject and both comparison groups are due to the patient-specific inputs. Since patient-specific CT and biomechanics data were used to assemble the models for FEA, the outputs were resulted as patient-specific as well.

The deformity of the femoral head could not have been exposed with a low ROM (Chegini, et al., 2009; Lamontagne, et al., 2009), such as one experienced at a standing position. As expected, MSS magnitudes were much higher for the FAI patients during the squatting position. Unlike the evaluations from previous studies (Anderson, et al., 2008; Anderson, et al., 2010; Chegini, et al., 2009; Russell, et al., 2006), the peak MSS values were not found on the cartilage layer, but instead were found on the underlying acetabulum. At squat, the MSS magnitudes on the cartilage layer for both patients were similar (3.595 $\pm$ 0.255 MPa) as were for the control subjects (3.575 $\pm$ 0.455 MPa). Comparing FAI Patient 1 with Control Subject 1 at squat, the MSS values on the cartilage layer were very similar (3.94 $\pm$ 0.09 MPa), as was the comparison between FAI Patient 2 and Control Subject 2 where similarities were noticed as well (3.23 $\pm$ 0.11 MPa). Therefore, the MSS values on the cartilage layer at stance and at squat were all very similar in magnitude. Even the MSS values on the acetabulum for the control subjects at squat were somewhat similar to the magnitudes found on the cartilage layer. The change in MSS magnitude was noticed on the acetabulum of the FAI patients, when proceeding from the standing position (3.455 $\pm$ 0.105 MPa) to the squatting position (15.145 $\pm$ 1.715 MPa), which was a much higher change than the control subjects' MSS magnitude from stance (3.340 $\pm$ 0.15 MPa) to squat (4.445 $\pm$ 0.085 MPa). Overall, the highest MSS values were noticed on the acetabulum during the squatting position, when the hip joint was at its most impinged state. These magnitudes, for both patient and control subjects, were higher than the MSS values found on the cartilage layer during the squat position.

The squat motion oriented the deformity into the acetabulum, increasing contact with the peripheral labral regions. The higher MSS values on the acetabulum could have been due to the lower elastic modulus of the cartilage layer. Since the cartilage was less stiff, it transferred the load onto the acetabulum and amplified the stimuli reaching the subchondral bone. The regions of highest cartilage deformation were consequently at the same regions of the highest MSS values. Based on our results, it is speculated that the amplification of high MSS in cam hips may increase the rate of remodelling in the subchondral bone, thus stiffening the bone plate and accelerating the onset of OA (Day, et al., 2004; Radin & Rose, 1986; Wang, et al., 2007; Wei, et al., 2005).

Of the two patients, FAI Patient 1 had the higher alpha angle in the axial plane, though FAI Patient 2 had a higher peak MSS value. FAI Patient 2 had a substantially much higher alpha angle in the radial plane, in addition to the high alpha angle in the axial plane. Furthermore, FAI Patient 2 had a higher CE angle of the acetabulum (37.38^{o}) in comparison with FAI Patient 1 (30.58^{o}), thus a greater over-coverage of the femoral head. A combination of a high alpha angle in both planes and a greater over-coverage could have justified the reason for the higher MSS value noticed in FAI Patient 2's simulation (16.86 MPa), in comparison with FAI Patient 1's peak MSS value (13.43 MPa). The peak stress values, determined in this research, correlate well with previous findings on cam FAI by Chegini and associates (Chegini, et al., 2009). The peak MSS value on the control subject's cartilage and acetabulum were slightly higher, but still within respectable range of Chegini et al.'s VM stresses for a normal subject ($40^{o} \leq \alpha \leq 50^{o}$, $20^{o} \leq$ CE $\leq 30^{o}$), as seen in Figure 6.1 and Figure 6.2. Since the VM stress analysis is considered to be a conservative failure criterion (Durr, et al., 2004; Jonkers, et al., 2008; Zienkiewicz, et al., 2005), the peak VM stresses might have been an underestimation, thus slightly lower in comparison with results derived from Tresca's MSS analysis.

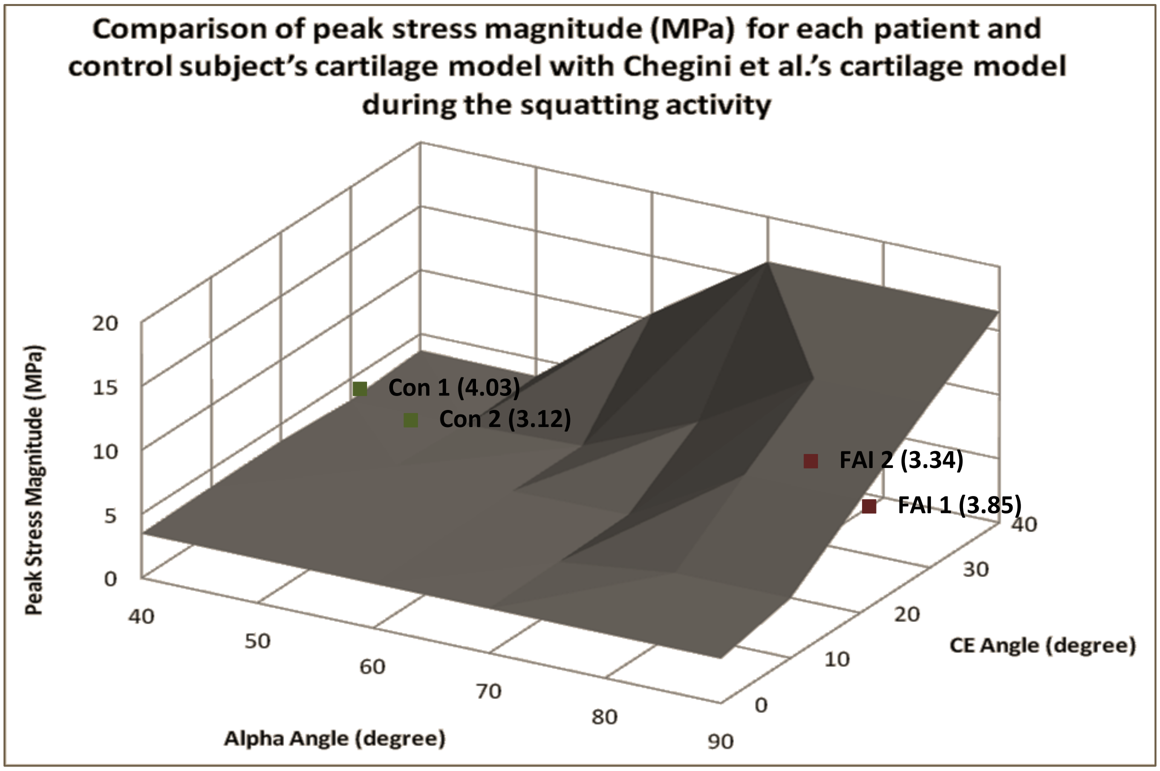

Figure 6.1: Comparing stress magnitudes of the FAI Patients' (red markers) and the Control Subjects' (green markers) cartilage models with Chegini and associates' cartilage model (plotted curve).

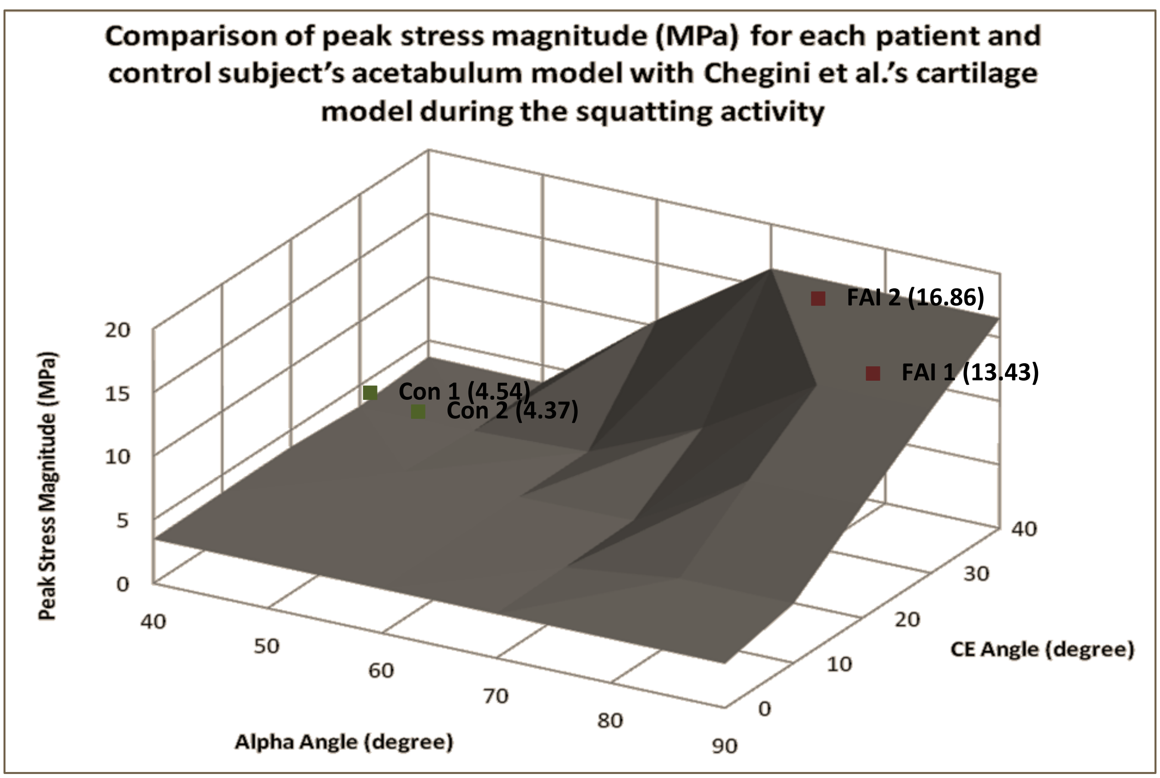

Figure 6.2: Comparing stress magnitudes of the FAI Patients' (red markers) and the Control Subjects' (green markers) acetabulum models with Chegini and associates' cartilage model (plotted curve).

The FAI patient's peak MSS magnitudes could not be directly associated with Chegini and associates' VM stresses. Chegini and associates' parameters (2009) were limited to an alpha and CE angle of 80^{o} and 40^{o}, respectively. The cam deformities of the two FAI patients presented in this study were more severe than the upper limit of 80^{o} established by Chegini and associates' work. Moreover, it was noted that the cartilage transferred much of the mechanical stimuli to the acetabulum in this study. Thus the peak MSS magnitudes found on the FAI patients' acetabulum, and not the FAI patients' cartilage layer, correlated well with the VM stress magnitudes determined by Chegini and associates. The peak contact pressures from Chegini et al.'s study at the highest alpha angle were found to be 12.84 MPa ($\propto = 80^{o}$, CE $=30^{o}$) and 16.51 MPa ($\propto = 80^{o}$, CE $= 40^{o}$). As seen in Figure 6.1 and Figure 6.2, Extrapolating Chegini et al.'s results could account for the higher cam severity and provide a more respectable range for the two FAI patients from our study. Again, VM stresses represent a more conservative failure criterion, thus the peak magnitudes were slightly less than the peak MSS values.

To the best of our knowledge, this research was the first of its kind to investigate loading effects at the underlying acetabulum due to cam FAI using patient-specific CT and biomechanics data. Therefore, a direct comparison between the current findings and previous works is difficult. In the previous computational work on cam FAI by Chegini and associates, an idealized parametric ball-and-socket joint was implemented analyzing only VM stresses on the cartilage surface.

SED values on the acetabulum were determined to observe the effects of the regulating constituent towards bone remodelling (Cowin, 1995; Huiskes, 2000; Huiskes, et al., 1987). The FAI group demonstrated a slight increase in peak SED values on the acetabulum when proceeding from a standing position (1.005 ± 0.076 kPa) to a squatting position (1.018 ± 0.082 kPa). However, the control group demonstrated marginal changes in SED values when proceeding from a standing (1.180 ± 0.180 kPa) to a squatting position (1.105 ± 0.095 kPa).

At the squat depth, the "bump" of the femoral head was at the highest points of contact with the labral regions of the acetabulum, when the joint was at its most impinged state. The SED values were all relatively low in magnitude. As a mechanical stimulus, SED is linearly proportional to the rate of bone turnover and formation (Vahdati & Rouhi, 2009), thus it was thought that an increase in SED above a patient-specific threshold would cause an increase in bone density. Though the FAI patients did confirm an increase in SED from stance to squat, the changes in magnitudes were very marginal to demonstrate any scalar effects of SED towards bone formation. The cam deformity caused a reduction in clearance within the socket, thus the interference fit distorted the elastic members from an unstressed state.

Similar to the MSS results, several factors could have affected the discrepancies of the SED results. The studied scenario involved linear elastic hip components simulated under quasi-static, non-cyclic loads. To yield more accurate representations of SED values, viscoelastic models under iterative cyclic loading should be considered (Gilbert, 2006; Johnson et al., 1994). Moreover, manipulating the rate of loading and the effect of hysteresis would be beneficial towards understanding patient-specific thresholds of SED that govern bone remodelling (Linde, 1994; Turner et al., 2009). In this study, the MSS and SED results were unique to their patient-specific loading parameters and conditions. It was not possible to determine a threshold that would provoke bone remodelling, since the level of mechanical stimuli varies from person to person.

6.2 Location of Peak Mechanical Stimuli

At stance, the MSS values between the cartilage and acetabulum were similar for both comparison groups. Similar observations were noted for the SED analysis. At squat, the highest MSS values were situated at the antero-superior region of the cartilage and acetabulum for both comparison groups. The MSS values were considerably higher for the FAI patients at the antero-superior acetabulum, where the cam deformity was in most contact with the labral regions. The SED concentrations were displaced anteriorly as well; however, marginal differences in SED were noticed. During the squatting position, both FAI patients exhibited concentrations of MSS and SED primarily at the antero-superior acetabulum, with secondary MSS and SED concentrations at the postero-inferior acetabulum (Figure 6.3). The FAI patient models revealed isolated concentrations of mechanical stimuli as opposed to the control subject models that exhibited more well-distributed and dissipated mechanical stimuli. The mechanical stimuli for the FAI patient group were situated more on the periphery of the acetabulum and labral region; whereas the mechanical stimuli for the control group were situated more medially and concentric towards the acetabular fossa. Based on experimental results, it is known that this peripheral location for the FAI patient group can be attributed to the region of impact between the femoral head-neck junction and the antero-superior rim (Beaule, et al., 2005).

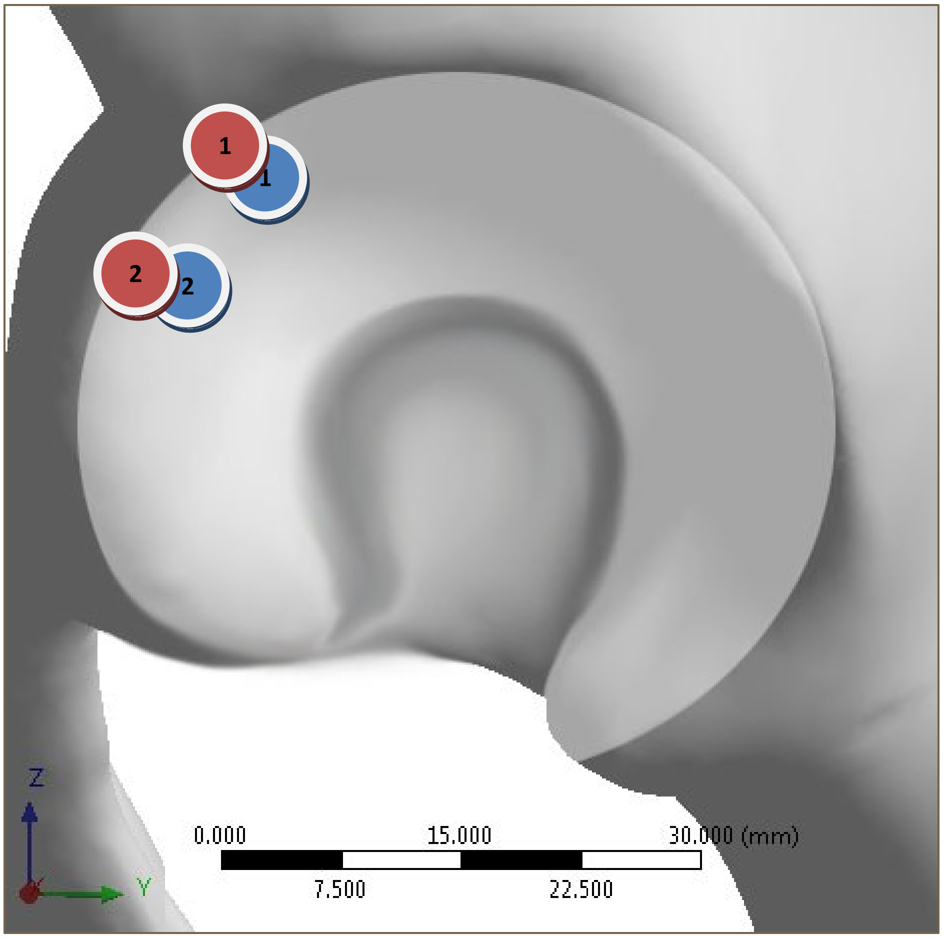

Figure 6.3: Acetabulum mapping locations of the peak MSS (red) and SED (blue) values for FAI Patient 1 (1) and FAI Patient 2 (2) at the squat position. The highest mechanical stimuli concentrations were situated at the antero-superior regions of the acetabulum.

The secondary MSS and SED concentrations may have been attributed to the axis of loading from the applied force vectors. The hip forces, acquired from the patient-specific biomechanics data, were applied to the hip models according to the component vectors of the net joint reactions. During the standing position, the joint reaction components summed up to a vector pointing in the superior direction, justifying the MSS and SED concentration at the superior acetabulum. During the squatting position, the force components summed up to a vector aligned with the axis of the femur. Therefore, the direction of the reaction force vector at squat was pointing posteriorly, also superiorly or inferiorly depending on the depth of squat and the orientation of the femur with respect to the pelvis. The cam deformity reduced the clearance within the socket, thus allowed the medio-posterior acetabulum to constrain the femoral head within the socket and representative of contre-coup lesions. It is expected that the inclusion of muscle forces would alter the magnitude and orientation of the forces; however, in comparison with previous studies related to the FEA of hip biomechanics and cam FAI (Anderson, et al., 2010; Chegini, et al., 2009), the acquisition of the force data in previous studies was elusive. In those previous studies, little to no information was provided on the method of hip loading to justify the discrepancies of the stress locations.

The locations of the peak mechanical stimuli for the hips with cam FAI, found in this FEA study, correspond well with experimental observations. In general, the articulation of healthy hip joints demonstrates higher stress concentrations at the antero-superior regions, distal to the acetabular fossa (Athanasiou, et al., 1994). The same regions of peak mechanical stimuli determined in our study using FEA, at the antero-superior regions of the cartilage and acetabulum, were previously noted during open surgical dislocation of hips with cam FAI (Beaule, et al., 2005; Beck, et al., 2005). In the cam FAI study comprised of 26 hips by Beck et al., severe damage was noticed at the antero-superior acetabular cartilage, between the cartilage and labrum with indications of OA (Beck, et al., 2005). In the similar 36-hip study by Beaulé and associates (2005), acetabular cartilage and labral lesions were observed from the 12 o'clock to 2 o'clock positions in the hips, referring to the antero-superior quadrant of the acetabulums. Furthermore, it was mentioned that the delamination of the cartilage was attributed to the shearing of the labrum and acetabular cartilage from the subchondral bone (Beaule, et al., 2005).

6.3 Loading and Motion Parameters

As mentioned in section 6.1, intersegmental forces were calculated from a combination of patient-specific kinematics and kinetics data using inverse dynamics. The secondary mechanical stimuli concentrations found in and around the acetabulum could have been attributed to the alignment of the combined force vectors, aligned with the axis of the femur with respect to the pelvis. Generally, the intersegmental forces would represent the net joint reaction forces acting through the hip, but not the hip joint contact forces acting at the hip. The net joint reaction forces provided a good estimation of mechanical stimuli values and an indication of the mechanical stimuli locations. However, hip joint contact forces are comprised of further equilibrium equations that account for internal muscle forces, thus produce a substantially higher hip force, in comparison with intersegmental forces (Bergmann, et al., 2001). Muscle forces were not considered in this FEA study. Though the redundancy of poorly assumed muscles cannot balance the external forces and moments of the joint properly (Andriachhi, 2005; Brand, et al., 1994; Mow & Huiskes, 2005; Pedersen, et al., 1997), the consideration for soft tissues and muscle vectors would greatly contribute to a more patient-specific and complete representation of the hip joint.

In the simulations, the FEMs were oriented to two quasi-static positions: (1) stance and (2) maximum force endured during the squat. The second position, at squat, took the absolute maximum that the intersegmental force exerted. In most cases, the maximum intersegmental force was at instances just prior to the maximal squat depth. Therefore, the highest force was not experienced necessarily at the greatest angle of hip flexion, as proposed by Chegini et al. (2009) in their idealized parametric simulation. There was very little difference in hip flexion between the instance at maximum hip force and maximal squat depth. If the FAI patient hip models were oriented according to the maximum squat depth, it would be expected that the location of the mechanical stimuli would be displaced superiorly from the antero-superior acetabulum to more superior region at the dome of the acetabulum.

Since quasi-static conditions were analyzed, dynamic motion was not considered in this FEA. The static simulations provided beneficial preliminary indications for the locations and magnitudes of mechanical stimuli, which correlate well with previous studies (Chegini, et al., 2009) and location of the mechanical stimuli (Beaule, et al., 2005; Beck, et al., 2005; Bittersohl, Steppacher, et al., 2009). Dynamic motion could be incorporated in the simulation to better understand the interference and visualize the kinematics of the impinged hip more accurately. In addition, the rate and speed of the motion can be considered to examine the adverse effects of the collisions between the femoral head-neck junction and the acetabulum (Arbabi, Boulic, & Thalmann, 2009). Since the current FEA considered two extreme static positions, the variables of speed and rate of motion were not considered.

To capture the kinematics data, a modified Helen-Hayes method was implemented to apply the markers onto the participants' anatomical landmarks. Additional markers were applied to identify the static joint angles and to reconstruct the hip joint centres, in circumstances where the adjacent axial markers were hidden from sight. It was understood that the implementation of skin markers may cause minor discrepancies during reconstructions of rigid bodies from motion data (Cappozzo, 1991). To alleviate these discrepancies and to better approximate the hip joint centre, a method to reduce skin marker artefacts should be considered and implemented (e.g. dynamic calibration method (Cappozzo, 1991), displacement dependency method (Ryu, Choi, & Chung, 2009), averaging coordinate system (Mun, 2003)).

6.4 Cartilage Model

The cartilage FEM was approximated using an offset method from the lunate surfaces of the acetabulum extruded onto the medio-superior articulating femoral head. The distance between the femoral head and acetabulum was predetermined from the CT data. All the participants were in a supine position during the acquisition of the CT scans and did not bear any BW onto the hip joints. Since the cartilage was never in a deformed state of loading, it was not feasible to develop patient-specific cartilage models from the radiographs for any quasi-static positions.

The incorporation of a weight-bearing cartilage model should be considered in the FEA of the hip joint to provide more accurate interpretations of mechanical stimuli within the hip. With the recent developments on orthopaedic imaging, the acquisition of full-body X-rays from biplane images has been made possible for participants in upright standing positions (Deschenes et al., 2010; Sapin et al., 2008). Using a vertical, low-dose scanner, the participants are scanned during an upright standing position,. As a result, the 3-D reconstruction from the biplane images reproduces models under weight-bearing loads. When loaded, the cartilage can demonstrate the "weeping" effect, where the interstitial fluid is squeezed in and out of the cartilage within the joint capsule (Macirowski, et al., 1994; McCutchen, 1983), displaying a deformed state of the articular cartilage and narrowing gap between the femoral head and the acetabulum. The weight-bearing profiles could further consolidate the hip model and provide a more patient-specific cartilage FEM. To the best of our knowledge, no imaging technology has been able to capture a full cycle under weight-bearing load (i.e. implementing a full-body scanner to record images during a full dynamic squat).

6.5 Accuracy of Segmented FEMs

The FEMs of the hip joints with cam FAI, comprised of the pelvis and femur geometries, were extracted from patient-specific CT radiographs; which was a different approach from previous works using an idealized ball-and-socket joint (Chegini, et al., 2009). As an expansion to previous 2-D hip models (Rudman, et al., 2006; Wei, et al., 2005), the 3-D constructed FEMs were able to account for loads acting on a third plane as well, providing a much needed representation of the reactions during the two different static positions. Moreover, the inclusion of the pelvis has often been overlooked and neglected (Chegini, et al., 2009; Russell, et al., 2006). Even when the pelvis was included in the assembly, the pelvis was never considered as an object of interest for mechanical stimuli analysis. The inclusion of the pelvis and acetabulum in our study provided a constraint for the acetabular cartilage and physiological rigidity to permit for proper representation of mechanical stimuli distributions on the cartilage layer and acetabulum. Since the objective was to examine the mechanical stimuli distributions and interaction on both components (cartilage and acetabulum), the inclusion of the pelvis was necessary and justified.

It was mentioned in Chegini et al.'s work that patient-specific models derived from CT data require a considerable amount of manual correction of the geometries, thus was a neglected approach in their study (Chegini, et al., 2009). In addition, it was acknowledged in their work that the direct use from patient-specific geometries may cause convergence problems in FE simulations. In our patient-specific approach, it was demonstrated that there are significant advantages in using FEMs derived from patient-specific CT data. Not only do the patient-specific geometries provide a more realistic representation for physiological functions and demands, the simulations can yield expected results to be in better agreement with experimental data (Anderson, et al., 2010; Arbabi, et al., 2009). The methodology to acquire a patient-specific FEM, demonstrated in this research, confirms the obstacles of FE modelling and simulation. However, with the implementation of the resurfacing process, using the NURBS principles, many of the uncertainties of FE modelling were alleviated. The resurfacing process presented an accurate method to reduce geometric artefacts and FEs, a common convergence issue in FEA, while maintaining the accuracy of the original patient-specific representations. Minimal convergence problems due to geometries were encountered in our FEA. Most of the convergence issues were due to improperly constrained models and lack of fixed boundaries, thus permitting the assembly to diverge freely in rigid motion.

7.0 Conclusion

7.1 Relevance and Fulfillment of Objectives

To the best of our knowledge, this research is the first to implement patient-specific data to model cam FAI, taking patient-specific CT, force, and motion data. The biomechanics data and CT data combined to create 3-D FEMs, representative of the hip joints with cam FAI. The segmented FEMs were deemed accurate and correlated well with the initial CT data, thus validating the use of the segmentation and resurfacing procedures. The direct comparison between the FAI patient group and the control group revealed many differences in peak mechanical stimuli locations and magnitudes. During the standing position, the mechanical stimuli were relatively well distributed on the superior cartilage layer and underlying acetabulum for both FAI patient and control subject groups. During the squatting position, it was determined that mechanical stimuli were most prominent at the antero-superior regions, with the cartilage transferring most of the load onto the underlying acetabulum for cam FAI patients during the squat position. It was determined that these magnitudes at the acetabulum of the FAI patients were substantially higher than the magnitudes at the cartilage. Therefore, high levels of mechanical stimuli were most prominent in patients with cam FAI during the squatting position, when the hips were at its most impinged state, near maximum ROM.

Direct comparisons with previous experimental studies were not possible, since there were no previous patient-specific studies conducted on the FEA of cam FAI. The location and magnitudes of the peak mechanical stimuli in this study were found to be quite consistent with the previous parametric study by Chegini et al. (Chegini, et al., 2009). However, their report on peak pressures of the cartilage layer used the VM method of stress analysis, which was considered to be a conservative failure criterion. In our study, the assembly of the pelvis and femur was considered. Since the focus was also on the mechanical stimuli on the acetabular surface, a less conservative stress analysis was implemented. Nevertheless, the peak magnitudes on the cartilage at stance and on the acetabulum at squat, determined from the MSS method, were considered to be within the range of Chegini et al.'s results. Even though a full motion cycle was not used to examine the MSS and SED values in the hip joint, it can be seen that reaction loads in the hip joint depend on the geometry, position of the hip, and external loading.

The order of the FEA was constrained to a non-cyclic loading simulation involving linear elastic solid models. It would be feasible to determine SED if the simulation involved cyclic loading parameters with poroelastic FEMs. Therefore, the implementation of SED as an indicator for mechanical stimulus was not as effective as the MSS method. Although the peak SED results were not able to predict the rate of bone turnover, the distribution of SED provided an indication for the expected stiffening regions of subchondral plate. Since SED is proportional to rate of bone remodelling, there will be varying rates of remodelling in order to equilibrate to a suitable configuration. However, since the SED results were unique to their patient-specific loading parameters and conditions, it was difficult to determine a patient-specific threshold that can regulate the bone remodelling process. It may be perceived that under the simulated quasi-static, linear-elastic conditions that MSS may be a better mechanical stimuli candidate to indicate the initiation of the bone remodelling process.

The locations of the highest mechanical stimuli, determined from our FEA, correspond with the locations of preliminary cartilage wear (Beaule, et al., 2005; Beck, et al., 2005; Bittersohl, Steppacher, et al., 2009). The elevated levels of mechanical stimuli, found at the subchondral surfaces, emphasize the need to further understand the intricacy of the pathomechanical process of cam FAI. It is suggested that the amplification of the mechanical stimuli, due to the cam deformity, leads to the delamination process of cartilage and the subsequent onset of OA. This coincides with previous theories that the subchondral plate plays a predominant role in the OA process (von Eisenhart-Rothe, et al., 1997; Wang, et al., 2007; Wei, et al., 2005). It may be seen that cartilage damage could come secondary to the stiffening of the subchondral bone.

7.2 Future Considerations

The next step, in this on-going research to understand the mechanisms of OA due to cam FAI, is to first implement an assembly of the hip with cam FAI to follow a dynamic squat motion. The quasi-static analysis, from this study, provided the mechanical stimuli distributions at specific instances during a squat cycle. The integration of patient-specific kinematics with the FEM assembly could suggest how the mechanical stimuli distributions fluctuate and displace from one region to another. The orientation of the femur and the pelvic tilt angle would move and vary with respect to the squat depth. Though a normalized dynamic cycle would merely represent hip motion, an additional measure of the velocity of the hip’s motion could be beneficial towards comprehending the possible effect of collisions between the cam deformity and the labral regions (Arbabi, et al., 2007, 2009). Therefore, applying dynamic motion to alter the orientation of the femur with respect to the pelvis and also parametrically adjusting the velocity of the squat motion could yield a better representation of the mechanical stimuli locations.

To yield more accurate and precise results of the mechanical stimuli magnitudes, the application of muscle forces could be considered. As the data used in this study was intersegmental hip forces calculated from inverse dynamics, the hip forces were estimated as the reactions acting through the joint as opposed to the contact forces at the hip. The use of intersegmental hip joint reaction forces is a conventional method to approximate hip loads; however, it is considered to be an underestimation of true hip forces. Though many muscles and soft tissues overlay the hip joint, the inclusion of muscle vectors and contact forces would better represent the physiological reactions and resultant mechanical stimuli of the hip (Bergmann, et al., 2001). This could be done by conducting electromyography (EMG) tests to evaluate the electrical activity of the skeletal muscles during a squat cycle. Moreover, it has been disputed that the seal of the synovial capsule has a residual effect to confine the femoral head in place, resisting lateral motion (Ferguson, Bryant, Ganz, & Ito, 2000a; Ferguson, et al., 2000b). Therefore, the inclusions of a capsular FEM and muscle vectors could improve the accuracy of the mechanical stimuli magnitudes, further improving the understanding of cam FAI.

More research will be conducted on the selection of each material property for each patient-specific case. To predict the rate of bone formation at the acetabulum, the next step in FE modelling is to take viscoelastic properties of the hip joint assemblies into account (Gilbert, 2006; Johnson, et al., 1994). If the parameters of the simulation were to include cyclic loading, the material property of the cartilage would be altered to a poroelastic model (Carter & Wong, 2003; Ferguson, et al., 2000a, 2000b). This would also make the cartilage model more susceptible to shear stresses (Ethier & Simmons, 2007; Hlavacek, 2001; Macirowski, et al., 1994)

To further enhance the quality of the patient-specific output, the input of patient-specific bone density would be calculated in future studies (Schileo et al., 2008; Trabelsi, Yosibash, & Milgrom, 2009; Yosibash, Tal, & Trabelsi, 2010). Since the bone density varies according to physiological function and demand, the density of bone varies from bone to bone and from individual to individual. Considering that the apparent density for each person is different, it would be beneficial to calculate the elastic modulus of bone according to the patient-specific apparent bone density. With the unique patient-specific bone density and resultant patient-specific elastic modulus for bone, the resultant output for the mechanical stimuli would be further considered as patient-specific. The inclusion of bone density in the analysis could help better approximate the mechanical stimuli on the subchondral bone. The aforementioned steps denote the possible future considerations to undertake. Figure 7.1 summarizes the process flow of the design process, modified to include the future considerations.

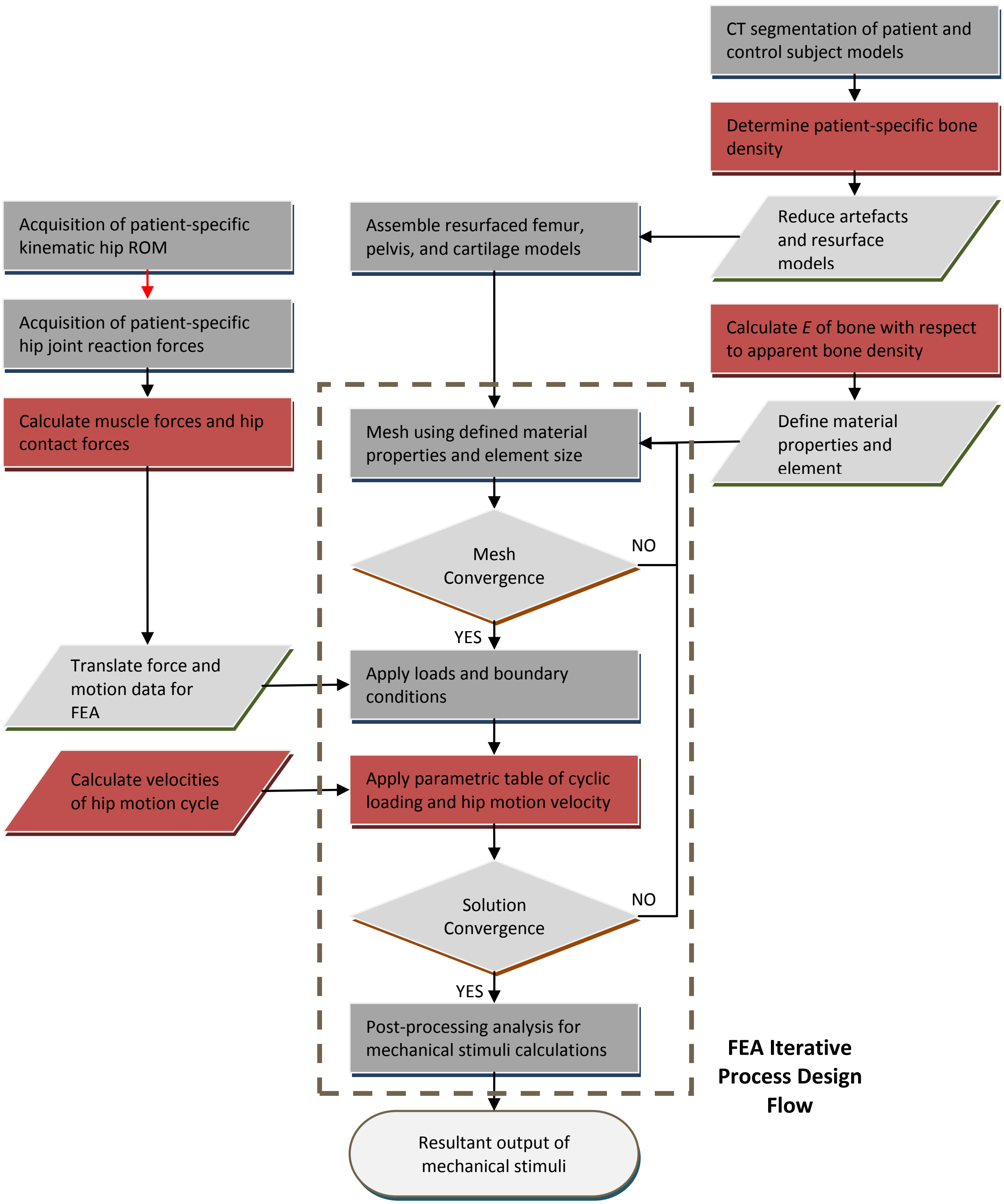

Figure 7.1: Modified flow chart of the iterative design process. Future considerations to the process flow are indicated in red.

8.0 Bibliography

Aigner, T., & McKenna, L. (2002). Molecular pathology and pathobiology of osteoarthritic cartilage. *Cell Mol Life Sci, 59*(1), 5-18.

Alkjaer, T., Simonsen, E. B., & Dyhre-Poulsen, P. (2001). Comparison of inverse dynamics calculated by two- and three-dimensional models during walking. *Gait Posture, 13*(2), 73-77.

Anderson, A. E., Ellis, B. J., Maas, S. A., Peters, C. L., & Weiss, J. A. (2008). Validation of finite element predictions of cartilage contact pressure in the human hip joint. *J Biomech Eng, 130*(5), 051008.

Anderson, A. E., Ellis, B. J., Maas, S. A., & Weiss, J. A. (2010). Effects of idealized joint geometry on finite element predictions of cartilage contact stresses in the hip. *J Biomech, 43*(7), 1351-1357.

Andriachhi, T. P., Johnson, T.S., Hurwitz, D.E., Natarajan, R.N. (2005). Musculoskeletal Dynamics, Locomotion, and Clinical Application. In V. C. Mow, Huiskes, R. (Ed.), *Basic Orthopaedic Biomechanics and Mechano-Biology* (Third ed., pp. 720). Philadelphia: Lippincott Williams & Wilkins.

Arbabi, E., Boulic, R., & Thalmann, D. (2007). A fast method for finding range of motion in the human joints. *Conf Proc IEEE Eng Med Biol Soc, 2007*, 5079-5082.

Arbabi, E., Boulic, R., & Thalmann, D. (2009). Fast collision detection methods for joint surfaces. *J Biomech, 42*(2), 91-99.

Aritan, S., Dabnichki, P., & Bartlett, R. (1997). Program for generation of three-dimensional finite element mesh from magnetic resonance imaging scans of human limbs. *Med Eng Phys, 19*(8), 681-689.

Asgari, S. A., Hamouda, A. M. S., Mansor, J. B., Singh, H., Mahdi, E., Wirza, R., et al. (2004). Finite element modeling of a generic stemless hip implant design in comparison with conventional hip implants. *Finite Element in Analysis and Design, 40*, 2027-2047.

Ateshian, G. A., Ellis, B. J., & Weiss, J. A. (2007). Equivalence between short-time biphasic and incompressible elastic material responses. *J Biomech Eng, 129*(3), 405-412.

Athanasiou, K. A., Agarwal, A., & Dzida, F. J. (1994). Comparative study of the intrinsic mechanical properties of the human acetabular and femoral head cartilage. *J Orthop Res, 12*(3), 340-349.

Beaule, P. E. (2009). Femoroacetabular impingement: current status of diagnosis and treatment: editorial comment. *Clin Orthop Relat Res, 467*(3), 603-604.

Beaule, P. E., Zaragoza, E., Motamedi, K., Copelan, N., & Dorey, F. J. (2005). Three-dimensional computed tomography of the hip in the assessment of femoroacetabular impingement. *J Orthop Res, 23*(6), 1286-1292.

Beck, M., Kalhor, M., Leunig, M., & Ganz, R. (2005). Hip morphology influences the pattern of damage to the acetabular cartilage: femoroacetabular impingement as a cause of early osteoarthritis of the hip. *J Bone Joint Surg Br, 87*(7), 1012-1018.

Behrens, B. A., Nolte, I., Wefstaedt, P., Stukenborg-Colsman, C., & Bouguecha, A. (2009). Numerical investigations on the strain-adaptive bone remodelling in the periprosthetic femur: influence of the boundary conditions. *Biomed Eng Online, 8*, 7.

Bergmann, G., Deuretzbacher, G., Heller, M., Graichen, F., Rohlmann, A., Strauss, J., et al. (2001). Hip contact forces and gait patterns from routine activities. *J Biomech, 34*(7), 859-871.

Bittersohl, B., Hosalkar, H. S., Kim, Y. J., Werlen, S., Siebenrock, K. A., & Mamisch, T. C. (2009). Delayed gadolinium-enhanced magnetic resonance imaging (dGEMRIC) of hip joint cartilage in femoroacetabular impingement (FAI): Are pre- and postcontrast imaging both necessary? *Magn Reson Med, 62*(6), 1362-1367.

Bittersohl, B., Steppacher, S., Haamberg, T., Kim, Y. J., Werlen, S., Beck, M., et al. (2009). Cartilage damage in femoroacetabular impingement (FAI): preliminary results on comparison of standard diagnostic vs delayed gadolinium-enhanced magnetic resonance imaging of cartilage (dGEMRIC). *Osteoarthritis Cartilage, 17*(10), 1297-1306.

Bohndorf, K., & Kilcoyne, R. F. (2002). Traumatic injuries: imaging of peripheral musculoskeletal injuries. *Eur Radiol, 12*(7), 1605-1616.

Bombelli, R. (1976). *Osteoarthritis of the Hip: Pathogenesis and Consequent Therapy*. Berlin: Springer-Verlag.

Bombelli, R. (1993). *Structure and Function in Normal and Abnormal hips* (3 ed.). Berlin: Springer-Verlag.

Brand, R. A., Pedersen, D. R., Davy, D. T., Kotzar, G. M., Heiple, K. G., & Goldberg, V. M. (1994). Comparison of hip force calculations and measurements in the same patient. *J Arthroplasty, 9*(1), 45-51.

Brandt, K. D., Dieppe, P., & Radin, E. L. (2008). Etiopathogenesis of osteoarthritis. *Rheum Dis Clin North Am, 34*(3), 531-559.

Brunner, A., Horisberger, M., & Herzog, R. F. (2009). Evaluation of a computed tomography-based navigation system prototype for hip arthroscopy in the treatment of femoroacetabular cam impingement. *Arthroscopy, 25*(4), 382-391.

Cabarrus, M. C., Ambekar, A., Lu, Y., & Link, T. M. (2008). MRI and CT of insufficiency fractures of the pelvis and the proximal femur. *AJR Am J Roentgenol, 191*(4), 995-1001.

Cappozzo, A. (1991). Three-dimensional analysis of human walking: Experimental methods and associated artifacts. *Human Movement Science, 10*(5), 589-602.

Carter, D. R., Van Der Meulen, M. C., & Beaupre, G. S. (1996). Mechanical factors in bone growth and development. *Bone, 18*(1 Suppl), 5S-10S.

Carter, D. R., & Wong, M. (2003). Modelling cartilage mechanobiology. *Philos Trans R Soc Lond B Biol Sci, 358*(1437), 1461-1471.

Chegini, S., Beck, M., & Ferguson, S. J. (2009). The effects of impingement and dysplasia on stress distributions in the hip joint during sitting and walking: a finite element analysis. *J Orthop Res, 27*(2), 195-201.

Clohisy, J. C., & McClure, J. T. (2005). Treatment of anterior femoroacetabular impingement with combined hip arthroscopy and limited anterior decompression. *Iowa Orthop J, 25*, 164-171.

Clohisy, J. C., St John, L. C., & Schutz, A. L. (2010). Surgical treatment of femoroacetabular impingement: a systematic review of the literature. *Clin Orthop Relat Res, 468*(2), 555-564.

Couteau, B., Hobatho, M. C., Darmana, R., Brignola, J. C., & Arlaud, J. Y. (1998). Finite element modelling of the vibrational behaviour of the human femur using CT-based individualized geometrical and material properties. *J Biomech, 31*(4), 383-386.

Couteau, B., Labey, L., Hobatho, M. C., Vander Sloten, J., Arlaud, J. Y., & Brignola, J. C. (1998). Validation of a three dimensional finite element model of a femur with a customised hip implant. In J. Middleton, M. L. Jones & G. N. Pande (Eds.), *Computer Methods in Biomechanics and Biomedical Engineering* (Vol. 2, pp. 147-154). Amsterdam: Gordon and Breach Science Publishers.

Cowin, S. C. (1995). On the minimization and maximization of the strain energy density in cortical bone tissue. *J Biomech, 28*(4), 445-447.

Davis, R. B. (1997). Reflections on clinical gait analysis. *J Electromyogr Kinesiol, 7*(4), 251-257.

Day, J. S., Van Der Linden, J. C., Bank, R. A., Ding, M., Hvid, I., Sumner, D. R., et al. (2004). Adaptation of subchondral bone in osteoarthritis. *Biorheology, 41*(3-4), 359-368.

de Luis-Garcia, R., & Alberola-Lopez, C. (2006). Parametric 3D hip joint segmentation for the diagnosis of developmental dysplasia. *Conf Proc IEEE Eng Med Biol Soc, 1*, 4807-4810.

Deschenes, S., Charron, G., Beaudoin, G., Labelle, H., Dubois, J., Miron, M. C., et al. (2010). Diagnostic imaging of spinal deformities: reducing patients radiation dose with a new slot-scanning X-ray imager. *Spine (Phila Pa 1976), 35*(9), 989-994.

Durr, H. D., Martin, H., Pellengahr, C., Schlemmer, M., Maier, M., & Jansson, V. (2004). The cause of subchondral bone cysts in osteoarthrosis: a finite element analysis. *Acta Orthop Scand, 75*(5), 554-558.

Eckstein, F., Merz, B., Schmid, P., & Putz, R. (1994). The influence of geometry on the stress distribution in joints--a finite element analysis. *Anat Embryol (Berl), 189*(6), 545-552.

Eijer, H., Myers, S. R., & Ganz, R. (2001). Anterior femoroacetabular impingement after femoral neck fractures. *J Orthop Trauma, 15*(7), 475-481.

El-Asfoury, M. S., & El-Hadek, M. A. (2009). Static and Dynamic Three-Dimensional Finite Element Analysis of Pelvic Bone. *International Journal of Mathematical, Physical and Engineering Sciences, 3*(1), 35-41.

Estivalezes, E., Couteau, B., & Darmana, R. (2001). 2D calculation method based on composite beam theory for the determination of local homogenised stiffnesses of long bones. *J Biomech, 34*(2), 277-283.

Ethier, C. R., & Simmons, C. A. (2007). *Introductory Biomechanics: from Cells to Organisms*. Cambridge: Cambridge University Press.

Federico, S., Grillo, A., La Rosa, G., Giaquinta, G., & Herzog, W. (2005). A transversely isotropic, transversely homogeneous microstructural-statistical model of articular cartilage. *J Biomech, 38*(10), 2008-2018.

Ferguson, S. J., Bryant, J. T., Ganz, R., & Ito, K. (2000a). The acetabular labrum seal: a poroelastic finite element model. *Clin Biomech (Bristol, Avon), 15*(6), 463-468.

Ferguson, S. J., Bryant, J. T., Ganz, R., & Ito, K. (2000b). The influence of the acetabular labrum on hip joint cartilage consolidation: a poroelastic finite element model. *J Biomech, 33*(8), 953-960.

Fessler, H. (1957). Load distribution in a model of a hip joint. *J Bone Joint Surg Br, 39-B*(1), 145-153.

Gaeta, M., Minutoli, F., Scribano, E., Ascenti, G., Vinci, S., Bruschetta, D., et al. (2005). CT and MR imaging findings in athletes with early tibial stress injuries: comparison with bone scintigraphy findings and emphasis on cortical abnormalities. *Radiology, 235*(2), 553-561.

Ganz, R., Bamert, P., Hausner, P., Isler, B., & Vrevc, F. (1991). [Cervico-acetabular impingement after femoral neck fracture]. *Unfallchirurg, 94*(4), 172-175.

Ganz, R., Leunig, M., Leunig-Ganz, K., & Harris, W. H. (2008). The etiology of osteoarthritis of the hip: an integrated mechanical concept. *Clin Orthop Relat Res, 466*(2), 264-272.

Ganz, R., Parvizi, J., Beck, M., Leunig, M., Notzli, H., & Siebenrock, K. A. (2003). Femoroacetabular impingement: a cause for osteoarthritis of the hip. *Clin Orthop Relat Res*(417), 112-120.

Garcia, J. J., & Cortes, D. H. (2006). A nonlinear biphasic viscohyperelastic model for articular cartilage. *J Biomech, 39*(16), 2991-2998.

Genda, E., Iwasaki, N., Li, G., MacWilliams, B. A., Barrance, P. J., & Chao, E. Y. (2001). Normal hip joint contact pressure distribution in single-leg standing--effect of gender and anatomic parameters. *J Biomech, 34*(7), 895-905.

Gilbert, J. L. (2006). Complexity in modeling of residual stresses and strains during polymerization of bone cement: effects of conversion, constraint, heat transfer, and viscoelastic property changes. *J Biomed Mater Res A, 79*(4), 999-1014.

Gilles, B., Moccozet, L., & Magnenat-Thalmann, N. (2006). Anatomical modelling of the musculoskeletal system from MRI. *Med Image Comput Comput Assist Interv, 9*(Pt 1), 289-296.

Goodman, D. A., Feighan, J. E., Smith, A. D., Latimer, B., Buly, R. L., & Cooperman, D. R. (1997). Subclinical slipped capital femoral epiphysis. Relationship to osteoarthrosis of the hip. *J Bone Joint Surg Am, 79*(10), 1489-1497.

Gu, D., Chen, Y., Dai, K., Zhang, S., & Yuan, J. (2008). The shape of the acetabular cartilage surface: a geometric morphometric study using three-dimensional scanning. *Med Eng Phys, 30*(8), 1024-1031.

Hadley, N. A., Brown, T. D., & Weinstein, S. L. (1990). The effects of contact pressure elevations and aseptic necrosis on the long-term outcome of congenital hip dislocation. *J Orthop Res, 8*(4), 504-513.

Harris, W. H. (1986). Etiology of osteoarthritis of the hip. *Clin Orthop Relat Res*(213), 20-33.

Henriksen, K., Neutzsky-Wulff, A.V., Bonewald, L.F., Karsdal, M.A. (2009). Local communication on and within bone controls bone remodeling. *Bone, 44*(6), 1026-1033.

Herman, G. T. (2009). *Fundamentals of Computerized Tomography: Image Reconstruction from Projection*. London: Springer-Verlag.

Herzog, W., & Federico, S. (2006). Considerations on joint and articular cartilage mechanics. *Biomech Model Mechanobiol, 5*(2-3), 64-81.

Hibbeler, R. C. (2010). *Mechanics of Materials*. New Jersey: Prentice Hall.

Hlavacek, M. (2001). The thixotropic effect of the synovial fluid in squeeze-film lubrication of the human hip joint. *Biorheology, 38*(4), 319-334.

Hosoda, N., Sakai, N., Sawae, Y., & Murakami, T. (2009). *Finite Element Analysis of Articular Cartilage Model Considering the Configuration and Biphasic Property of the Tissue.* Paper presented at the ICBME 2008.

Huebner, K. H., Dewhirst, D. L., Smith, D. E., & Byrom, T. G. (2001). *The Finite Element Method for Engineers* (4th ed.). New York: Wiley.

Huiskes, R. (2000). If bone is the answer, then what is the question? *J Anat, 197 (Pt 2)*, 145-156.

Huiskes, R., Ruimerman, R., van Lenthe, G. H., & Janssen, J. D. (2000). Effects of mechanical forces on maintenance and adaptation of form in trabecular bone. *Nature, 405*(6787), 704-706.

Huiskes, R., Weinans, H., Grootenboer, H. J., Dalstra, M., Fudala, B., & Slooff, T. J. (1987). Adaptive bone-remodeling theory applied to prosthetic-design analysis. *J Biomech, 20*(11-12), 1135-1150.

Hutton, D. V. (2004). *Fundamentals of Finite Element Analysis*. New York: McGraw-Hill.

Ilizaliturri, V. M., Jr., Orozco-Rodriguez, L., Acosta-Rodriguez, E., & Camacho-Galindo, J. (2008). Arthroscopic treatment of cam-type femoroacetabular impingement: preliminary report at 2 years minimum follow-up. *J Arthroplasty, 23*(2), 226-234.

Ito, K., Minka, M. A., 2nd, Leunig, M., Werlen, S., & Ganz, R. (2001). Femoroacetabular impingement and the cam-effect. A MRI-based quantitative anatomical study of the femoral head-neck offset. *J Bone Joint Surg Br, 83*(2), 171-176.

Jaberi, F. M., & Parvizi, J. (2007). Hip pain in young adults: femoroacetabular impingement. *J Arthroplasty, 22*(7 Suppl 3), 37-42.

Jang, I. G., Kim, I. Y., & Kwak, B. B. (2009). Analogy of strain energy density based bone-remodeling algorithm and structural topology optimization. *J Biomech Eng, 131*(1), 011012.

Johnson, G. A., Tramaglini, D. M., Levine, R. E., Ohno, K., Choi, N. Y., & Woo, S. L. (1994). Tensile and viscoelastic properties of human patellar tendon. *J Orthop Res, 12*(6), 796-803.

Johnston, R. C., & Smidt, G. L. (1970). Hip motion measurements for selected activities of daily living. *Clin Orthop Relat Res, 72*, 205-215.

Jonkers, I., Sauwen, N., Lenaerts, G., Mulier, M., Van der Perre, G., & Jaecques, S. (2008). Relation between subject-specific hip joint loading, stress distribution in the proximal femur and bone mineral density changes after total hip replacement. *J Biomech, 41*(16), 3405-3413.

Kadaba, M. P., Ramakrishnan, H. K., & Wootten, M. E. (1990). Measurement of lower extremity kinematics during level walking. *J Orthop Res, 8*(3), 383-392.

Kang, C., Hwang, D. S., & Cha, S. M. (2009). Acetabular labral tears in patients with sports injury. *Clin Orthop Surg, 1*(4), 230-235.

Kang, Y., Engelke, K., & Kalender, W. A. (2003). A new accurate and precise 3-D segmentation method for skeletal structures in volumetric CT data. *IEEE Trans Med Imaging, 22*(5), 586-598.

Kassarjian, A., Brisson, M., & Palmer, W. E. (2007). Femoroacetabular impingement. *Eur J Radiol, 63*(1), 29-35.

Kellgren, J. (1961). Osteoarthrosis in patients and populations. *British Medical Journal*(2), 1-6.

Kennedy, M. J., Lamontagne, M., & Beaule, P. E. (2009). Femoroacetabular impingement alters hip and pelvic biomechanics during gait Walking biomechanics of FAI. *Gait Posture, 30*(1), 41-44.

Kerr, J., Ratiu, P., & Sellberg, M. (1996). Volume rendering of visible human data for an anatomical virtual environment. *Stud Health Technol Inform, 29*, 352-370.

Klaue, K., Durnin, C. W., & Ganz, R. (1991). The acetabular rim syndrome. A clinical presentation of dysplasia of the hip. *J Bone Joint Surg Br, 73*(3), 423-429.

Konrath, G. A., Hamel, A. J., Olson, S. A., Bay, B., & Sharkey, N. A. (1998). The role of the acetabular labrum and the transverse acetabular ligament in load transmission in the hip. *J Bone Joint Surg Am, 80*(12), 1781-1788.

Korhonen, R. K., Julkunen, P., Wilson, W., & Herzog, W. (2008). Importance of collagen orientation and depth-dependent fixed charge densities of cartilage on mechanical behavior of chondrocytes. *J Biomech Eng, 130*(2), 021003.

Krishnan, R., Park, S., Eckstein, F., & Ateshian, G. A. (2003). Inhomogeneous cartilage properties enhance superficial interstitial fluid support and frictional properties, but do not provide a homogeneous state of stress. *J Biomech Eng, 125*(5), 569-577.

Kubiak-Langer, M., Tannast, M., Murphy, S. B., Siebenrock, K. A., & Langlotz, F. (2007). Range of motion in anterior femoroacetabular impingement. *Clin Orthop Relat Res, 458*, 117-124.

Lamontagne, M., Kennedy, M. J., & Beaule, P. E. (2009). The effect of cam FAI on hip and pelvic motion during maximum squat. *Clin Orthop Relat Res, 467*(3), 645-650.

Larson, C. M., & Giveans, M. R. (2008). Arthroscopic management of femoroacetabular impingement: early outcomes measures. *Arthroscopy, 24*(5), 540-546.

Laude, F., Boyer, T., & Nogier, A. (2007). Anterior femoroacetabular impingement. *Joint Bone Spine, 74*(2), 127-132.

Lavigne, M., Parvizi, J., Beck, M., Siebenrock, K. A., Ganz, R., & Leunig, M. (2004). Anterior femoroacetabular impingement: part I. Techniques of joint preserving surgery. *Clin Orthop Relat Res*(418), 61-66.

Lee, C., Lodwick, D., & Bolch, W. E. (2007). NURBS-based 3-D anthropomorphic computational phantoms for radiation dosimetry applications. *Radiat Prot Dosimetry, 127*(1-4), 227-232.

Leunig, M., Beaule, P. E., & Ganz, R. (2009). The concept of femoroacetabular impingement: current status and future perspectives. *Clin Orthop Relat Res, 467*(3), 616-622.

Leunig, M., Beck, M., Dora, C., & Ganz, R. (2005). Femoroacetabular Impingement: Etiology and Surgical Concept. *Oper Tech Orthop 15*, 247-255.

Leunig, M., Beck, M., Kalhor, M., Kim, Y. J., Werlen, S., & Ganz, R. (2005). Fibrocystic changes at anterosuperior femoral neck: prevalence in hips with femoroacetabular impingement. *Radiology, 236*(1), 237-246.

Leunig, M., Casillas, M. M., Hamlet, M., Hersche, O., Notzli, H., Slongo, T., et al. (2000). Slipped capital femoral epiphysis: early mechanical damage to the acetabular cartilage by a prominent femoral metaphysis. *Acta Orthop Scand, 71*(4), 370-375.

Leunig, M., & Ganz, R. (2005). [Femoroacetabular impingement. A common cause of hip complaints leading to arthrosis]. *Unfallchirurg, 108*(1), 9-10, 12-17.

Linde, F. (1994). Elastic and viscoelastic properties of trabecular bone by a compression testing approach. *Dan Med Bull, 41*(2), 119-138.

Loder, R. T., Aronsson, D. D., Weinstein, S. L., Breur, G. J., Ganz, R., & Leunig, M. (2008). Slipped capital femoral epiphysis. *Instr Course Lect, 57*, 473-498.

Long, J. P., & Bartel, D. L. (2006). Surgical variables affect the mechanics of a hip resurfacing system. *Clin Orthop Relat Res, 453*, 115-122.

Luo, Y. (2008). 3D Nearest-Nodes Finite Element Method for Solid Continuum Analysis. *Adv. Theor. Appl. Mech., 1*(3), 131-139.

Macirowski, T., Tepic, S., & Mann, R. W. (1994). Cartilage stresses in the human hip joint. *J Biomech Eng, 116*(1), 10-18.

Mahfouz, M. R., Hoff, W. A., Komistek, R. D., & Dennis, D. A. (2005). Effect of segmentation errors on 3D-to-2D registration of implant models in X-ray images. *J Biomech, 38*(2), 229-239.

Martin, T. J., & Seeman, E. (2008). Bone remodelling: its local regulation and the emergence of bone fragility. *Best Pract Res Clin Endocrinol Metab, 22*(5), 701-722.

McCutchen, C. W. (1983). Joint lubrication. *Bull Hosp Jt Dis Orthop Inst, 43*(2), 118-129.

Menschik, F. (1997). The hip joint as a conchoid shape. *J Biomech, 30*(9), 971-973.

Meyer, D. C., Beck, M., Ellis, T., Ganz, R., & Leunig, M. (2006). Comparison of six radiographic projections to assess femoral head/neck asphericity. *Clin Orthop Relat Res, 445*, 181-185.

Mitchell, M. D., Kundel, H. L., Steinberg, M. E., Kressel, H. Y., Alavi, A., & Axel, L. (1986). Avascular necrosis of the hip: comparison of MR, CT, and scintigraphy. *AJR Am J Roentgenol, 147*(1), 67-71.

Mow, V. C., & Huiskes, R. (2005). *Basic Orthopaedic Biomechanics & Mechano-Biology* (Third ed.). Philadelphia: Lippincott Williams & Wilkins.

Mun, J. (2003). A method for the reduction of skin marker artifacts during walking : Application to the knee. *Journal of Mechanical Science and Technology, 17*(6), 825-835.

Murphy, M. J. (1999). The importance of computed tomography slice thickness in radiographic patient positioning for radiosurgery. *Med Phys, 26*(2), 171-175.

Murray, R. O. (1965). The aetiology of primary osteoarthritis of the hip. *Br J Radiol, 38*(455), 810-824.

Myers, S. R., Eijer, H., & Ganz, R. (1999). Anterior femoroacetabular impingement after periacetabular osteotomy. *Clin Orthop Relat Res*(363), 93-99.

Nordin, M., Frankel, V. (2001). *Basic Biomechanics of the Musculoskeletal System*. New York: Lippincott Williams & Wilkins.

Notzli, H. P., Wyss, T. F., Stoecklin, C. H., Schmid, M. R., Treiber, K., & Hodler, J. (2002). The contour of the femoral head-neck junction as a predictor for the risk of anterior impingement. *J Bone Joint Surg Br, 84*(4), 556-560.

Nouh, M. R., Schweitzer, M. E., Rybak, L., & Cohen, J. (2008). Femoroacetabular impingement: can the alpha angle be estimated? *AJR Am J Roentgenol, 190*(5), 1260-1262.

Owen, J. R., & Wayne, J. S. (2006). Influence of a superficial tangential zone over repairing cartilage defects: implications for tissue engineering. *Biomech Model Mechanobiol, 5*(2-3), 102-110.

Park, J. H., Park, S. H., & Won, Y. H. (2007). Geometry-Based Muscle Forces and Inverse Dynamics for Animation. *Lecture Notes in Computer Science, 4469/2007*, 584-595.

Pedersen, D. R., Brand, R. A., & Davy, D. T. (1997). Pelvic muscle and acetabular contact forces during gait. *J Biomech, 30*(9), 959-965.

Phillips, A. T. (2009). The femur as a musculo-skeletal construct: a free boundary condition modelling approach. *Med Eng Phys, 31*(6), 673-680.

Prescott, J. W., Pennell, M., Best, T. M., Swanson, M. S., Haq, F., Jackson, R., et al. (2009). An automated method to segment the femur for osteoarthritis research. *Conf Proc IEEE Eng Med Biol Soc, 2009*, 6364-6367.

Rab, G. T. (1999). The geometry of slipped capital femoral epiphysis: implications for movement, impingement, and corrective osteotomy. *J Pediatr Orthop, 19*(4), 419-424.

Radcliffe, I. A., & Taylor, M. (2007). Investigation into the affect of cementing techniques on load transfer in the resurfaced femoral head: a multi-femur finite element analysis. *Clin Biomech (Bristol, Avon), 22*(4), 422-430.

Radin, E. L., Paul, I. L., & Tolkoff, M. J. (1970). Subchondral bone changes in patients with early degenerative joint disease. *Arthritis Rheum, 13*(4), 400-405.

Radin, E. L., & Rose, R. M. (1986). Role of subchondral bone in the initiation and progression of cartilage damage. *Clin Orthop Relat Res*(213), 34-40.

Roger, D. F. (2001). *An Introduction to NURBS: with Historical Perspective*. London: Academic Press.

Ruan, J. S., El-Jawahri, R., Barbat, S., Rouhana, S. W., & Prasad, P. (2008). Impact response and biomechanical analysis of the knee-thigh-hip complex in frontal impacts with a full human body finite element model. *Stapp Car Crash J, 52*, 505-526.

Rudman, K. E., Aspden, R. M., & Meakin, J. R. (2006). Compression or tension? The stress distribution in the proximal femur. *Biomed Eng Online, 5*, 12.

Ruimerman, R., Van Rietbergen, B., Hilbers, P., & Huiskes, R. (2005). The effects of trabecular-bone loading variables on the surface signaling potential for bone remodeling and adaptation. *Ann Biomed Eng, 33*(1), 71-78.

Russell, M. E., Shivanna, K. H., Grosland, N. M., & Pedersen, D. R. (2006). Cartilage contact pressure elevations in dysplastic hips: a chronic overload model. *J Orthop Surg Res, 1*, 6.

Ryan, T. M., & van Rietbergen, B. (2005). Mechanical significance of femoral head trabecular bone structure in Loris and Galago evaluated using micromechanical finite element models. *Am J Phys Anthropol, 126*(1), 82-96.

Ryu, T., Choi, H. S., & Chung, M. K. (2009). Soft tissue artifact compensation using displacement dependency between anatomical landmarks and skin markers - a preliminary study. *International Journal of Industrial Ergonomics, 39*(1), 152-158.

Safont, L. V., & Marroquin, E. L. (1999). *3D Reconstruction of Third Proximal Femur (31-) with Active Contours.* Paper presented at the 10th International Conference on Image Analysis and Processing (ICIAP'99), Venice, Italy.

Sapin, E., Briot, K., Kolta, S., Gravel, P., Skalli, W., Roux, C., et al. (2008). Bone mineral density assessment using the EOS low-dose X-ray device: a feasibility study. *Proc Inst Mech Eng H, 222*(8), 1263-1271.

Schileo, E., Dall'ara, E., Taddei, F., Malandrino, A., Schotkamp, T., Baleani, M., et al. (2008). An accurate estimation of bone density improves the accuracy of subject-specific finite element models. *J Biomech, 41*(11), 2483-2491.

Schmitt, J., Meiforth, J., & Lengsfeld, M. (2001). [Influence of cartilage cap modelling on FEM simulation of femoral head stress]. *Biomed Tech (Berl), 46*(1-2), 29-33.

Semelka, R. C. (2005). When Do I Need an MRI Study of My Body?: Cost and Weighing Other Imaging Alternatives. *Medscape Today* Retrieved May 1, 2010, from http://www.medscape.com/viewarticle/511853_3

Shaffer, E., & Garland, M. (2005). A multiresolution representation for massive meshes. *IEEE Trans Vis Comput Graph, 11*(2), 139-148.

Shepherd, D. E., & Seedhom, B. B. (1999). Thickness of human articular cartilage in joints of the lower limb. *Ann Rheum Dis, 58*(1), 27-34.

Siebenrock, K. A., Wahab, K. H., Werlen, S., Kalhor, M., Leunig, M., & Ganz, R. (2004). Abnormal extension of the femoral head epiphysis as a cause of cam impingement. *Clin Orthop Relat Res*(418), 54-60.

Sims, K. (1999). The development of hip osteoarthritis: implications for conservative management. *Manual Therapy, 4*(3), 127-135.

Skaggs, D. L., & Tolo, V. T. (1996). Legg-Calve-Perthes Disease. *J Am Acad Orthop Surg, 4*(1), 9-16.

Solomon, L. (1972). Pathogenesis of osteoarthritis. *Lancet, 1*(7759), 1072.

Speirs, A. D., Heller, M. O., Duda, G. N., & Taylor, W. R. (2007). Physiologically based boundary conditions in finite element modelling. *J Biomech, 40*(10), 2318-2323.

Standaert, C. J., Manner, P. A., & Herring, S. A. (2008). Expert opinion and controversies in musculoskeletal and sports medicine: femoroacetabular impingement. *Arch Phys Med Rehabil, 89*(5), 890-893.

Standring, S. (Ed.). (2008). *Gray's Anatomy - Anatomical Basis of Clinical Practice* (39th ed.). Maryland Heights: Elsevier Churchill Livingstone.

Stulberg, S., Cordell, L., Harris, W., Ramsey, P., & MacEwen, G. (1975). *Unrecognized childhood disease: A major cause of idiopathic osteoarthritis of the hip.* Paper presented at the Proceedings of the Third Open Scientific Meeting of The Hip Society, St. Louis, MO.

Taddei, F., Martelli, S., Reggiani, B., Cristofolini, L., & Viceconti, M. (2006). Finite-element modeling of bones from CT data: sensitivity to geometry and material uncertainties. *IEEE Trans Biomed Eng, 53*(11), 2194-2200.

Tannast, M., Kubiak-Langer, M., Langlotz, F., Puls, M., Murphy, S. B., & Siebenrock, K. A. (2007). Noninvasive three-dimensional assessment of femoroacetabular impingement. *J Orthop Res, 25*(1), 122-131.

Tannast, M., Siebenrock, K. A., & Anderson, S. E. (2007). Femoroacetabular impingement: radiographic diagnosis--what the radiologist should know. *AJR Am J Roentgenol, 188*(6), 1540-1552.

Taylor, W. R., Roland, E., Ploeg, H., Hertig, D., Klabunde, R., Warner, M. D., et al. (2002). Determination of orthotropic bone elastic constants using FEA and modal analysis. *J Biomech, 35*(6), 767-773.

Tepper, S., & Hochberg, M. C. (1993). Factors associated with hip osteoarthritis: data from the First National Health and Nutrition Examination Survey (NHANES-I). *Am J Epidemiol, 137*(10), 1081-1088.

Trabelsi, N., Yosibash, Z., & Milgrom, C. (2009). Validation of subject-specific automated p-FE analysis of the proximal femur. *J Biomech, 42*(3), 234-241.

Turner, C. H., Warden, S. J., Bellido, T., Plotkin, L. I., Kumar, N., Jasiuk, I., et al. (2009). Mechanobiology of the skeleton. *Sci Signal, 2*(68), pt3.

Ueo, T., Tsutsumi, S., Yamamuro, T., & Okumura, H. (1987). Biomechanical analysis of Perthes' disease using the finite element method: the role of swelling of articular cartilage. *Arch Orthop Trauma Surg, 106*(4), 202-208.

Unsworth, A., Dowson, D., & Wright, V. (1975). Some new evidence on human joint lubrication. *Ann Rheum Dis, 34*(4), 277-285.

Vahdati, A., & Rouhi, G. (2009). A model for mechanical adaptation of trabecular bone incorporating cellular accommodation and effects of microdamage and disuse. *Mech Res Comm, 36*(3), 284-293.

von Eisenhart-Rothe, R., Eckstein, F., Muller-Gerbl, M., Landgraf, J., Rock, C., & Putz, R. (1997). Direct comparison of contact areas, contact stress and subchondral mineralization in human hip joint specimens. *Anat Embryol (Berl), 195*(3), 279-288.

Walde, T. A., Weiland, D. E., Leung, S. B., Kitamura, N., Sychterz, C. J., Engh, C. A., Jr., et al. (2005). Comparison of CT, MRI, and radiographs in assessing pelvic osteolysis: a cadaveric study. *Clin Orthop Relat Res*(437), 138-144.

Wang, Y., Wei, H. W., Yu, T. C., & Cheng, C. K. (2007). Parametric analysis of the stress distribution on the articular cartilage and subchondral bone. *Biomed Mater Eng, 17*(4), 241-247.

Wei, H. W., Sun, S. S., Jao, S. H., Yeh, C. R., & Cheng, C. K. (2005). The influence of mechanical properties of subchondral plate, femoral head and neck on dynamic stress distribution of the articular cartilage. *Med Eng Phys, 27*(4), 295-304.

Wempner, G., & Talaslidis, D. (2003). *Mechanics of Solids and Shells*. New York: CRC Press.

Wirtz, D. C., Pandorf, T., Portheine, F., Radermacher, K., Schiffers, N., Prescher, A., et al. (2003). Concept and development of an orthotropic FE model of the proximal femur. *J Biomech, 36*(2), 289-293.

Wirtz, D. C., Schiffers, N., Pandorf, T., Radermacher, K., Weichert, D., & Forst, R. (2000). Critical evaluation of known bone material properties to realize anisotropic FE-simulation of the proximal femur. *J Biomech, 33*(10), 1325-1330.

Yokota, F., Okada, T., Takao, M., Sugano, N., Tada, Y., & Sato, Y. (2009). Automated segmentation of the femur and pelvis from 3D CT data of diseased hip using hierarchical statistical shape model of joint structure. *Med Image Comput Comput Assist Interv, 12*(Pt 2), 811-818.

Yosibash, Z., Tal, D., & Trabelsi, N. (2010). Predicting the yield of the proximal femur using high-order finite-element analysis with inhomogeneous orthotropic material properties. *Philos Transact A Math Phys Eng Sci, 368*(1920), 2707-2723.

Zienkiewicz, O. C., Taylor, R. L., & Zhu, J. Z. (2005). *The finite element method: its basis and fundamentals* (6th ed.). Oxford: Elsevier Butterworth-Heinemann.

Zoroofi, R. A., Sato, Y., Sasama, T., Nishii, T., Sugano, N., Yonenobu, K., et al. (2003). Automated segmentation of acetabulum and femoral head from 3-D CT images. *IEEE Trans Inf Technol Biomed, 7*(4), 329-343.

9.0 Appendix

9.1 Appendix A – Research Consent Form

uOttawa

L'Université canadienne
Canada's university

School of Human Kinetics
University of Ottawa

RESEARCH CONSENT FORM

Research Project Title:	**The Effect of Femoroacetabular Impingement on Hip Biomechanics during Level Walking, Sit-to-Stand, Stand-to-Sit and Maximal Squatting Depth**
	(Part II of Hip Reconstruction and Modeling for Surgical Pre-Operative Planning)
Principal Investigator:	**Dr. Mario Lamontagne xxx-xxx-xxxx ext xxxx**
Research assistant:	**Matthew Kennedy B.Sc. xxx-xxx-xxxx ext xxxx**

Before you give consent to be a research volunteer, please take time to read carefully and consider the following information which describes the purpose and procedures, the possible risks and benefits, and other information about the proposed research study. You are encouraged to discuss any questions with the research personnel.

Background and Purpose of the Study: You are being asked to participate in this pilot study because your surgeon believes that are a good candidate for the study.

One of the leading causes of hip arthritis is femoroacetabular impingement which means the hip joint is deformed such that the hip joint jams in the front when the hip is bent all the way forward. This can lead to significant damage to the hip joint and may result in the need for a total hip replacement. However, if detected early, this deformity can be treated surgically by reshaping the hip joint. If the hip joint could be better visualized before surgery, then surgeons would be able to develop less invasive surgical techniques to correct this deformity.

The imaging data of your hip taken at The Ottawa Hospital will be combined with the movement analysis from this part of the study, in order to develop a computer model of the hip which will aid in surgery. As well as helping with surgical treatment, the information from this portion of the study will be useful in finding out how femoroacetabular impingement affects movement. This information will help clinicians know what to look for in order to diagnose this condition as early as possible, and will help in developing rehabilitation strategies.

Description of Study Procedures: Approximately 20 participants will take part in this study: 15 patients and 5 healthy volunteers. If you consent to participate in this portion of the study at the University of Ottawa biomechanics lab, you will be asked to wear a head band, two wrist bands, tight short sleeved shirt and tight shorts with reflective markers on them. A researcher will also put 14 extra reflective markers, on your legs, feet and arms. Finally, after some skin preparation (shave off small portions of hair, and wipe with alcohol swab), the researcher will put some sensors on your legs which are used to read the electrical stimuli produced by your muscles.

You will then be asked to perform a maximal dynamic range of motion session, consisting of you standing upright and holding onto a support frame while you swing your leg in 4 different directions. Following this, you will be asked to perform 5 trials of walking down a level walkway, rising from a stool and sitting back down, and performing a squat above a height adjustable stool. For the squat, you will be asked to sit on the stool, and its height will be adjusted to the point where your knees are at a 60 degree angle. After this, you will be asked to squat down as deep as you successfully can before your buttocks touch the seat, and rise back to a standing position.

Possible Risks and Discomforts: The t-shirt and shorts which you will be asked to wear are skin tight, and may make you feel uncomfortable. You will also have small portions of your legs shaved (if covered in hair), and wiped down with an alcohol swab, to allow for the sensors to accurately pick up the electrical signals produced by your muscles. If you are allergic to rubbing alcohol, the area can be wiped clean with water and cloth. There is a possibility that you may experience mild skin irritation from the tape used to attach reflective markers and electrodes or the gel used to moisten the electrodes. This potential irritation is similar to that caused by a bandage, and typically fades quickly. The movements which you will be asked to perform have no more risks than most common daily activities.

Possible Benefits: You may not benefit directly from participating in this study. The results of this study will greatly add to our knowledge in the area of femoroacetabular impingement and may benefit patients and physicians in the future.

Voluntary Participation: You are not obliged to participate in this study; participation in this study is voluntary. As with the first part of the study, the quality of medical care you receive now or in the future will not be affected by whether or not you choose to participate. You may also withdraw from the study at any time, without affecting your care now or in the future at this institution.

Confidentiality: Records of your participation in this study will be kept confidential. All documents will be identified only by code number (which includes your initials) and will be kept in a locked filing cabinet at the University of Ottawa biomechanics lab. The data will kept for a maximum of 25 years before being destroyed. You will not be identified by name in any reports of the completed study. However, The University of Ottawa Health Sciences and Science Research Ethics Board may review data from your relevant records for audit purposes. No records bearing your name or birth date will leave the University of Ottawa. The information from this study may be used in a future study, and may be used for a Master's thesis. All investigators mentioned at the bottom of this consent form will have access to the data collected from this study.

Compensation: Your parking costs for this visit will be paid.

Questions About The Study: If you have any questions regarding your participation in this study, you can contact the research coordinator or the principal investigators.

The University of Ottawa Health Sciences and Science Research Ethics Board have approved this protocol. This committee considers ethical aspects of all research projects. If I have any questions with regards to the ethical conduct of this research, I may contact the **Protocol Officer for Ethics in Research, tel.: (xxx) xxx-xxxx, email : xxx.**

Consent:
I have read this 3-page Consent Form (or have had this read to me) and have had an opportunity to ask the research personnel any questions I had about the study.

My questions and/or concerns have been answered to my satisfaction and I agree to participate in this study. I am aware of the risks and benefits of participating. I may withdraw at any time without compromising my care.

Records relating to me and my care will be kept confidential and no information will be released or printed that would disclose my personal identity without my permission. I have been given sufficient time to read and understand the above information. There are two copies of this consent form, one of which is mine to keep.

If at any time during this study I wish to withdraw I would like the data already gathered to be:

Destroyed ☐ (Please check one box) Used if Useful ☐

I hereby consent to participate.

____
Name of Patient (printed)

____________________________ ____________________
Signature of Patient Date

____
Name of Investigator/Delegate (printed)

____________________________ ____________________
Signature of Investigator/Delegate Date

9.2 Appendix B – Biomechanics Data

Table 9.1: Subject list and clinical assessment for cam FAI patients and control subjects

Subject	Affected Leg	Gender	Age (yrs)	Weight (kg)	Height (cm)	BMI (kg/m^2)	α (°)	Clinical Assessment	Label
14_NG_FAI	Left	Male	44	72.7	177.7	23.0	> 80 axial	Extreme Cam	FAI 1
18_LD_FAI	Left	Male	29	74.9	182	22.6	> 70 axial > 80 radial	Extreme Cam	FAI 2
27_GM_Cont	Left	Male	54	67.4	169	23.6	< 50 axial	Control	Control 1
29_JD_Cont	Left	Male	36	67.9	163.5	25.4	< 40 axial	Control	Control 2
2_MH_FAI	Left	Female	47	55.8	163.5	20.9	> 40 axial > 70 radial	Mild Cam	Pilot

The kinematics motion data is reported in degrees with reference to the left hip. A positive value for motion in the sagittal plane indicates hip flexion (negative value suggests hip extension); positive value for motion in the frontal plane indicates hip adduction; positive value for motion in the transverse plane indicates hip internal hip rotation.

The force magnitudes are reported as a normalized reaction vector, broken down in three components: (1) posterior direction, (2) medial to the left leg, and (3) superior direction. The reaction magnitudes are reported in N/kg, thus independent of the subject's BW. The hip motions are also normalized with the hip cycle and broken down in three planes: (1) sagittal, (2) frontal, and (3) transverse.

9.2.1 Hip Forces

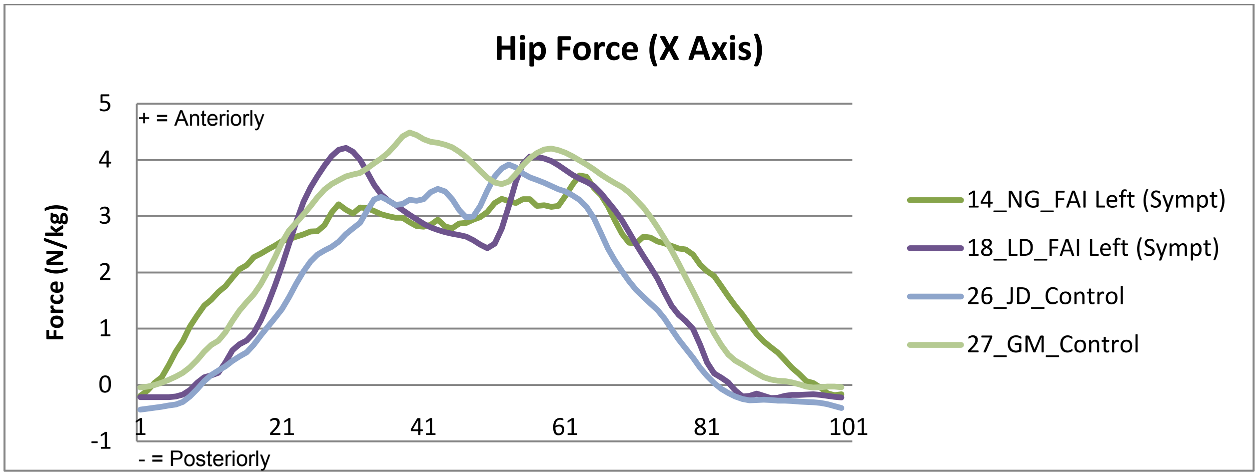

Figure 9.1: Force in the anterior-posterior direction of each subject's left hip

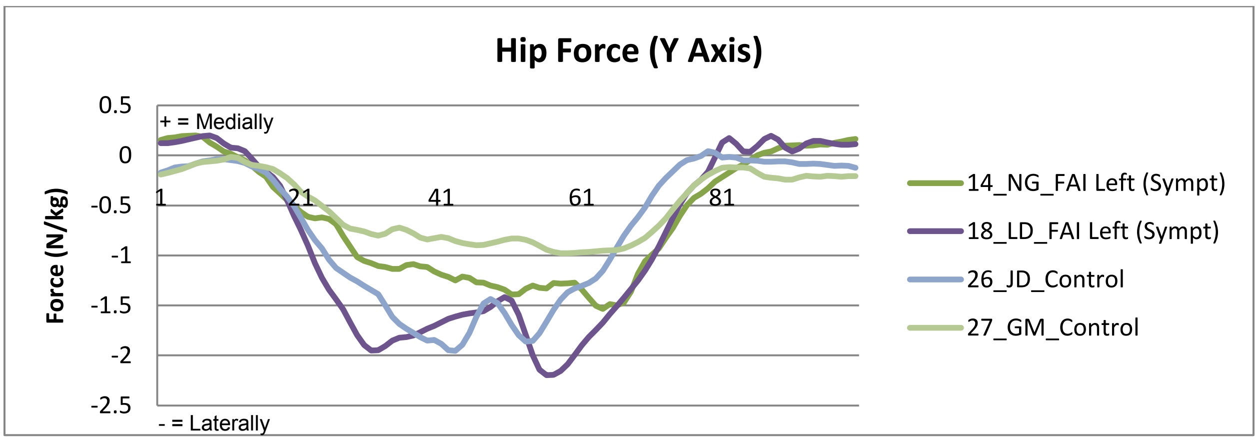

Figure 9.2: Force in the medial-lateral direction of each subject's left hip

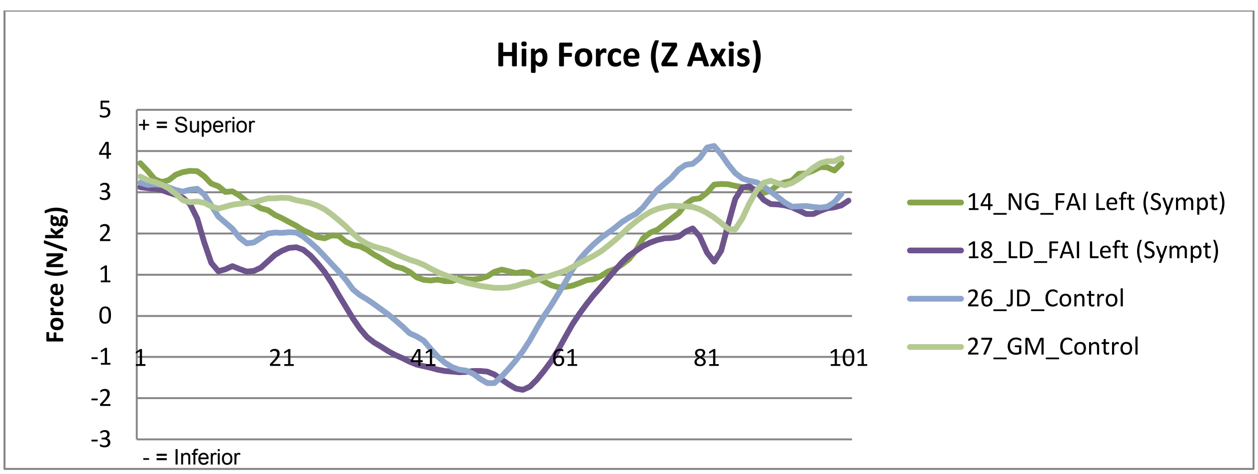

Figure 9.3: Force in the superior-inferior direction of each subject's left hip

9.2.2 Hip Motions

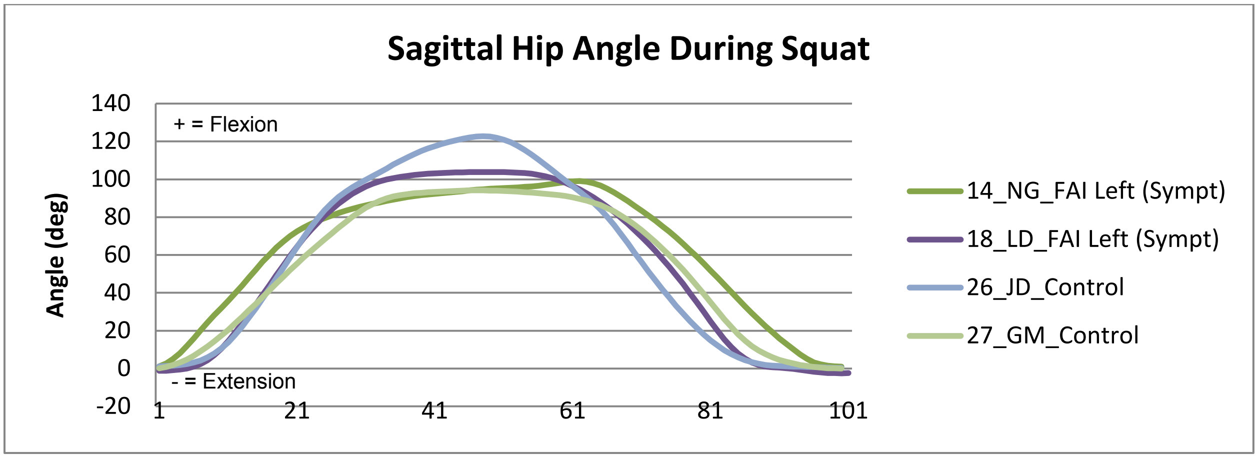

Figure 9.4: Sagittal hip flexion cycle of each subject's left hip

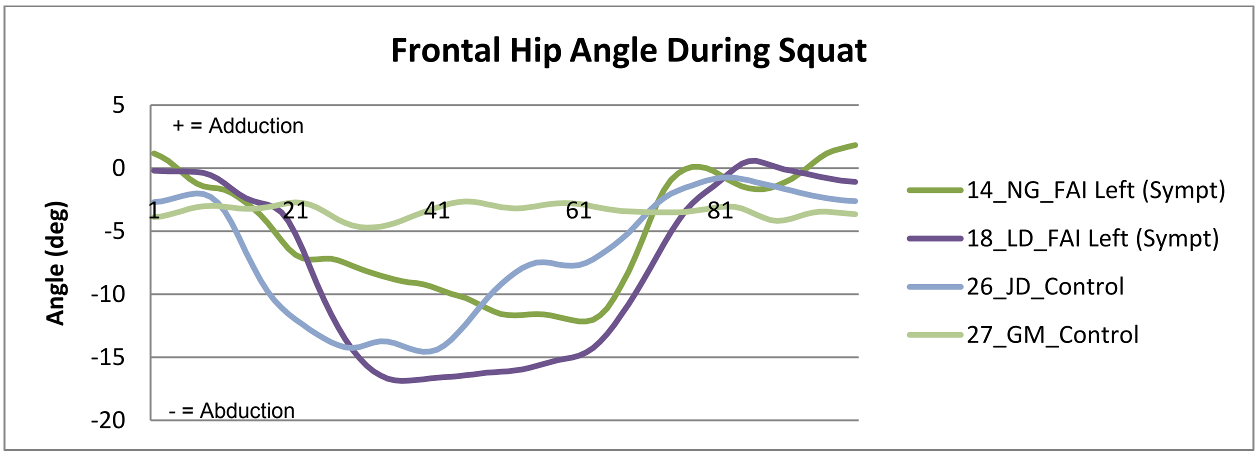

Figure 9.5: Frontal hip abduction cycle of each subject's left hip

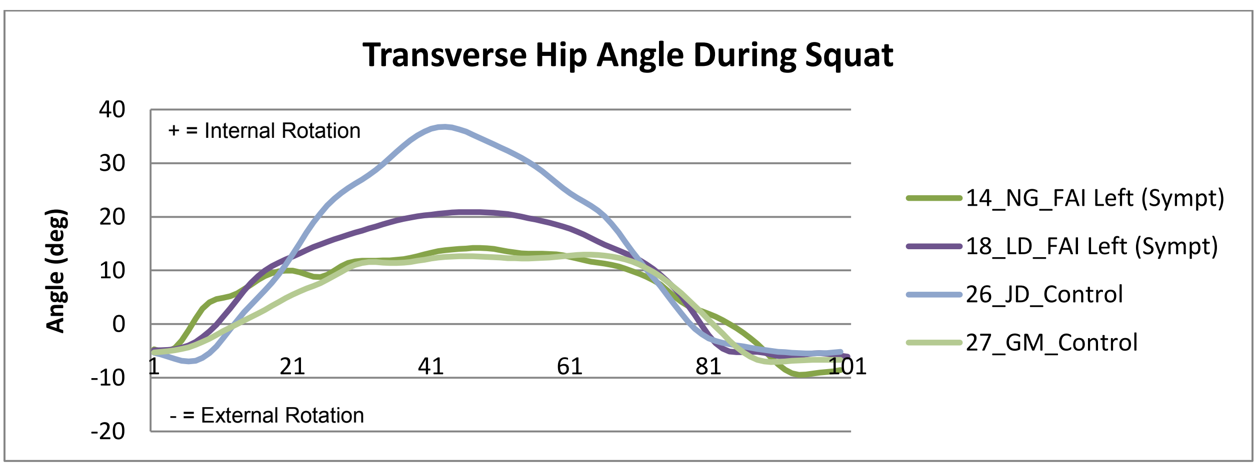

Figure 9.6: Transverse hip internal rotation of each subject's left hip

9.3 Appendix C – Segmentation Procedure

CT segmentation was performed using 3D-Doctor 4.0 (Able Software Corp., MA, USA). DICOM sets were imported using the "Create 3D Image Stack" command (Figure 9.7). The whole series of image files were included using the "Add Files" button. The "Split Image Series" box was checked to ensure that any DICOM sets that were labelled for a different series, but still for the same subject, be separated accordingly.

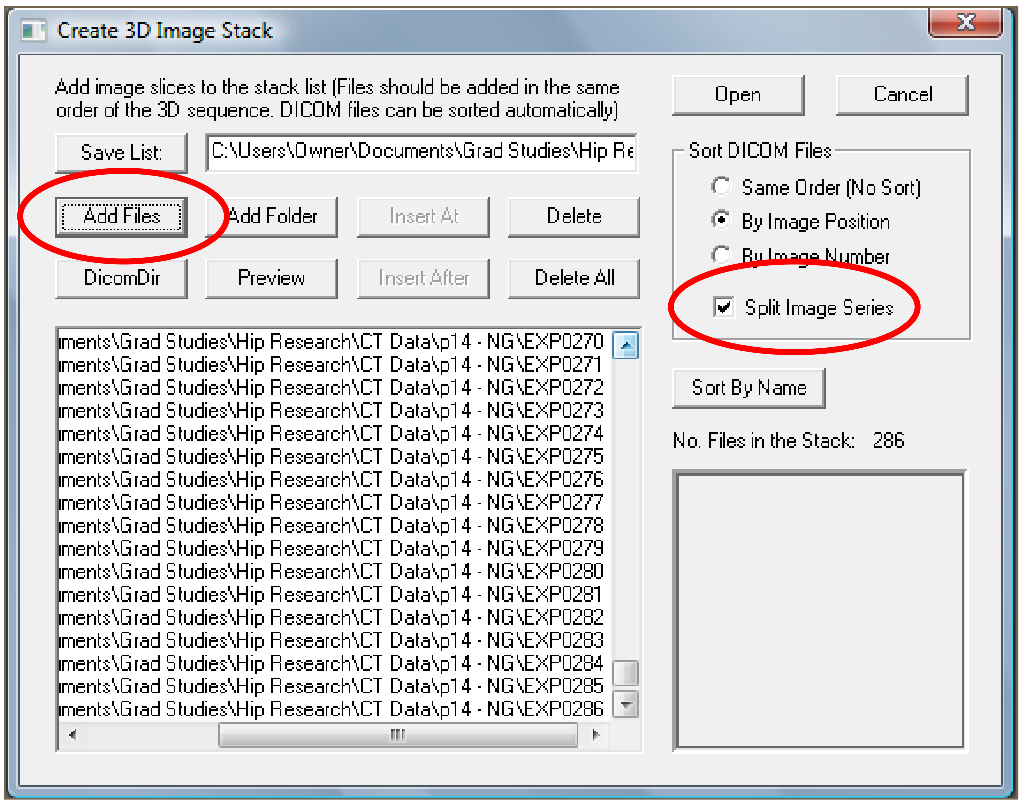

Figure 9.7: The "Create 3D Image Stack" command where the DICOM sets, containing the CT data, were imported into 3D-Doctor. The "Split Image Series" separates the stacks into different series according to the labelled properties (i.e. Dunn view A-P or axial oblique S-I slices).

The correct image sets were selected from the subsequent "Select DICOM Image Series" window (Figure 9.8). The number of images per set provided indication of the type of view. The lower number of images for a series (e.g. 2 images) suggested an A-P Dunn view of the patient, while a higher number (e.g. 142 images) suggested an axial oblique S-I view of the patient. With the desired series selected, the image stacks were viewed by clicking the "Get Series" button.

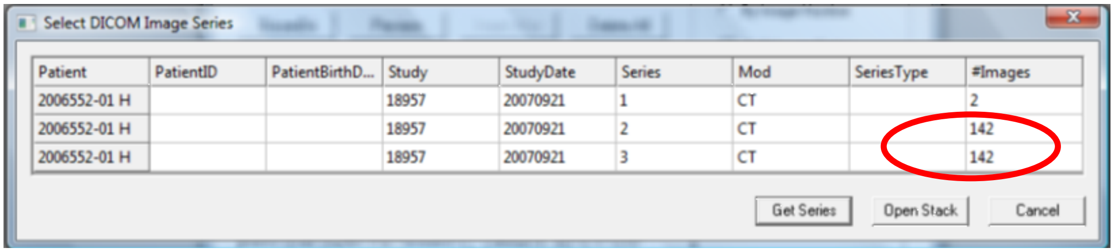

Figure 9.8: The "Select DICOM Image Series" window, where the appropriate series for viewing.

After the series was opened, the layout displayed a single slice of the stack on the left side and a montage of the compiled series of image stacks on the right side (Figure 9.9). The slices were reviewed to ensure continuity. Right-clicking on the image, in the left view pane, brought up a list of quick options to select from. By selecting the "Calibrations" options, the "Image Calibration Parameters" were displayed in a separate window (Figure 9.10). The "Image Calibration Parameters" provided information pertaining to the dimension (height and width) of the voxel as well as the thickness of the slices. Changing the default values of the slice thickness may compress or lengthen the height of the final 3-D output, thus distorting the structure.

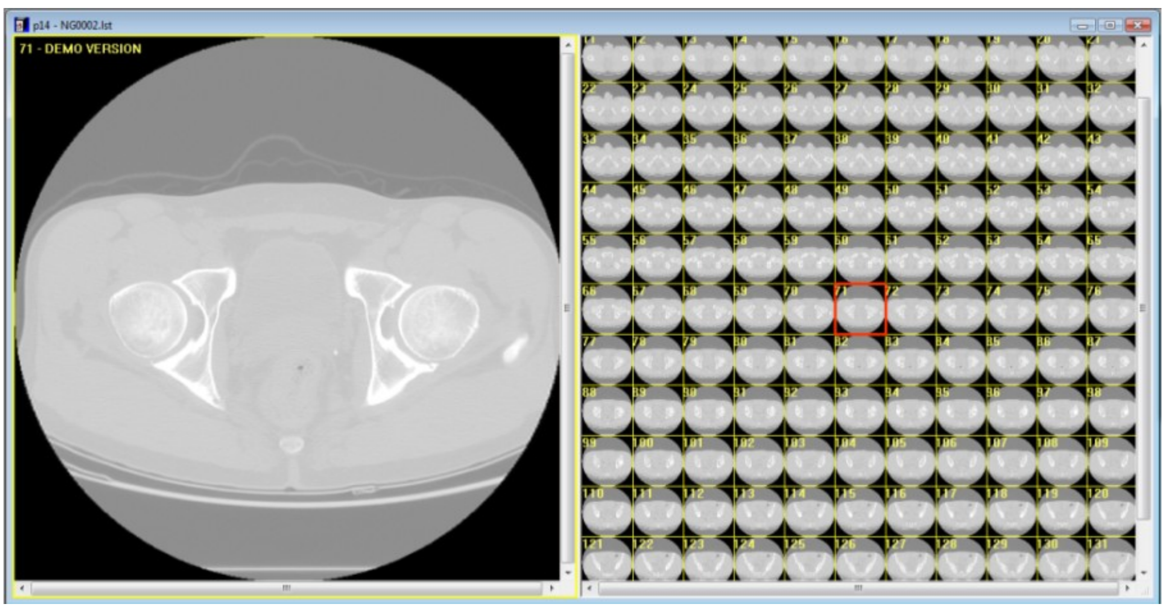

Figure 9.9: The layout of the DICOM series with the image of a single slice on the left and a montage view of the entire series on the right. Slice 71 is currently viewed in the single image view and is highlighted in the montage view.

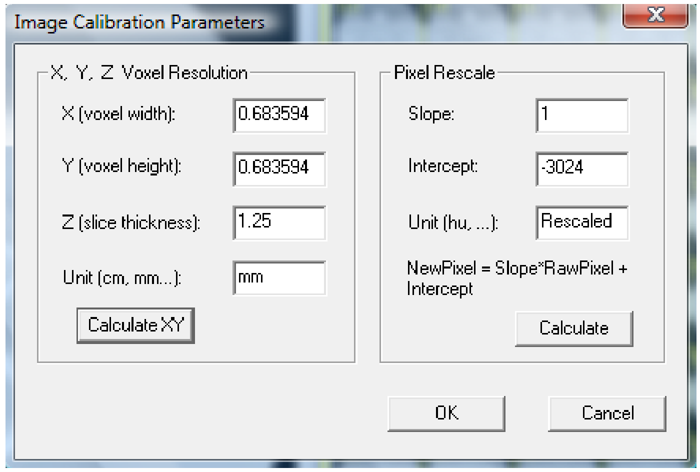

Figure 9.10: The "Image Calibration Parameters" window displaying information pertaining to the dimensions of the voxels (measured in mm) in the Cartesian XY and Z thickness plane.

Prior to segmenting the objects, the contrast of the images were adjusted to prevent contour artefacts and to limit extraneous segmentation of nearby objects. The desired objects to segment were the innominate structures of the femur and the pelvis. Hounsfield units (HU) were calibrated and set at the time of CT acquisition, thus were not adjusted during the CT segmentation process. Both the femur and pelvis, being hard tissues with similar densities, were the objects of focus. The contrast scale was adjusted to account for the hard tissues (Figure 9.11).

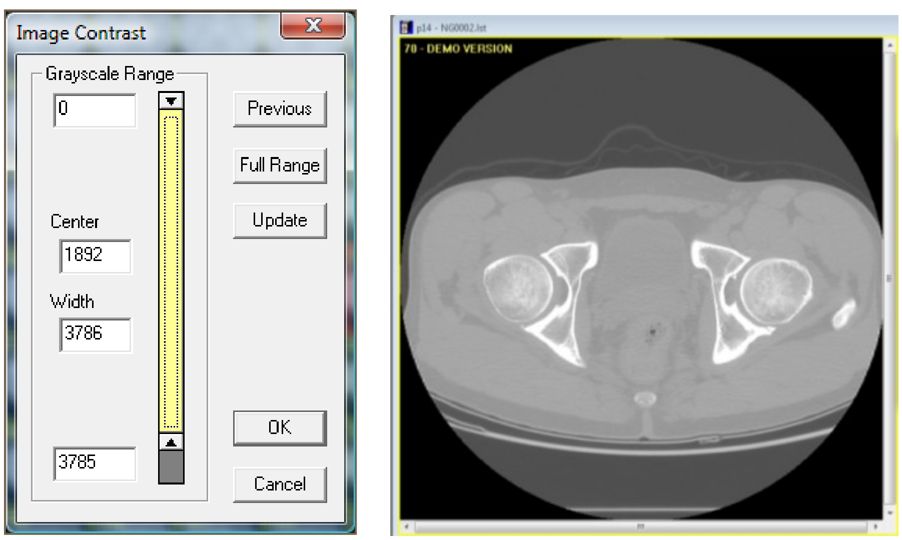

Figure 9.11: The image contrast level set at the default level prior to a square-root scale adjustment and limiting the upper threshold. The image depicts the patient in the supine position, the brighter objects represent the femur and pelvis region; however, much of the other objects remain in view and may cause problems during object definition and segmentation.

A square-root scale was used to limit the upper threshold of the grayscale range (Figure 9.12). By lowering the upper threshold and limiting the overall range, much of the other soft tissues become less visible, bringing the femur and the pelvis structures into focus for segmentation.

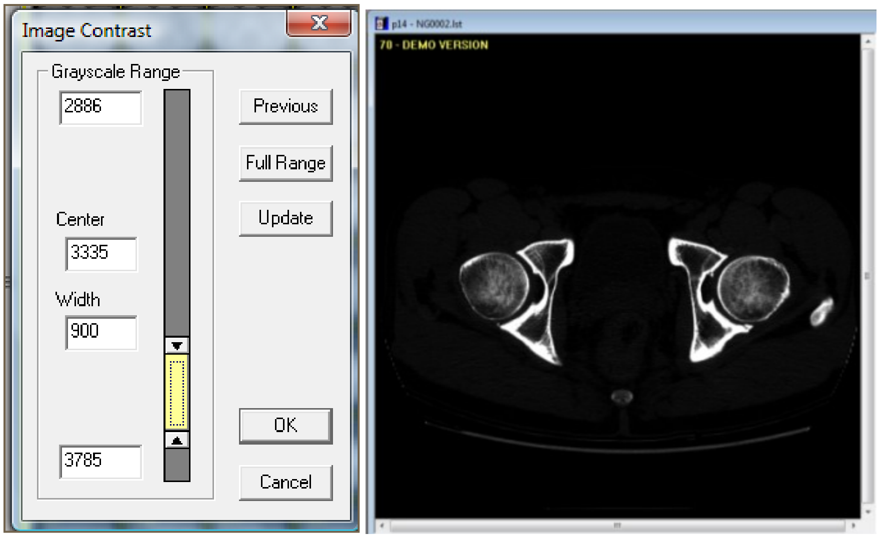

Figure 9.12: Adjusted contrast scale with a range of 900 to isolate the hard tissues.

Separate objects were needed to define and identify the femur and acetabulum. The “Set Object” command was used to manage and define objects (Figure 9.13). With two defined objects, the femur and acetabular, two resultant objects were identified and segmented in the view panes.

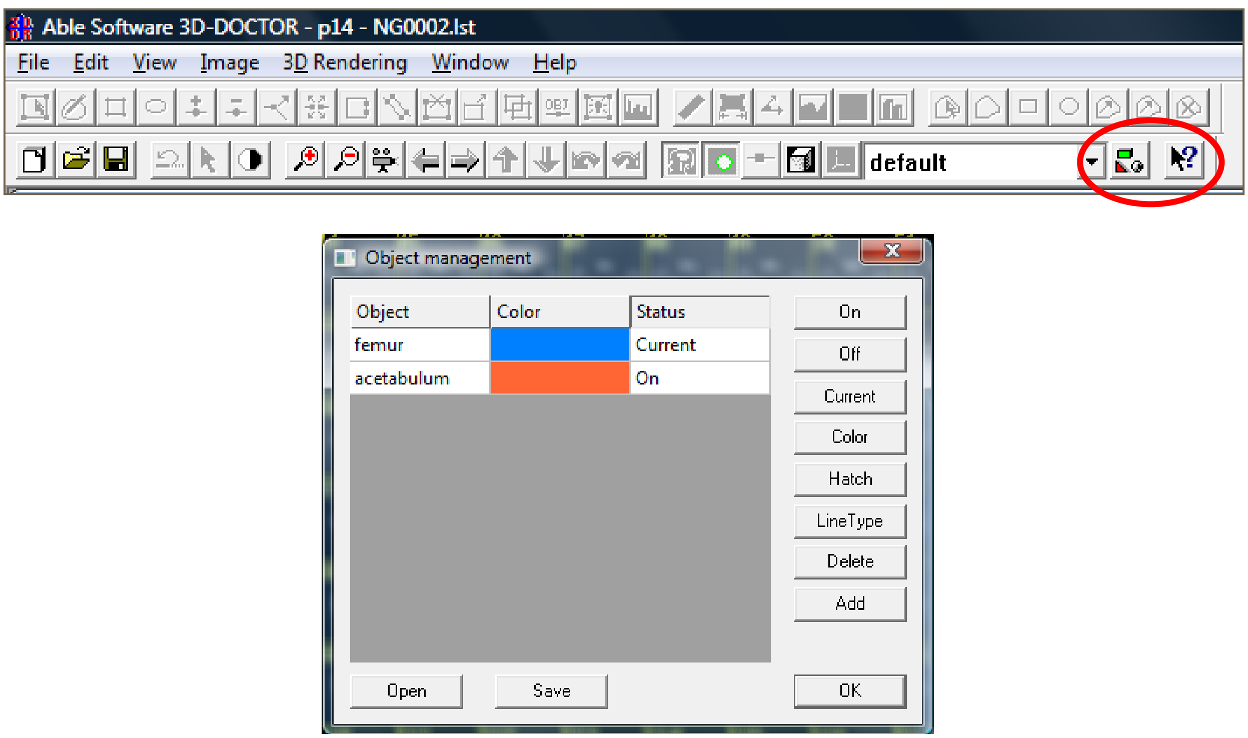

Figure 9.13: The “Set Object” command (top) brings the “Object Management” window (bottom) to define and identify separate objects within the view pane. The objects defined in this case are the femur (blue) and the acetabulum (orange).

A region of interest (ROI) was then defined around the left hip (femur and pelvis) by selecting the ROI tool and confining a boundary around the left hip (Figure 9.14). During the segmentation process, no objects outside this ROI was identified and segmented. Thus, by creating a ROI around the left hip region, only detected objects within the constrained ROI was defined and segmented. The boundary must be within bounds to account for the innominate structure on every slice.

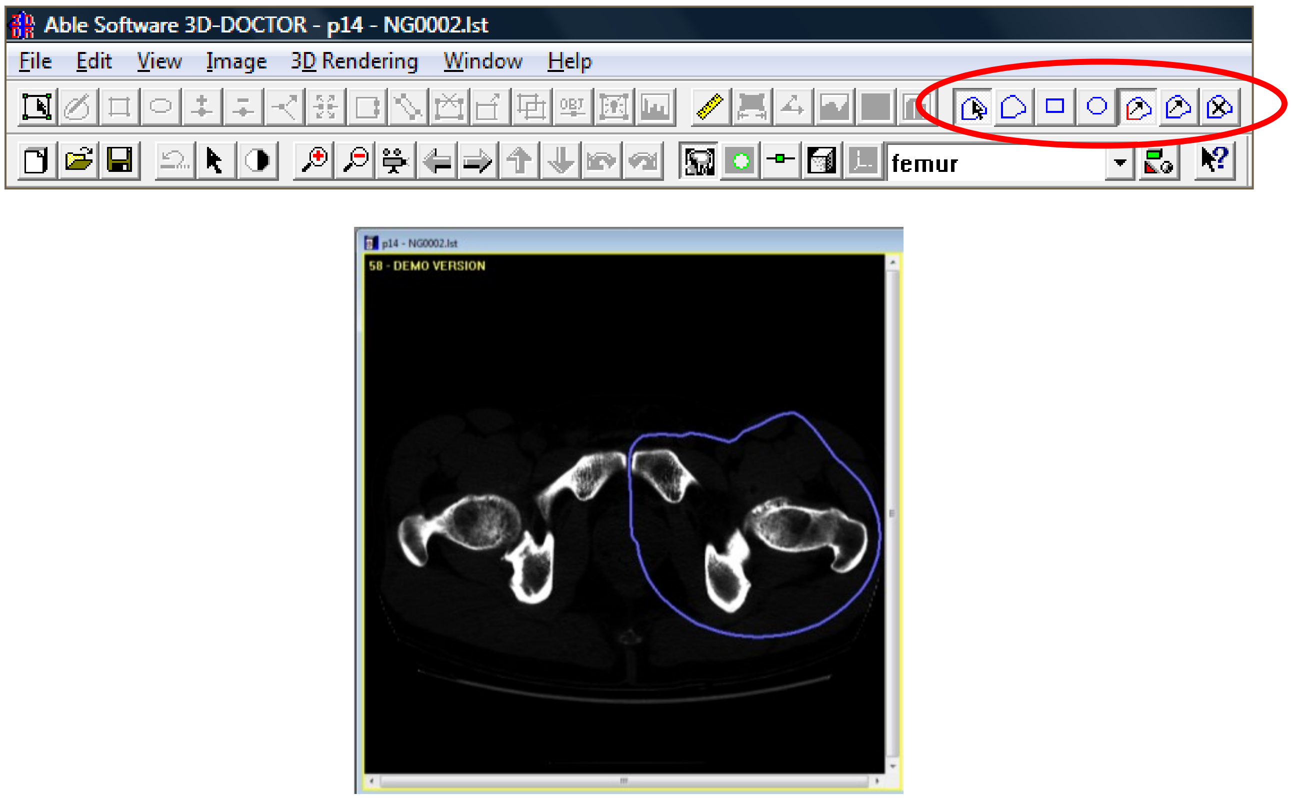

Figure 9.14: The ROI tool (top) provides an option to create boundaries around the left hip region (the symptomatic hip in focus). Only objects within the ROI (bottom), outlined in blue, is defined and segmented.

The segmentation process was accessed through the drop-down menu or by right-clicking the image view pane. The "Interactive Segmentation" window provided contrast thresholds for segmentation (Figure 9.15). Initially, all the planes in the entire series were automatically segmented using the "Segment All" method, within the ROI boundary, using an automated edge-detection segmentation method. This method detected the contour of the dense cortical bone structure, characterizing the geometry of the volume. The issue with this "Segment All" method was that all the detectable objects within the ROI were first defined as a single object. Thus, if the selected object to segment was the femur, the software recognized anything with similar resolution and visual contrast as a femur (i.e. pelvis and femur were defined as the femur). Moreover, as the femoral head approached the acetabulum in some image slices, the software assumed that the structure was connected, thus identified the femur and the pelvis as a single linked object in several of the image slices (Figure 9.16).

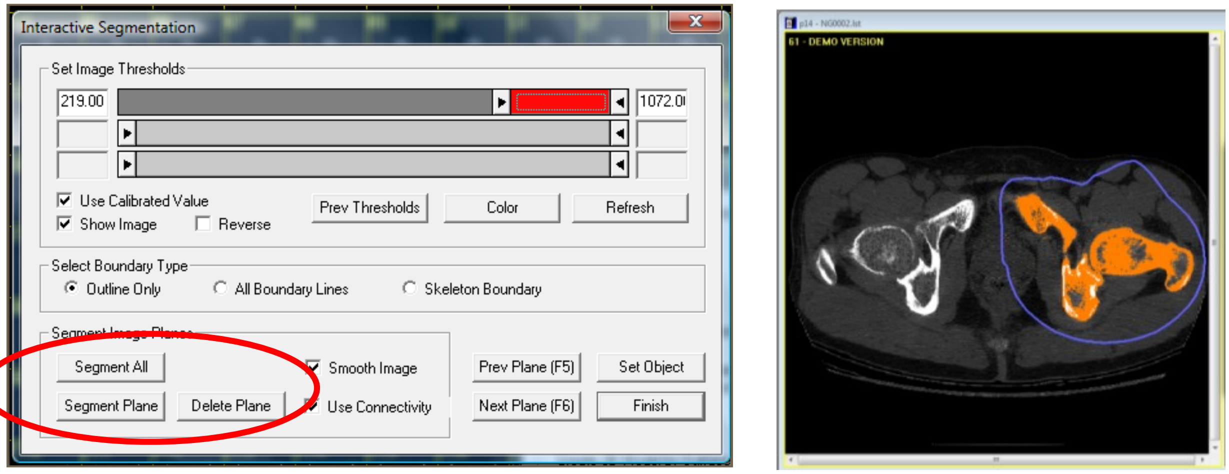

Figure 9.15: The "Interactive Segmentation" window (left) provides the options to set image thresholds and to segment all of the planes or a selection of the planes, as seen in the image view pane (right).

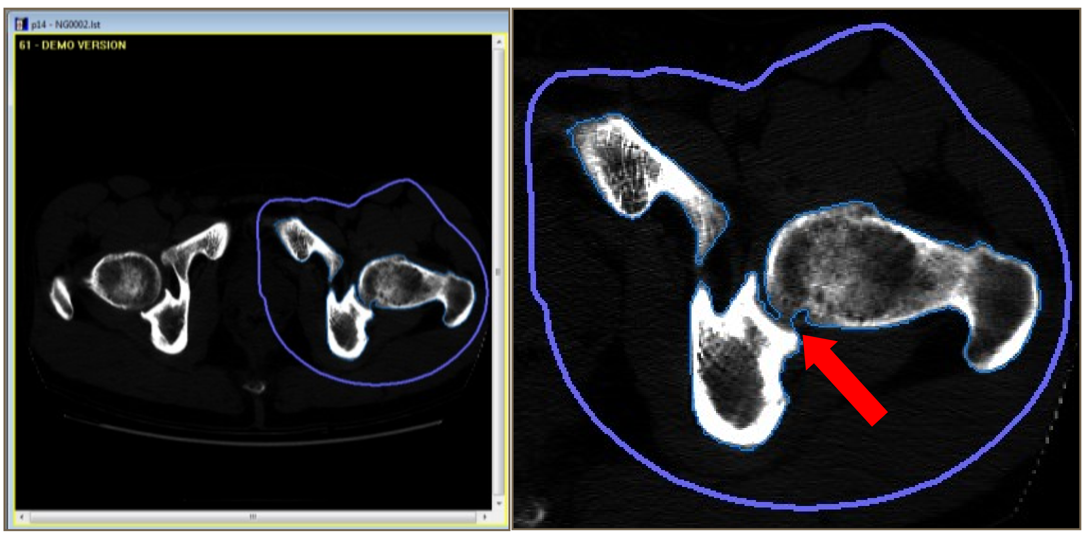

Figure 9.16: The automated "Segment All" feature defines a single object and segments every slice. In many of the slices, where the femoral head is in proximity with the acetabular structure, the software links both components and defines them as a single object (as indicated by the arrow).

The "Boundary Editor" command was selected to break the connections between the femoral head and the acetabulum to manually separate the linked objects (Figure 9.17). The "Split Boundary" command, from the editor toolbar, separated the linked object into two separate entities (femur and pelvis). The "Set Object" command allowed the two separate objects to be re-identified as respective femur and pelvis objects. Additional nodes were manually added to the each of the, now, two separate objects to provide a more accurate contour.

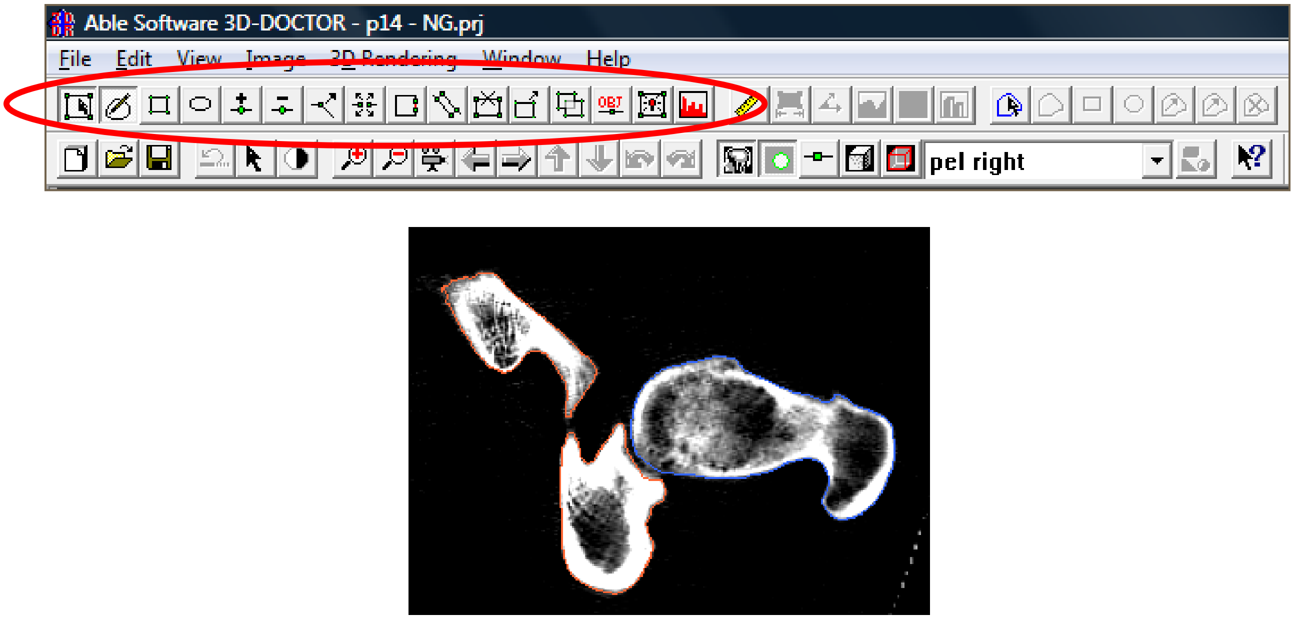

Figure 9.17: The “Boundary Editor” tools allow for manually adjusting the contours that were initially set by the automated edge-detection method. The “Split Boundary” command first breaks the linked objects into two separate objects. The “Set Object” command allows the two objects to be redefined to respective identities of femur and pelvis.

The whole series of image stacks were verified to ensure continuity and the correct object boundaries were defined on each plane. On the slices where the femoral head was in proximity to the acetabulum, the object boundary for the femoral head was manually segmented and defined to ensure that the correct contour of the cam deformity could be well represented (Figure 9.18). Additional nodes were added to contours on any slice that lacked geometric accuracy and conformance to the objects’ edges. The objects, as defined by the contouring boundaries, were then segmented as 3-D volumes.

Figure 9.18: Each slice was verified to ascertain the accuracy and precision of the boundaries. For the slices where the femoral head was in close proximity to the acetabulum, additional nodes were added to the contours of the cam deformity so to manually form and ensure a more accurate representation.

To render the models into 3-D, the “Complex Surface” command was selected from the 3-D surface rendering options. The denseness of the triangular meshes was considered during the “Complex Surface Rendering” (Figure 9.19). The smaller the value of the denseness generated a higher number of triangular surface polygons, thus took longer for computational processing. The opposite parameters yielded a lower number of polygons, thus provided a more simplified geometry with a quick return rate. All subject models were generated with a denseness setting of 1-1-1 for the X-Y-Z surface polygons to yield a more accurate model and to limit contour artefacts. The final rendered output depicted the two separate, segmented objects (Figure 9.20).

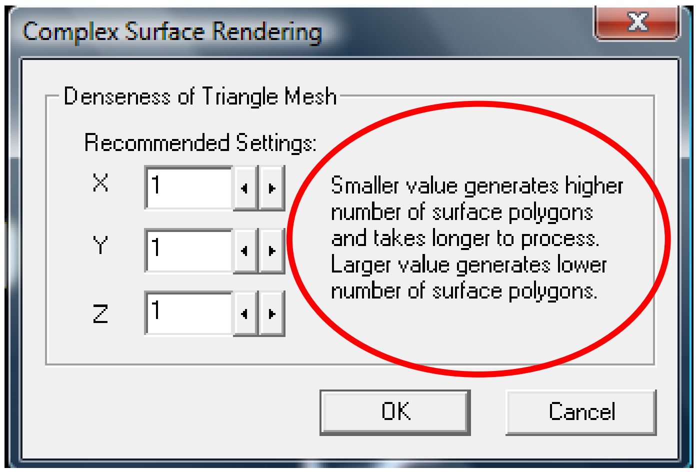

Figure 9.19: The "Complex Surface Rendering" command where the numbers of the triangular meshes were generated according to the denseness factor value of the surface polygons. A lower number generated more meshes, but took longer to process. A higher number generated less meshes, providing a simplified model with more geometric artefacts.

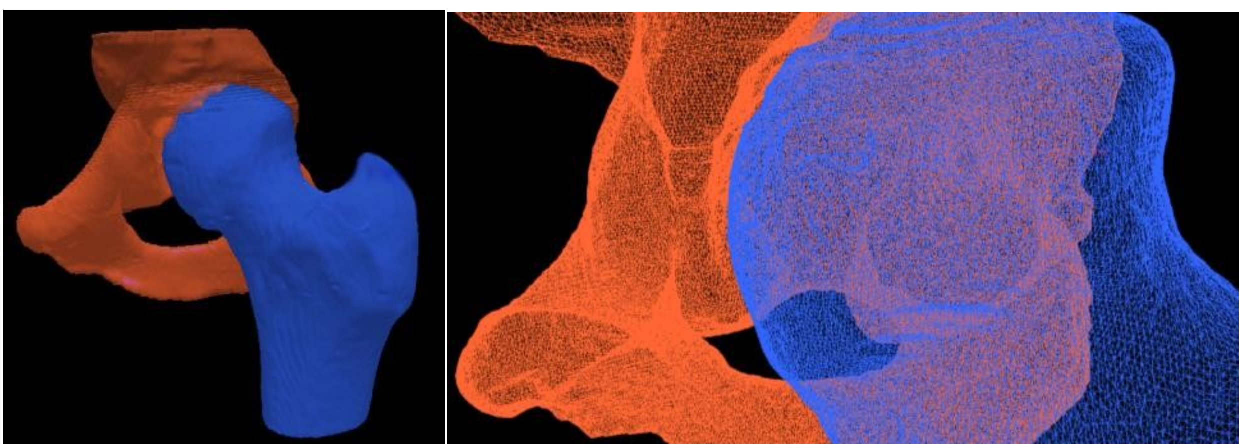

Figure 9.20: The final rendered output of the 3-D model (left) depicting the femur model (blue) and the separate pelvis model (orange). The denseness of the meshes limited the contour artefacts (right).

The slices were overlaid onto the models to provide a final verification of the alignment of the 3-D models (Figure 9.21) prior to exporting the models as STL files (Figure 9.22). Each of the two objects (the femur and the pelvis model) for all the subject models were each exported individually from 3D-Doctor as STL files.

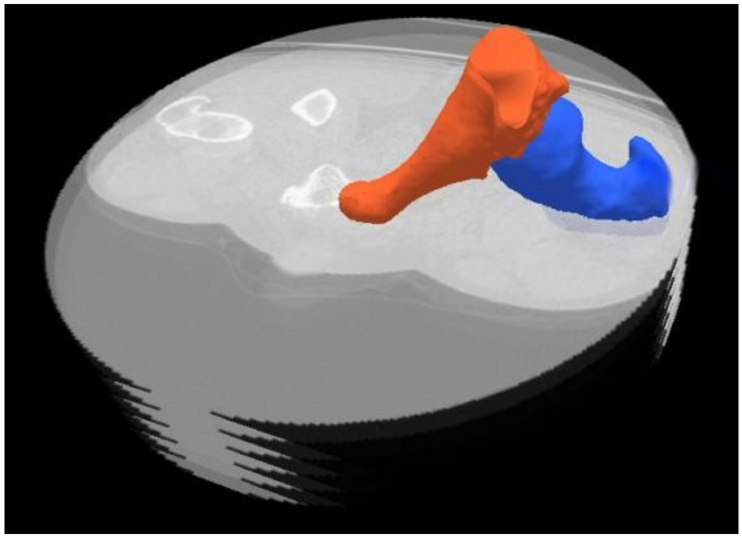

Figure 9.21: Overlaid image series of the DICOM stacks to ascertain relative alignment of the 3-D models with respect to the image series.

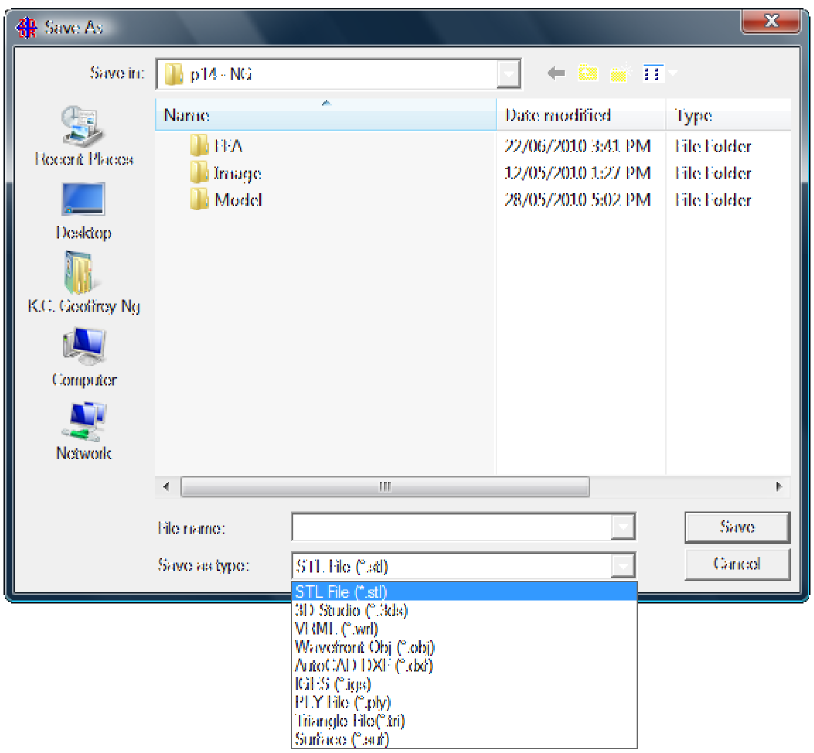

Figure 9.22: File options for exporting function. Each object from the 3-D model assemblies was exported individually from 3D-Doctor as STL files.

9.4 Appendix D – Alpha Angle and CE Angle Measurements

Figure 9.23: Alpha and CE angle measurements for FAI Patient 1 (14_NG_FAI). The alpha angle of the femoral head measured 83.217081° (left) and the CE angle of the acetabulum measured 30.26448° (right).

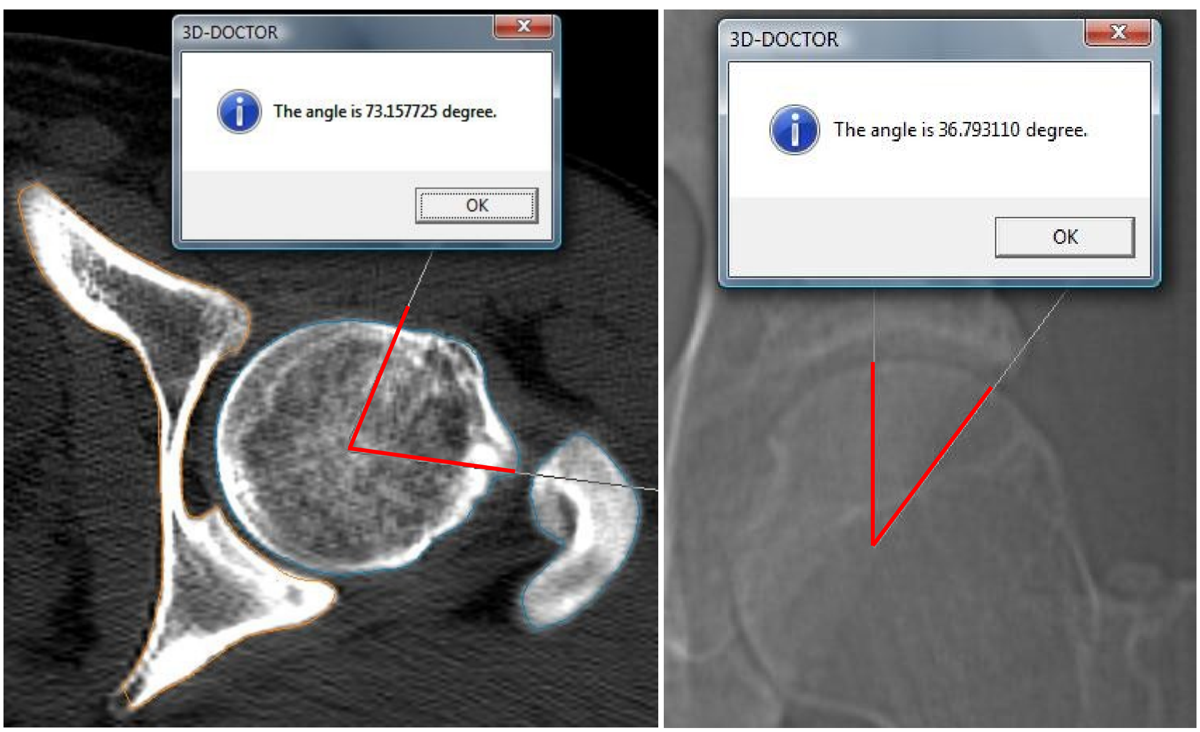

Figure 9.24: Alpha and CE angle measurements for FAI Patient 2 (18_LD_FAI). The alpha angle of the femoral head measured 73.17725° (left) and the CE angle of the acetabulum measured 36.793110° (right).

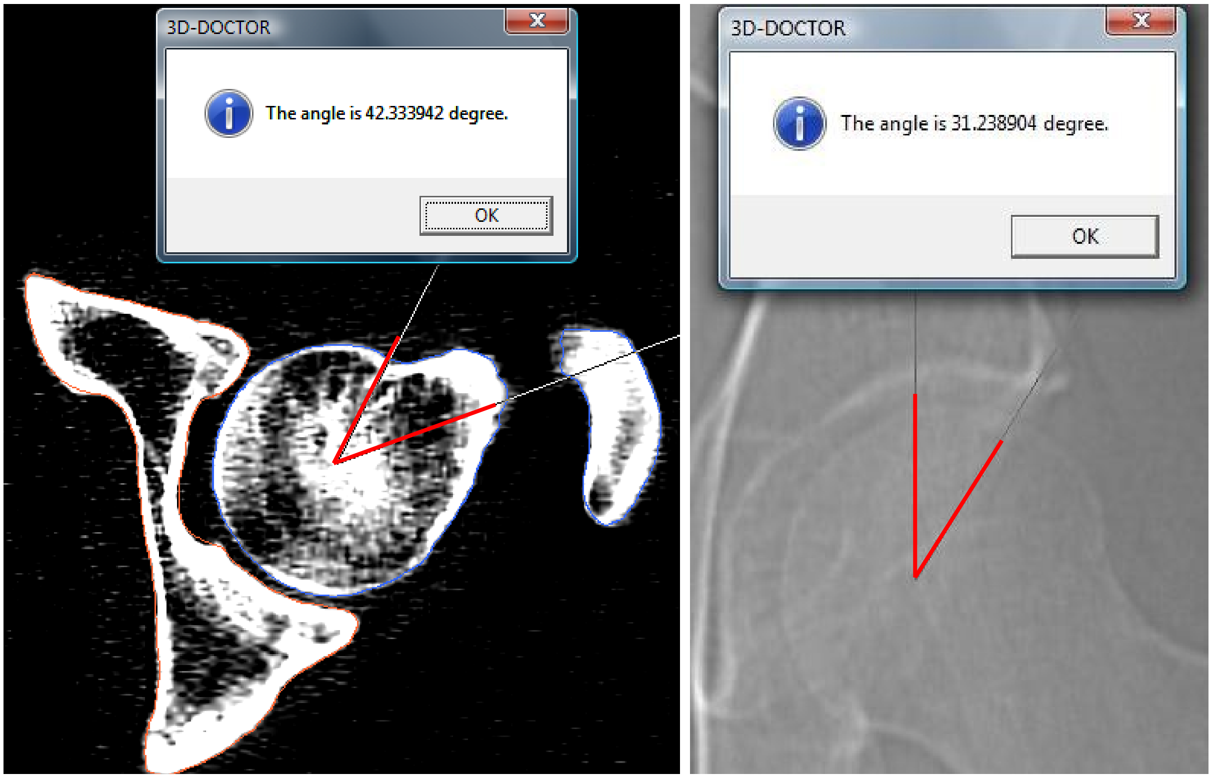

Figure 9.25: Alpha and CE angle measurements for Control Subject 1 (26_JD_Control). The alpha angle of the femoral head measured 42.333942 (left) and the CE angle of the acetabulum measured 31.238904^{o} (right).

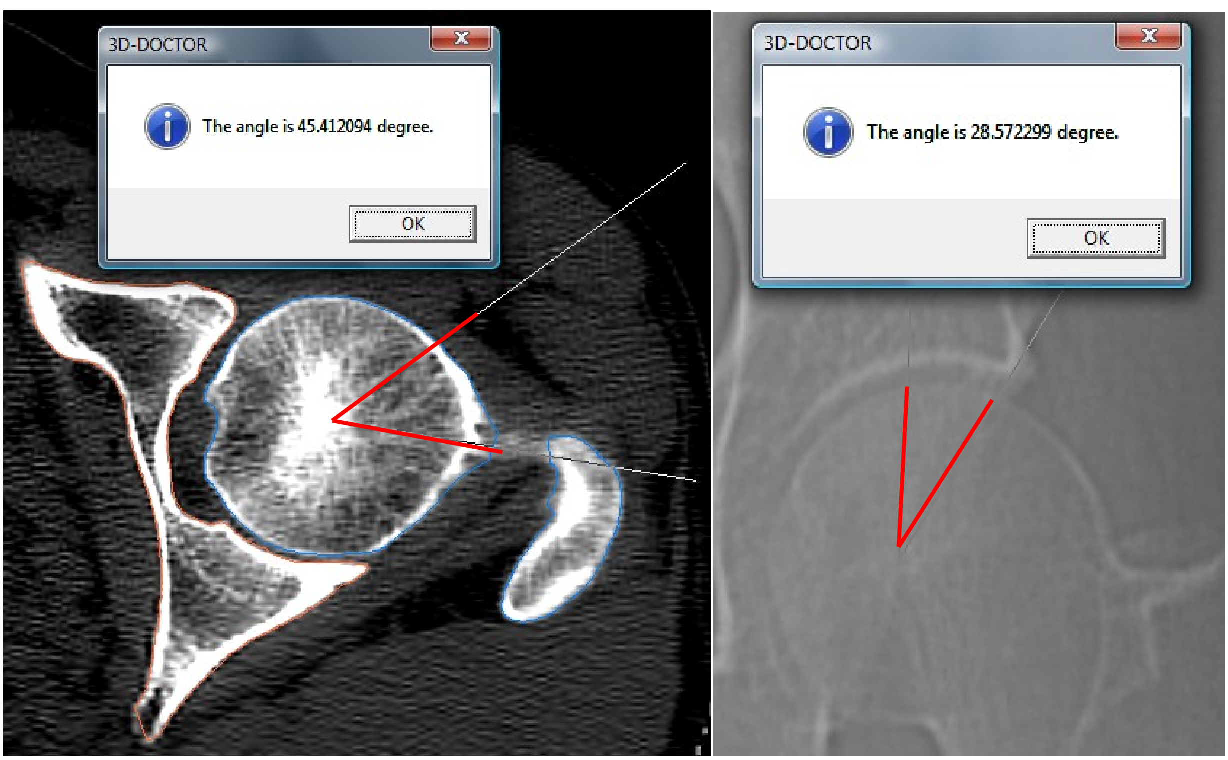

Figure 9.26: Alpha and CE angle measurements for Control Subject 2 (27_GM_Control). The alpha angle of the femoral head measured 83.412094^{o} (left) and the CE angle of the acetabulum measured 28.572299^{o} (right).

Table 9.2: Paired t-Test for Means Comparing the Methods to Measure the Alpha Angle

	Alpha Angle of Femoral Head from Axial CT Radiograph	Alpha Angle of Femoral Head Post-Resurfacing
Mean	61.03	61.485
Variance	411.0691333	458.8472333
Observations	4	4
Pearson Correlation R	0.99972447	
R square	0.999449016	
Hypothesized Mean Difference	0	
Degrees of Freedom	3	
t Stat	-0.730372206	
P(T<=t) one-tail	0.259015466	
t Critical one-tail	2.353363435	
P(T<=t) two-tail	0.518030932	
t Critical two-tail	3.182446305	

- Confidence interval of 95% (0.05)
- Reject if $t > t_{critical\ two\text{-}tail}$ or if $t < -t_{critical\ two\text{-}tail}$
- ∵ -0.730372206 ≮ -3.182446305
- ∴ Cannot reject hypothesized mean
- ∴ No significant difference

Table 9.3: Paired t-Test for Means Comparing the Methods to Measure the CE Angle

	CE Angle of Acetabulum from A-P Radiograph	CE Angle of Acetabulum Post-Resurfacing
Mean	31.715	31.8325
Variance	12.6631	15.06169167
Observations	4	4
Pearson Correlation R	0.99782264	
R Square	0.99565002	
Hypothesized Mean Difference	0	
Degrees of Freedom	3	
t Stat	-0.580129031	
P(T<=t) one-tail	0.301264162	
t Critical one-tail	2.353363435	
P(T<=t) two-tail	0.602528325	
t Critical two-tail	3.182446305	

- Confidence interval of 95% (0.05)
- Reject if $t > t_{critical\ two\text{-}tail}$ or if $t < -t_{critical\ two\text{-}tail}$
- ∵ -0.580129031 ≮ -3.182446305
- ∴ Cannot reject hypothesized mean
- ∴ No significant difference

9.5 Appendix E – Computational FEA Output

Table 9.4: Number of nodes and elements allocated to each component of each model assembly

Subject	Component	Nodes	Elements
FAI 1 (14_NG_FAI)	**Pelvis**	91580	60757
	Cartilage	46627	26547
	Femur	69964	48446
FAI 2 (18_LD_FAI)	**Pelvis**	105960	69903
	Cartilage	64666	38167
	Femur	71385	49447
Control 1 (26_JD_Control)	**Pelvis**	104494	69469
	Cartilage	58684	33658
	Femur	56750	39047
Control 2 (27_GM_Control)	**Pelvis**	115940	76242
	Cartilage	60934	35266
	Femur	58759	40706

9.5.1 Location of Peak Maximum-shear Stresses for FAI Patient 1

Table 9.5: Location of peak maximum-shear stresses of FAI Patient 1's cartilage during stance

ANSYS Node Number	X Location (mm)	Y Location (mm)	Z Location (mm)	Maximum Shear Stress (MPa)
5637	99.35	7.6208	29.541	*3.703*
6217	99.97	7.3216	28.923	*3.443*
5635	99.286	7.9044	28.612	*3.207*
4116	100	8.0454	28.963	*2.768*
4151	99.139	6.7977	28.584	*2.608*
16682	99.701	7.4631	29.292	*2.595*
16664	99.945	8.0302	29.132	*2.416*
415	99.827	8.0187	29.261	*2.371*
33859	99.59	7.0619	28.609	*2.300*
16676	99.691	7.9772	28.652	*2.259*

Table 9.6: Location of peak maximum-shear stresses of FAI Patient 1's acetabulum during stance

ANSYS Node Number	X Location (mm)	Y Location (mm)	Z Location (mm)	Maximum Shear Stress (MPa)
50990	98.181	2.7372	29.274	*3.353*
102730	97.253	1.7291	29.247	*2.776*
46681	96.312	0.73485	29.184	*2.749*
127236	98.794	4.0603	29.489	*2.208*
55539	99.368	1.1452	28.512	*2.169*
102843	98.767	1.9514	28.86	*2.129*
113459	96.766	2.447	29.727	*1.922*
133530	95.823	1.4563	29.658	*1.785*
102837	99.228	-1.63E-02	28.135	*1.581*
127235	99.868	3.1808	29.041	*1.539*

Table 9.7: Location of peak maximum-shear stresses of FAI Patient 1's cartilage during squat

ANSYS Node Number	X Location (mm)	Y Location (mm)	Z Location (mm)	Maximum Shear Stress (MPa)
95711	86.784	-16.17	11.471	*3.853*
95370	77.151	-11.591	10.588	*3.671*
92076	86.64	-15.908	11.503	*3.392*
95349	77.34	-12.364	5.721	*3.331*
110978	77.506	-11.701	10.723	*3.303*
105618	86.729	-16.02	11.466	*3.130*
96619	77.863	-11.809	10.857	*3.005*
128998	77.089	-12.202	5.9451	*2.967*
97980	76.832	-12.05	6.17	*2.961*
95371	76.875	-11.769	8.9148	*2.941*

Table 9.8: Location of peak maximum-shear stresses of FAI Patient 1's acetabulum during squat

ANSYS Node Number	X Location (mm)	Y Location (mm)	Z Location (mm)	Maximum Shear Stress (MPa)
5091	99.374	-1.6346	27.477	*13.432*
7232	72.888	25.531	-2.6901	*10.146*
52557	99.06	-2.5701	27.153	*9.582*
52536	100.29	-1.8775	27.215	*9.441*
84832	73.662	26.412	-2.3076	*9.101*
11359	74.47	27.246	-1.8961	*8.995*
3676	101.06	-4.2373	26.157	*8.279*
26149	100.96	-1.0504	27.565	*8.191*
52554	98.182	-2.0687	27.593	*8.156*
24288	101.13	-3.1886	26.574	*8.083*

9.5.2 Location of Peak Maximum-shear Stresses for FAI Patient 2

Table 9.9: Location of peak maximum-shear stresses of FAI Patient 2's cartilage during stance

ANSYS Node Number	X Location (mm)	Y Location (mm)	Z Location (mm)	Maximum Shear Stress (MPa)
2574	95.047	38.998	15.737	*4.0538*
7226	95.399	38.91	16.363	*3.5152*
5080	92.26	39.688	13.299	*3.4227*
32508	94.898	39.15	16.553	*3.0546*
5101	92.625	39.487	12.867	*2.9815*
7233	94.398	39.392	16.742	*2.9785*
7254	97.978	37.469	22.389	*2.9536*
32477	95.225	38.955	16.049	*2.9118*
32483	94.722	39.195	16.24	*2.5613*
7235	96.847	38.323	19.579	*2.5135*

Table 9.10: Location of peak maximum-shear stresses of FAI Patient 2's acetabulum during stance

ANSYS Node Number	X Location (mm)	Y Location (mm)	Z Location (mm)	Maximum Shear Stress (MPa)
145556	97.752	30.322	31.739	*3.5638*
164875	97.373	31.037	31.015	*3.4601*
138012	96.997	31.768	30.305	*3.4295*
170572	98.538	29.811	32.156	*3.3195*
237507	96.27	32.024	30.211	*3.2474*
141928	99.322	29.294	32.566	*3.2400*
170574	98.67	30.245	31.651	*3.1823*
152690	96.521	30.651	31.738	*3.1631*
150588	95.546	32.292	30.128	*3.1504*
152375	97.358	29.767	32.558	*3.1362*

Table 9.11: Location of peak maximum-shear stresses of FAI Patient 2's cartilage during squat

ANSYS Node Number	X Location (mm)	Y Location (mm)	Z Location (mm)	Maximum Shear Stress (MPa)
114607	82.521	-13.483	17.852	*3.3405*
114611	84.216	-13.277	20.593	*3.2946*
154439	83.789	-13.286	20.214	*3.1047*
167511	84.862	-13.412	20.749	*3.0721*
109666	85.173	-12.01	21.124	*3.069*
109670	84.795	-12.969	19.71	*3.0512*
114608	83.362	-13.292	19.835	*2.9791*
114612	86.818	-13.318	22.593	*2.9604*
163890	84.638	-11.861	21.079	*2.9407*
107480	85.499	-13.572	20.915	*2.887*

Table 9.12: Location of peak maximum-shear stresses of FAI Patient 2's acetabulum during squat

ANSYS Node Number	X Location (mm)	Y Location (mm)	Z Location (mm)	Maximum Shear Stress (MPa)
2401	91.292	-13.622	25.369	*16.862*
150	85.389	-13.055	21.958	*13.744*
3999	91.36	-14.035	25.264	*12.06*
718	81.345	-12.258	21.033	*10.892*
4934	91.127	-13.253	25.527	*10.83*
34817	90.938	-13.53	25.118	*9.5654*
28918	91.064	-13.837	25.061	*9.2768*
66848	85.667	-12.693	22.988	*8.1412*
66851	84.869	-12.617	22.704	*7.8828*
28912	91.341	-13.824	25.308	*7.7862*

9.5.3 Location of Peak Maximum-shear Stresses for Control Subject 1

Table 9.13: Location of peak maximum-shear stresses of Control Subject 1's cartilage during stance

ANSYS Node Number	X Location (mm)	Y Location (mm)	Z Location (mm)	Maximum Shear Stress (MPa)
115385	67.836	-17.751	-42.755	*3.4468*
107294	65.957	-10.201	-35.711	*2.5751*
107270	66.02	-9.7851	-33.345	*2.4228*
60427	68.148	-11.626	-32.769	*2.3384*
65724	66.082	-10.218	-35.083	*2.3086*
56770	66.039	-9.9411	-33.894	*2.28*
65538	66.077	-10.093	-34.443	*2.1796*
65141	68.533	-11.57	-31.491	*2.1784*
64038	67.51	-10.811	-32.174	*2.168*
65667	72.946	4.8833	-16.782	*2.1666*

Table 9.14: Location of peak maximum-shear stresses of Control Subject 1's acetabulum during stance

ANSYS Node Number	X Location (mm)	Y Location (mm)	Z Location (mm)	Maximum Shear Stress (MPa)
123527	71.981	7.8044	-15.579	*3.4962*
171880	71.685	6.0893	-15.661	*3.1305*
123658	71.436	4.3701	-15.799	*3.0122*
171869	73.403	8.3319	-14.774	*2.968*
208819	72.323	9.5032	-15.557	*2.9646*
171879	70.865	7.5469	-16.18	*2.8738*
171865	73.222	6.2369	-14.751	*2.8465*
123672	74.832	8.858	-13.982	*2.8009*
123671	72.719	11.19	-15.621	*2.7033*
171871	74.649	6.7624	-13.946	*2.665*

Table 9.15: Location of peak maximum-shear stresses of Control Subject 1's cartilage during squat

ANSYS Node Number	X Location (mm)	Y Location (mm)	Z Location (mm)	Maximum Shear Stress (MPa)
65747	69.844	-12.326	-30.39	*4.0283*
65469	75.414	-15.243	-29.44	*3.9929*
59285	74.659	-14.664	-26.006	*3.943*
65455	76.181	-16.738	-27.651	*3.8807*
58748	74.797	-15.566	-27.444	*3.8254*
65330	71.096	-13.164	-30.172	*3.716*
80208	76.364	-16.536	-27.314	*3.6462*
64234	68.696	-11.636	-31.246	*3.5997*
114595	69.261	-11.992	-30.814	*3.5671*
59349	76.546	-16.334	-26.975	*3.507*

Table 9.16: Location of peak maximum-shear stresses of Control Subject 1's acetabulum during squat

ANSYS Node Number	X Location (mm)	Y Location (mm)	Z Location (mm)	Maximum Shear Stress (MPa)
119528	76.906	-16.383	-26.771	*4.5342*
127148	74.676	-16.819	-29.197	*4.477*
119526	77.74	-15.329	-25.016	*4.4126*
199384	77.333	-15.831	-25.913	*4.3621*
119541	79.568	-21.166	-23.626	*4.1763*
143356	78.772	-15.726	-25.031	*4.0602*
186389	78.848	-21.831	-22.218	*4.0594*
117792	15.684	-35.958	-53.528	*4.0452*
126510	78.119	-22.177	-20.716	*4.0221*
157623	76.429	-16.948	-27.61	*4.0128*

9.5.4 Location of Peak Maximum-shear Stresses for Control Subject 2

Table 9.17: Location of peak maximum-shear stresses of Control Subject 2’s cartilage during stance

ANSYS Node Number	X Location (mm)	Y Location (mm)	Z Location (mm)	Maximum Shear Stress (MPa)
63925	84.067	19.115	-8.2499	*2.0202*
66846	80.064	12.43	-13.344	*1.9382*
66893	79.541	11.18	-13.997	*1.9373*
93377	79.805	11.801	-13.665	*1.9364*
60604	85.962	20.877	-9.0137	*1.723*
99982	84.228	18.974	-8.5108	*1.7163*
63947	85.031	20.051	-6.9767	*1.7076*
63067	86.225	21.627	-7.7865	*1.6603*
92295	85.734	20.676	-9.2036	*1.6491*
110800	80.409	13.112	-12.974	*1.6414*

Table 9.18: Location of peak maximum-shear stresses of Control Subject 2’s acetabulum during stance

ANSYS Node Number	X Location (mm)	Y Location (mm)	Z Location (mm)	Maximum Shear Stress (MPa)
123600	63.996	9.04	-6.2413	*3.1873*
123599	64.402	9.2891	-8.3484	*3.0242*
119858	63.55	8.5508	-5.0797	*2.9879*
160292	63.755	8.8047	-5.6634	*2.9655*
223196	64.385	9.3232	-8.8469	*2.9586*
120802	90.242	27.472	-3.9708	*2.9369*
130976	64.364	9.3654	-9.3445	*2.9055*
132282	84.384	23.968	3.0525	*2.9022*
121129	83.64	20.373	-8.4879	*2.8905*
126731	91.339	27.269	-2.6309	*2.8866*

Table 9.19: Location of peak maximum-shear stresses of Control Subject 2’s cartilage during squat

ANSYS Node Number	X Location (mm)	Y Location (mm)	Z Location (mm)	Maximum Shear Stress (MPa)
6683	79.362	19.083	-5.3403	*3.1237*
4836	83.112	21.85	5.7287	*3.0295*
10770	82.67	21.715	5.8271	*2.8108*
90	82.228	21.58	5.9255	*2.6238*
6651	78.825	18.909	-5.1046	*2.4893*
6347	84.485	-12.146	24.788	*2.3086*
4142	78.049	9.9421	-14.237	*2.3043*
6345	85.392	-12.371	25.027	*2.2856*
6652	78.955	18.703	-5.745	*2.2529*
5173	79.418	19.847	-3.2333	*2.2322*

Table 9.20: Location of peak maximum-shear stresses of Control Subject 2’s acetabulum during squat

ANSYS Node Number	X Location (mm)	Y Location (mm)	Z Location (mm)	Maximum Shear Stress (MPa)
63551	85.237	20.693	-8.8218	*4.3683*
144405	85.177	21.024	-8.1913	*3.7839*
63247	89.949	-20.387	21.105	*3.6368*
62588	85.122	21.344	-7.5542	*3.3940*
144401	85.69	21.15	-8.3084	*3.0391*
62589	83.621	20.229	-8.7265	*3.0211*
142915	84.43	20.458	-8.7723	*2.7787*
79017	90.903	-20.045	21.578	*2.7439*
88015	85.006	20.24	-9.4709	*2.6553*
127237	89.75	-19.831	21.809	*2.6305*

9.6 Appendix F – Strain Energy Density Calculations

The result files, processed in ANSYS Simulation, were opened in ANSYS Environment as RST files. The SE, volume, and location (in XYZ coordinate system) was obtained from the “Element Table” command of the “General Post-Processing” methods. Since the result files included all components of the full assembly (femur, cartilage, pelvis) (Figure 9.27), the surfaces exposed to the acetabulum were isolated for the post-processing analysis. The defined table of the elements were exported to Microsoft Excel, where the SE values were divided by the elemental volume, using Equation 9.1, to determine SED. This was performed first for the squatting position, then the exact same element and location was calculated for the standing position. Table 9.21 summarizes the peak SED value taken from the volume and SE of the element.

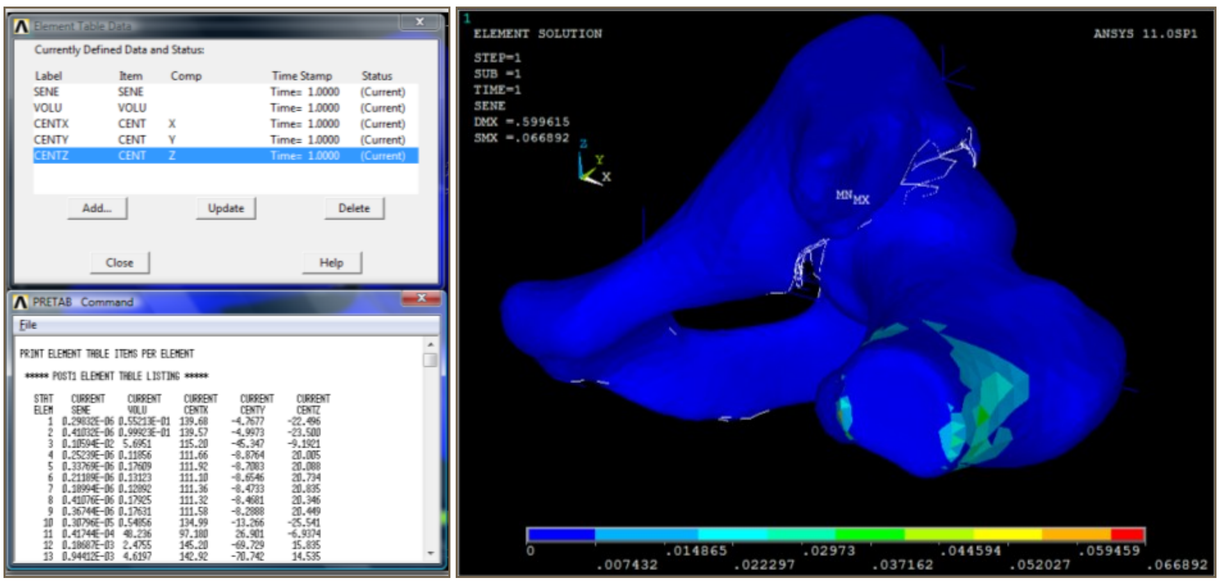

Figure 9.27: Layout of ANSYS Environment indicating the post-processing commands for the element data table. Data was obtained on the SE, volume, and location of each element on the acetabulum’s surface.

$$SED = \frac{SE}{Volume_{element}} = \frac{(J)}{(m^3)} = Pa \qquad \textbf{(9.1)}$$

Table 9.21: Summary of peak SED values and the associated elements and SE values on the acetabulum

Subject	Volume of Element (m^3)	SE at Stance (J)	SED at Stance (Pa)	SE at Squat (J)	SED at Squat (Pa)
FAI 1	3.3935E-09	3.6723E-06	*1082.17*	3.7494E-06	*1104.90*
FAI 2	2.7791E-09	2.5818E-06	*928.99*	2.6005E-05	*9357.23*
Con 1	3.0818E-09	4.1878E-06	*1358.90*	3.6840E-06	*1195.42*
Con 2	2.5401E-09	2.5410E-06	*1000.37*	2.5775E-06	*1014.74*